



HAL
open science

Application of Lorentz Force in Ultrasound-electromagnetic-field-coupled Electrical Impedance Tomography and Elastography

Zhishen Sun

► **To cite this version:**

Zhishen Sun. Application of Lorentz Force in Ultrasound-electromagnetic-field-coupled Electrical Impedance Tomography and Elastography. Medical Physics [physics.med-ph]. Université de Lyon; University of Chinese academy of sciences, 2019. English. NNT : 2019LYSE1261 . tel-03018104

HAL Id: tel-03018104

<https://theses.hal.science/tel-03018104>

Submitted on 22 Nov 2020

HAL is a multi-disciplinary open access archive for the deposit and dissemination of scientific research documents, whether they are published or not. The documents may come from teaching and research institutions in France or abroad, or from public or private research centers.

L'archive ouverte pluridisciplinaire **HAL**, est destinée au dépôt et à la diffusion de documents scientifiques de niveau recherche, publiés ou non, émanant des établissements d'enseignement et de recherche français ou étrangers, des laboratoires publics ou privés.



中国科学院大学
University of Chinese Academy of Sciences

N°d'ordre NNT : 2019LYSE1261

THESE de DOCTORAT DE L'UNIVERSITE DE LYON

opérée au sein de

l'Université Claude Bernard Lyon 1

Ecole Doctorale N° 205

Ecole Doctorale Interdisciplinaire Sciences-Santé

Spécialité de doctorat : Physique Appliquée

Discipline : Ingénierie Biologique et Médicale

Soutenue publiquement/à huis clos le 21/11/2019, par :

SUN Zhishen

Application of Lorentz Force in Ultrasound-electromagnetic-field-coupled Electrical Impedance Tomography and Elastography

Devant le jury composé de :

Mme. BENSAMOUN Sabine	Directrice de Recherche CNRS Université de Technologie de Compiègne, BMBI CNRS UMR 7338	Présidente
M. BOU MATAR Olivier	Professor École Centrale de Lille AIMAN-FILMS DE L'IEMN	Rapporteur
M. TANTER Mickaël	Directeur de Recherche INSERM ESPCI Paris, Physics for Medicine Paris	Rapporteur
M. BASSET Olivier	Professor Université Claude Bernard Lyon 1 CREATIS, CNRS UMR 5220 – INSERM U1206	Examineur
Mme. BRUSSEAU Elisabeth	Chargé de Recherche CNRS CREATIS, CNRS UMR 5220 – INSERM U1206	Examinatrice
M. JIA Kebin	Professor Beijing University of Technology	Examineur
Mme. RIBAY Guillemette	Ingénieur de Recherche - Chef de Projet CEA CEA-LIST, NDE Department	Examinatrice
M. LIU Guoqiang	Directeur de Recherche IEECAS Professor University of Chinese Academy of Sciences	Directeur de Thèse
M. CATHELIN Stefan	Directeur de Recherche INSERM Université de Lyon	Directeur de Thèse

ENCADREMENT:

Thesis supervisor: LIU Guoqiang

Thesis supervisor: CATHELINÉ Stefan

Complete title of the thesis:

Application of Lorentz force in ultrasound-electromagnetic-field-coupled electrical impedance tomography and elastography

Key words:

Hall effect imaging, linear frequency modulation, step-frequency technique, passive elastography, transient magnetic stimulation

INSTITUTION DELIVERING THE DOCTOR GRADE:

University of Chinese Academy of Sciences

Université Claude Bernard Lyon 1

NAME AND ADDRESS OF HOST LABORATORIES:

Institute of Electrical Engineering, Chinese Academy of Sciences (IEECAS)

No. 6 Beiertiao, Zhongguancun,

100190 Beijing P. R. China

Laboratory of Therapeutic Applications of Ultrasound (LabTAU, INSERM U1032)

151 Cours Albert Thomas,

69424 Lyon Cedex 03 France

Acknowledgements

I thank:

- My father who always tells me to be truthful, sincere, and courageous, and my mother who shows me through her own acts how to be industrious, smart and tenacious. And with the edification and encouragement from my parents, I accomplish the thesis through five years of work.

- My elder sister SUN Meixia, younger sister SUN Tingting, and younger brother SUN Haishen for the continuous and firm care, support, and encouragement that they always give to me.

- Professor LIU Guoqiang and Professor CATHELINE Stefan. I would like to thank Professor LIU specially for accepting me to be his PhD student and the supervision that he gives to me. I also would like to thank Professor CATHELINE specially for accepting me to work in LabTAU as a joint-PhD student under his supervision, and for the help on my life in Lyon and the supervision on my research in LabTAU.

- Professor BOU MATAR Olivier and Professor TANTER Mickaël for accepting to be the rapporteurs of this work, Professor BASSET Olivier, Professor BENSAMOUN Sabine, Professor BRUSSEAU Elisabeth, Professor JIA Kebin and RIBAY Guillemette for accepting to be the jury member.

- Professor TONG Jianzhong and Professor WU Shizeng specially for the recommendations on choosing the research topic, carrying out the research, and writing the thesis.

- XIA Hui, LI Shiqiang, LI Xiaonan, XIA Zhengwu, SONG Xianjin, GUO Liang, YANG Yanju, LI Yuanyuan, SUN Wenxiu, AN Huilin, WANG Zheng, and ZHANG Wenfeng specially for the lively discussion on my work, which broadens my mind and helps me find solutions to the problems encountered.

- Professor CHAPELON Jean-Yves and Professor LAFON Cyril specially for helping me register in Université Claude Bernard Lyon 1.

- BIRER Alain and THOMAS Gilles specially for their work on the thyristor modulator, which successfully loads solenoid coils and altogether generates transient

magnetic fields. Using the magnetic stimulation system, I successfully accomplished the experiments in the second part of the thesis.

- N'DJIN W. Apoutou and BAWIEC Christopher specially for their instructions and help on using the interferometric laser probe, under which I quickly learned how to use the probe to measure the nanometer-level displacement and successfully accomplished the experiments in Chapter 4.

- SOUCHON Rémi specially for the training, instructions and help on the usage of Verasonics Vantage Research Ultrasound Systems; and ZORGANI Ali, GIAMMARINARO Bruno, ZEMZEMI Chadi and AICHELE Johannes specially for the usage of Verasonics Vantage Research Ultrasound Systems and on making the agar phantom samples. With the assistance from them, I accomplished the ultrafast ultrasound imaging experiments in the second part of the thesis.

- LIU Guoqiang, TONG Jianzhong, WU Shizeng, RONG Juan, XIA Hui, LI Shiqiang, LI Yanhong, LI Xiaonan, ZHANG Chao, XIA Zhengwu, LIU Jing, YAN Xiaoheng, SONG Xianjin, GUO Liang, YANG Yanju, LV Jingxiang, NIU Chaoqun, LI Yuanyuan, SUN Wenxiu, AN Huilin, ZHAO Xiaohe, LI Cailian, DING Guangxin, SONG Jiaxiang, ZHAO Xinzhe, LI Xiaokai, WANG Lili, LIU Min, LI Liang, HAN Yaning, CHEN Hui, WU Ranran, and SHI Xiaoyu for the help and assistance during my work in the Institute of Electrical Engineering, Chinese Academy of Sciences.

- LAFON Cyril, CHAPELON Jean-Yves, CATHELIN Stefan, BIRER Alain, MESTAS Jean-Louis, MELODELIMA David, N'DJIN W. Apoutou, BERA Jean-Christophe, INSERRA Claude, GREILLIER Bernard, CHAVIRIER Françoise, SOUCHON Rémi, ZORGANI Ali, GIAMMARINARO Bruno, YE Wenfeng, DELATTRE Victor, NGO Jacqueline, PERIER Magali, BELABHAR Soufiane, CHAPELON Anthony, CHEN Yao, GUESSOUM Leila, IOCHEM Sandrine, GAREL Catherine, BAWIEC Christopher, SUAREZ Ivan, MATSUI Kazuhiro, GREILLIER Paul, CORNU Corentin, ZEMZEMI Chadi, THOMAS Gilles, VION Jérémy, AICHELE Johannes, DAUNIZEAU Loïc, LE GARREC Morgane, NGUYEN Anais, ASQUIER Nicolas, BARRERE Victor, FANT Cécile, SANCHEZ Marine, FAUCONNIER Maxime, CAO Elodie, ROBERT Jade, GANEAU Alice,

CAMBRONERO Sophie, and DERUELLE Tristan for the help on my life in Lyon and assistance on my work in LabTAU.

- LI Yang, ZHANG Huiliang, LI Shangkun, and MIAO Jiawei specially for the care they give to me when living in Room 428 of Building F in Youth Apartment, 80 Zhongguancun East Road, Beijing.

Abstract

The Lorentz force, as the linkage between the mechanical displacement and the electrical current, is investigated in this thesis in two fields of the medical acoustics, i.e. scanning electric conductivity gradients with ultrasonically induced Lorentz force (SECG-UILF) and elastography.

The first part of the thesis studies the SECG-UILF. To reduce the instantaneous stimulation power to the transmitting transducer and at the same time the peak acoustic pressure from the transducer, this thesis proposes to apply the linearly frequency-modulated ultrasound pulse excitation or the sinusoidal step-frequency ultrasound pulse excitation in SECG-UILF.

For the scanning electric conductivity gradients with linearly frequency-modulated ultrasound-induced Lorentz force (SECG-LFM-UILF), first, two schemes - the coherent demodulation scheme and the pulse compression scheme - of reconstruction of the longitudinal distance of the electric conductivity gradients to the transducer are studied independently. The SECG-LFM-UILF uses electrical signal of peak instantaneous power of 39.54 dBm to excite the transmitting transducer, which is 25.5 dB lower than the peak instantaneous power of the negative high-voltage narrow pulse (65.05 dBm) adopted in traditional SECG-UILF; and at the same time, the peak transmitting acoustic pressure in SECG-LFM-UILF is 0.44 MPa lower than that in traditional SECG-UILF. Experiments are done to confirm the feasibility and the performance of SECG-LFM-UILF with either the coherent demodulation scheme or the pulse compression scheme, using multi-shaped saline agar phantoms of conductivity ranging from 0.2 S/m to 0.5 S/m. The experiment results show that: (1) the SECG-LFM-UILF can detect precisely the longitudinal distance of the electric conductivity gradients; (2) the signal-to-noise ratio of the reconstructed B-scan images of the electrical conductivity gradient distribution by the SECG-LFM-UILF are comparable to that obtained through the traditional SECG-UILF; and (3) using modulation frequency bandwidth of 2 MHz and modulation duration of 500 μ s, a longitudinal resolution of 1 mm is achieved.

For scanning electric conductivity gradients with step-frequency ultrasound induced Lorentz force (SECG-SF-UILF), the theory of application of the step-frequency technique to reconstruction of the longitudinal distance of the electric conductivity gradients is formulated in terms of the in-phase demodulation scheme and the in-phase/quadrature-phase (IQ) demodulation scheme. Compared with the IQ demodulation scheme, the in-phase demodulation scheme is simple in hardware implementation but can only detect half of the longitudinal range. Experiments of SECG-SF-UILF are done on a sample of two-layer copper foil, and the results demonstrate that, using a frequency bandwidth of 2 MHz and 64 discrete frequencies, the longitudinal range of the sample can be detected precisely.

The second part of the thesis studies elastography which uses the cross-correlation approach to reconstruct the shear wave velocity. To expand the frequency bandwidth of the shear wave displacement field so as to improve the quality of the shear wave velocity map reconstructed using the cross-correlation approach, this part studies application of the Lorentz force for generation of shear wave sources that utilized for elastography.

First, generation of shear wave sources on the soft medium surface is investigated by stimulating a non-ferromagnetic conductive ring or patch with a transient magnetic field. Due to the Faraday's law of induction, an eddy current is generated remotely in the conductive ring or patch by the transient magnetic field. The eddy current at the same time couples with the magnetic field, generating the Lorentz force, which constitutes a torque on the ring or patch and vibrates the ring or patch. The origin and the frequency and amplitude characteristics of the Lorentz force acting on the conductive ring are confirmed by the displacement measurement using an interferometric laser probe: (1) the eddy current induced by the transient magnetic field and the orthogonal component of the magnetic field constitute the two essential elements of the Lorentz force; (2) the carrier frequency of the Lorentz force equals the sum of the carrier frequencies of the stimulating transient magnetic field and its time derivative; and (3) the amplitude of the Lorentz force increases quadratically upon the amplitude of the stimulating current to the coil. Under a transient magnetic field of

changing rate of 10.44 kTs^{-1} , the patch generates a shear wave field source of amplitude of $100 \mu\text{m}$ at the surface of the sample of polyvinyl alcohol (PVA) phantom. The shear wave fields created and propagating in the PVA phantom by experiments agree qualitatively well with the theoretical shear wave fields calculated through the analytical Green function solution.

Then, the potential of the generated shear wave fields for the cross-correlation based shear wave velocity reconstruction is explored. The displacement fields in the multi-shaped soft biological tissue mimicking agar phantoms are recorded at a sampling rate of 1000 frames/s as the multiple shear wave sources propagate in the phantoms. Based on the cross-correlation approach, the shear wave velocity maps are reconstructed from 100 frames of the displacement fields, which show that: (1) the interfaces or boundaries between regions of different stiffness can be clearly recognized, which are completely concealed in the ultrasound images; (2) cylindrical inclusions of diameter as small as 5 mm can be differentiated from the background, but at the same time, there are phony boundaries in the homogeneous areas which undermine the performance of the method; and (3) using the cross-correlation approach, it is possible to qualitatively but not quantitatively reconstruct the shear wave velocity in the samples from 100 frames of the displacement fields.

Key Words: Hall effect imaging, linear frequency modulation, step-frequency technique, passive elastography, transient magnetic stimulation

Résumé

La force de Lorentz, en tant que le lien entre le déplacement mécanique et le courant électrique, est étudié dans cette thèse dans les deux domaines de l'acoustique médicale: le balayage des gradients de conductivité électrique avec la force de Lorentz induite par ultrasons (SECG-UILF) et l'élastographie.

La première partie de la thèse étudie le SECG-UILF. Pour réduire la puissance de stimulation instantanée du transducteur émetteur et en même temps la pression acoustique maximale du transducteur, cette thèse propose d'appliquer l'excitation de l'impulsion ultrasonore à la modulation de fréquence linéaire ou l'excitation de l'impulsion ultrasonore à fréquence sinusoïdale dans SECG-UILF.

Pour les gradients de conductivité électrique à balayage avec la force de Lorentz induite par l'ultrasons à la modulation de fréquence linéaire (SECG-LFM-UILF), deux schémas - le schéma de démodulation cohérente et le schéma de compression d'impulsions - de reconstruction de la distance longitudinale des gradients de conductivité électrique au transducteur sont étudiés indépendamment. Le SECG-LFM-UILF utilise un signal électrique de puissance instantanée maximale de 39,54 dBm pour exciter le transducteur de transmission, ce qui est inférieur de 25,5 dB à la puissance instantanée maximale de l'impulsion étroite haute tension négative (65,05 dBm) adopté dans le SECG-UILF traditionnel. Et en temps, la pression acoustique d'émission maximale dans le SECG-LFM-UILF est inférieure de 0,44 MPa à celle du SECG-UILF traditionnel. Des expériences sont effectuées pour confirmer la faisabilité et la performance de SECG-LFM-UILF avec le schéma de démodulation cohérent ou le schéma de compression d'impulsions, en utilisant des fantômes de conductivité à plusieurs formes d'agar salin allant de 0,2 S/m à 0,5 S/m. Les résultats de l'expérience montrent que: (1) le SECG-LFM-UILF peut détecter avec précision la distance longitudinale des gradients de conductivité électrique; (2) le rapport signal sur bruit des images de balayage B reconstituées de la distribution de gradient de conductivité électrique par le SECG-LFM-UILF est comparable à celui obtenu par le biais du SECG-UILF traditionnel; et (3) en utilisant une largeur de bande de

fréquence de modulation de 2 MHz et une durée de modulation de 500 μ s, une résolution longitudinale de 1 mm est obtenue.

Pour balayer des gradients de conductivité électrique avec une force de Lorentz induite par ultrasons à fréquence fréquentielle (SECG-SF-UILF), la théorie de l'application de la technique de fréquence incrémentielle à la reconstruction de la distance longitudinale des gradients de conductivité électrique est formulée en termes de schéma de démodulation de phase et le schéma de démodulation en phase/quadrature-phase (IQ). Comparé au schéma de démodulation IQ, le schéma de démodulation en phase est simple à implémenter en matériel mais ne peut détecter que la moitié de la plage longitudinale. Des expériences de SECG-SF-UILF sont effectuées sur un échantillon de feuille de cuivre à deux couches et les résultats démontrent qu'en utilisant une largeur de bande de fréquences de 2 MHz et 64 fréquences discrètes, la plage longitudinale de l'échantillon peut être détectée avec précision.

La deuxième partie de la thèse étudie l'élastographie, qui utilise l'approche decorrélation croisée pour reconstruire la vitesse d'onde de cisaillement. Pour étendre la largeur de bande de fréquence du champ de déplacement de l'onde de cisaillement afin d'améliorer la qualité de la carte de vitesse de l'onde de cisaillement reconstruite à l'aide de l'approche decorrélation croisée, cette partie étudie l'application de la force de Lorentz pour la génération des sources d'onde de cisaillement utilisées en élastographie.

Tout d'abord, la génération des sources des ondes de cisaillement sur la surface du support souple est étudiée en stimulant un anneau ou un patch conducteur non ferromagnétique avec un champ magnétique transitoire. En raison de la loi d'induction de Faraday, un courant de Foucault est généré à distance dans l'anneau ou le patch conducteur par le champ magnétique transitoire. Le courant de Foucault en même temps se couple avec le champ magnétique, générant la force de Lorentz, qui constitue un couple sur la bague ou le timbre et fait vibrer la bague ou le timbre. La mesure de déplacement à l'aide d'une sonde laser interférométrique confirme les caractéristiques d'origine, de fréquence et d'amplitude de la force de Lorentz agissant

sur l'anneau conducteur: (1) le courant de Foucault induit par le champ magnétique transitoire et la composante orthogonale du champ magnétique constituent les deux éléments essentiels de la force de Lorentz; (2) la fréquence porteuse de la force de Lorentz égale la somme des fréquences porteuses du champ magnétique transitoire stimulant et de sa dérivée temporelle; et (3) l'amplitude de la force de Lorentz augmente quadratiquement avec l'amplitude du courant de stimulation dans la bobine. Sous un champ magnétique transitoire dont la vitesse de changement est de $10,44 \text{ kTs}^{-1}$, le patch génère une source de champ des ondes de cisaillement d'amplitude de $100 \text{ }\mu\text{m}$ à la surface de l'échantillon de fantôme d'alcool polyvinylique (PVA). Les champs d'ondes de cisaillement créés et se propageant dans le fantôme de PVA par des expériences concordent bien qualitativement avec les champs des ondes de cisaillement théoriques calculés au moyen de la solution de fonction analytique de Green.

Ensuite, le potentiel des champs d'ondes de cisaillement générés pour la reconstruction de la vitesse des ondes de cisaillement basée sur la corrélation croisée est exploré. Les champs de déplacement dans le tissu biologique souple multiforme imitant les fantômes d'agar sont enregistrés à un taux d'échantillonnage de 1000 frames/s , les multiples sources des ondes de cisaillement se propagent dans les fantômes. Sur la base de l'approche de corrélation croisée, les cartes de vitesse d'onde de cisaillement sont reconstituées à partir de 100 frames de champs de déplacement, ce qui montre que: (1) les interfaces entre les régions de rigidité différente peuvent être clairement reconnues par les images échographiques; (2) des inclusions cylindriques d'un diamètre aussi petit que 5 mm peuvent être différenciées de l'arrière-plan, mais en même temps, il existe des frontières factices dans les zones homogènes qui compromettent la performance de la méthode; et (3) en utilisant l'approche de corrélation croisée, il est possible de reconstruire qualitativement mais non quantitativement la vitesse de l'onde de cisaillement dans les échantillons à partir de 100 frames des champs de déplacement.

Mots-clés: imagerie à effet Hall, modulation de fréquence linéaire, technique de fréquence progressive, élastographie passive, stimulation magnétique transitoire

摘要

洛伦兹力通过磁场可以实现导体运动与导体中电流的相互转化。本文研究了洛伦兹力在基于超声激发洛伦兹力的电导率梯度成像 (Scanning Electric Conductivity Gradients with Ultrasonically Induced Lorentz Force, SECG-UILF) 和弹性成像 (Elastography) 中的应用。

本文的第一部分研究基于超声激发洛伦兹力的电导率梯度成像。为了降低发射超声换能器的瞬时激励功率,同时也为了降低超声脉冲激励的峰值声压,本文提出在基于超声激发洛伦兹力的电导率梯度成像中应用线性调频超声脉冲激励或步进频超声脉冲激励。

对于基于线性调频超声脉冲激发洛伦兹力的电导率梯度成像 (Scanning Electric Conductivity Gradients with Linearly Frequency-Modulated Ultrasound-Induced Lorentz Force, SECG-LFM-UILF), 本部分首先研究了两种存在电导率跳变的介质的纵向距离的求解方案 - 基于相干解调技术的求解方案和基于脉冲压缩技术的求解方案。基于线性调频超声脉冲激发洛伦兹力的电导率梯度成像用瞬时峰值功率为 39.54 dBm 的电信号激励发射超声换能器,比传统方法所用的负高压脉冲信号 (瞬时峰值功率为 65.05 dBm) 低 25.5 dB, 同时,产生的超声脉冲激励的峰值声压比传统方法低 0.44 MPa。利用电导率介于 0.2 S/m 至 0.5 S/m 的多形琼脂仿体样本,实验验证了基于线性调频超声脉冲激发洛伦兹力的电导率梯度成像 (包括相干解调实现方案和脉冲压缩实现方案) 的可行性和性能。实验结果表明,基于线性调频超声脉冲激发洛伦兹力的电导率梯度成像:(1) 可以准确地测得样本中存在电导率跳变的介质的纵向距离;(2) 重建的样本电导率梯度二维图的信噪比与传统方法相当;(3) 利用 2 MHz 的调频带宽和 500 μ s 的脉冲宽度,可以实现 1 mm 的纵向分辨率。

对于基于步进频率超声脉冲激发洛伦兹力的电导率梯度成像 (Scanning Electric Conductivity Gradients with Step-Frequency Ultrasound-Induced Lorentz Force, SECG-SF-UILF), 基于单通道同相解调方案和基于双通道同相/正交相解调方案,本文首先建立了应用步进频技术求解存在电导率跳变的介质的纵向距离的数学模型。与双通道同相/正交相解调方案相比,单通道同相解调方案硬件实现简单但纵向成像范围减半。然后,用双层铜箔样本做基于步进频率超声脉冲激

发洛伦兹力的电导率梯度成像实验。实验结果表明：利用 2 MHz 频率带宽和 64 个均匀步长的频点，这种成像方法可以准确测得样本的纵向距离。

本文第二部分研究基于互相关运算求解剪切波速度的弹性成像。为了产生宽频带的剪切波位移源以提高基于互相关运算重建的剪切波速度图的质量，本文研究了应用洛伦兹力产生剪切波位移源并应用于弹性成像。

首先，本部分首先研究了利用瞬变磁场激励非铁磁性导电金属片环（或金属片）振动并在软介质表面产生剪切波源。由于法拉第电磁感应，瞬变磁场在金属片环（或金属片）中产生电流涡流。电流涡流同时与磁场耦合产生洛伦兹力。这些洛伦兹力在金属片上构成功矩，使金属片振动。利用激光干涉测距仪测量金属片环的位移，证实了作用在金属片环上的洛伦兹力的起源、频率和幅度特征：（1）瞬变磁场在金属片环上感应出的涡流电流和正交向的磁场构成洛伦兹力的两个基本要素；（2）洛伦兹力的载波频率等于瞬变磁场信号和其变化率信号的载波频率之和；并且（3）其幅度随线圈激励电流幅度二次方率增长。利用变化率为 10.44 kTs^{-1} 的瞬变磁场激励金属片可以在聚乙烯醇（Polyvinyl alcohol, PVA）仿体样本表面产生幅度达 $100 \mu\text{m}$ 的剪切波位移。实验测得的在 PVA 仿体内部传播的剪切波位移与用格林函数求得的剪切波位移的理论值定性地吻合。

然后，本部分探索了产生的多个剪切波位移源在基于互相关运算的剪切波速度重建方面的性能。采集多个剪切波位移源在多形软生物组织琼脂仿体样本中传播的位移场（采样率为 1000 帧/秒），并用互相关方法由 100 帧位移图重建仿体中剪切波速度的二维图。重建的波速二维图表明：（1）样本中软硬区域间的分界面或边沿可以清楚地被识别，而在超声图像中，这些分界面完全不能被发现；（2）直径小至 5 mm 的圆柱内含物（其硬度不同于背景部分的仿体）可以被识别；但同时，在软硬度均匀的区域，存在伪分界面，降低了波速图的质量；（3）基于互相关运算的剪切波速度重建方法只能从 100 帧剪切波位移图求得样本中剪切波速度的定性值，但无法求得定量值。

关键词：霍尔效应成像，线性调频技术，步进频技术，被动弹性成像，瞬变磁场激励

Content

Acknowledgements.....	I
Abstract.....	V
Résumé.....	IX
摘 要.....	XIII
Chapter 1 Introduction	1
1.1 Significance of the topic and supporting programs	1
1.1.1 Electrical impedance tomography.....	1
1.1.2 Elastography	3
1.1.3 Supporting programs.....	7
1.2 Summary of the status of the research topic	8
1.2.1 The Lorentz force.....	8
1.2.2 The role of Lorentz force in electrical impedance tomography.....	8
1.2.2.1 Magneto-acoustic imaging of bioelectric currents.....	8
1.2.2.2 Forward mode of the Hall effect imaging.....	10
1.2.2.3 Reverse mode of the Hall effect imaging.....	12
1.2.2.4 Scanning electric conductivity gradients with ultrasonically- induced Lorentz force	14
1.2.2.5 Magneto-acoustic tomography with magnetic induction.....	16
1.2.2.6 Magneto-acousto-electrical tomography	18
1.2.3 The role of Lorentz force in functional magnetic resonance imaging (fMRI).....	20
1.2.3.1 Lorentz effect imaging of action current using MRI	20
1.2.4 Application of Lorentz force in elastography	21
1.2.4.1 Electromagnetic actuator in MR elastography.....	22
1.2.4.2 Direct generation of shear wave in soft tissues.....	22
1.3 Structure of the thesis.....	25
1.4 Highlights of innovations in the thesis.....	27
Part 1 Scanning electric conductivity gradients with ultrasonically-induced Lorentz	

force	29
Chapter 2 Scanning electric conductivity gradients with linearly frequency-modulated ultrasound-induced Lorentz force	31
2.1 Measured current signal in SECG-UILF	32
2.2 Linearly frequency-modulated ultrasound pulse stimulation and the current signal generated	34
2.3 Calculation of the longitudinal distance - using coherent demodulation scheme	35
2.4 Calculation of the longitudinal distance - using pulse compression scheme ..	39
2.5 Experimental setup and methods	41
2.5.1 LFM ultrasound pulse generation system	42
2.5.2 Magnetic field	46
2.5.3 Sample	47
2.5.4 Signal detection system	49
2.5.5 Four SECG-LFM-UILF experiments using linearly frequency modulated ultrasound pulse	50
2.5.6 SECG-UILF using high-voltage narrow pulse signal	53
2.6 Experiment results and discussion	55
2.6.1 The first group of experiment - confirmation of the feasibility of SECG-LFM-UILF	55
2.6.2 The second group of experiments - B-scan image of multi- shaped agar phantoms	59
2.6.2.1 SECG-UILF on a multi-shaped saline agar phantom with a rectangular hole inside	59
2.6.2.2 SECG-UILF on a multi-shaped 3-layer saline agar phantom	63
2.6.3 The third group of experiments - demonstration of the longitudinal resolution	65
2.6.4 The fourth group of experiments - retrieving the conductivity gradient polarity by the IQ-coherent-demodulation-scheme-based SECG-LFM-UILF	70

2.7 Chapter summary	71
Chapter 3 Scanning electric conductivity gradients with step-frequency ultrasound induced Lorentz force	73
3.1 Application of step-frequency technique	73
3.1.1 Calculation of the longitudinal distance - the in-phase coherent demodulation scheme	76
3.1.2 Calculation of the longitudinal distance - the in-phase/quadrature-phase (IQ) coherent demodulation scheme.....	77
3.2 Theoretical analysis and experiments	78
3.3 Results and discussion	80
3.4 Chapter summary	81
Part 2 Shear wave generation by the Lorentz force and its application in elastography	83
Chapter 4 Shear wave generation by remotely exciting aluminum patches with a transient magnetic field.....	87
4.1 Characteristics of the Lorentz force induced	87
4.2 Displacement of the aluminum patch under the stimulation of a transient magnetic field	89
4.2.1 The transient pulsed magnetic field	90
4.2.2 Three groups of experiments measuring the displacements of the aluminum ring.....	92
4.3 The Shear wave displacement fields in the soft medium generated by the aluminum patch under the transient Lorentz force	93
4.3.1 Ultrafast ultrasound imaging and calculation of the shear wave displacement of the medium.....	93
4.3.2 Two experiments measuring the medium displacements.....	94
4.3.3 Theoretical longitudinal displacement field in the PVA phantom calculated using the Green function	95
4.4 Results and discussion	97
4.4.1 Confirmation of the Lorentz force origins	97

4.4.2	The frequency characteristics of the Lorentz force.....	99
4.4.3	The amplitude characteristic of the Lorentz force	101
4.4.4	The propagation of shear wave displacement in the PVA phantom....	102
4.4.5	Propagation of multiple shear wave sources in multi-shaped agar phantom	104
4.5	Chapter summary	104
Chapter 5	Ultrasound elastography with the shear wave source generated by vibrating aluminum patches with a transient magnetic field	107
5.1	Elastography experiments on multi-shaped agar phantoms.....	107
5.1.1	The transient pulsed magnetic field and the aluminum patches actuators	109
5.1.2	Ultrafast ultrasound imaging and calculation of the shear wave displacement fields	110
5.1.3	Shear wave velocity reconstruction using the cross-correlation- based approach.....	111
5.1.4	Five samples of multi-shaped agar phantoms.....	113
5.1.5	Three groups of ultrasound elastography experiments	120
5.1.6	The control experiment - generation of shear waves using a mechanical actuator	122
5.2	Results and discussion	123
5.2.1	Elastography of the 3-layer multi-shaped agar phantom sample.....	123
5.2.2	Elastography of the multi-shaped agar phantoms samples with four cylinder inclusions.....	126
5.2.3	Qualitative rather than quantitative reconstruction of shear wave velocity	130
5.3	Chapter summary	140
Chapter 6	Conclusions and future work.....	141
6.1	Overall conclusions.....	141
6.2	Challenges and possible solutions	143
Appendix 1	Derivation of (2.8).....	145

Appendix 2: Derivation of (3.4)..... 149

Appendix 3: Derivation of (3.7)..... 151

Bibliography 153

Biography..... 165

Chapter 1 Introduction

The Lorentz force, which connects the electrical current and the mechanical motion, attracted researchers' attention and had been explored a lot during the past two decades in many fields of biomedical imaging, such as electrical impedance tomography, elastography, etc. For the conductive medium placed in the magnetic field, the induced Laplace force - when there is electrical current passing through the medium (the electrical current density is not completely parallel with the magnetic field) - introduces movement into the medium. This is the electrics-to-mechanics mechanism of the Lorentz force. And for the moving conductive medium in the magnetic field (the direction of the movement is not totally parallel with the magnetic field), the charged particles (like ions in saline solutions) deviate toward the direction perpendicular with both the magnetic field and the movement. This is the mechanics-to-electrics mechanism of the Lorentz force.

1.1 Significance of the topic and supporting programs

1.1.1 Electrical impedance tomography

The electrical properties of biological tissue include conductivity and permittivity. Among various biological tissues, the conductivity and permittivity have broad ranges. Basically, the human fluids, for instance the cerebrospinal fluid and the plasma, have relatively high conductivity, while the bone and the adipose tissue have low conductivity. These parameters also are indicators of underlying physiological and pathological conditions in the body. For example, the measurement of thorax impedance is useful in monitoring cardiac and pulmonary functions such as stroke volume (Bache *et al.* 1969) and lung ventilation (Baker and Geddes 1970); and it also may be used for early breast cancer screening as many researches have shown that cancerous breast tissue has significantly higher conductivity than its surrounding tissues (Surowiec *et al.* 1988, Jossinet 1998).

In addition, the conductivity and the permittivity of the biological tissue are important biophysical parameters in modeling living systems. For instance, an

accurate volume conductor model plays an important role in studying the electrophysiological activities of excitable organs such as the heart and the brain (Malmivuo and Plonsey 1995). This could be used to improve the accuracy of locating the source of this electrical activity in the excitable organs through surface recordings of the resultant electrical signals, as in electroencephalograms (EEG) and electrocardiograms (ECG) (He 2004). And a bio-impedance model of the body is also needed in understanding the interactions of the electromagnetic stimulations applied to the biological tissue as a part of a diagnostic or therapeutic system. Such modeling could be used to manage the application of electromagnetic energy delivered to the tissue, as in a high field MRI system or with electrical neural stimulation systems like transcranial magnetic stimulation (TMS). Therefore, a high resolution, cost-effective and non-invasive imaging modality that can give accurate estimation of the electrical properties of biological tissue is highly desired.

Over the past few decades, several techniques have been explored to estimate the electrical property distribution in biological tissue. These techniques involve inducing some form of electromagnetic field in the tissue being studied and estimating the impedance distribution in the tissue from the electromagnetic field measured. Because of the nonlinear dependence of the electromagnetic fields on the impedance, the estimating procedure is quite complicated. Various electromagnetic methods are used for imaging tissue impedance including electrical impedance tomography (EIT) (Barber and Brown 1984), magnetic resonance electrical impedance tomography (MREIT) (Khang *et al* 2002), magnetic induction tomography (MIT) (Griffiths *et al.* 1999), and microwave imaging (Maeney *et al* 2000). However, due to the limited number of unique points on the surface at which the voltages can be measured, the EIT inverse problem suffers from ill-posedness. This results in the low spatial resolution impedance image that can be obtained by the EIT method. MREIT can provide impedance distribution of high spatial resolution, but compared with the EIT or the MIT methods, it relies on the magnetic resonance imaging and therefore suffers from long operating time and high cost. So far none of these methods have gained broad clinical applications. In order to improve the spatial resolution, the hybrid

methods using ultrasound and electromagnetic fields coupling have been proposed, which include magneto-acoustic tomography (Towe and Islam 1988), Hall effect imaging (HEI) (Wen *et al.* 1998), scanning electric conductivity gradients with ultrasonically induced Lorentz force (SECG-UILF) (Montalibet *et al.* 2001a, 2001b), magneto-acoustic tomography with magnetic induction (He 2005), and magneto-acousto-electrical tomography (MAET) (Xu *et al.* 2007, Haider *et al.* 2008, Renzhiglova *et al.* 2010, Guo *et al.* 2015). These ultrasound-electromagnetic-field coupling methods inherit the merit of high spatial resolution of ultrasound and the merit of high contrast of electrical impedance tomography. The first part of the thesis aims to study and develop the SECG-UILF.

1.1.2 Elastography

Mechanical properties of the human tissues are determined by tissue compositions, inflammation effects, cell proliferation, etc, which vary among different biological tissues and upon various pathological states for the same biological tissue. For instance, the human muscle tissue is remarkably stiffer than the healthy liver tissue. And, cirrhotic livers tend to be stiffer than healthy livers because of fibrosis (Yeh *et al.* 2002). Variations in the mechanical properties of tissue also go with therapeutic procedures, such as radio-frequency (RF) ablation which results in the denaturing of proteins and an inflammatory response stiffening the induced lesion (Varghese *et al.* 2002). Therefore, the mechanical characteristics of the soft tissue are considered as biomarkers for disease diagnosis. Since ancient time, the palpation has been one of the most common practices in tradition medicine. Nowadays, with the emergence of advanced medical imaging technologies, a more objective and less operator dependent method has been developed, which is called elastography.

From a mechanical point of view, these mechanical properties are characterized by the Lamé constants: λ referred as bulk modulus and characterizing the response of the solid to compression and μ the shear modulus quantifying the response to shear stress. The compressive modulus of the biological soft tissue is significantly higher than the shear modulus, therefore the biological tissue can be considered as virtually

incompressible, having a like behavior of fluids when subjected to a compressive stress. Among the various biological tissues, the bulk modulus has a narrow window of variation between 1 GPa and 10 GPa while the shear modulus varies several orders of magnitude, from 100 Pa to 100 MPa (Sarvazyan *et al.* 1998).

In an elastic, isotropic and homogeneous soft medium, the displacement field can be divided into three components: the compression wave field, the shear wave field, and the coupling between the two previous waves (Aki and Richards 2002). The amplitude of the coupling term decreases in $1/r^3$ while the compression and the shear waves decrease in $1/r$. The coupling term therefore is the near field wave compared to the other two components of the wave field. The compression wave speed equals $\sqrt{(\lambda + 2\mu)/\rho}$ while the shear wave speed equals $\sqrt{\mu/\rho}$. The majority of the human body is made of water (around 70%) and the variation of density among various soft tissues is less than 5% (Cobbold 2006). So if the density is considered as constant, the shear wave speed is exclusively determined by the shear modulus, and vice versa. In soft media, the compression wave speed is significantly greater than the shear wave speed, and the amplitudes of both waves are inversely proportional to the square of their propagation speed. The compression wave therefore propagates instantly and has a very negligible amplitude in the far field, compared to the shear wave. Therefore, using a fast imaging device, the shear wave displacement can be captured, from which the shear wave speed and the shear modulus can be computed. This is the fundamental principle of dynamic elastography.

Generally, elastography consists of three elementary steps: (1) exciting to generate tissue displacement; (2) acquiring the displacement field; and (3) reconstruction of mechanical parameters. Since the emergence of elastography about 37 years ago (Dickinson and Hill 1982), innovations have taken place in all three elementary steps. A variety of approaches have been proposed. Among them are:

(1) Quantification of natural motion of human organs (Dickinson and Hill 1982) and echoseismography using controlled monochromatic vibrations (Eisensher *et al.* 1983). These two methods qualitatively distinguished the soft from the stiff tissues based on the displacement amplitude of the tissues.

(2) Sono-elastography first realized in 1987 (Krouskop *et al.* 1987) and given the name in 1988 (Lerner *et al.* 1988). The method used Doppler ultrasound to measure the oscillations under the externally applied vibrations but could only measure qualitatively the shear elasticity of biological tissue.

(3) Strain Elastography (Ophir *et al.* 1991). The method based on the scalar Hooke's Law and consisted of applying a stress using the ultrasound probe and measuring the induced strain using the standard speckle tracking technique. This method still only provided a qualitative measurement of the tissue's shear modulus. Nowadays, Siemens, Hitachi, BK Medical *et al.* have installed the strain elastography in their ultrasound systems.

(4) Magnetic resonance elastography (MRE) (Muthupillai *et al.* 1995). This method was similar to sono-elastography in applying monochromatic excitation on the medium under investigation but could obtain a quantitative shear wave speed in the medium. In their experiments, they cleverly utilized the Lorentz force from the coupling of the main magnetic field of the MRI scanner and the oscillating current in the actuating coil and created the shear wave displacement at the medium surface. As the MRI scanner measured the three components of the displacement field, MRE could measure the anisotropy and the viscosity of the biological tissue (Sinkus *et al.* 2005).

(5) 1D transient elastography developed around 1998 by S. Catheline and 2D transient elastography developed around 2004 by J. Bercoff during their PhD theses respectively (Catheline 1998, Bercoff 2004). These two methods used an external mechanical actuator or a piston integrated into the ultrasound probe to exert an impulsive excitation on the surface of the medium and used a focused transducer to record the shear displacement at a sampling rate higher than 1300 samples per second (5000 samples per second in 2D transient elastography). The transient elastography opened a reliable alternative providing quantitative elastography measurements. Due to its effectiveness, this approach was finally implemented in a stand-alone device the Fibroscan manufactured by Echosens to characterize the stage of the liver fibrosis.

(6) Vibro-acoustography (Fatemi and Greenleaf 1999). This method employs a

confocal transducer to produce two intersecting continuous ultrasound waves with slight frequency difference Δf , which creates an oscillating radiation force of the difference frequency Δf over the region of interests. The sound from the vibration of the medium was detected by a hydrophone tuning to the difference frequency. The limitation of this method was that the measured sound wave may be affected by the geometry of the target medium and was not directly related to the medium viscoelastic properties.

(7) Shear Wave Elasticity Imaging (SWEI) (Sarvazyan *et al.* 1998) and Acoustic Radiation Force Impulse (ARFI) imaging (Nightingale *et al.* 2002). These two approaches were quite similar and they focused an ultrasonic beam for a few microseconds to a given depth and a variety of parameters were evaluated by analyzing the mechanical response of the tissue under this solicitation. The ultrasound probe served both as the excitation device and as the acquisition device, allowing the system to be more compact. But the technique did not provide a quantitative measurement of the shear modulus.

(8) Supersonic Shear Imaging (SSI) developed also around 2004 by Bercoff during his PhD thesis (Bercoff 2004). This technique actually was a revised version of 2D transient elastography by incorporating the idea of ARFI. To increase the shear wave propagation depth, the ultrasound pulses were focused successively at different depths of the target media to create constructive interference along a Mach cone. And by recording the propagation of the induced shear wave, a quantitative 2D elasticity map can be obtained in real time. The success of this method gave birth to the clinical imaging system - Aixplorer - by Supersonic Imaging.

(9) Natural Shear Waves Imaging or Passive Elastography. In 1996, H. Kanai *et al.* evaluated the thickness change of the heart wall accompanying the cardiac motion based on the vibration amplitude of the heart wall and used the information for heart disease diagnosis (Kanai *et al.* 1996). In 2002, E. Konogagou *et al.* estimated the local cardiac muscle displacement and strain in a human heart utilizing the passive cardiac muscle motion during a cardiac cycle as the mechanical stimulus. The method was qualitative as only a strain map was given (Konofagou *et al.* 2002). In 2007, K. Sabra

et al. succeeded retrieval of the tissue's shear modulus and shear viscosity parameters from the shear wave profile, which was extracted by applying cross correlation to the noise-like displacement measurements from sixteen miniature accelerometers mounted on the vastus laterali muscle (Sabra *et al.* 2007). In 2011, T. Gallot *et al.* measured the natural displacement inside a healthy human liver using an ultrasound scanner and retrieved the shear wave speed map using the noise correlation method (Gallot *et al.* 2011). In 2016, A. Zorgani *et al.* recorded the passive shear waves in the brain tissue using MRI scanner and retrieved the shear wavelength tomography of the brain tissue from these noise-like field using the noise correlation method (Zorgani *et al.* 2016).

The second part of the thesis aims to study and develop generating the shear wave displacement sources for elastography using the Lorentz force.

1.1.3 Supporting programs

The thesis is mainly supported by the following programs:

(1) The Key Program of the National Natural Science Foundation of China (Grant No. 51137004): Research on the Lorentz-force-acoustic-source-based magneto-acoustic imaging of the biological conductivity.

(2) The Major Scientific Instrument and Equipment Development Program of the National Natural Science Foundation of China (Grant No. 61427806): Research and instrument and equipment development of the acoustic-radiation-force-Lorentz-force-based ultrasound magneto-electric dual-modality imaging method.

(3) The Scientific Instrument and Equipment Development Program of the Chinese Academy of Sciences (Grant No. YZ201507): The scientific instrument and equipment development of the focused acoustic-radiation-force-based magneto-acousto-electrical imaging.

(4) The State-Sponsored Post-graduate Studying Abroad Program of the China Scholarship Council (Grant No. 201604910849): Ultrasound elastography using the shear wave source generated by the Lorentz force.

(5) DEVweCAN LabEx - Cancer Development and Targeted Therapies - awarded

by Government in Lyon (France) and supported by University of Lyon.

1.2 Summary of the status of the research topic

1.2.1 The Lorentz force

The expression of the Lorentz force has the microscopic and the macroscopic forms. The microscopic form applies to charged particles moving in the magnetic field while the macroscopic form applies to conductors or conductive medium with electricity passing through.

The microscopic form: Consider a particle with charge q and moving in the speed \mathbf{v} in the magnetic field \mathbf{B} , the Lorentz force \mathbf{F} experienced by the particle then is:

$$\mathbf{F} = q \mathbf{v} \times \mathbf{B} \quad (1.1)$$

where \times stands for cross product, the orientation of \mathbf{v} , \mathbf{B} and \mathbf{F} follows the right-hand rule.

The macroscopic form: Consider a conductor of length L with electricity I passing through and placed in the magnetic field \mathbf{B} , the Lorentz force \mathbf{F} acting on the conductor then is:

$$\mathbf{F} = \int_L d\mathbf{l} \times \mathbf{B} \quad (1.2)$$

And for the conductive medium with electrical current density distribution \mathbf{J} and placed in the magnetic field \mathbf{B} , the Lorentz force $d\mathbf{F}$ working on the small volume element $d\tau$ is:

$$d\mathbf{F} = \mathbf{J} d\tau \times \mathbf{B} \quad (1.3)$$

1.2.2 The role of Lorentz force in electrical impedance tomography

In the following sections, we list all the biomedical imaging methods using the Lorentz force in a chronological order. For methods with the same working principle, we use the name of the earliest method to honor the originality of the author(s) who found it first.

1.2.2.1 Magneto-acoustic imaging of bioelectric currents

In 1988, TOWE *et al.* invented the magneto-acoustic method for the noninvasive measurement of bioelectric currents (Towe and Islam 1988). In their experiments (Figure 1.1), samples such as electrolytes or hamsters were placed in magnetic fields, and electric currents of microampere-level were driving through the samples. Using microphone coupled to the sample, acoustic responses induced due to Lorentz force could be detected. The experiments were implemented either with steady currents and oscillating magnetic fields (5-10 mT at frequencies of 500-1000 Hz) or with audio frequency currents (3 kHz) and steady magnetic fields. And the acoustic response amplitude increased linearly with the current amplitudes, the magnetic field intensity and the comparative orientation of the electric current density and the magnetic field. And computerized assisted tomography (CAT) obtained from simulated data showed that the locations, magnitudes and orientations of the vector dipoles could be reconstructed (Islam and Towe 1988). Based on fundamental equations of continuum mechanics and electromagnetism, ROTH *et al.* derived the theoretical model of magneto-acoustic current imaging (Roth *et al.* 1994).

$$\rho \frac{\partial^2 \mathbf{u}}{\partial t^2} = \left(K + \frac{4}{3} G \right) \nabla(\nabla \cdot \mathbf{u}) - G \nabla \times (\nabla \times \mathbf{u}) + \mathbf{J} \times \mathbf{B} \quad (1.4)$$

where ρ , K , and G are the density, bulk modulus and shear modulus of the sample medium. \mathbf{u} , \mathbf{J} and \mathbf{B} are the displacement, electric current and magnetic field intensity within the sample medium.

ROTH *et al.* derived that the magnitude of the displacement on the surface of the sphere medium was on the order of $qB/(4\pi Ga)$ when a current dipole of strength q was placed at the center, where a was the radius of the sphere medium, and that the pressure produced in the medium was on the order of $qB/(4\pi r^2)$, where r was distance between the center of the dipole and the measurement field. Using a dipole moment of $1 \mu\text{A}$ (the typical cardiac equivalent dipoles), the shear modulus of 10^4 N/m for soft tissues, radius of the spherical medium of 1 cm, and the magnetic field of 1 T, ROTH *et al.* calculated that the surface displacements were about 1 nm and pressure was about 0.166 Pa, which indicated that magneto-acoustic imaging of biomedical currents was significantly difficult to achieve (Roth *et al.* 1994).

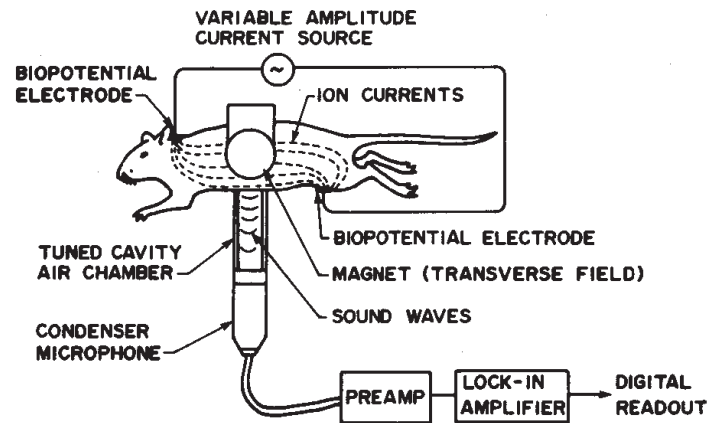


Figure 1.1. Schematic of the experimental setup for magneto-acoustic imaging of bioelectric currents.

(Towe and Islam, 1988)

1.2.2.2 Forward mode of the Hall effect imaging

In 1997, WEN *et al.* introduced the Hall effect imaging method (Wen *et al.* 1998), which worked either in the forward mode (with ultrasonic stimulation and electric detection) or in the reverse mode (with electric stimulation and ultrasound detection). In the forward mode (Figure 1.2.a), an object sample was suspended in a plastic chamber filled with 0.4% NaCl solution and placed in the field of a 4 T magnet in the Y direction. A unipolar nominal pulse with an amplitude of -500 V and a duration of 150 ns from a pulser (Panametric 5058PR) was used to stimulate the planar piezoelectric transducer (Panametric V314). The transducer had a nominal element size of 1.9 cm, a center frequency of 1 MHz and a -6 dB bandwidth of 600 kHz. The transducer transmitted compression waves in the $-Z$ direction towards the sample and the sample moved back and forth along the Z direction under the ultrasound stimulation. The induced electromotive force across the sample in the X direction because of the Lorentz force was detected through electrodes placed in the solution. The weak voltage signal then was amplified by 60 dB by a low noise preamplifier (Miteq), bandpass-filtered, and amplified again by 30 dB. Figure 1.2.b was the recorded signal with a sample of polycarbonate block. WEN *et al.* misunderstood the working principle of the method as the classical Hall effect, but actually the effect upon which the method worked is Faraday induction, wherein the electromotive force appears across the conductive medium when it moves transverse to the magnetic field

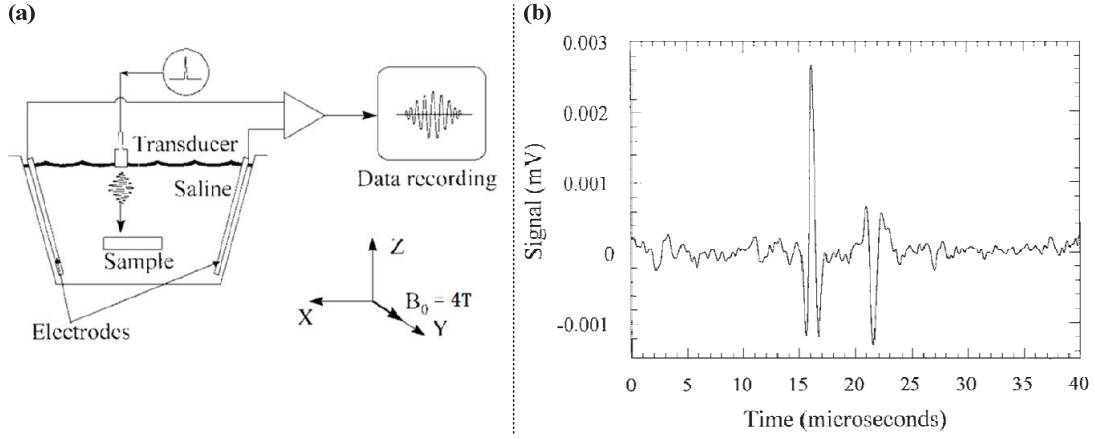


Figure 1.2. (a) Schematic of the experimental setup of the Hall effect imaging in forward mode. (b) Voltage signal from a rectangular polycarbonate block sample. (Wen *et al.* 1998)

(Roth *et al.* 1998). Based on the basic equations of fluid mechanics, WEN *et al.* derived the theoretical model of the voltage signal detected (Wen *et al.* 1998).

$$V(t) = \alpha WR_d B_0 \int_{\text{soundpath}} \left\{ \frac{\partial}{\partial z} \left[\frac{\sigma(z)}{\rho(z)} \right] \int_{-\infty}^t p(z, \tau) d\tau \right\} dz \quad (1.5)$$

where α is a coefficient, W is the ultrasound beam-width, R_d is the electrical impedance of the detection circuit, B_0 is the static magnetic field, $\sigma(z)$ and $\rho(z)$ are respectively the conductivity and density of the conductive medium, and $p(z, t)$ is the ultrasound pressure along the ultrasound propagation path.

Using the electromagnetic reciprocity theorem, WEN derived the voltage across the detecting electrodes (Wen 2000).

$$\begin{cases} U(\omega, \mathbf{R}) = \frac{\omega}{i4\pi c^2} \iiint \left[\mathbf{s}^*(\mathbf{r}, \omega) \cdot \mathbf{n}_{\mathbf{r}-\mathbf{R}} \frac{e^{-ik|\mathbf{r}-\mathbf{R}|}}{|\mathbf{r}-\mathbf{R}|} Q(\mathbf{n}_{\mathbf{r}-\mathbf{R}}, \omega) \right] d^3 \mathbf{r} & (1.6.a) \\ \mathbf{s}(\mathbf{r}, \omega) = \mathbf{B}_0 \times \mathbf{j}(\mathbf{r}, \omega) & (1.6.b) \\ Q(\mathbf{n}, \omega) = \iint_{\text{sample surface}} P_0(\mathbf{r}, \omega) e^{ik\mathbf{n} \cdot (\mathbf{r}-\mathbf{R})} (\mathbf{n} \cdot \mathbf{n}_\perp) d^2 \mathbf{r} & (1.6.c) \end{cases}$$

where \mathbf{R} is the coordinates of the ultrasound transducer element, \mathbf{B}_0 is the applied static magnetic field, $\mathbf{j}(\mathbf{r}, \omega)$ is the electrical current density distribution in the sample when the oscillating current of 1 A and of frequency of ω is injected into the sample, $P_0(\mathbf{r}, \omega)$ is the resulting acoustic pressure at the ultrasound transducer surface, \mathbf{n}_\perp represents the unit normal vector of the sample surface, and $Q(\mathbf{n}, \omega)$ represents the angular beam profile of the transducer.

1.2.2.3 Reverse mode of the Hall effect imaging

The reverse mode of the Hall effect imaging is similar to the magneto-acoustic imaging of biomedical current since both methods use electric stimulation and ultrasonic detection. The major difference between the two methods is the working frequency band in the two methods. In the reverse mode of Hall effect imaging (Figure 1.3.a) (Wen *et al.* 1997), WEN *et al.* used almost the same experimental setup as that in the forward mode except that the output signal from the pulser was used to stimulate the electrodes and that the transducer - used as detection - was connected to the preamplifier. The transducer and the preamplifier were refitted in a conical copper shield, which effectively suppressed the direct cross-talk noise (Wen *et al.* 1998). Figure 1.3.b showed the B-scan image of a sample of bacon or streaky pork, from which the fat and muscle interfaces were better differentiated than from the echography image (Wen *et al.* 1998).

WEN succeeded the 2D tomographic image reconstruction of sample (Wen 1999). The principle was showed in Figure 1.4. The transducer scanned an evenly distributed

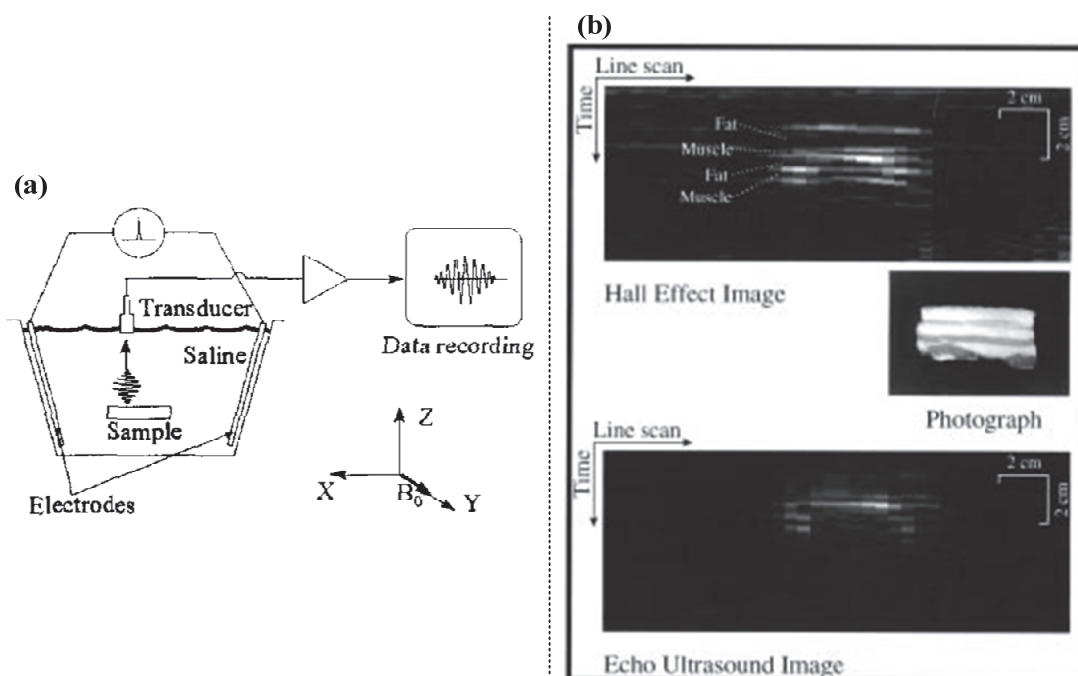


Figure 1.3. (a) Schematic of the experimental setup of the Hall effect imaging in reverse mode. (Wen *et al.* 1997) (b) B-scan reverse mode Hall effect image (top) and the echo ultrasound image (bottom) of the sample of bacon (middle). (Wen *et al.* 1998)

grid pattern $R(i, j)$, and the image of any point r within the sample could be expressed as (1.7).

$$A(\mathbf{r}) = \sum_{i,j} \frac{S_{ij}(t_d + \frac{|r-R(i,j)|}{c})}{|r-R(i,j)|} P(\theta) \quad (1.7)$$

where, $S_{ij}(t)$ is the detected ultrasound signal at point (i, j) , t_d is the delay introduced by the transducer standoff, and $P(\theta)$ is the angular sensitivity profile of the transducer.

Using the electromagnetic reciprocity theorem, WEN derived the acoustic pressure signal at the transducer when electrical current stimulated the sample as (1.8.a) (Wen 2000). From (1.8), WEN pointed three steps needed to derive the conductivity distribution from the pressure signal: first, reconstructing $s(\mathbf{r}, \omega)$ from $P(\omega, \mathbf{R})$;

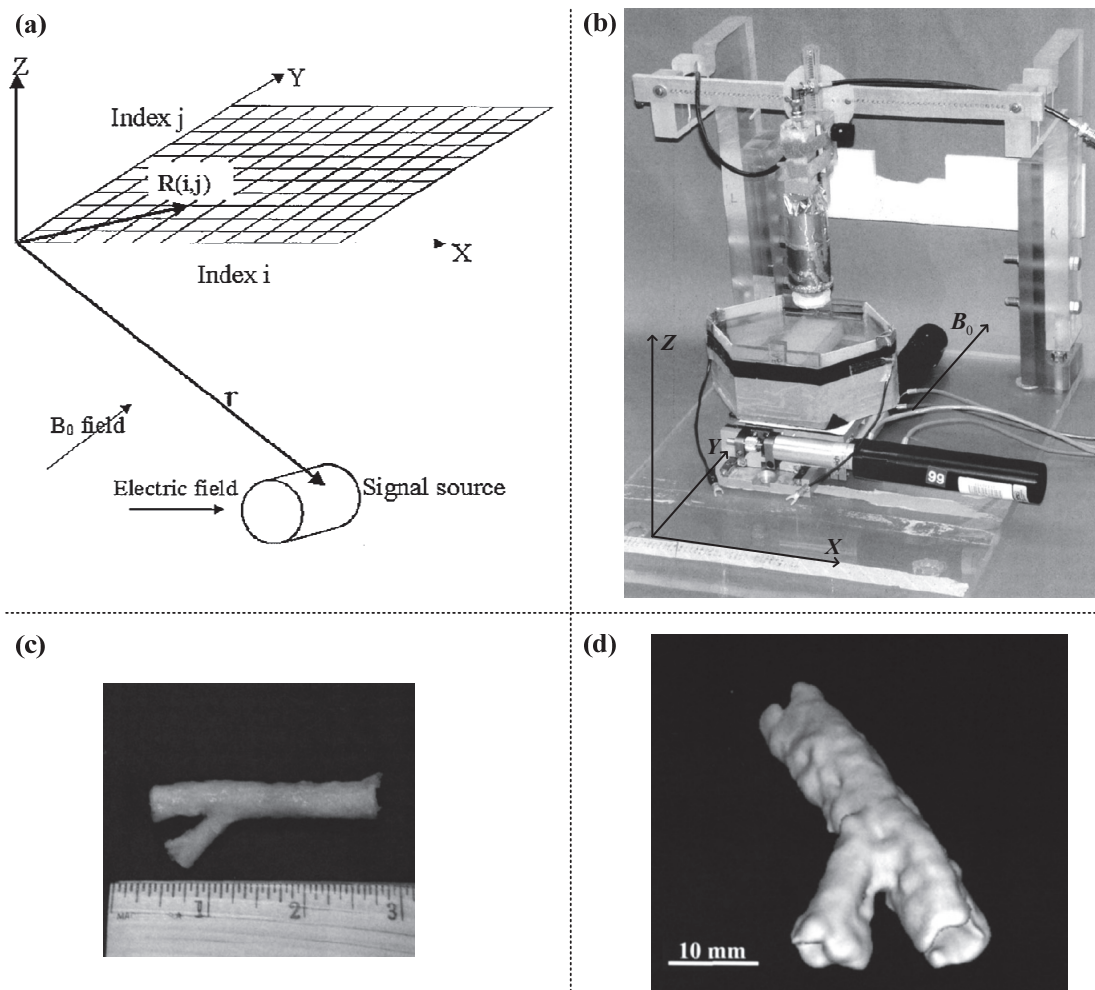


Figure 1.4. (a) The schematic of the 2D scan geometry (Wen 1999). (b) Experimental setup for the 2D tomographic scan (Wen 2000). (c) A sample of a section of aorta of an NIH mini-pig (Wen 2000). (d) The combined 3D image of the aorta section (Wen 2000).

second, retrieving the current distribution $\mathbf{j}(\mathbf{r}, \omega)$ from $\mathbf{s}(\mathbf{r}, \omega)$; finally, reconstructing the electrical conductivity distribution $\sigma(\mathbf{r}, \omega)$ from the current distribution $\mathbf{j}(\mathbf{r}, \omega)$.

$$\left\{ \begin{array}{l} P(\omega, \mathbf{R}) = \frac{i\omega}{4\pi c} \iiint \left[\mathbf{s}(\mathbf{r}, \omega) \cdot \mathbf{n}_{\mathbf{r}-\mathbf{R}} \frac{e^{-ik|\mathbf{r}-\mathbf{R}|}}{|\mathbf{r}-\mathbf{R}|} D(\mathbf{n}_{\mathbf{r}-\mathbf{R}}, \omega) \right] d^3\mathbf{r} \quad (1.8-a) \\ \mathbf{s}(\mathbf{r}, \omega) = \mathbf{B}_0 \times \mathbf{j}(\mathbf{r}, \omega) \quad (1.8-b) \\ D(\mathbf{n}, \omega) = \iint_{\text{transducer area}} e^{ik\mathbf{n} \cdot (\mathbf{r}-\mathbf{R})} d^2\mathbf{r} \quad (1.8-c) \end{array} \right.$$

Based on (1.8) and the experimental setup, WEN pointed out the limitations of the imaging method: (1) the frequency band of the transducer used was limited to 1.4-3.0 MHz and information about $\mathbf{s}(\mathbf{r}, \omega)$ only within this band was contained in $P(\omega, \mathbf{R})$. Therefore the resolvable spatial structure of the imaging method was on the scale between 0.5 mm and 1.5 mm; (2) The acoustic window of the transducer was limited to a small area and only part of $\mathbf{s}(\mathbf{r}, \omega)$ was sensed; (3) For most biological samples, the boundary conditions are not known and the current distribution is partially mapped, so the conductivity distribution could not be uniquely determined from the current distribution.

1.2.2.4 Scanning electric conductivity gradients with ultrasonically-induced Lorentz force

In 2001, MONTALIBET *et al.* proposed and developed the imaging method of scanning electric conductivity gradients with ultrasonically-induced Lorentz force (Montalibet *et al.* 2001a). The fundamental principle of this method is same as that of the forward mode of Hall effect imaging: ultrasound was used to move the sample placed in the magnetic field and electrodes were used to detect the electrical current induced by the Lorentz force, as shown in Figure 1.5.a. But MONTALIBET *et al.* still did innovative works: (1) analytical expression of the induced electrical current density \mathbf{J}_y under the ultrasound stimulation was derived as (1.9), which was in-phase with the sample movement in practical experimental setup (Montalibet *et al.* 2001b); (2) Instead of nominal pulse of short duration and planar transducer, bursts of sinusoidals (500 kHz, 5 pulses) with Wiener inverse filtering and focused transducer (the transducer element $\phi = 50$ mm, $R = 120$ mm) were used to realize the imaging

method (Montalibet *et al.* 2001a). Experiments were done with samples of two-layer gel phantoms (with conductivity 0.5 S/m and 1.4 S/m) and multi-layered pork. The results showed that the method could recognize the electric conductivity variation interfaces in the sample.

$$\mathbf{J}_y = \sigma V_z B_x \text{ and } \sigma = F \sum_i n_i C_i \mu_i \quad (1.9)$$

Where F , n_i , C_i , μ_i are respectively the molar electric charge, and the charge, the volume concentration and mobility of each species of ion.

In 2013, GRASLAND-MONGRAIN *et al.* continued MONTALIBET's work. GRASLAND-MONGRAIN *et al.* got the B-scan images of samples of gel phantom

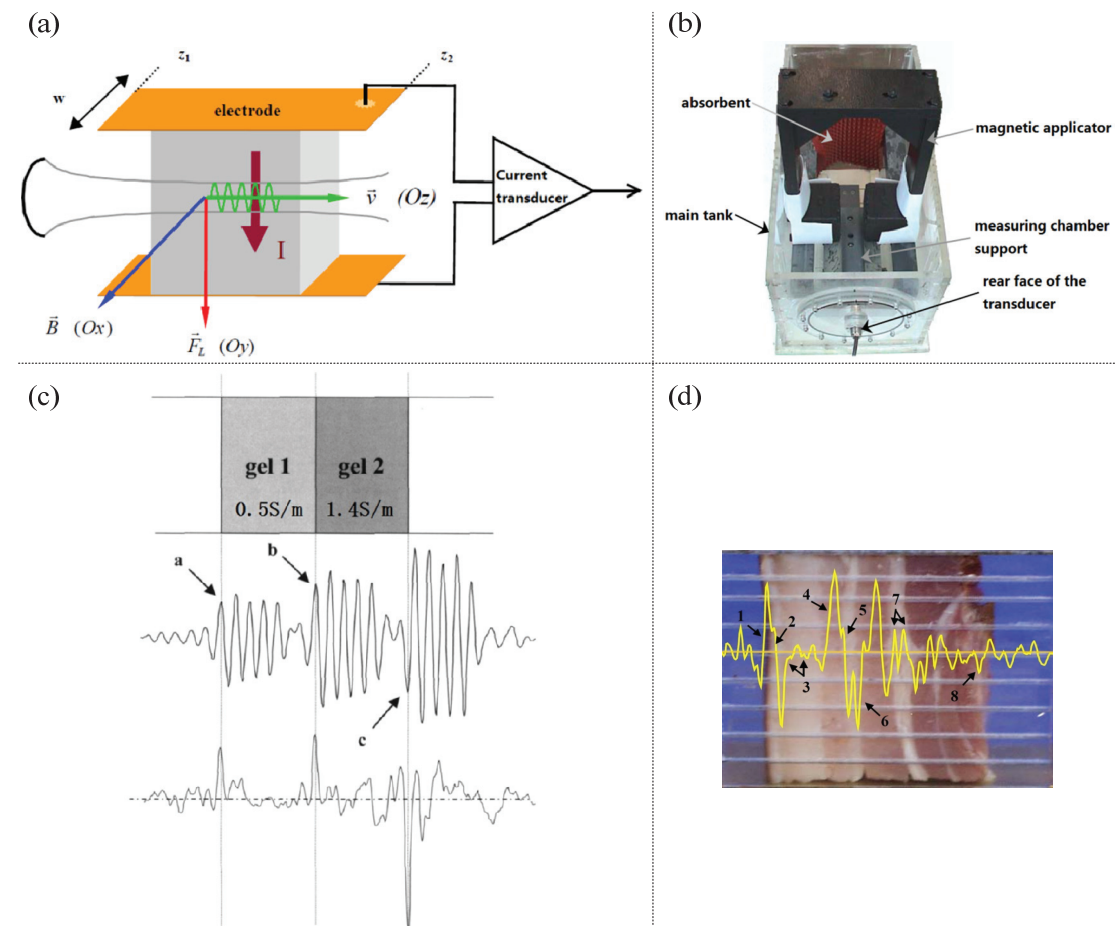


Figure 1.5. (a) Schematic of the experimental setup of scanning electric conductivity gradients with ultrasonically-induced Lorentz force. (b) Photo of the experimental setup. (c) Experiments with a sample of 2-layer gel phantom (top); the received current signal (middle); and the reconstructed variation interface using the Wiener inverse filtering (bottom). (d) Experiments with a sample of multi-layered pork. (Montalibet 2002)

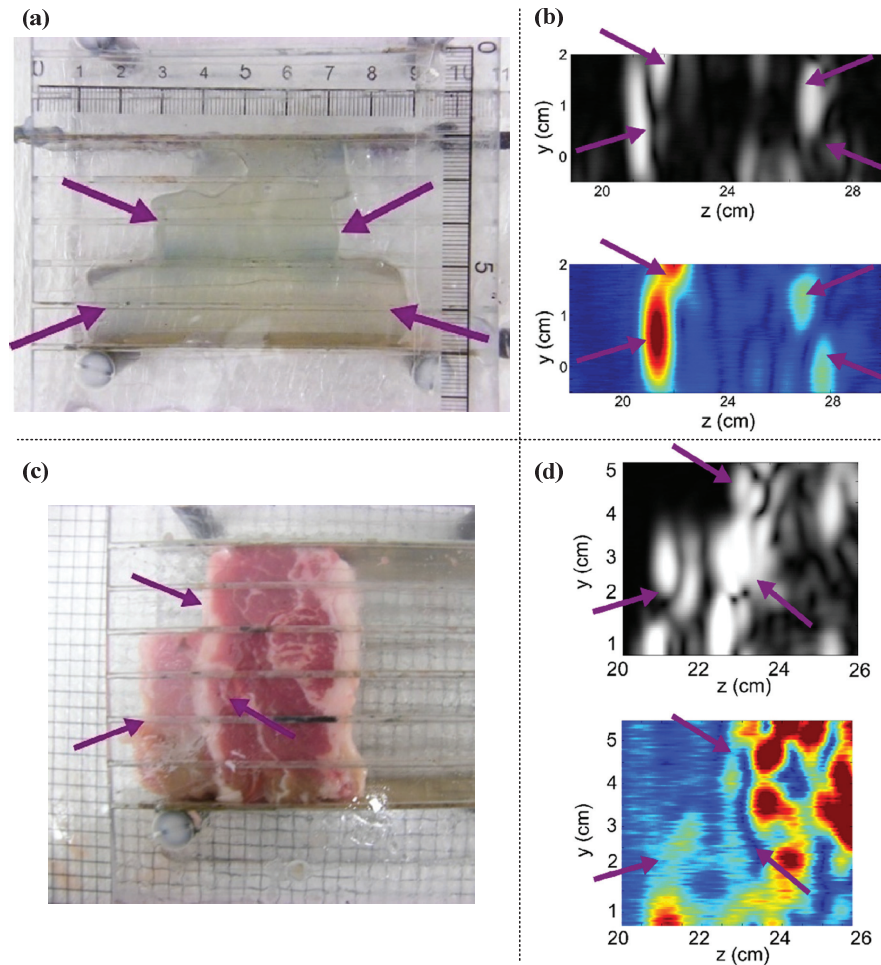


Figure 1.6. (a) 2-layer salty gelatin sample. (b) Echography image (top figure) and SECG-UILF image (bottom figure) of the 2-layer salty gelatin sample. (c) The sample of the L-shape beef. (d) Echography image (top figure) and SECG-UILF image (bottom figure) of the sample of L-shape beef. (Grasland-Mongrain *et al.* 2013)

blocks (Figure 1.6.a and b) and L-shape beef (Figure 1.6.c and d) by scanning the samples at laterally different places and uniting each line of data together (Grasland-Mongrain 2013). GRASLAND-MONGRAIN *et al.* changed the name of the imaging method to Lorentz force electrical impedance tomography to describe both the imaged parameter and the method.

1.2.2.5 Magneto-acoustic tomography with magnetic induction

To overcome the shielding effect (Wen 1999, Tidswell *et al.* 2001), in 2005, XU and HE proposed the imaging modality of magneto-acoustic tomography with

magnetic induction (MAT-MI) (Xu and He 2005). In MAT-MI, the weakly conductive sample is placed in the static and quasi-uniform magnetic field \mathbf{B}_0 and a transient fast-changing magnetic field \mathbf{B}_1 (of duration about $1 \mu\text{s}$) was used to induce electrical eddy current in the sample. Because of the eddy current and the static magnetic field, Lorentz force is generated and vibrated the sample. The vibration of the sample generated ultrasounds, which were measured around the sample by the transducers and used to reconstruct the ultrasound pressure source and the electrical conductivity distribution within the sample. XU and HE formulated the equations in the forward and inverse problems of MAT-MI and demonstrated experimentally the imaging method using metal wire loop (Xu and He 2005).

In the following decade, the MAT-MI had been rapidly developing (Li *et al.* 2016). LI *et al.* realized MAT-MI using saline samples with salinity of 1wt % (electrical conductivity 1.9 S/m), in which conductivity difference between water and the saline sample could be distinguished (Li *et al.* 2016). XIA *et al.* tried MAT-MI with two permanent magnets (one above and one below the sample), a Helmholtz coil as the stimulating coil and an acoustic lens for ultrasound focusing. Using the system, XIA *et al.* demonstrated 3D MAT-MI in saline phantoms and, for the first time, the ability of MAT-MI to recognize conductivity variations in salt biological tissue (Xia *et al.* 2007). HU *et al.* used a customized coil driver (the maximum of the charging voltage was 24 kV) and demonstrated the capability of the MAT-MI in imaging real soft tissue (electrical conductivity lower than 1 S/m) (Hu *et al.* 2010). LI and HE employed the multi-excitation in MAT-MI and demonstrated that the MAT-MI with multi-excitation could reconstruct the accurate conductivity contrast from acoustic data of unlimited bandwidth whereas the relative conductivity contrast from acoustic data of limited bandwidth (Li and He 2010). HU *et al.* demonstrated the feasibility of MAT-MI imaging to recognize with high spatial resolution the small electrical conductivity contrast between liver tumor tissues and normal tissues (Hu *et al.* 2011). HU and HE showed experimentally their MAT-MI system had spatial resolution of 1.51 mm by a parallel-line-source phantom upon the Rayleigh criterion and better than 2 mm by biological tissue, which suggested the potential application to early

detection of small-size tumor (Hu and He 2011). MARIAPPAN and HE developed the ultrasound beam forming method to map the electrical conductivity through the estimation of induced eddy current vector, which they named as vector source imaging (Mariappan and He 2013). And they demonstrated that MAT-MI using vector source method was capable of conductivity reconstruction with the prior range of the conductivity. By using the static magnetic field 9.4 T of MRI, MARIAPPAN *et al.* realized reliable reconstruction of conductivity contrast of real tissue sample (Mariappan *et al.* 2014). MARIAPPAN *et al.* also tried MAT-MI imaging of magnetic iron oxide nano-particles, but the force acting on the sample was magneto-motive force rather than the Lorentz force (Mariappan *et al.* 2016). YU *et al.* developed a high-frequency (1.5 MHz) MAT-MI (hfMAT-MI) system with 2D spatial resolution of 1 mm, besides, they verified that not only the boundaries between cancerous and healthy tissues but also the internal structures of the tumor could be resolved and the growing tumor could be tracked using the hfMAT-MI system, which altogether demonstrated the hfMAT-MI was effective for the detection and diagnosis of early-stage tumors (Figure 1.4) (YU *et al.* 2016).

1.2.2.6 Magneto-acousto-electrical tomography

In 2007, XU *et al.* developed the idea first proposed by WEN: upon the electromagnetic reciprocity theorem, the voltage detected in the forward mode of Hall effect imaging could be formulated using the electrical current density distribution in the sample when 1 Ampere electrical current was injected into the sample, and the relative electrical conductivity contrast of the sample could be reconstructed from the detected voltage (Xu *et al.* 2007, Haider *et al.* 2008). XU *et al.* renamed this method as magneto-acousto-electrical tomography (MAET). HAIDER demonstrated MAET using thin gel phantom sample, 2-layer (muscle-fat) and 4-layer muscle-fat-muscle-fat biological samples (Haider 2008). One problem with the forward mode of HEI and MAET is that there are only signals corresponding to conductivity variations but no signal for places with uniform conductivity. RENZHIGLOVA and XU applied ultrasound-induced radiation force in MAET and voltage was generated even at places

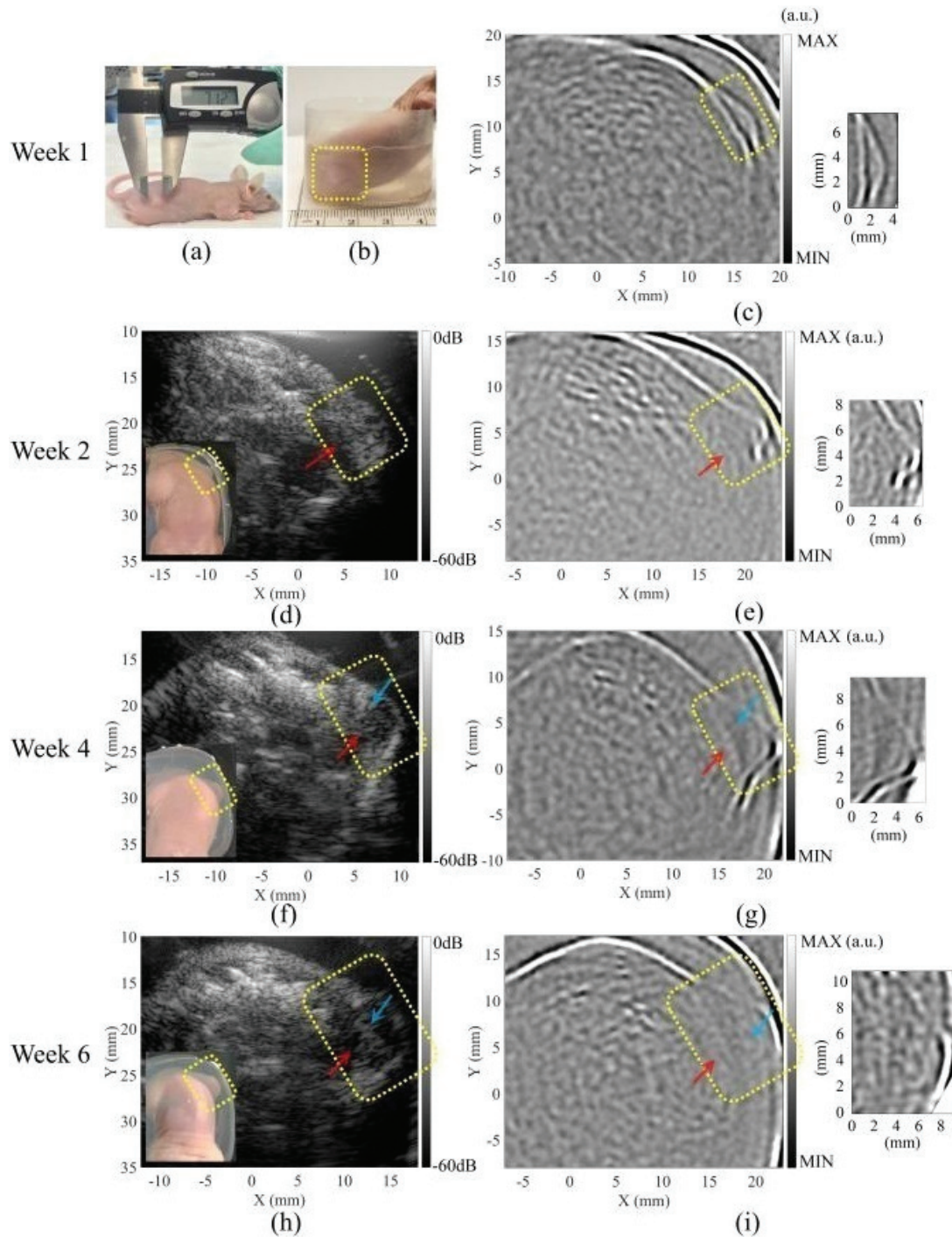


Figure 1.4. (a and b) The tumor appearance in the 1st week after a transplantation of the human cancer cell line. (d, f and h) The ultrasound images of the tumor-bearing mouse in the 2nd, the 4th and the 6th weeks, and the insets in these three images show the tumor growth in top views. (c, e, g and i) The hfMAT-MI images of the mouse abdomen, and its growing tumor in the 1st, the 2nd, the 4th and the 6th weeks respectively. (Yu *et al.* 2016)

with uniform conductivity (Renzhiglova *et al.* 2010). GUO *et al.* proposed the method

of MAET with coil detection - magneto-acousto-electrical tomography with magnetic induction (MAET-MI) (Guo *et al.* 2015), which was the reverse mode of MAT-MI. The MAET-MI could also get rid of the shielding effect.

1.2.3 The role of Lorentz force in functional magnetic resonance imaging (fMRI)

Since the early 1990s, functional magnetic resonance imaging (fMRI) has become a dominant modality for brain imaging research because of its totally non-invasiveness. The primary form of fMRI was based on the blood oxygenation level-dependent (BOLD) contrast (Ogawa *et al.* 1990a, Ogawa *et al.* 1990b, Ogawa and Lee 1990, Glover 2011). However, BOLD fMRI could not in time localize accurately the neuronal activation because of the delays and spatial dispersions within the hemodynamic response (Kim *et al.* 1997). On the other hand, techniques like electroencephalography (EEG), magneto-encephalography (MEG), and event-related potential (ERP) recordings merited excellent temporal resolutions on the order of milliseconds, but all have poor spatial resolutions. Therefore, fMRI directly imaging the electromagnetic changes accompanying the neuronal activity appeared, which combined the merits of non-invasiveness and high spatial resolution of MRI with the merit of high temporal resolution of EEG, MEG or ERP. For instance, several researches used MRI to detect the minute magnetic field changes produced due to the neuronal currents during the brain activity (Joy *et al.* 1989). The Lorentz effect imaging was one of such method that took advantage of the strong static and gradient magnetic fields in MRI to detect the minute electrical current changes (Song and Takahashi 2001).

1.2.3.1 Lorentz effect imaging of action current using MRI

In 2001, SONG and TAKAHASHI proposed the Lorentz effect imaging (LEI) to explore additional sensitivity of neuronal current detection using MRI (Song and Takahashi 2000, Song and Takahashi 2001). The Lorentz effect imaging relied on the

Lorentz force - more specifically the Laplace force. When electrical current passed through a thin string conductor placed inside an elastic sample in MRI, the thin string conductor experienced Laplace force due to the strong static magnetic field of MRI. The movement of the conductor compressed the adjacent medium, resulting in a spatial change of the density distribution of the spins in the regions pressed. And in the presence of the gradient magnetic field, the change in the density distribution resulted in a change in the accumulated phase and finally a change of the signal within the voxel. SONG *et al.* demonstrated Lorentz effect imaging with 5 μA current passing carbon wire inside gelatin phantom (Truong *et al.* 2006) and 1 mA-level current passing ionic solution (2.8 g/l CuSO_4) (Truong *et al.* 2008). SONG *et al.* demonstrated the feasibility of imaging the human median nerve activation in vivo when applying electrical stimulation of the wrist (Truong and Song 2006). ROTH and his colleagues derived the mechanical model of neural tissue displacement during Lorentz effect imaging (Roth and Basser 2009). Upon the model and using practical values for the parameters of human median nerve in a 4 T field, ROTH *et al.* got the results: the displacement induced by the Lorentz effect was 5 nm or less (Roth *et al.* 2014); the phase shifts caused by the magnetic field of action currents were on the order of 0.01° (Roth and Basser 2009); and the displacement distributed broadly throughout the tissue rather than locally near the nerve (Roth and Basser 2009). In summary, Lorentz effect imaging of neuronal stimulation still had some technical challenges to resolve (Roth and Hobbie 2014).

1.2.4 Application of Lorentz force in elastography

Elastography is a rapidly developed technology for qualitatively and/or quantitatively assessing the mechanical properties of biological tissues. Elastography is viewed as an imaging version of palpation, which is commonly used by physicians to diagnose and characterize disease. The principle of palpation relies on the fact that the mechanical properties of tissues usually change dramatically in the presence of biological, pathological or even physiological changes. Elastography obtains the elastic parameter information by assessing the propagation of shear waves in the

tissues, which essentially involves three steps: (1) generation of shear waves in the tissue; (2) successive imaging of displacements of each small element with the tissue; (3) construction of map of elastic parameter of the tissue, i.e. the elastogram. The methods of inducing shear waves in the tissue mainly include compressions generated by external mechanical force (Eisenscher *et al.* 1983, Catheline *et al.* 1999), acoustic radiation force (Sarvazyan *et al.* 1998, Nightingale *et al.* 2002, Bercoff *et al.* 2004), impulse Lorentz force (Basford *et al.* 2005, Grasland-Mongrain *et al.* 2014, Grasland-Mongrain *et al.* 2016b) or magneto-motive force (Urban *et al.* 2014, Oldenburg *et al.* 2012), etc. This thesis explores the method using the Lorentz force.

1.2.4.1 Electromagnetic actuator in MR elastography

In 1995, MUTHUPILLAI *et al.* developed the Magnetic Resonance Elastography (MRE) technique (Muthupillai *et al.* 1995, Muthupillai and Ehman 1996, Muthupillai *et al.* 1996), in which a driver device based on the Lorentz force mechanism was used to apply harmonic vibrations of acoustic-range frequencies in tissue (Figure 1.8.a) (Rossman *et al.* 1999). An electrical coil positioned in the MRI core was driven by the electrical current at 50-1000 Hz and oscillated due to the Lorentz force. The motion of the coil then was transferred to the sample through a pivot bar. SINKUS *et al.* developed a similar mechanical oscillator to induce oscillations in the longitudinal direction in the breasts of the patients (Sinkus *et al.* 2000, Sinkus *et al.* 2004). To assess the varying shear wave speed in spatially different directions, BRAUN *et al.* developed an electromagnetic actuator capable of generating variably oriented shear waves (Figure 1.8.b) (Braun *et al.* 2003). Through a redirection plate, motion of coil in the direction of the main magnetic field can be converted to other directions by changing the conversion angle.

1.2.4.2 Direct generation of shear wave in soft tissues

External shaking actuators, which rely on the acoustic, pneumatic, piezoelectric or electromagnetic mechanisms, have two main drawbacks: (1) the attenuation along

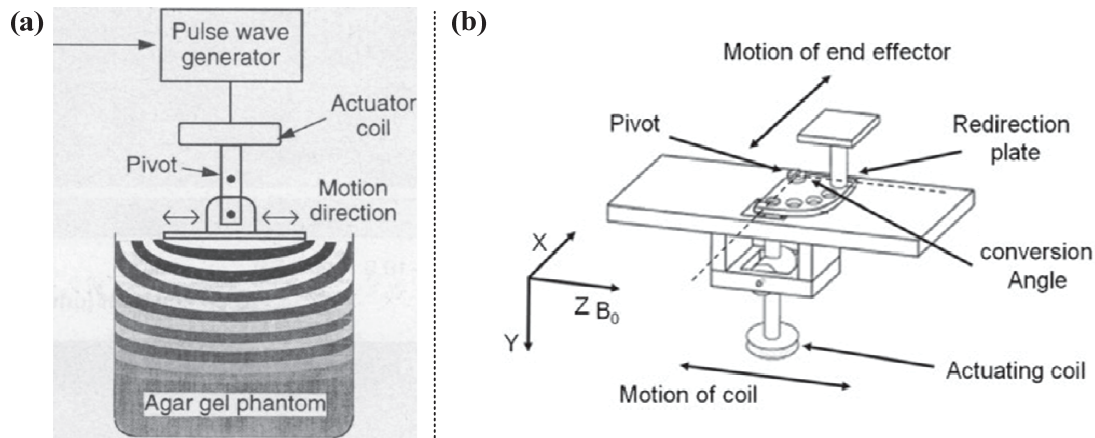


Figure 1.8. (a) The electromagnetic actuator consists of an electrical coil attached to a pivot bar and is driven by a wave generator at 50 to 1000 Hz. The alternating flux of the coil interacts with the main magnetic field of the imager, yielding a cyclic force, which is coupled by a contact plate to the surface of the sample to be studied (Muthupillai *et al.* 1995). (b) A variable direction change of motion is achieved with an additional pivoted redirection plate. The plate is connected with a standard actuator mounted piggyback onto an adapted base plate (Braun *et al.* 2003).

the shear wave propagation pathway from source to destination prevents efficient transmission of shear wave, especially for targets like the brain tissue, which locates behind the skull and is surrounded by the cerebrospinal fluid; (2) the shaking induces pain in patients, and patients' biological or physiological reactions to the pain, like muscle contraction or neuronal activity, change the elastic characteristics of the targets and undermine the accuracy of the results. To overcome the drawbacks of the external shakers, since 2014, GRASLAND-MONGRAIN *et al.* have developed the method of generating shear waves directly in the tissue through the Lorentz force mechanism. Using current injection method (Grasland-Mongrain *et al.* 2014), for a water-based phantom with 1 wt% salt and 0.1 wt% graphite placed in a 100 mT magnetic field, the 100 mA peak-to-peak electrical current burst can create shear wave displacement reaching a magnitude of $1 \mu\text{m}$ (Figure 1.9.a). Because of the shielding effect on the skin, the electrical current could not be efficiently injected into the body. In 2016, GRASLAND-MONGRAIN *et al.* proposed the contactless method of generating shear waves, which employed induction of eddy current in biological

tissue through transcranial magnetic stimulation (TMS) (Figure 1.9.b) (Grasland-Mongrain *et al.* 2016b). The induced eddy current coupled with the static magnetic field and generated the Lorentz force, which finally generated shear wave displacement in the biological tissue target.

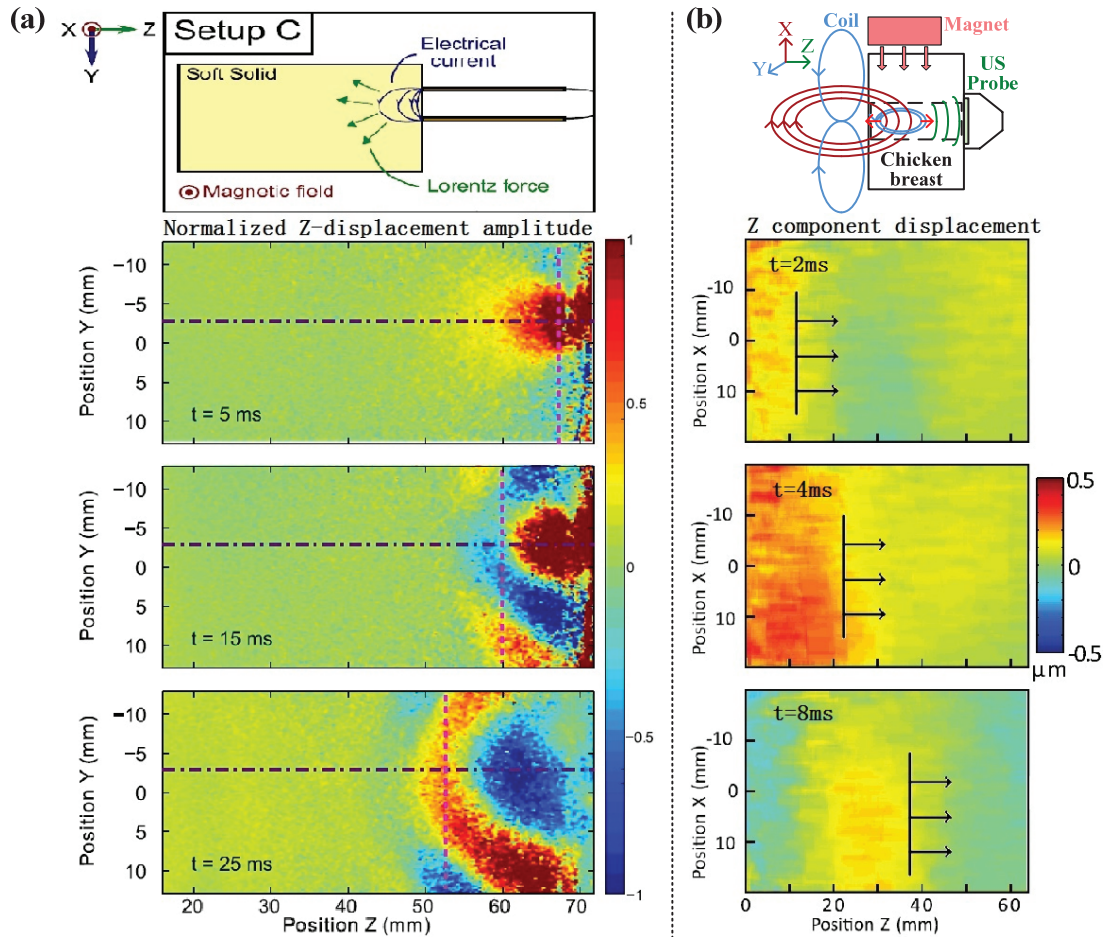


Figure 1.9. (a) An electrical current was applied through two plane electrodes in a soft solid placed in a magnetic field (top figure). This induced displacements observed with an ultrasound probe at, respectively, 5 ms, 15 ms, and 25 ms after current injection are shown (bottom three figures) (Grasland-Mongrain *et al.* 2014). (b) A coil is inducing remotely an electrical current (blue circles) in a sample. A magnet creates a magnetic field (pink arrows) in the sample. The combination of the electrical current and the magnetic field induces the Lorentz force (red arrows), which creates shear wave displacements (green lines) in the sample (top figure). The z component maps of the displacement in the chicken breast tracked through an ultrasound array, respectively 2 ms, 4 ms and 8 ms after the current emission (bottom three figures) (Grasland-Mongrain *et al.* 2016b).

1.3 Structure of the thesis

This thesis studies the application of the Lorentz force in scanning electric conductivity gradients with ultrasonically induced Lorentz force (SECG-UILF) and elastography. The first part of the thesis studies the SECG-UILF. To reduce the peak instantaneous stimulating power to the ultrasound transducer, and also at the same time to reduce the peak instantaneous transmitted acoustic pressure while keeping the longitudinal resolution, this thesis proposes to apply linearly frequency- modulated ultrasound stimulation or step-frequency ultrasound stimulation in SECG- UILF. The second part of the thesis studies the cross-correlation-approach-based elastography. In order to remotely generate the shear wave displacement fields for elastography in the target regions behind a strongly reflective medium, like the heart behind the sternum and ribs or the brain behind the skull, this thesis studies using the Lorentz force to generate the shear wave displacement fields for elastography.

Focusing on the above purposes, the thesis is organized into the following chapters:

In Chapter 1, the significance of electrical impedance tomography (EIT) and elastography and the relevant supporting programs in the hosting laboratories are first presented. Then a brief overview of the evolution and status of application of the Lorentz force in biomedical imaging, including EIT and elastography, is given. Finally, the structure of the thesis and highlights of innovations in the thesis are summarized.

In Chapter 2, study on the scanning electric conductivity gradients with linearly frequency-modulated ultrasound induced Lorentz force (SECG-LFM-UILF) is presented. Two methods of calculation of the longitudinal distance - one uses coherent demodulation scheme and the other uses pulse compression scheme - are first presented. Then, the feasibility and performance of SECG-LFM-UILF are confirmed by experiments using saline agar phantom samples of electrical conductivity ranging between 0.2 S/m and 0.5 S/m.

In Chapter 3, study on the scanning electric conductivity gradients with step-

frequency ultrasound induced Lorentz force (SECG-SF-UILF) is presented. Based on the in-phase coherent demodulation scheme and the in-phase/quadrature-phase coherent demodulation scheme, the theory of calculation of the longitudinal distance using the step-frequency technique is first formulated. Then, using the two-layer copper foil sample, the feasibility of SECG-LFM-UILF is verified experimentally.

In Chapter 4, study on the generation of shear waves in soft media by stimulating an aluminum patch using a transient magnetic field is presented. Through measuring the displacement of the aluminum ring using an interferometric laser probe, the source and the frequency and amplitude characteristics of the Lorentz force acting on the aluminum ring are first confirmed. Then, by stimulating an aluminum patch using a transient magnetic field, the shear wave displacement fields in the polyvinyl alcohol (PVA) phantom sample are generated and its propagation in the PVA is captured by the ultrafast ultrasound imaging. Finally, the theoretical shear wave displacement fields in a homogeneous, isotropic and purely elastic solid medium, which are calculated through the Green function, are compared with the shear wave displacement fields from experiments.

In Chapter 5, investigation of calculation of the shear wave velocity from the shear wave displacement fields generated by the method in Chapter 4 and through the cross-correlation approach is presented. By stimulating an array of aluminum patches using a transient magnetic field, the shear wave displacement fields from multiple sources are first generated in the agar phantom samples. Then, the shear wave velocity maps are reconstructed from 100 frames of displacement fields. Finally, we confirm through experiments on multi-shaped agar phantom samples: (1) whether interfaces between regions of different stiffness can be differentiated from the velocity maps; (2) whether boundaries of the cylinder inclusions of different stiffness from the background part can be recognized from the velocity maps; (3) the velocity maps are quantitative or qualitative.

In Chapter 6, the advancements obtained within the framework of the thesis are summarized. And the challenges in SECG-UILF and cross-correlation approach based elastography and the possible solutions are given.

1.4 Highlights of innovations in the thesis

(1) This thesis proposes application of the coherent demodulation technique in scanning electrical conductivity gradients with linearly frequency-modulated ultrasound induced Lorentz force (SECG-LFM-UILF). Replacing the negative spike signal with the linearly frequency-modulated wide signal, the peak instantaneous stimulating power to the ultrasound transducer is decreased by 25.5 dB, and the peak instantaneous transmitted acoustic pressure decreases by 0.44 MPa. Through experiments of the coherent demodulation scheme based SECG-LFM-UILF on saline agar phantom samples of electrical conductivity ranging between 0.2 S/m and 0.5 S/m, the results confirm: (1) the SECG-LFM-UILF can locate the electrical conductivity variations precisely; (2) the SNR of the 2D conductivity variation map by SECG-LFM-UILF is comparable to that by traditional SECG-UILF using spike pulse; (3) using a modulation frequency band of 2 MHz and a modulation duration of 500 μ s, the SECG-LFM-UILF succeeds a longitudinal resolution of 1 mm.

(2) This thesis succeeds a longitudinal resolution of 1 mm in the pulse compression based SECG-LFM-UILF. Through experiments of the pulse compression scheme based SECG-LFM-UILF on saline agar phantom samples of electrical conductivity ranging between 0.2 S/m and 0.5 S/m, the results confirm: (1) the SECG-LFM-UILF can locate the electrical conductivity variations precisely; (2) using a modulation frequency band of 2 MHz and a modulation duration of 500 μ s, the SECG-LFM-UILF succeeds a longitudinal resolution of 1 mm.

(3) The thesis proposes the scanning electric conductivity gradients with step-frequency ultrasound induced Lorentz force (SECG-SF-UILF), in which the step-frequency technique is utilized to calculate the longitudinal distance. Through experiments of SECG-FS-UILF on a two-layer copper foil sample, the principle of SECG-SF-UILF is validated.

(4) The thesis proposes generation of shear wave displacement fields through stimulating the aluminum patches with a transient magnetic field. The source and the frequency and amplitude characteristics of the Lorentz force acting on an aluminum

ring is confirmed by measuring the displacement of the aluminum ring using an interferometric laser probe. Using a transient magnetic field of peak changing rate of 10.44 kTs^{-1} , shear wave displacement source of amplitude of $100 \mu\text{m}$ is successfully generated at the surface of the polyvinyl alcohol phantom sample.

(5) The thesis succeeds building a qualitative shear wave velocity map of the agar phantom sample from 100 frames of the shear wave displacement fields. From the shear wave velocity maps reconstructed: (1) the interfaces between regions of different stiffness can be clearly recognized; (2) cylinder inclusions of diameter as small as 5 mm and having different stiffness from the background part can be recognized.

Part 1 Scanning electric conductivity gradients with ultrasonically-induced Lorentz force

In any pulse-echo method of ultrasound imaging systems, the signal-to-noise ratio (SNR) and also the penetration depth is directly proportional to the energy of the transmitted ultrasound pulse. In such cases, however, the transducer is limited by its peak power capacity far before its average power limit. In the special case of medical ultrasound transducer, the peak power limit comes from the risk of reaching the biomedical hazard limit rather than the hardware capability limit. At the other hand, the pulse-echo methods must have both a sufficient overall system-bandwidth and a transmitting signal of wide frequency bandwidth to achieve the desired longitudinal resolution.

As in ultrasound imaging, the trade-off between longitudinal resolution and penetration depth also exists in scanning electric conductivity gradients with ultrasonically induced Lorentz force (SECG-UILF). Given the short pulse in the traditional pulse-echo-based-SECG-UILF, the ultrasound penetration can be increased by either increasing the pulse amplitude or the pulse duration. However, as pulse amplitudes of commercial transducers already near the regulatory limit and the mechanical index (MI), which is related to peak negative pressure, the only feasible alternative is to extend the pulse duration, which has the undesirable consequence of reducing the longitudinal resolution.

To overcome this peak power (penetration depth)-longitudinal resolution problem, it is well known that the spread energy method is almost the only solution, by prior experience in radar and sonar.

In chapter 2, we carry out an in-depth study of SECG-UILF using linearly frequency-modulated ultrasound pulse stimulation for increasing SNR (also the penetration depth) while keeping the longitudinal resolution. The homodyne coherent detection method and the heterodyne pulse compression filter method are studied independently, transforming the induced current signal so as to locate the electrical conductivity gradients.

In chapter 3, we study the step frequency ultrasound stimulation and application of the step-frequency technique in SECG-UILF.

Chapter 2 Scanning electric conductivity gradients with linearly frequency-modulated ultrasound-induced Lorentz force

Coded excitation based on a linearly frequency-modulated (LFM) excitation and a pulse compression filter in medical ultrasound is used to improve the SNR and also the penetration depth, as long as the side-lobe level, the energy and the longitudinal resolution are kept acceptable for ultrasound imaging (Parks and Linzer 1976, O'Donnell 1992, Takeuchi 1995, Misaridis and Jensen 1999, Misaridis *et al.* 2000, Chiao and Hao 2005). An improvement in SNR of 10 dB or more is expected, depending on the code parameters, and the available bandwidth (Takeuchi 1995). Clinical images of the liver from two healthy volunteers demonstrated an improvement in penetration depth of at least 4 to 5 cm at 4 MHz with temporal side-lobe levels lower than -35 dB (Misaridis *et al.* 2000). LFM waveforms have been used as coded excitation because of their important symmetry properties and their linear group delay. The narrowest -3 dB main-lobe width is achieved with a constant waveform, although the range side-lobe level (RSL) is only -13 dB below the main-lobe. The LFM waveform with apodization trades off the main-lobe width for the low RSL. For instance, a Gaussian and cosine square apodization window results in -100 dB RSL performance with tradeoff in SNR gain and main-lobe width (Takeuchi 1995). Mismatched filtering with different transmitting and receiving apodization may be used to optimize the energy transmitted into tissue (Misaridis and Jensen 1999).

Using linearly frequency-modulated pulse for the reduction of peak stimulating power originated in radar applications (Stove 1992) and in recent years has already been used in ultrasound nondestructive testing (Battaglini *et al.* 2014, Kunita *et al.* 2008, Kunita 2007) and magneto-acoustic imaging (Aliroteh *et al.* 2014, Aliroteh *et al.* 2016). In this chapter, we carry out an in-depth study of scanning electric conductivity gradients with linearly frequency-modulated ultrasound induced Lorentz force (SECG-LFM-UILF). This method employs linearly frequency-modulated pulse to stimulate the ultrasound transducer, and therefore compared with the traditional

method using the negative spike of high peak instantaneous power, it can reduce the peak instantaneous stimulating power to the ultrasound transducer and at the same time the peak acoustic pressure produced from the transducer. We first summarize the theoretical foundation of scanning electric conductivity gradients with ultrasonically-induced Lorentz force (SECG-UILF) using linearly frequency-modulated pulse signal. The feasibility and performance of this imaging modality was then evaluated experimentally using weakly conductive phantoms samples. (Sun *et al.* 2017, 2018b)

2.1 Measured current signal in SECG-UILF

The scenario of SECG-UILF is illustrated using Figure 2.1. Ultrasound waves are transmitted along the direction e_x into a conductive sample placed in the quasi-uniform static magnetic field of direction e_y . As the positive and negative ions inside the sample move along e_x together with the sample, they deviate from their tracks due to the Lorentz forces acting on them in the direction of e_z . As the Lorentz forces acting on the positive and negative ions are in opposite directions, the positive and negative ions deviate to the opposite directions, which results in local electrical current density \mathbf{J} in the sample that can be calculated by the following (Montalibet *et al.* 2001a):

$$\mathbf{J} = \sigma v_x B_y \mathbf{e}_z \quad (2.1)$$

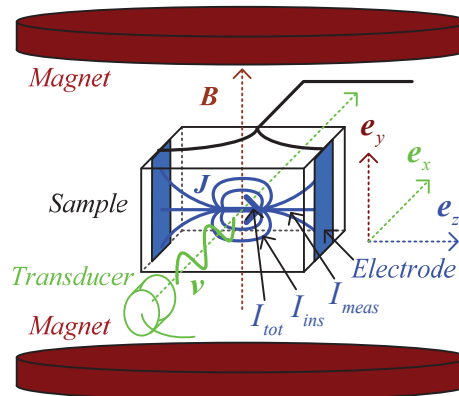


Figure 2.1. Ultrasound waves are sent into a conductive sample placed in a static magnetic field, which induces electrical current density due to the electrical field created by the Lorentz force acting on the positive and negative ions (Sun *et al.* 2018b). The induced current I_{tot} separates into two parts, I_{ins} locating inside the sample, and I_{meas} collected by the electrodes.

where σ is the local electrical conductivity, v_x is the ion vibration velocity along e_x , and B_y is the magnetic induction density along e_y .

To calculate the electrical current collected by the electrodes, an approximation is assumed that the ultrasound waves propagate in the form of a plane wave in the direction e_x , within a cylindrical area of which the diameter is W . The total current I_{tot} generated then can be approximated by the average of the surface integrals of the current density on all planes normal to e_z within the cylindrical area, i.e., (Wen *et al.* 1998)

$$I_{tot} = \frac{1}{W} \int \iint \mathbf{J} \cdot d\mathbf{S} dz = \frac{1}{W} \int \iint \sigma v_x B_y dx dy dz \quad (2.2)$$

In practice, only a fraction of the total current I_{tot} induced by the Lorentz force can be detected. The quantity of the detected current I_{meas} can be derived using Ohm's law as follows (Grasland-Mongrain *et al.* 2015):

$$I_{meas} = I_{tot} \cdot R_{in} / (R_{in} + R_{meas}) \quad (2.3)$$

where R_{in} is the resistance experienced by the part of the induced current inside the sample, and R_{meas} is the resistance passed through by the remaining current.

For a linear and inviscid medium, using the relationship between the medium velocity and the ultrasound pressure wave $p(t, x)$, $\frac{\partial v_x(t, x)}{\partial t} = -\frac{1}{\rho} \frac{\partial p(t, x)}{\partial x}$ (ρ being the density of the sample), the detected current signal can be calculated by the following (Wen *et al.* 1998).

$$I_{meas} = \frac{\alpha}{W} \int \iint_{x_1}^{x_2} \left\{ B_y \frac{\partial}{\partial x} \left[\frac{\sigma(x)}{\rho(x)} \right] \int_{-\infty}^t p(\tau, x) d\tau \right\} dx dy dz \quad (2.4)$$

where $\alpha = R_{in} / (R_{in} + R_{meas})$.

Because the density only differs by less than ten percent over different biological soft tissues (Cobbold 2006), whereas the electrical conductivity can differ more than several tenfold (Gabriel *et al.* 1996), gradient of $\sigma(x)/\rho(x)$ is, for the most part, determined by the gradient of $\sigma(x)$. Thus, (2.4) is reduced to the following (Wen *et al.* 1998).

$$I_{meas} = \frac{\alpha}{W} \int \iint_{x_1}^{x_2} \left[\frac{B_y}{\rho(x)} \frac{\partial \sigma(x)}{\partial x} \int_{-\infty}^t p(\tau, x) d\tau \right] dx dy dz \quad (2.5)$$

When ultrasound waves pass by places where the gradients of $\sigma(x)$ along the

waves' propagation direction are zero, the integrand is zero and contributes none to the final integral. And only when the ultrasound waves pass by discontinuities of $\sigma(x)$ in the propagation direction can then be integrand so huge that its value can be reflected in the final integral. In this way, discontinuity distribution of $\sigma(x)$ in the xoz plane can be mapped in B-mode by placing the ultrasound transducer (along e_x) at evenly distributed points along e_z and joining all channels of measured current signals together.

2.2 Linearly frequency-modulated ultrasound pulse stimulation and the current signal generated

Linearly frequency-modulation is a technique often used in continuous wave imaging mode to reduce the peak power requirement while maintaining the same average power, SNR, etc. In this work, linearly frequency-modulation doesn't work in continuous wave mode but uses wide pulses. As shown in Figures 2.2 and 2.4, a linearly frequency-modulated RF pulse T_x (2.6.1) is generated and used to stimulate the ultrasound transducer, yielding the transmitted ultrasound pressure signal T_{us} (2.6.2) towards the target sample:

$$T_x = A_0 \sin \left\{ 2\pi \left[f_0 + \frac{\Delta f}{2T} (t - kT_1) \right] (t - kT_1) + \phi_0 \right\},$$

$$kT_1 \leq t < kT_1 + T, k = 0, \pm 1, \pm 2, \dots \quad (2.6.1)$$

$$T_{us} = A_1(t) \sin \left\{ 2\pi \left[f_0 + \frac{\Delta f}{2T} (t - kT_1) \right] (t - kT_1) + \phi_1 \right\},$$

$$kT_1 \leq t < kT_1 + T, k = 0, \pm 1, \pm 2, \dots \quad (2.6.2)$$

where A_0 is the amplitude of the transmitted signal, $A_1(t)$ is the amplitude of the ultrasound pressure signal T_{us} , f_0 is the initial frequency, T is the modulation period or the pulse duration, Δf is the modulation frequency bandwidth, T_1 is the linearly frequency-modulated pulse repeat period, ϕ_0 is the initial phase of the T_x , ϕ_1 is the initial phase of the T_{us} , and k is any integer.

In the presence of an electrical conductivity variation, an electrical current signal is generated due to the Lorentz force (2.1). As shown in (2.5), the induced current signal is the time-domain integral of the ultrasonic pressure signal. Because the

time-domain integral of a sinusoid results in a sinusoid of the same frequency, the resulting current signal has the same instantaneous frequency as the ultrasound pressure signal. But because that T_{us} is linearly frequency modulated and that the time domain integral in (2.5) produces the current signal with its instantaneous amplitude inversely proportional to the instantaneous frequency of T_{us} - the integral of ultrasound of low frequency produces a relatively large amplitude while the integral of ultrasound of high frequency produces a relatively small amplitude, amplitude variations are generated in the electrical current produced, which means new frequencies are introduced into the electrical current.

The electrical current signal produced is detected by the electrodes, and amplified by the low noise pre-amplifier, and finally becomes the radio-frequency signal received R_x (2.7). Comparing (2.6.1) with (2.7), we can get that the frequency difference between the instantaneous T_x and R_x is proportional to the time-of-flight (TOF) of the ultrasound waves from the transducer to the target.

$$R_x = A(t) \sin \left\{ 2\pi \left[f_0 + \frac{\Delta f}{2T} \left(t - kT_1 - \frac{R}{c} \right) \right] \left(t - kT_1 - \frac{R}{c} \right) + \phi_0 \right\},$$

$$kT_1 + R/c \leq t < kT_1 + R/c + T, k = 0, \pm 1, \pm 2, \dots \quad (2.7)$$

where $A(t)$ is the amplitude of the received signal which takes account of the amplitude variation of the ultrasound signal during propagation and the amplitude variation during the mechanics-to-electrics transformation, R is the distance of the ultrasound transducer to the medium where electrical conductivity variation exists, and c is the ultrasound (mainly the compression wave or the longitudinal wave) propagation velocity in the sample.

2.3 Calculation of the longitudinal distance - using coherent demodulation scheme

The implementation of the coherent demodulation technique in scanning electric conductivity gradients with linearly frequency-modulated ultrasound-induced Lorentz force (SECG-LFM-UILF) is shown in Figure 2.2. The instantaneous frequency difference between R_x and T_x can be obtained through coherent demodulation. The R_x

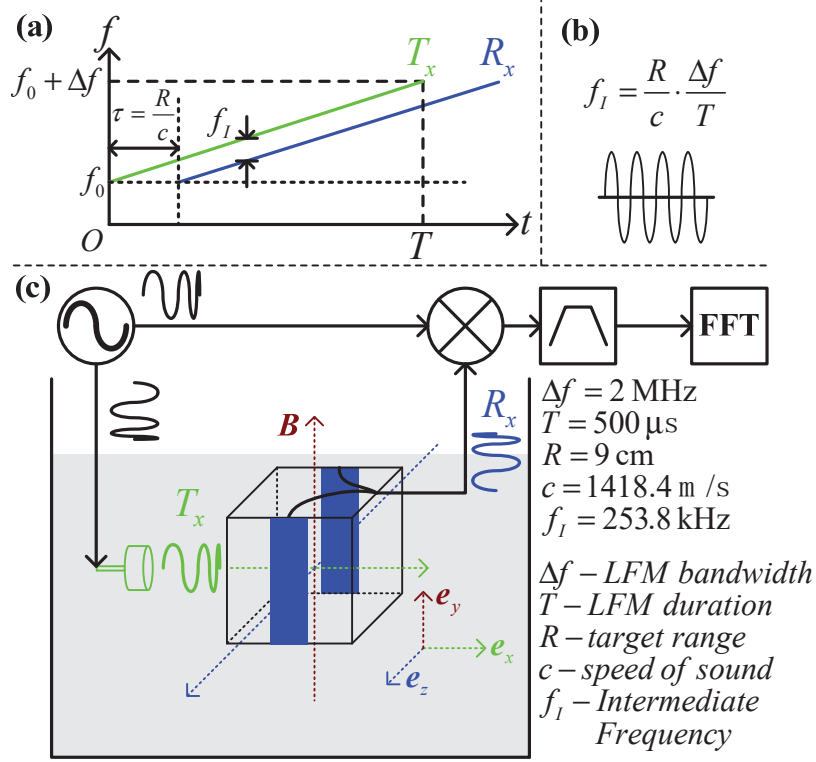


Figure 2.2. SECG-LFM-UILF using coherent demodulation technique (Sun *et al.* 2018b). (a) Frequency characteristics of the T_x and R_x . (b) Intermediate frequency. (c) Schematic of SECG-LFM-UILF system using coherent demodulation technique.

multiplies with the local oscillator signal L_x , which is also linearly frequency-modulated with the same modulation frequency-band and time-period as T_x and originates from the same source as the T_x . After filtering the double frequency signal, the output signal is the intermediate frequency signal I , whose instantaneous frequency equals the frequency difference between R_x and T_x . There are two schemes of coherent demodulation: the in-phase coherent demodulation scheme and the in-phase/quadrature-phase (IQ) coherent demodulation scheme.

For the in-phase coherent demodulation scheme, the in-phase local oscillator signal L_I has the same linear frequency modulation and the same phase as the T_x . The in-phase intermediate frequency signal (I_I) is obtained by demodulating the detected current signal R_x through multiplying (2.8) with the coherent in-phase local oscillator signal L_I and low-pass filtering (LPF) (2.9). The detailed derivation of (2.8) from (2.6.2) and (2.7) is listed in appendix 1.

$$\begin{aligned}
 L_I \cdot R_x = & -\frac{A_0 A(t)}{2} \cos \left\{ \begin{aligned} & 4\pi \left[f_0 + \frac{\Delta f}{2T} \left(t - kT_1 - \frac{R}{c} \right) \right] (t - kT_1) \\ & -2\pi \left(f_0 - \frac{\Delta f}{2T} \cdot \frac{R}{c} \right) \frac{R}{c} + 2\phi_0 \end{aligned} \right\} \\
 & + \frac{A_0 A(t)}{2} \cos \left[2\pi (t - kT_1) \frac{\Delta f}{T} \cdot \frac{R}{c} + 2\pi \left(f_0 - \frac{\Delta f}{2T} \cdot \frac{R}{c} \right) \frac{R}{c} \right] \\
 & kT_1 + R/c \leq t < kT_1 + R/c + T, k = 0, \pm 1, \pm 2, \dots. \quad (2.8)
 \end{aligned}$$

$$\begin{aligned}
 I_I = LPF\{T_x \cdot R_x\} \propto & A(t) \cos \left[2\pi (t - kT_1) \frac{\Delta f}{T} \cdot \frac{R}{c} + 2\pi \left(f_0 - \frac{\Delta f}{2T} \cdot \frac{R}{c} \right) \frac{R}{c} \right] \\
 & kT_1 + R/c \leq t < kT_1 + R/c + T, k = 0, \pm 1, \pm 2, \dots. \quad (2.9)
 \end{aligned}$$

For the IQ coherent demodulation scheme, the R_x is divided into two equal channels, of which one is demodulated by the L_I to obtain the I_I and the other is demodulated by the quadrature-phase local oscillator signal (L_Q), which has the same linear frequency modulation as T_x but keeps ahead of T_x in phase by $\pi/2$, also through multiplication (2.10) and LPF (2.11) to obtain the quadrature-phase intermediate frequency signal (I_Q).

$$\begin{aligned}
 L_Q \cdot R_x = & \frac{A_0 A(t)}{2} \sin \left\{ \begin{aligned} & 4\pi \left[f_0 + \frac{\Delta f}{2T} \left(t - kT_1 - \frac{R}{c} \right) \right] (t - kT_1) \\ & -2\pi \left(f_0 - \frac{\Delta f}{2T} \cdot \frac{R}{c} \right) \frac{R}{c} + 2\phi_0 \end{aligned} \right\} \\
 & + \frac{A_0 A(t)}{2} \sin \left[2\pi (t - kT_1) \frac{\Delta f}{T} \cdot \frac{R}{c} + 2\pi \left(f_0 - \frac{\Delta f}{2T} \cdot \frac{R}{c} \right) \frac{R}{c} \right] \\
 & kT_1 + R/c \leq t < kT_1 + R/c + T, k = 0, \pm 1, \pm 2, \dots. \quad (2.10)
 \end{aligned}$$

$$\begin{aligned}
 I_Q = LPF\{L_Q \cdot R_x\} \propto & A(t) \sin \left[2\pi (t - kT_1) \frac{\Delta f}{T} \cdot \frac{R}{c} + 2\pi \left(f_0 - \frac{\Delta f}{2T} \cdot \frac{R}{c} \right) \frac{R}{c} \right] \\
 & kT_1 + R/c \leq t < kT_1 + R/c + T, k = 0, \pm 1, \pm 2, \dots. \quad (2.11)
 \end{aligned}$$

Then, the complex form of the intermediate frequency signal (I) is obtained by combining I_I and I_Q :

$$\begin{aligned}
 I = I_I + jI_Q \propto & A(t) \exp \left[j2\pi (t - kT_1) \frac{\Delta f}{T} \cdot \frac{R}{c} + j2\pi \left(f_0 - \frac{\Delta f}{2T} \cdot \frac{R}{c} \right) \frac{R}{c} \right] \\
 & kT_1 + R/c \leq t < kT_1 + R/c + T, k = 0, \pm 1, \pm 2, \dots. \quad (2.12)
 \end{aligned}$$

From (2.9) and (2.12), we can get that the intermediate frequency (f_I) equals to:

$$f_I = \frac{\Delta f}{T} \cdot \frac{R}{c} \quad (2.13)$$

Therefore, f_I is linearly related to the distance R from the transducer to the medium where electrical conductivity changes exist. And the R can be reconstructed

from the spectrum of the intermediate frequency signals based on (2.13), which is the central result of the method.

As mentioned above, the resulting current signal's varying amplitude changes its frequency components. Instead of deriving the analytical solution of the integral of linearly frequency-modulated ultrasound pressure signal, theoretical analysis is adopted here to show that the varying amplitude barely changes R_x 's frequency component and the integrity of the final intermediate frequency signal is comparable to that with constant amplitude. As shown in Figure 2.3, the -3 dB bandwidths of the two intermediate frequency signals' spectra are same, but the spectrum side lobe level of the intermediate frequency signal obtained by demodulation of the integral of the delayed sinusoid is a little higher than that obtained by demodulation of the delayed sinusoid.

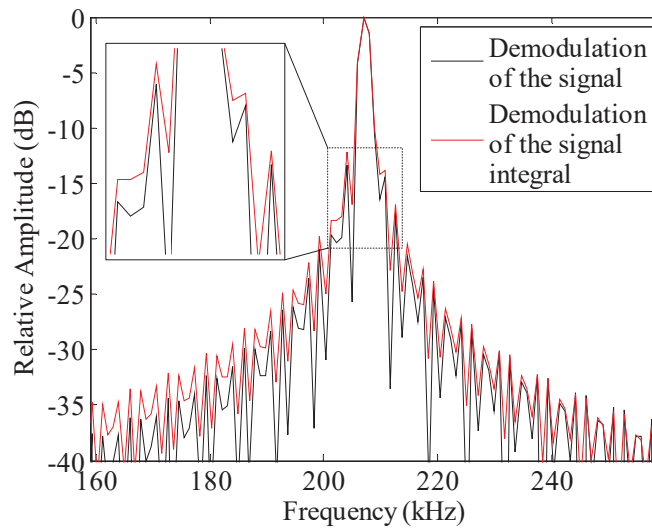


Figure 2.3. Comparison of the spectra of the intermediate frequency signals obtained by demodulation of the delayed linearly frequency-modulated signal (black line) and by demodulation of the integral of the delayed linearly frequency-modulated signal (red line) (Sun *et al.* 2018b).

The longitudinal resolution is determined by the modulation duration, the linearly frequency-modulation bandwidth, the effective intermediate frequency signal duration (T_e), and the sound speed, i.e. as (2.14).

$$\Delta R = \frac{T}{\Delta f} \cdot \frac{1}{T_e} \cdot c, \text{ where } T_e = T - \frac{R}{c} \quad (2.14)$$

Therefore, if using modulation duration of 500 μs and bandwidth of 2 MHz, longitudinal resolution is better than 1 mm for longitudinal imaging range less than 100 mm ($T_e = 429.5 \mu\text{s}$).

The lateral resolution of the 2D electrical conductivity gradient map is determined by the -6 dB beam width of the ultrasound, and for Olympus immersion focal transducers, -6 dB beam diameter of 3 mm can be obtained.

2.4 Calculation of the longitudinal distance - using pulse compression scheme

The implementation of pulse compression in SECG-LFM-UILF is shown in Figure 2.4. The tank is filled with transformer oil so that both the transducer and the sample are under the surface of the oil and the ultrasound can be transmitted easily into the sample. A LFM ultrasound pulse is used to stimulate the sample, which is placed in the static magnetic field. Electrical current density is generated as the Lorentz force acts on the positive and negative moving ions. The detected current signal then is sampled with the high sampling-rate ADC. Finally the digital SECG-LFM-UILF wide pulse is compressed by convolving it with the filter's impulse response function. Theoretically, the width of the compressed pulse equals the inverse of the bandwidth of the LFM ultrasound signal and the signal to noise ratio improves by a factor of the square root of the modulation period and bandwidth.

The selected matched pulse compression filter has the impulse response of the form:

$$h(t) = \cos \left\{ 2\pi \left(f_0 + \Delta f - \frac{\Delta f}{2T} t \right) t + \phi_0 \right\}, \quad 0 \leq t < T \quad (2.15)$$

where f_0 is the initial frequency, T is the frequency modulation period or the pulse duration, Δf is the modulation frequency bandwidth, and ϕ_0 is the initial phase of the T_x in (2.6.1).

$h(t)$'s instantaneous frequency decreases linearly at the same absolute rate as R_x , and $H(f)$'s phase group delay (τ_H) decreases linearly at the rate of $T/\Delta f$ (Figure 2.4.a). The characteristics of the compression filter enable it to compress R_x into a narrow

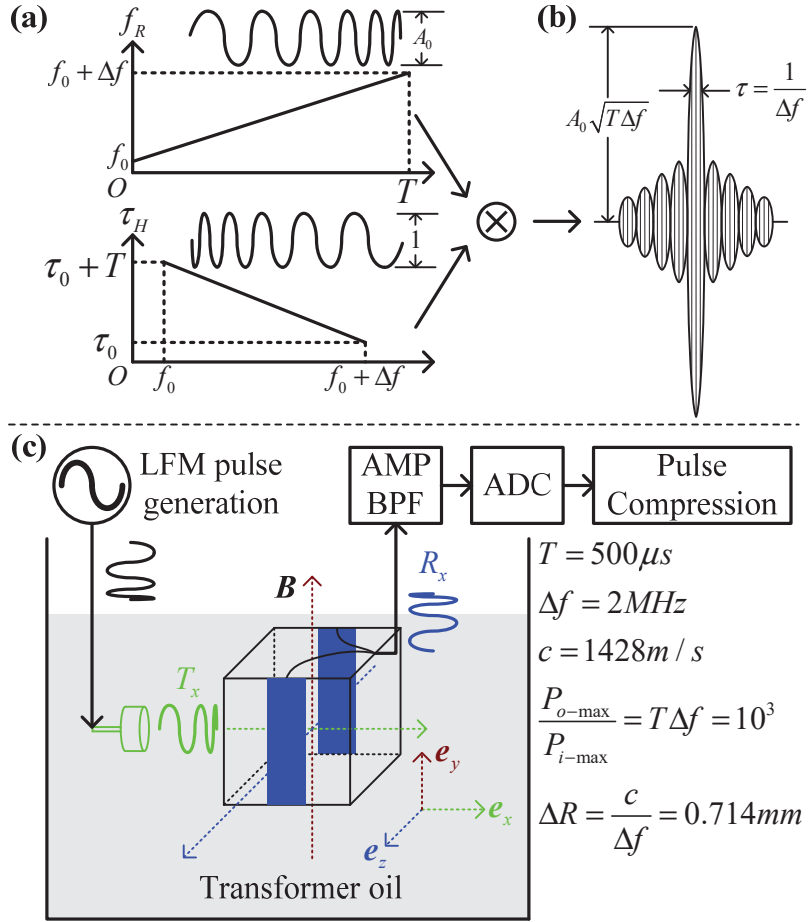


Figure 2.4. SECG-LFM-UILF using pulse compression technique (Sun *et al.* 2017). (a) Frequency characteristics of the R_x and the group delay characteristics of the pulse compression filter function H . (b) The output signal of the pulse compression filter. (c) Schematic of SECG-LFM-UILF system using pulse compression technique.

pulse with high effective peak power (Figure 2.4.b). The peak instantaneous power of the pulse increases by a ratio of $T\Delta f$, and the temporal width (measured at appropriate point) of the compressed pulse equals $1/\Delta f$. The longitudinal resolution therefore is:

$$\Delta R = c/\Delta f \quad (2.16)$$

Instead of deriving the analytical solution of the compressed pulse, theoretical analysis is done to get a view of the compressed signal, as shown in Figure 2.5. The generation of the SECG-LFM-UILF signal (of duration of $500 \mu s$) has taken into consideration of the uneven amplitude-frequency response of the transducer and the integral in the acousto-electrical transformation. As shown in Figure 2.5, although the

compressed pulse's waveform degrades from one sharp peak into two peaks due to R_x 's varying amplitude, SECG-LFM-UILF signal's width is compressed a lot and a high longitudinal resolution is achieved.

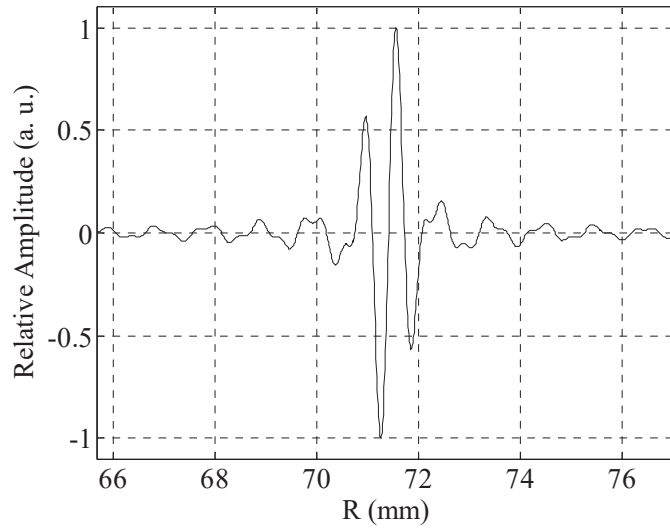


Figure 2.5. SECG-LFM-UILF signal - induced by electrical conductivity discontinuity located at 71.4 mm from the transducer - is compressed (Sun *et al.* 2018b). The ultrasound propagation speed of 1428 m/s in the medium is used here.

2.5 Experimental setup and methods

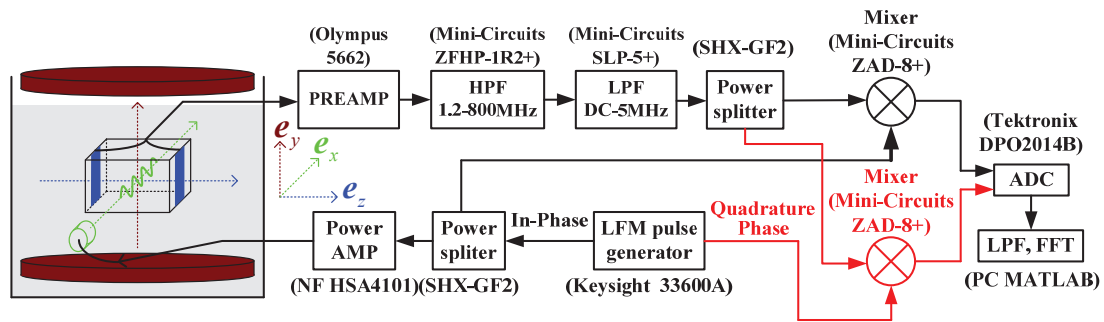


Figure 2.5. Schematic layout of SECG-LFM-UILF experiment setup using the coherent demodulation method. The parts in red were specific to the IQ demodulation scheme.

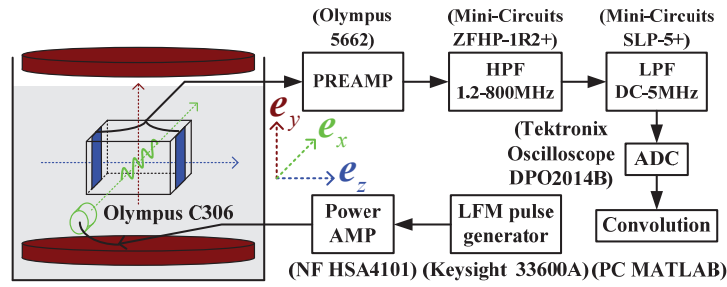


Figure 2.6. Schematic layout of SECG-LFM-UILF experiment setup using the pulse compression technique.

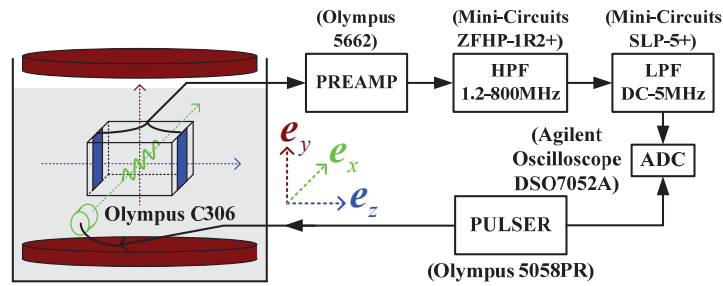


Figure 2.7. Schematic layout of SECG-UILF experiment setup using high-intensity wide-band ultrasound pulse signal.

2.5.1 LFM ultrasound pulse generation system

Two linearly frequency-modulated (LFM) RF pulse signals are generated using the Arbitrary Waveform Generator (AWG) (Keysight 33612A). Both of them are generated with a modulation time of $500 \mu\text{s}$, a sweep frequency ranging from 1.4 MHz to 3.4 MHz, a pulse repeat frequency (PRF) of 100 Hz. The first LFM pulse signal had an initial phase of 0 degrees while the second LFM pulse signal had an initial phase of $\pi/2$. The two LFM pulse signals are triggered by the same source and are perfectly synchronized. The first LFM pulse signal has an amplitude of 1.1 peak-to-peak voltage (V_{pp}) and the second pulse signal has an amplitude of 2.2 V_{pp} . The first LFM pulse signal is attenuated (Shanghai Huaxiang, Step attenuator GKTS10-8-90-1-B) by 20 dB and then used as the quadrature-phase local oscillator signal. The first LFM pulse is equally split (Shanghai Huaxiang, SHX-GF2) into two channels, of which one channel is attenuated (Shanghai Huaxiang, Step attenuator GKTS10-8-90-1-B) by 20 dB and then used as the in-phase local oscillator signal

while the other channel is power amplified to the level of 60 V_{pp} (Figure 2.8) and used to stimulate the ultrasound transducer (Olympus C306) to generate the linearly frequency-modulated ultrasound pulse. The peak stimulating power to the transducer therefore is 39.54 dBm. The Olympus C306 is a flat transducer, with an element size of 1.27 cm in diameter and -6 dB frequency band starting at 1.4MHz and ending at 3.38 MHz (Figure 2.9.b).

We use a needle hydrophone (Institute of Acoustics, Chinese Academy of Sciences, model PT-1704365) and measured the acoustic pressure generated by the transducer. Linearly frequency-modulated electric pulse of amplitude 60 V_{pp} is used to stimulate the ultrasound transducer (Olympus C306). Figure 2.10.a shows the peak electric signal output from the hydrophone when the hydrophone is placed 60 mm in front of the C306. But, we can not calculate the acoustic pressure at any time point because the sensitivity of the hydrophone (Table 2.1) is not constant between 1.4 MHz and 3.4 MHz and only values of sensitivity at several discrete frequencies are known. We use the sensitivity values of 2.28 $\mu\text{V}/\text{Pa}$ for frequency between 1.4 and 2.4 MHz) and 0.8 $\mu\text{V}/\text{Pa}$ for frequency between 2.4 and 3.4 MHz when calculating the corresponding acoustic pressure, as shown in Figure 2.11. The calculated acoustic peak pressure is 0.395 MPa, the mechanical index (*MI*) is 0.16, and the spatial peak temporal average intensity (*I_{SPTA}*) is 17.4 mW/cm².

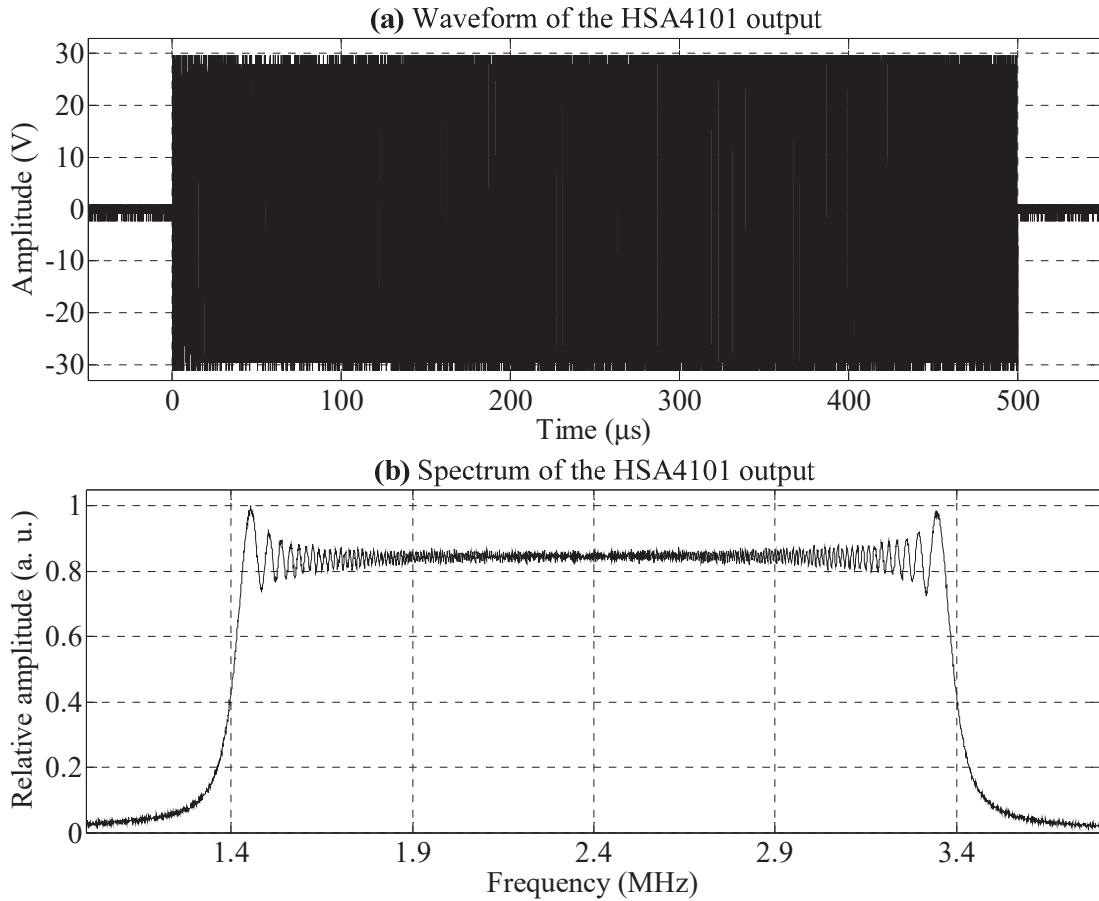


Figure 2.8. Linearly frequency-modulated wide voltage pulse stimulating the ultrasound transducer. (a) The waveform. (b) The spectrum.

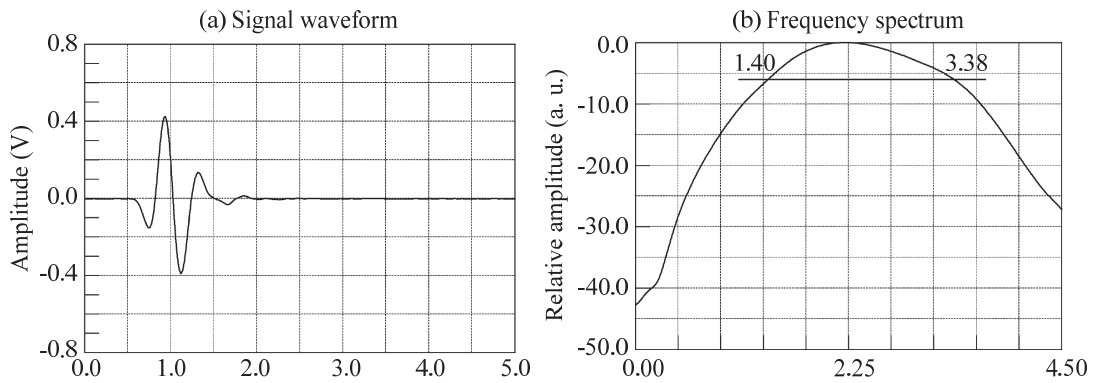


Figure 2.9. Ultrasound pulse produced by the ultrasound transducer when feeding with a wide-band spike voltage signal. (a) Signal waveform. (b) Frequency spectrum.

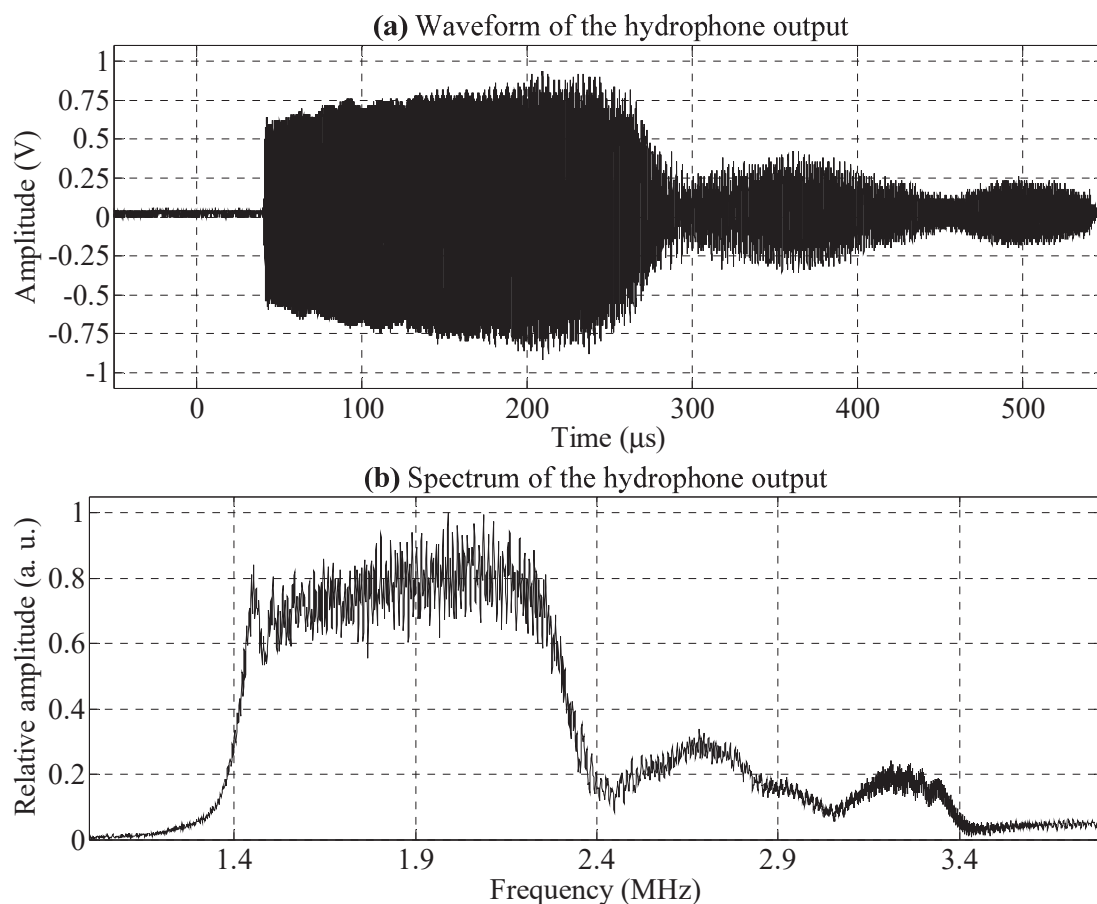


Figure 2.10. The voltage output signal of the needle hydrophone. (a) The waveform. (b) The Spectrum.

Table 2.1. Sensitivity of the hydrophone (PT-1704365).

f (MHz)	M ($\mu\text{V}/\text{Pa}$)	M (dB)
1	2.38	-232.5
2	2.28	-232.8
3	0.66	-243.6
4	1.00	-240.0

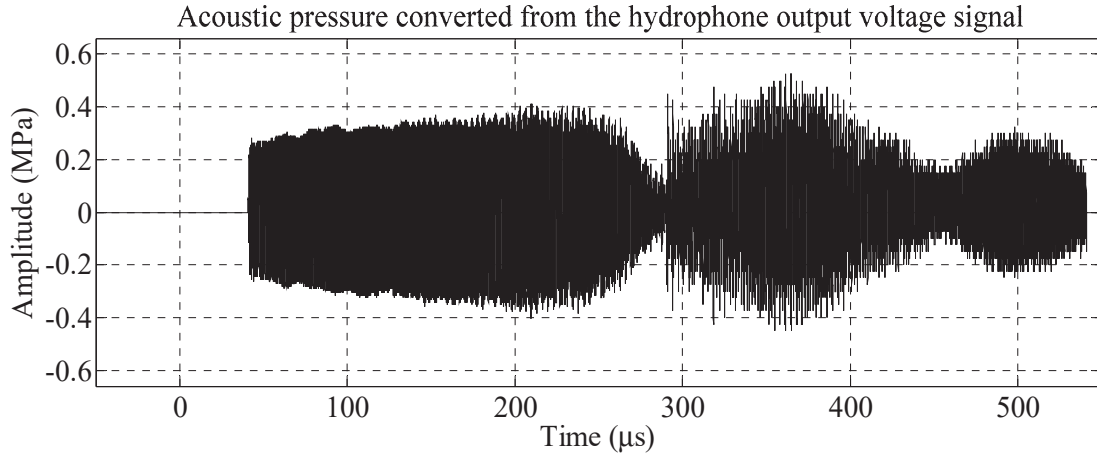


Figure 2.11. Acoustic pressure signal converted from the hydrophone output voltage signal using the hydrophone sensitivity.

2.5.2 Magnetic field

The quasi-uniform static magnetic field is generated using a pair of permanent magnets placed along the same axis and in the same direction. Both of the two magnets are made from the compound material of Neodymium Iron Boron (Ningbo Yunsheng, NdFeB N45) (Table 2.2). The two magnets are shaped in cylinders and of the same dimensions. The diameter of the cylinder is 150 mm and the height is 30 mm. The surface distance between the two magnets is 83 mm. The two magnets are fixed in a framework made of aluminum (Figure 2.12.a). Static magnetic field numerical calculation using the software Maxwell 15.0 shows that the average magnetic induction density within the 50 mm×50 mm×50 mm of the space between the two magnets is about 260 mT with homogeneity greater than 94.5% (Figure 2.12.c).

Table 2.2. The magnetic characteristics of the compound material of Neodymium Iron Boron N45.

Remanence (B_r/T)		Coercive Field Intensity ($H_{cB}/kA/m$)	Intrinsic Coercive Field Intensity ($H_{cJ}/kA/m$)	Max Energy Product ($BH_{max}/KJ/m^3$)		Temperature ($^{\circ}C$)
Min	Max	Min	Min	Min	Max	20
1.32	1.37	876	955	342	346	

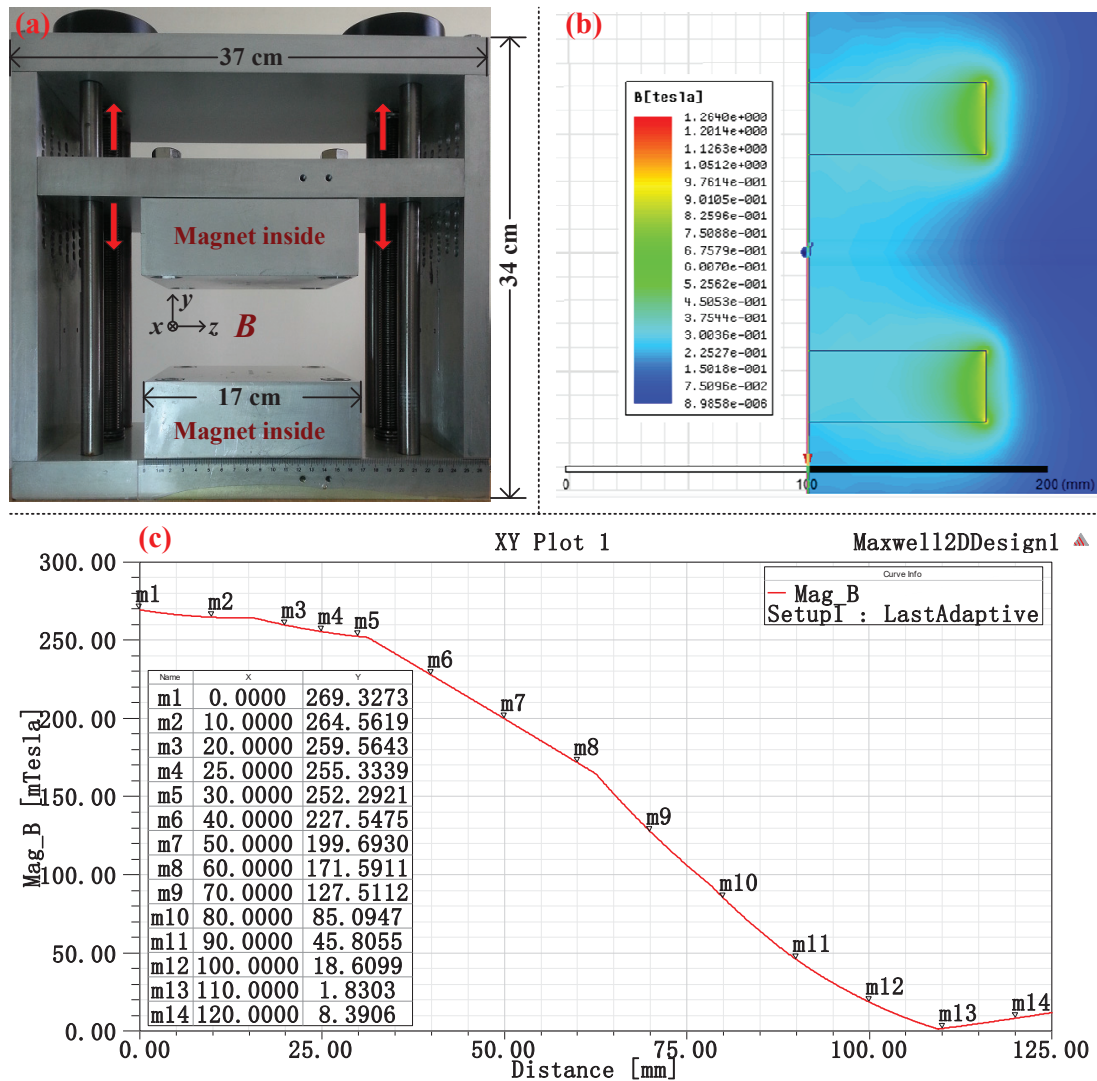


Figure 2.12. The static magnetic field system. (a) The aluminum frame used for holding the magnets. (b) The 2D magnetic field intensity distribution. (c) The magnetic field intensity along the axial coordinate in the plane of $y = 0$.

2.5.3 Sample

The samples used in our experiments are agar phantoms made using salt, agar powder and water. The agar phantoms are made by the following procedures: (1) stir and heat the saline water to the boil; (2) add the agar powder, heat the mixture to the boil again, and then stop heating but keep stirring the mixture; (3) stop stirring the mixture when it cools down to around 40 degrees Celsius; and (4) put the mixture in a refrigerator of 5 degrees Celsius for more than 2 hours. The quantity of agar powder used is 1 wt%. And the electrical conductivity of the agar phantom is controlled by

varying the salt concentration. The electrical conductivity of the agar phantom ranges from 0.2 S/m (salt concentration $1.351 \cdot 10^{-3}$ g/ml) to 0.5 S/m ($3.379 \cdot 10^{-3}$ g/ml). The electrical conductivity of normal human biological tissue is approximately 0.4 S/m while that of tumor tissue is more than 13% larger (Haemmerich *et al.* 2003), therefore, the electrical conductivity of the agar phantoms thus made can represent that of biological tissue. The agar phantoms are 75 mm wide (z) and 50 mm (y) high with varying dimension in the ultrasound propagation direction, as shown in Figure 2.13. The agar phantom sample is placed stably in a framework made by acrylic board. The acrylic board framework holding the agar phantom is placed on top of the bottom aluminum shell which holds the magnet. The acrylic board framework holding the agar phantom, the aluminum framework holding the magnets, and the ultrasound transducer are put in a water tank filled with the transformer oil. The transformer oil acts as the ultrasound conductive medium. Two rectangular hole of dimensions of 45 mm \times 30 mm ($z \times y$) are cut from the front and back sides of the acrylic board framework so that the ultrasound can propagate directly from the transformer oil to the sample and then back to the transformer oil. Another use of the acrylic framework is to hold the detection electrodes and the sample tightly so that electrical current signal can be well detected.

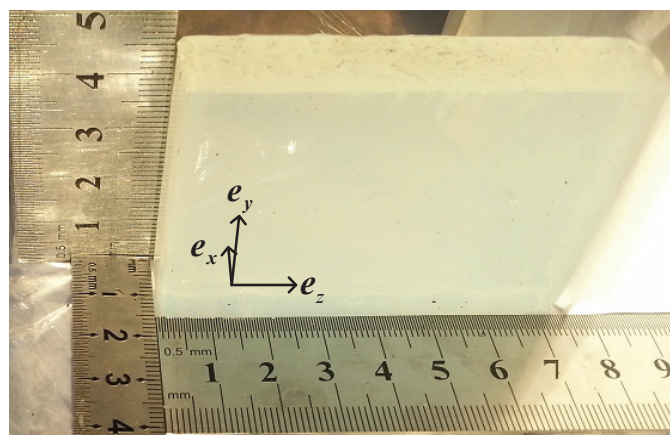


Figure 2.13. Agar phantom sample (Sun *et al.* 2018b). Its dimensions are 50 mm \times 75 mm ($y \times z$).

2.5.4 Signal detection system

Plane electrodes made from copper foil (0.1 mm thick) are used to collect the electrical current signal. The length of the rectangular electrodes is 50 mm while the width varies in 7.5 mm, 12.5 mm and 22 mm. Experiments show that the width of the electrodes makes little difference to the current signal detected. The detected electrical current signal is firstly amplified by 34 dB (Olympus PREAMP 5662), and then band-pass filtered (Mini-Circuits, ZFHP-1R2+ cascaded with SLP-5+).

For the method of calculation of the longitudinal distance using the coherent demodulation scheme, the filter output signal is equally divided into two channels by a power splitter (Shanghai Huaxiang, SHX-GF2). And for the in-phase coherent demodulation scheme, only one channel of the signal is mixed (Mini-Circuits ZAD-8+) with the in-phase coherent local oscillator signal, while for the IQ coherent demodulation scheme, two channels of signals are mixed (Mini-Circuits ZAD-8+) with the in-phase and the quadrature-phase coherent local oscillator signals respectively. The output(s) of the mixer(s) which contain(s) the intermediate frequency (IF) signals is (are) sampled at a rate of 125 mega samples per second (MSPS) by the oscilloscope (Tektronix DPO2014B). The DPO2014B also implements coherent averaging by 512 times on the digital data to increase the SNR by 27.1 dB. The DPO2014B finally saves the averaged data in CSV files, which are transferred to PC for spectrum calculation through FFT using MATLAB (Figure 2.5).

For the method of calculation of the longitudinal distance using the pulse compression scheme, the output of the filter is directly sampled at a rate of 125 mega samples per second (MSPS) by the oscilloscope (Tektronix DPO2014B). The DPO2014B also implements coherent averaging by 512 times on the digital signal to increase the SNR by 27.1 dB. And similarly, the DPO2014B saves the averaged signals in CSV files, which are transferred to PC. Using MATLAB, the digital signal convolves with the impulse response of the pulse compression filter. After the TOF/distance transformation, the longitudinal distance of the medium having conductivity gradient are retrieved from the compressed signal.

2.5.5 Four SECG-LFM-UILF experiments using linearly frequency modulated ultrasound pulse

The first experiment is to verify the feasibility of SECG-LFM-UILF to recognize the electrical conductivity variations and it is done with a three-layer agar phantom sample. Each layer of the sample has dimensions of 10 mm×50 mm×75 mm ($X \times Y \times Z$). Viewing from the transducer side, the electrical conductivities of each layer of the phantom are, respectively, 0.2 S/m, 0.2 S/m and 0.4 S/m, as in Figure 2.14.a. Plastic film (0.015 mm thick) is used to separate the three layers and to stop Na^+ and Cl^- in one layer from entering into the neighboring layers. The three layers and the plastic film are placed so closely to each other that there are few air pockets between them. In experiments, the ultrasound is transmitted along e_x . Intermediate frequency signals are collected at linearly increasing distances between the transducer and the agar phantom.

The second experiment is to demonstrate the performance of the SECG-LFM-UILF and it is done with two multi-shaped agar phantoms. The first agar phantom has a rectangular hole in the center. The electrical conductivity of the agar phantom is 0.2 S/m. The agar phantom is of dimensions 30 mm×50 mm×75 mm ($X \times Y \times Z$), while the dimensions of the middle rectangular hole were 10 mm×50 mm×15 mm ($X \times Y \times Z$), as shown in Figure 2.14.b. When doing experiments, the rectangular hole is filled with transformer oil. The second agar phantom has three layers, with electrical conductivities 0.2 S/m, 0.4 S/m and 0.2 S/m respectively. The dimensions of each layer are clearly shown in Figure 2.14.c. The middle parts of the first and third layers are 2.5 mm thinner than other parts, while that of the second layer is 5 mm thicker than the remaining parts. Each layer has a dimension of 50 mm in y . Plastic film (0.015 mm thick) is used to separate the three layers and to stop Na^+ and Cl^- in one layer from entering into the neighboring layers. The three layers and the plastic film are placed so closely to each other that there are few air pockets between them. In experiments, the ultrasound is transmitted along e_x , and the ultrasound transducer keeps a distance of 70 mm to the front surface of the agar phantom sample.

The third experiment is to verify the longitudinal resolution of SECG-LFM-UILF as (2.14) and (2.16). The B-scan experiments were done on a saline agar phantom with two slots. The electrical conductivity of the agar phantom was 0.5 S/m. The agar phantom had the dimensions of 30 mm×50 mm×75 mm. Both of the two top-bottom-through slots were 15 mm wide. In the compression wave propagation direction, the dimension of the first slot was 1 mm and that of the second slot was 2 mm. And the distances - from the front interface to the center of the first slot, between the centers of the slots and from the center of the second slot to the back interface - all are 10 mm, as shown in Figure 2.14.d. In experiments, the ultrasound is transmitted along e_x . And the distance between the transducer and the front interface of the agar phantom sample is 70 mm, so T_e in (2.14) for the whole agar phantom was greater than 423.0 μ s. The two slots are filled with transformer oil when doing experiments.

The fourth experiment is to evaluate the capability of the coherent IQ demodulation scheme based SECG-LFM-UILF in retrieving the polarity information of the conductivity variations. In SECG-LFM-UILF, the detected current signal contains the polarity information of the conductivity variation, but the in-phase demodulation method fails to retrieve the initial phase of the intermediate frequency (IF) signal through the Fast Fourier Transform (FFT), which prevents from retrieving the polarity of conductivity variation. To get the initial phase of the IF signal, we tried the coherent IQ demodulation scheme in SECG-LFM-UILF. The experiments were done on a saline agar phantom of electrical conductivity of 2 S/m. The agar phantom had the dimensions of 15 mm×50 mm×75 mm ($X \times Y \times Z$)(2.14.e). In experiments, the ultrasound is transmitted along e_x . The in-phase and quadrature-phase IF signals are collected at linearly increasing distances to the transducer.

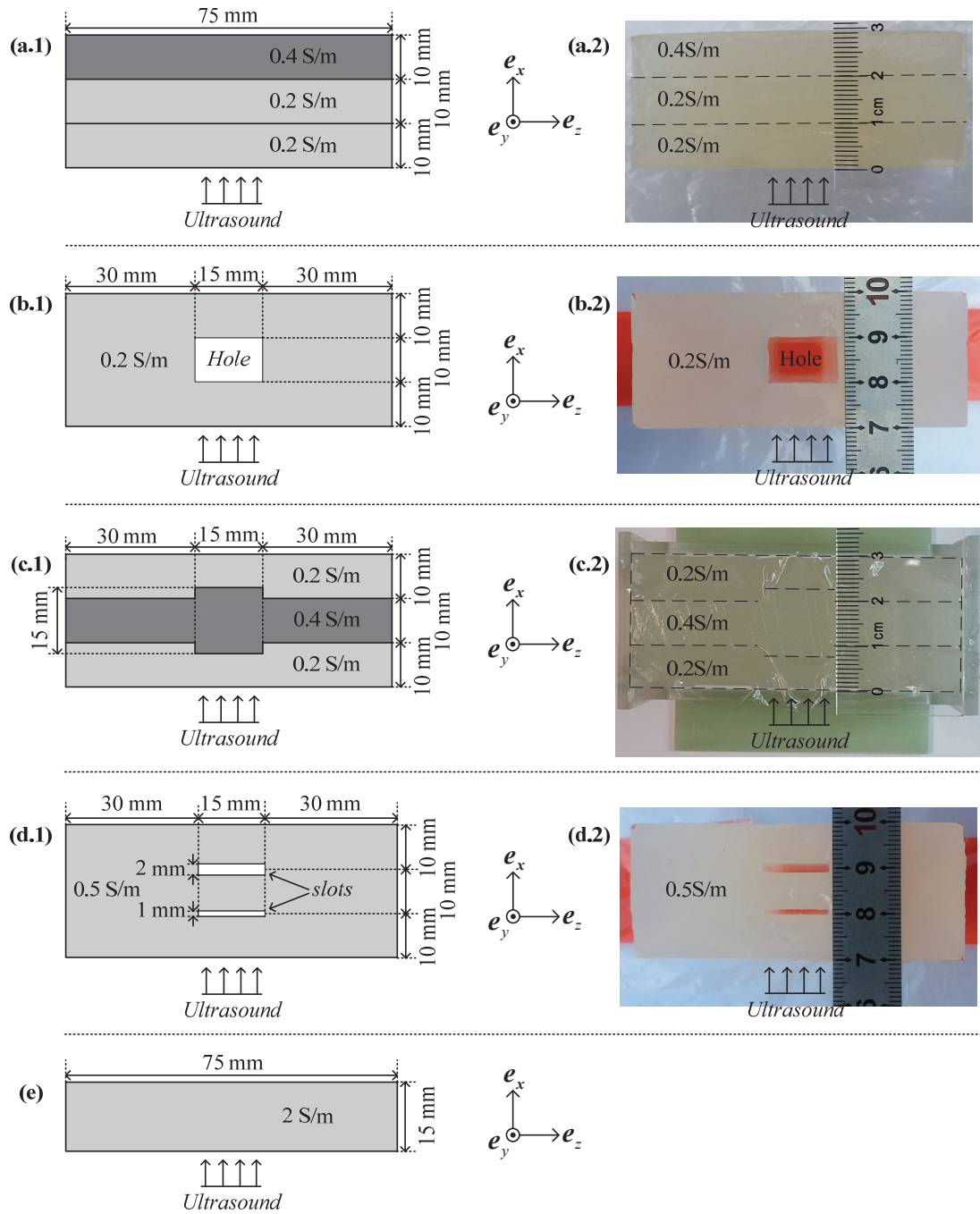


Figure 2.14. Multi-shaped agar phantoms samples (Sun *et al.* 2017, 2018b). (a) The 3-layer agar phantom for the first group of experiments. (b) The agar phantom with a rectangular hole inside for the second group of experiments. (c) The 3-layer agar phantom with the middle part of the second layer protruding outside for the second group of experiments. (d) The agar phantom with two top-bottom-through slots for the third group of experiments. (e) The 1-layer agar phantom for the fourth group of experiments.

2.5.6 SECG-UILF using high-voltage narrow pulse signal

For each sample in the experiments in section 2.5.5, conventional SECG-UILF using high acoustic pressure wide band pulse as the control experiment is carried out on it. The experimental setup (Figure 2.7) has the same sonication system as that of SECG-LFM-UILF but different stimulation and detection systems. The stimulating signal to the transducer (Olympus C306) is generated by a commercial pulser (Olympus 5058PR). The stimulating pulse has a negative peak of -400 volts (figure 2.15) - which corresponds to a peak instantaneous power of 65.05 dBm - and a PRF of 100 Hz. Under the stimulation by the negative broadband spike signal, the ultrasound transducer transmits ultrasound pulse towards the sample. Figure 2.16.a is the output signal of the hydrophone when the hydrophone is placed 60 mm in front of the C306. And figure 2.16.b is the spectrum of the hydrophone output signal. The spectrum peak is at round 2 MHz. Using the sensitivity of the hydrophone at 2 MHz ($M = 2.28 \mu\text{V}/\text{Pa}$), the acoustic pressure signal and its spectrum are calculated, as shown in figure 2.17.a and b. The calculated acoustic peak pressure is 0.965 MPa, the mechanical index (MI) is 0.40, and the spatial peak temporal average intensity (I_{SPTA}) is $1.90 \text{ mW}/\text{cm}^2$.

The induced current signal is detected using electrodes and then amplified by 54 dB using pre-amplifier (Olympus 5662). The amplified SECG-UILF signal is sampled at a rate of 10 MSPS by the oscilloscope (Agilent DSO7052A). The DSO7052A also implements coherent averaging by 1024 times on the digital data to increase the SNR by 30.1 dB. The DSO7052A finally saves the averaged data in CSV files, which are transferred to PC for further processing with MATLAB.

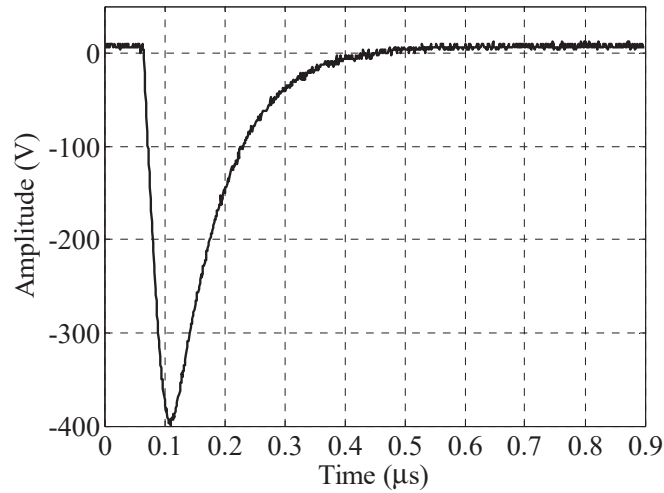


Figure 2.15. The negative high-voltage spike signal generated by the Olympus 5058PR.

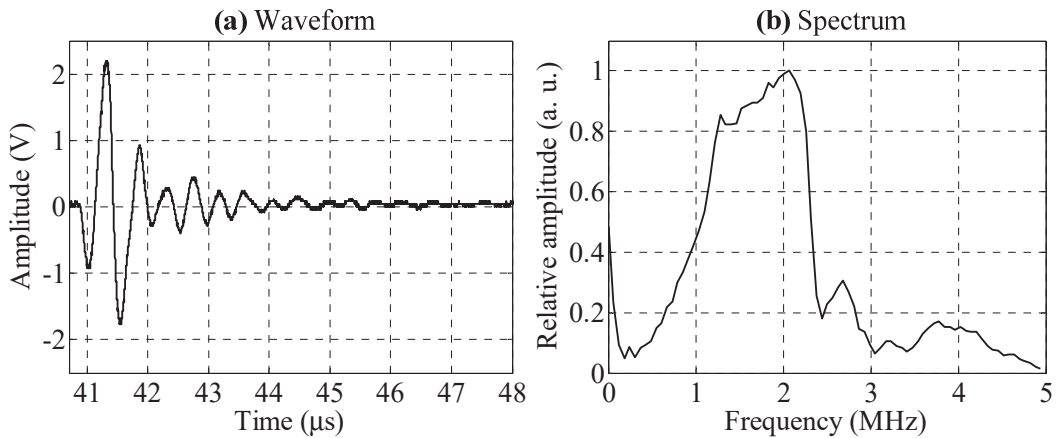


Figure 2.16. The output signal of the hydrophone when its distance to the transducer is 60 mm. (a) The waveform. (b) The spectrum.

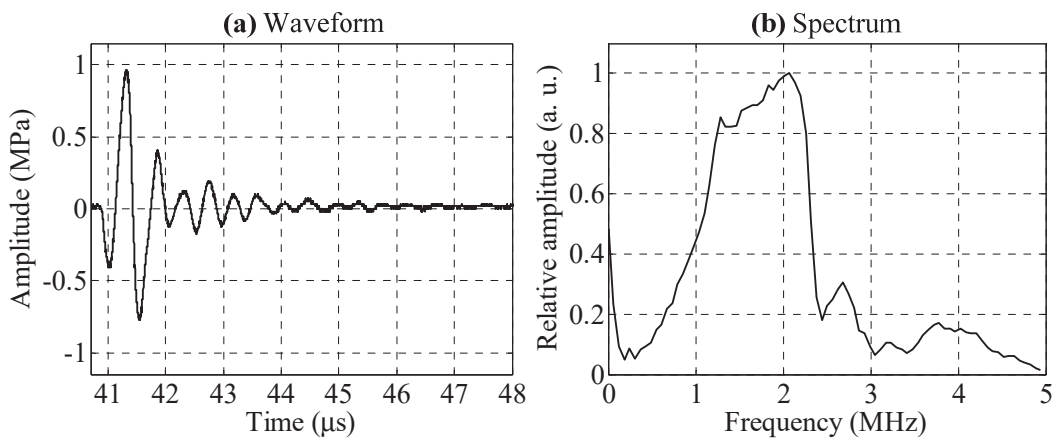


Figure 2.17. Acoustic pressure signal converted from the hydrophone output using $M = 2.28 \mu\text{V}/\text{Pa}$. (a) The waveform. (b) The spectrum.

2.6 Experiment results and discussion

2.6.1 The first group of experiment - confirmation of the feasibility of SECG-LFM-UILF

The first group of experiments is done with the three-layer agar phantom sample (Figure 2.14.a).

Figure 2.18.a.1 shows the spectrum of the intermediate frequency signal obtained by the in-phase-coherent-demodulation-scheme-based SECG-LFM-UILF when the transducer locates at the distance of 70 mm in e_x to the first interface. Intermediate frequency signals at 198.4, 254.6, and 282.3 kHz correspond to the first, the third, and the fourth interfaces of the agar phantoms, respectively. The weak signal at 227.0 kHz can not be judged as the intermediate frequency signal induced by the second interface, because the signal disappears rather than decreases or increases in frequency when the transducer is moved toward or far away from the phantom. Figures 2.18.a.2-4 show the relationship between the resulting intermediate frequency (the red squares) and the varying distances from the transducer to the first, the third, and the fourth interfaces, respectively. Theoretical values of the intermediate frequencies (the blue circles) for the distances to the three interfaces are also presented in Figures 2.18.a.2-4 for comparison. The compression wave propagation speed used for the transformer oil and the agar phantom are, respectively, 1418.4 and 1428.6 m/s at 17 °C, which has been confirmed experimentally before the experiments.

Figure 2.18.b.1 shows the compressed signal obtained by the pulse-compression-scheme-based SECG-LFM-UILF when the transducer locates at the distance of 70 mm in e_x to the first interface. The compressed pulses at time-of-flights (TOFs) of 49.35 μs , 63.48 μs , and 70.40 μs correspond to the first, the third, and the fourth interfaces of the agar phantoms, respectively. The weak signal at 56.53 μs can not be judged as the intermediate frequency signal induced by the second interface, because the signal disappeared rather than decreased or increased in TOF when the transducer is moved toward or far away from the phantom. Figures 2.18.b.2-4 show the

relationship between the resulting TOFs (the red squares) and the varying distances from the transducer to the first, the third, and the fourth interfaces, respectively. Theoretical values of the TOFs (the blue circles) for the distances to the three interfaces - which are calculated by R/c , where R is the longitudinal distance to the interface and c is the compression wave velocity - are also presented in Figures 2.18.a.2-4 for comparison.

Figure 2.18.c.1 shows the signal obtained by the traditional high-acoustic-pressure-based SECG-UILF when the transducer locates at the distance of 70 mm in e_x to the first interface. The pulses at time-of-flights (TOFs) of 49.38 μs , 63.58 μs , and 70.58 μs correspond to the first, the third, and the fourth interfaces of the agar phantoms, respectively. There is no pulse generated for the second interface. Figures 2.18.c.2-4 show the relationship between the resulting TOFs (the red squares) and the varying distances from the transducer to the first, the third, and the fourth interfaces, respectively. Theoretical values of the TOFs (the blue circles) for the distances to the three interfaces - which are calculated by R/c , where R is the longitudinal distance to the interface and c is the compression wave velocity - are also presented in Figures 2.18.a.2-4 for comparison.

The plastic film (0.015 mm thick) separating neighboring layers of the phantom creates a negative change of the $\sigma(x)$ at the front surface and a positive change of the $\sigma(x)$ at the back surface of the plastic film. Therefore, the gradient of $\sigma(x)$ in direction x had a negative delta function signal at the front surface and a positive delta function signal at the back surface of the plastic film, with the signals' amplitude being equal to the values of $\sigma(x)$ at corresponding sides of the plastic film. At the front and back surfaces of the plastic film, the negative and positive gradients of $\sigma(x)$ were 0.015 mm apart in space, and the compression waves differed in phase by between 5.2° (at $f = 1.4$ MHz) and 12.6° (at $f = 3.4$ MHz). The compression waves at the front and back surfaces of the plastic film canceled out each other a lot but not totally in the integral in (2.5) because of the opposite polarity of the gradient signals and the small phase difference between the compression waves at two surfaces of the plastic film. Theoretical analysis shows that the amplitude of the SECG-UILF signal due to the

second interface is between 9.1% (at $f = 1.4$ MHz) and 21.8% (at $f = 3.4$ MHz) of the amplitude of the SECG-UILF signal induced by a positive change of $\sigma(x)$ from 0 to 0.2 S/m, while that due to the third interface is between 100.8% (at $f = 1.4$ MHz) and 104.7% (at $f = 3.4$ MHz) of the amplitude of the LFEIT signal induced by a positive change of $\sigma(x)$ from 0 to 0.2 S/m. The result of the first experiment confirmed the theoretical analysis - in Figures 2.18.a-c.1, the SECG-UILF signals induced by the second interface are too weak to be recognized from the background noise while those induced by the third interface have the same level of amplitude as those induced by the first interface.

In this group of experiments, there are four interfaces where the discontinuities of the $\sigma(x)$ in direction x exist in the agar phantom. For the first interface, from the transformer oil to the first layer of the agar phantom, and the fourth interface, from the saline agar phantom to the transformer oil, gradients of $\sigma(x)$ are theoretically huge as the electrical conductivity $\sigma(x)$ changed in the form of a step function. For the second interface, as discussed earlier, the negative and positive gradients of $\sigma(x)$ at the front and back surfaces of the plastic film greatly reduce their overall effect in generating the SECG-UILF signal, and for the third interface, it has almost the same effect as a gradient of $\sigma(x)$ from 0 to 0.2 S/m in generating SECG-UILF signal. Besides the discontinuities of $\sigma(x)$, acoustic discontinuities also exist at these four interfaces. The phenomenon that only the three signals (the intermediate frequencies, the compressed pulses, and the spike pulses) are observed in the first experiment demonstrated that it are the discontinuities of $\sigma(x)$ rather than the acoustic discontinuities that generate the SECG-UILF signals.

The intermediate frequency of the signal obtained through the in-phase-coherent-demodulation-scheme-based SECG-LFM-UILF is less than 350 kHz for distance less than 110 mm, so the sampling rate of analog-to-digital conversion (ADC) can be as low as 700 KSPS whereas in the pulse-compression-scheme-based SECG-LFM-UILF, the ADC rate is at least 6.8 MSPS. To achieve this, SECG-LFM-UILF using the in-phase coherent demodulation scheme uses more complex circuit than SECG-LFM-UILF using the pulse compression scheme.

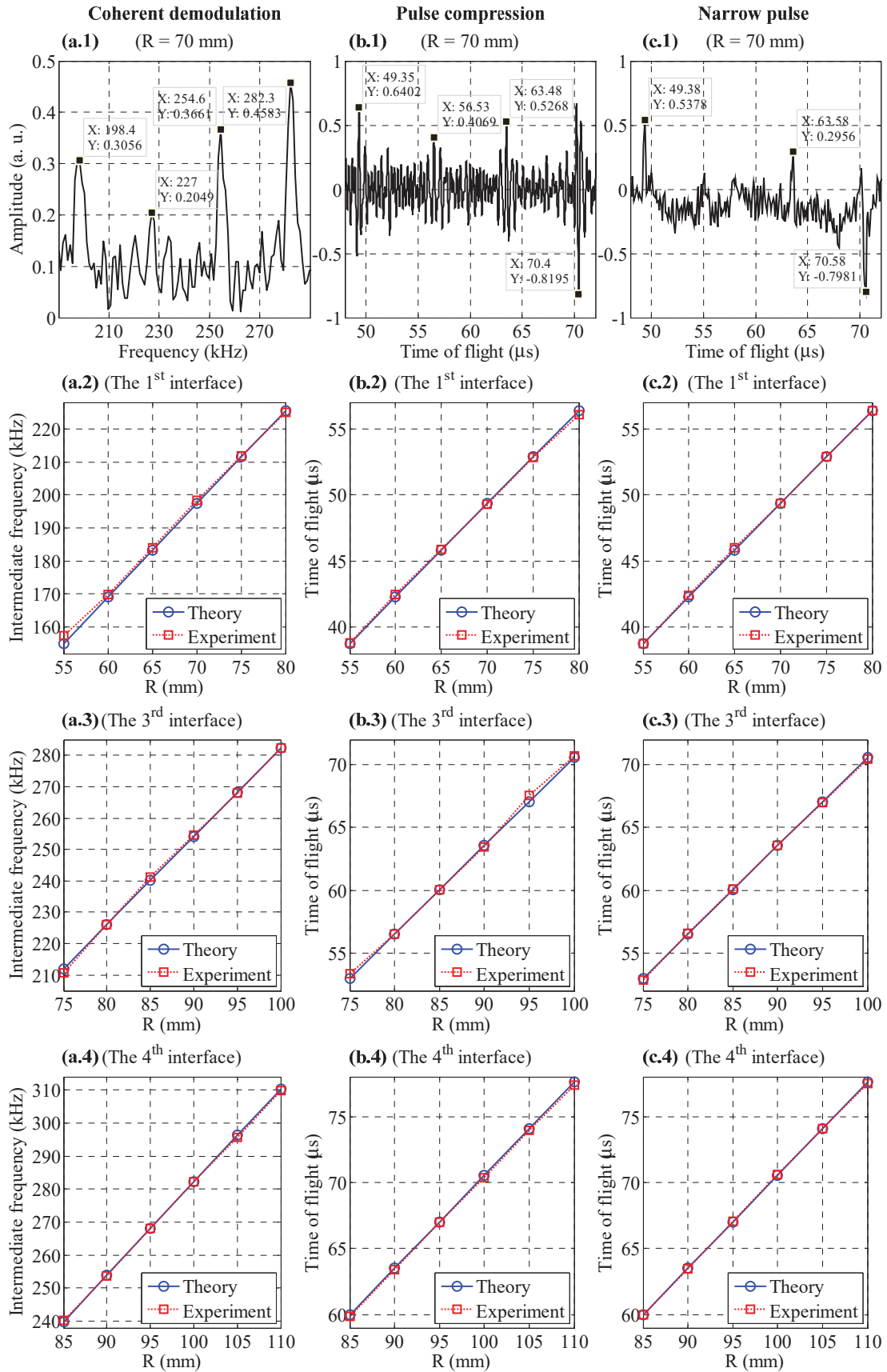


Figure 2.18. SECG-LFM-UILF (using both the coherent demodulation method (a) (Sun *et al.* 2018b) and the pulse compression method (b) (Sun *et al.* 2017)) and SECG-UILF based on the high acoustic-

pressure wide-band ultrasound pulse stimulation (c). (a.1) Spectrum of the intermediate frequency signal due to the conductivity gradients at the first, the third and the fourth interfaces of the agar phantom at the distance of 70 mm from the first interface to the transducer. (a.2-4) Intermediate frequencies for the first, the third and the fourth interfaces increase linearly with distance from the transducer to the agar phantom (the red squares are for values gotten through experiments and the blue circles are for values gotten theoretically). (b.1) Compressed SECG-LFM-UILF pulse signals induced by the conductivity gradients at the first, the third and the fourth interfaces of the agar phantom. (b.2-4) The time-of-flights (TOF) of the compressed SECG-LFM-UILF signals corresponding to the conductivity gradients at the first, the third and the fourth interfaces of the agar phantom (the red squares are for values gotten through experiments, and the blue circles are for values gotten theoretically). (c.1) SECG-UILF signals induced by the conductivity gradients at the first, the third and the fourth interfaces of the agar phantom, using the conventional high acoustic pressure wide-band ultrasound pulse stimulation method. (c.2-4) The time-of-flights (TOFs) of the SECG-UILF signals corresponding to the conductivity gradients at the first, the third and the fourth interfaces of the agar phantom (the red squares are for values gotten through experiments, and the blue circles are for values gotten theoretically), using the conventional high pressure narrow ultrasound pulse stimulation.

2.6.2 The second group of experiments - B-scan image of multi-shaped agar phantoms

2.6.2.1 SECG-UILF on a multi-shaped saline agar phantom with a rectangular hole inside

The first half of the second group of experiments is done using a multi-shaped agar phantom with a rectangular hole inside as the sample (Figure 2.14.b).

Using the in-phase-coherent-demodulation-scheme-based SECG-LFM-UILF, the intermediate frequency signal is recorded and its spectrum is calculated at each position when moving the transducer in 1-mm step across the z -direction. The 2-D image of the relative gradient of the electrical conductivity of the multi-shaped phantom sample was formed by joining all tracks of the spectra together (Figure 2.19.a.1). The relative amplitude values were converted, using the color map HOT, to

128 colors. The spectra of intermediate frequency signals of individual tracks at positions $z = -13$ mm (Figure 2.19.a.2), $z = 0$ mm (Figure 2.19.a.3), and $z = +12$ mm (Figure 2.19.a.4) are also provided here for detailed examination of the spectra of the intermediate frequency signals. From Figure 2.19.a.1, four $\sigma(x)$ discontinuities, including two at the outer front and back interfaces and two at the rectangular hole of the sample, are clearly recognized. The lengths of the recognized inner discontinuity are approximately 15 mm, equal to the real width of the hole.

Similarly, using the pulse-compression-scheme-based SECG-LFM-UILF, the induced wide pulse current signal is recorded at each position when moving the transducer in 1-mm step across the z -direction. The 2-D image of the relative gradient of the electrical conductivity of the multi-shaped phantom sample is formed by compressing the detected wide pulse signals and joining all tracks of the compressed signals together (Figure 2.19.b.1). As the compressed pulses have bi-polarities, the relative amplitude values are converted, using the color map HSV, to 128 colors. The compressed signals of individual tracks at positions $z = -13$ mm (Figure 2.19.b.2), $z = 0$ mm (Figure 2.19.b.3), and $z = +12$ mm (Figure 2.19.b.4) are also provided here for detailed examination of the compressed signals. From Figure 2.19.b.1, four $\sigma(x)$ discontinuities, including two at the outer front and back interfaces and two at the rectangular hole of the sample, are clearly recognized. The lengths of the recognized inner discontinuity are approximately 15 mm, equal to the real width of the hole.

And using the traditional high-acoustic-pressure-wide-band-ultrasound-signal-based SECG-UILF, the induced current signal is recorded at each position when moving the transducer in 1-mm step across the z -direction. The 2-D image of the relative gradient of the electrical conductivity of the multi-shaped phantom sample is formed by joining all tracks of the signals together (Figure 2.19.c.1). Since the pulses have bi-polarities, the relative amplitude values are converted, using the color map FIREICE (which has the same colors as HOT for values from 0 to 1), to 128 colors. The signals of individual tracks at positions $z = -13$ mm (Figure 2.19.c.2), $z = 0$ mm (Figure 2.19.c.3), and $z = +12$ mm (Figure 2.19.c.4) are also provided here for detailed examination of the signals. From Figure 2.19.c.1, four $\sigma(x)$ discontinuities,

including two at the outer front and back interfaces and two at the rectangular hole of the sample, are clearly recognized. The lengths of the recognized inner discontinuity are approximately 15 mm, equal to the real width of the hole.

Two abnormalities are observed on the reconstructed interfaces (Figures 2.19.a-c.1): (1) the dimension of the agar phantom along e_x becomes shorter and (2) the back interface is broken into three parts. These two abnormalities are due to the facts that the ultrasound propagated slower in the transformer oil (1418.4 m/s, 17 °C) than in the saline agar phantom (1428.6 m/s, 17 °C) and that, when reconstructing the longitudinal distance of the discontinuities of $\sigma(x)$, one unique compression wave speed (1418.4 m/s) is used. Because the compression waves propagated faster in the agar phantom than in the transformer oil, the resulting intermediate frequency increment within the agar phantom is less than that within the transformer oil for the same distance. Therefore, the reconstructed distance of the agar phantom is smaller than the real distance.

Comparison of Figure 2.19.a.1 (with an SNR of 9.28 dB), Figure 2.19.b.1 and Figure 2.19.c.1 (with an SNR of 8.16) shows that: (1) the SECG-LFM-UILF, including calculation of the longitudinal distance through the in-phase coherent demodulation scheme and that through the pulse compression scheme, can recognize the variations of $\sigma(x)$ in the agar phantom sample; (2) the SNR in recognizing gradients of $\sigma(x)$ in the agar phantom sample obtained by the in-phase-coherent-demodulation-scheme-based SECG-LFM-UILF is comparable to that obtained by the traditional high-acoustic-pressure-wide-band-ultrasound-stimulation-based SECG-UILF, but the peak instantaneous power of the LFM pulse to the transducer was 25.5 dB lower than that of the negative high-voltage spike pulse.

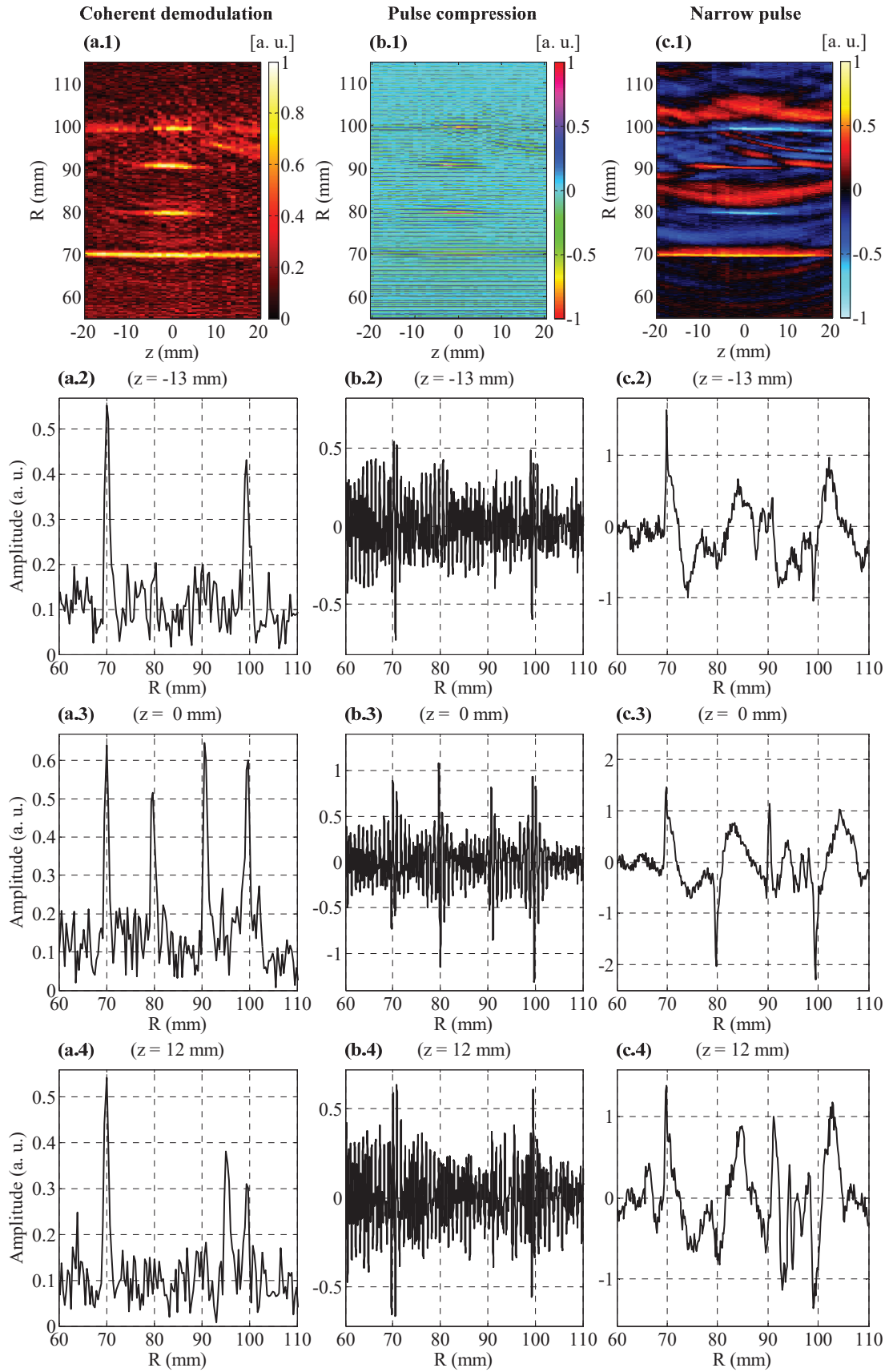


Figure 2.19. B-scan images of the conductivity gradients in the saline agar phantom having a rectangular hole inside ((a.1) Using linearly frequency-modulated ultrasound pulse stimulation and the

in-phase coherent demodulation method (Sun *et al.* 2018b). (b.1) Using linearly frequency-modulated ultrasound pulse stimulation and the pulse compression technique (Sun *et al.* 2017). (c.1) Using the conventional high acoustic pressure wide-band ultrasound pulse stimulation). (a.2-4) The spectra of the intermediate frequency signal when the ultrasound transducer is at $z = -13$ mm, 0 mm, and +12 mm, using linearly frequency-modulated ultrasound pulse stimulation and the coherent demodulation method. (b.2-4) The compressed signals got when the ultrasound transducer is at $z = -13$ mm, 0 mm, and +12 mm, using linearly frequency-modulated ultrasound pulse stimulation and the pulse compression technique. (c.2-4) The signals got when the ultrasound transducer is at $z = -13$ mm, 0 mm, and +12 mm, using the conventional high acoustic pressure wide-band ultrasound pulse stimulation.

2.6.2.2 SECG-UILF on a multi-shaped 3-layer saline agar phantom

The second half of the second group of experiments is done using a multi-shaped 3-layer agar phantom as the sample (Figure 2.14.c).

Using the in-phase-coherent-demodulation-scheme-based SECG-LFM-UILF, the intermediate frequency signal is recorded and its spectrum is calculated at each position when moving the transducer in 1-mm step across the z -direction. The 2-D image of the relative gradient of the electrical conductivity of the multi-shaped phantom sample is formed by joining all tracks of the spectra together (Figure 2.20.a.1). The relative amplitude values are converted, using the color map HOT, to 128 colors. The spectra of intermediate frequency signals of individual tracks at positions $z = -12$ mm (Figure 2.20.a.2), $z = 0$ mm (Figure 2.20.a.3), and $z = +12$ mm (Figure 2.20.a.4) are also provided here for detailed examination of the spectra of the intermediate frequency signals. From Figure 2.20.a.1, the front and back interfaces on the agar phantom and the first internal interface can be clearly recognized. The third internal interface except the middle part can also be clearly recognized. The middle part of the third internal interface is vague because the corresponding induced intermediate frequency signals are comparatively weak. The lengths of the recognized inner discontinuity on the internal interfaces are approximately 15 mm, which is equal to the real width of the middle part of the second layer.

Similarly, using the pulse-compression-scheme-based SECG-LFM-UILF, the

induced wide pulse current signal is recorded at each position when moving the transducer in 1-mm step across the z -direction. The 2-D image of the relative gradient of the electrical conductivity of the multi-shaped phantom sample is formed by compressing the detected wide pulse signals and joining all tracks of the compressed signals together (Figure 2.20.b.1). As the compressed pulses have bi-polarities, the relative amplitude values are converted, using the color map HSV, to 128 colors. The compressed signals of individual tracks at positions $z = -12$ mm (Figure 2.20.b.2), $z = 0$ mm (Figure 2.20.b.3), and $z = +12$ mm (Figure 2.20.b.4) are also provided here for detailed examination of the compressed signals. From Figure 2.20.b.1, the front and back interfaces on the agar phantom and the two internal interfaces are clearly recognized. The lengths of the recognized inner discontinuity on the internal interfaces are approximately 15 mm, which is equal to the real width of the middle part of the second layer.

And using the traditional high-acoustic-pressure-wide-band-ultrasound-stimulation-based SECG-UILF, the induced current signal is recorded at each position when moving the transducer in 1-mm step across the z -direction. The 2-D image of the relative gradient of the electrical conductivity of the multi-shaped phantom sample is formed by joining all tracks of the signals together (Figure 2.20.c.1). Since the pulses have bi-polarities, the relative amplitude values were converted, using the color map FIREICE (which has the same colors as HOT for values from 0 to 1), to 128 colors. The signals of individual tracks at positions $z = -13$ mm (Figure 2.20.c.2), $z = 0$ mm (Figure 2.20.c.3), and $z = +12$ mm (Figure 2.20.c.4) are also provided here for detailed examination of the signals. From Figure 2.20.c.1, the front and back interfaces on the agar phantom and the two internal interfaces could be clearly recognized. The lengths of the recognized inner discontinuity on the internal interfaces are approximately 15 mm, which is equal to the real width of the middle part of the second layer.

While the B-scan image by the traditional high-acoustic-pressure-wide-band-ultrasound-stimulation-based SECG-UILF (Figures 2.19.c.1 and 2.20.c.1) provides the polarity information of the electrical conductivity variations, the B-scan images

obtained through the in-phase-coherent-demodulation-scheme-based SECG-LFM-UILF (Figure 2.19.a.1 and Figure 2.20.a.1) loses the polarity information although the detected current signal keeps the polarity information of the conductivity gradients. This is because FFT can get only the amplitudes but no phases of various frequency components of the intermediate frequency (IF) signal in the SECG-LFM-UILF. To retrieve the phase information of the IF signal, the SECG-LFM-UILF needs to adopt the in-phase/quadrature-phase (IQ) demodulation scheme.

2.6.3 The third group of experiments - demonstration of the longitudinal resolution

To verify the longitudinal resolution of SECG-LFM-UILF including calculation of the longitudinal distance through the in-phase coherent demodulation scheme and that through the pulse compression scheme, B-scan experiments are done on the sample of saline agar phantom with two slots (Figure 2.14.d).

Using the in-phase-coherent-demodulation-scheme-based SECG-LFM-UILF, the intermediate frequency signal is recorded and its spectrum is calculated at each position when moving the transducer in 1-mm step across the z -direction. The 2-D image of the relative gradient of the electrical conductivity of the multi-shaped phantom sample is formed by joining all tracks of the spectra together (Figure 2.21.a.1). The relative amplitude values are converted, using the color map HOT, to 128 colors. The spectra of intermediate frequency signals of individual tracks at positions $z = -12$ mm (Figure 2.21.a.2), $z = 0$ mm (Figure 2.21.a.3), and $z = +12$ mm (Figure 2.21.a.4) are also provided here for detailed examination of the spectra of the intermediate frequency signals. Besides the front and back interfaces on the agar phantom, the front and back interfaces on each slot are clearly identified in Figure 2.21.a.1. The widths of the interfaces recognized are approximately 15 mm, and the distances between the recognized interfaces on the first and the second slots are approximately 1 and 2 mm, respectively. So, longitudinal resolution of 1 mm by (2.14) is verified experimentally.

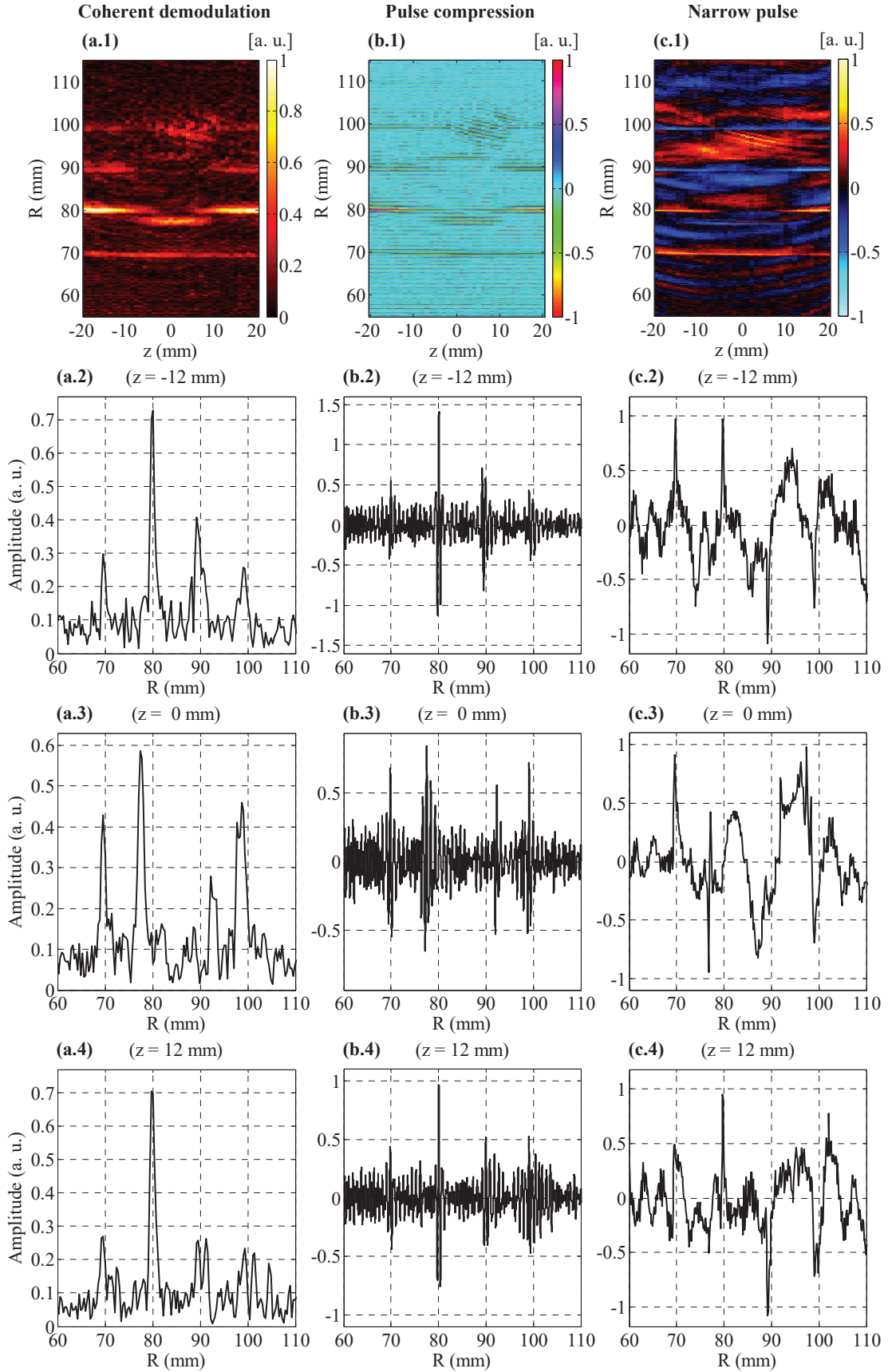


Figure 2.20. B-scan images of the conductivity gradients in the saline agar phantom having 3 multi-shaped layers ((a.1) Using linearly frequency-modulated wide ultrasound pulse stimulation and

the coherent demodulation method (Sun *et al.* 2018b). (b.1) Using linearly frequency-modulated wide ultrasound pulse stimulation and the pulse compression technique (Sun *et al.* 2017). (c.1) Using the conventional high acoustic pressure wide-band ultrasound pulse stimulation). (a.2-4) The spectra of the intermediate frequency signal when the ultrasound transducer is at $z = -12$ mm, 0 mm, and +12 mm, using linearly frequency-modulated wide ultrasound pulse stimulation and the coherent demodulation method. (b.2-4) The compressed signals got when the ultrasound transducer is at $z = -12$ mm, 0 mm, and +12 mm, using linearly frequency-modulated wide ultrasound pulse stimulation and the pulse compression technique. (c.2-4) The signals got when the ultrasound transducer is at $z = -12$ mm, 0 mm, and +12 mm, using the conventional high acoustic pressure wide-band ultrasound stimulation.

Similarly, using the pulse-compression-scheme-based SECG-LFM-UILF, the induced wide pulse current signal is recorded at each position when moving the transducer in 1-mm step across the z -direction. The 2-D image of the relative gradient of the electrical conductivity of the multi-shaped phantom sample is formed by compressing the detected wide pulse signals and joining all tracks of the compressed signals together (Figure 2.21.b.1). As the compressed pulses have bi-polarities, the relative amplitude values were converted, using the color map HSV, to 128 colors. The compressed signals of individual tracks at positions $z = -12$ mm (Figure 2.21.b.2), $z = 0$ mm (Figure 2.21.b.3), and $z = +12$ mm (Figure 2.21.b.4) are also provided here for detailed examination of the compressed signals. Besides the front and back interfaces on the agar phantom, the front and back interfaces on each slot are clearly identified in Figure 2.21.b.1. The widths of the interfaces recognized are approximately 15 mm, and the distances between the recognized interfaces on the first and the second slots are approximately 1 and 2 mm, respectively. So, longitudinal resolution of 1 mm by (2.16) is also verified experimentally.

And using the traditional high-acoustic-pressure-wide-band-ultrasound-stimulation-based SECG-UILF, the induced current signal is recorded at each position when moving the transducer in 1-mm step across the z -direction. The 2-D image of the relative gradient of the electrical conductivity of the multi-shaped phantom sample is formed by joining all tracks of the signals together (Figure 2.21.c.1). Since the

pulses have bi-polarities, the relative amplitude values are converted, using the color map FIREICE (which has the same colors as HOT for values from 0 to 1), to 128 colors. The signals of individual tracks at positions $z = -12$ mm (Figure 2.21.c.2), $z = 0$ mm (Figure 2.21.c.3), and $z = +12$ mm (Figure 2.21.c.4) are also provided here for detailed examination of the signals. Besides the front and back interfaces on the agar phantom, the front and back interfaces on each slot are clearly identified in Figure 2.21.c.1. The widths of the interfaces recognized are approximately 15 mm, and the distances between the recognized interfaces on the first and the second slots are approximately 1 and 2 mm, respectively. So, longitudinal resolution of 1 mm is also verified experimentally.

Regarding the lateral resolution, in all the above experiments, we used the flat ultrasound transducer (Olympus C306), of which the -6 dB beam diameter was large compared with the focal transducer. But the width of the recognized interfaces does not widen much. Future experiments using focal ultrasound transducer are planned to study the lateral resolution.

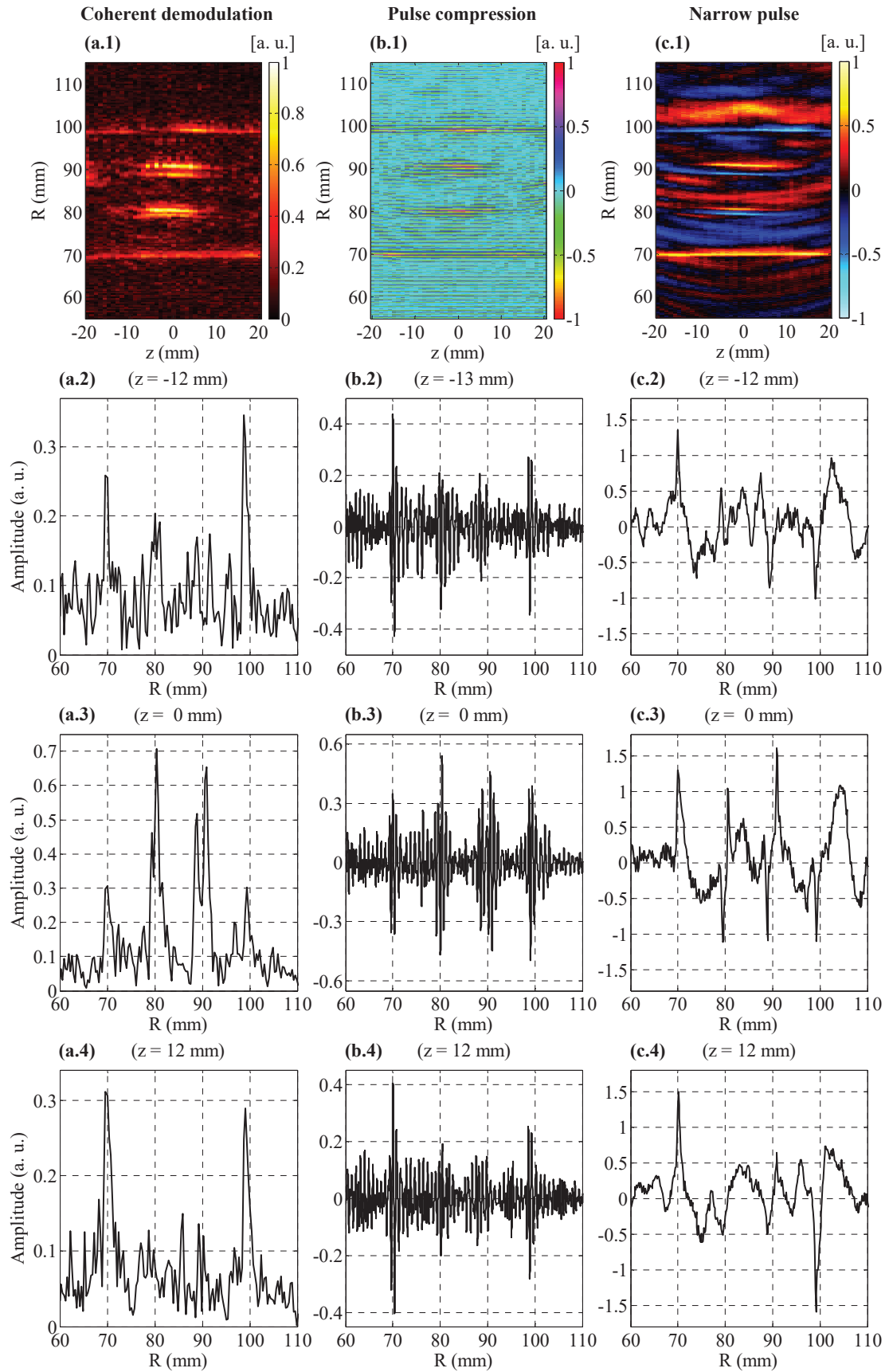


Figure 2.21. B-scan images of the conductivity gradients in the saline agar phantom having two slots ((a.1) Using linearly frequency-modulated narrow ultrasound pulse stimulation and the coherent

demodulation method (Sun *et al.* 2018b). (b.1) Using linearly frequency-modulated wide ultrasound pulse stimulation and the pulse compression technique (Sun *et al.* 2017). (c.1) Using the conventional high acoustic pressure wide band ultrasound stimulation). (a.2-4) The spectra of the intermediate frequency signal when the ultrasound transducer is at $z = -12$ mm, 0 mm, and +12 mm, using linearly frequency-modulated wide ultrasound pulse stimulation and the coherent demodulation method. (b.2-4) The compressed signals got when the ultrasound transducer is at $z = -12$ mm, 0 mm, and +12 mm, using linearly frequency-modulated wide ultrasound pulse stimulation and the pulse compression technique. (c.2-4) The signals obtained when the ultrasound transducer is at $z = -12$ mm, 0 mm, and +12 mm, using the conventional high acoustic pressure wide-band ultrasound stimulation.

2.6.4 The fourth group of experiments - retrieving the conductivity gradient polarity by the IQ-coherent-demodulation-scheme-based SECG-LFM-UILF

Figures 2.22.a-f are the spectra with polarity of the complex intermediate frequency signals, which are produced by combinations of the in-phase and the quadrature-phase intermediate frequency signals as (2.12) when the ultrasound transducer locates respectively 67.5, 72.5, 77.5, 82.5, 87.5 and 92.5 mm in front of the front surface of the saline agar phantom sample. The method has not been maturely developed by us yet - sometimes it works (Figure 2.22.a and d) while other times it fails (Figure 2.22.b, c, e and f). The biggest problem with the IQ demodulation method is that the Fast Fourier Transform (FFT) itself also introduces phase variations into the complex spectrum, which prevents deducing the phase of the intermediate frequency signal precisely from the complex spectrum obtained through FFT. We still work on the SECG-LFM-UILF using the IQ demodulation method. We are trying methods to get rid of the phase variations produced by FFT itself.

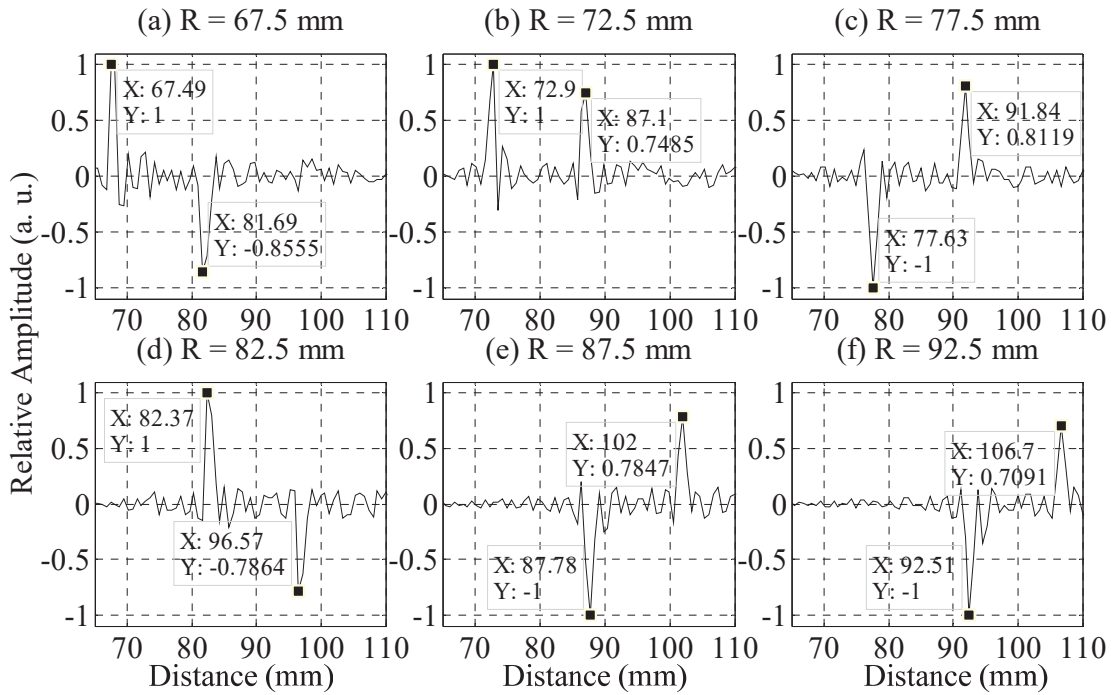


Figure. 2.22. The spectra with polarity of the complex intermediate frequency signals (2.12). The distances (R) from the front surface of the agar phantom to the ultrasound transducer are respectively 67.5 mm (a), 72.5 mm (b), 77.5 mm (c), 82.5 mm (d), 87.5 mm (e), and 92.5 mm (f). Both the distance and the polarity information can be correctly retrieved from the spectra of the complex intermediate frequency signals when the front surface of the agar phantom locates at distances of 67.5 mm (a) and 82.5 mm (d); Only the distance information rather than the polarity information can be correctly obtained from the spectra with polarity of the complex intermediate frequency signals when the front surface of the agar phantom located at distances of 72.5 mm (b), 77.5 mm (c), 87.5 mm (e) and 92.5 mm (f).

2.7 Chapter summary

In this chapter, we carried out an in-depth study of scanning of electrical conductivity gradients with linearly frequency-modulated ultrasound induced Lorentz force (SECG-LFM-UILF). First, two methods of calculation of the longitudinal distance of the medium having conductivity variations - the coherent demodulation scheme and the pulse compression scheme - were studied. Although, in the frequency range 1.4-3.4 MHz, the ultrasound transducer's amplitude-frequency response was not flat, and the integral of the ultrasound pressure signal in the mechanics-to-electrics

transformation also produced variation in the amplitude of the induced SECG-LFM-UILF current signal, theoretical analysis showed that: (1) the resulting intermediate frequency signal was hardly undermined and its side lobe level increased little; and (2) the signal after pulse compression still exhibited as a narrow pulse. SECG-LFM-UILF experiments on agar phantoms of electrical conductivity ranging between 0.2 S/m and 0.5 S/m demonstrated its feasibility and performance. The SECG-LFM-UILF used LFM signal of peak instantaneous power of 39.54 dBm to stimulate the ultrasound transducer, while the traditional SECG-UILF used the negative spike signal of peak instantaneous power of 65.05 dBm; and in SECG-LFM-UILF, the transmitted ultrasound had a peak acoustic pressure of 0.525 MPa, while that in the traditional SECG-UILF had a peak acoustic pressure of 0.965 MPa. The experiment results showed: (1) the SECG-LFM-UILF, calculating the longitudinal distance either through the in-phase coherent demodulation scheme or through the pulse compression scheme, located the electrical conductivity discontinuities precisely; (2) the SECG-LFM-UILF could get the comparable SNR in detection of electrical conductivity variations as the traditional SECG-UILF; (3) using modulation frequency bandwidth of 2 MHz and modulation time of 500 μ s, the SECG-LFM-UILF achieved a longitudinal resolution of 1 mm within the range of 100 mm.

Chapter 3 Scanning electric conductivity gradients with step-frequency ultrasound induced Lorentz force

In this chapter, we explore the use of step-frequency technique in scanning electric conductivity gradients with ultrasonically induced Lorentz force (SECG-UILF). This technique originated from ground penetrating radar (GPR) (Iizuka *et al.* 1976, Iizuka and Freundorfer 1983, Iizuka *et al.* 1984), where it was used to overcome mutually conflicting demands of lower operating frequency and higher resolution which were both necessary for the GPR. The step-frequency technique utilizes information from both the phase and the amplitude of a target-reflected signal with the emphasis on the phase information. With accurate phase measurement, a resolution of much less than one wavelength was proven to be achievable. In recent years, besides its continuous usage in GPR (Oyan *et al.* 2012), it has been applied in microwave-induced thermo-acoustic imaging (Nan and Arbabian 2014), magneto-acoustic tomography (Aliroteh *et al.* 2014) and accurate ultrasound ranging (Natarajan *et al.* 2010, Podilchuk *et al.* 2012). This chapter is organized as follows: first, the theory of scanning electric conductivity gradients with step-frequency ultrasound induced Lorentz force (SECG-SF-UILF) is presented. Then, theoretical analysis and experiments with copper foils are done to demonstrate the feasibility of this method. (Sun *et al.* 2018a)

3.1 Application of step-frequency technique

The set-up of application of step-frequency technique in SECG-UILF is shown in Figure 3.1. A collection of monotonic signals with frequency increasing in equal step are in turn used to generate the sinusoidal ultrasound bursts. And the sample placed in the quasi-uniform static magnetic field is vibrated by the generated ultrasound and SECG-UILF current signal is induced in the sample. The detected SECG-UILF current signal is demodulated by the coherent local reference signal. The resulting DC signals contain the accumulated phase as the ultrasound propagates to the places of variations of $\sigma(x)$. Equivalently, the range information of the electrical conductivity

variations is contained in the collection of DC signals via the accumulated phases. Craftily, by using step frequencies and by assuming that the electrical conductivity variations' distances to the transducer increase in equal step, the DC signals represent the Fast Fourier Transform (FFT) - at the specific frequency points - of the existence function of the electrical conductivity variations. Inversely, the distribution of the electrical conductivity variation can be deduced by performing Inverse Fast Fourier Transform (IFFT) on the collection of the DC signals. In the real situation, the ultrasound is transmitted in the form of wide pulse rather than continuously to reduce the power of the transmitting system. Besides, the transmission of the ultrasound pulse of the same frequency and collection of its induced current signal is repeated multiple times to apply the coherent addition before jumping to the next frequency.

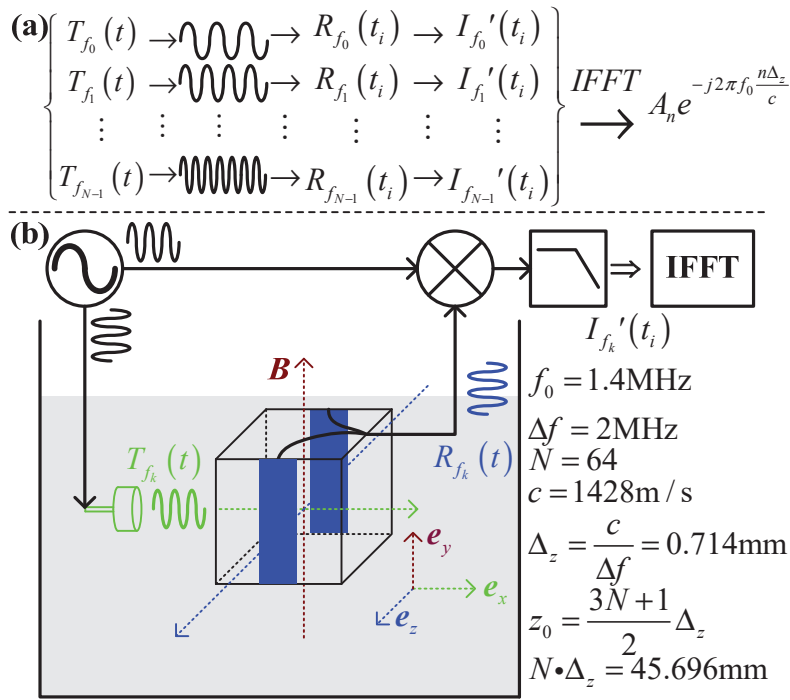


Figure 3.1. Schematic of the SECG-SF-UILF using step frequency technique (Sun *et al.* 2018a). (a) The signal transformations from the stimulating signals $T_{f_k}(t)$ and the detected SECG-SF-UILF current signals $R_{f_k}(t)$ to the IF signals $I'_{f_k}(t)$ and finally to the existence function $A_n e^{-j2\pi f_0 \frac{n\Delta_z}{c}}$. (b) Schematic of SECG-SF-UILF system. The restriction of $z_0 = \frac{3N+1}{2} \Delta_z$ is specific to the direct demodulation method, which guarantees the artificial target mirrors with the real target with respect to $z = z_0 + \frac{N}{2} \Delta_z$.

The stimulating signal to the ultrasound transducer is of the form as (3.1).

$$T_{f_k}(t) = A_0 \sin \left[2\pi \left(f_0 + \frac{\Delta f}{N} k \right) t + \phi_0 \right], 0 \leq t < T \text{ and } k = 0, 1, \dots, N - 1. \quad (3.1)$$

where A_0 is the amplitude of the stimulating signal, f_0 is the initial frequency, Δf is the total frequency bandwidth, ϕ_0 is the initial phase, N is the number of steps, and T is the stimulating pulse width.

Because the amplitude-frequency response of the ultrasound transducer is not flat within the frequency band of 1.4 - 3.4 MHz, the transmitted ultrasound pulses from the transducer do not have the same amplitude although the stimulating signals to the ultrasound transducer have the same amplitude. But the frequency of the transmitted ultrasound pulse signal still has the same frequency as that of the stimulating signal to the transducer. The induced current signal, as shown in (2.5), is the time-domain integral of the ultrasonic pressure signal. The resulting current signal has the same instantaneous frequency as the ultrasound pressure signal because the time-domain integral of a sinusoid results in a sinusoid of the same frequency. But as the frequency increases between different $T_{f_k}(t)$ s, the integral of ultrasound pressure also introduces amplitude variation between different $R_{f_k}(t)$ s. To sum up, we get $R_{f_k}(t)$ as (3.2).

$$R_{f_k}(t) = \sum_{n=0}^{N-1} A_n(t) \sin \left[2\pi \left(f_0 + \frac{\Delta f}{N} k \right) \left(t - \frac{z_n}{c} \right) + \phi_0 \right],$$

$$\frac{z_0}{c} \leq t < \frac{z_{N-1}}{c} + T \text{ and } k = 0, 1, \dots, N - 1. \quad (3.2)$$

where z_{n+1} is the n^{th} target range, z_0 the 1st target range, and $A_n(t)$ accounts for the overall amplitude-frequency response of the transducer, the ultrasound propagating medium and the acousto-electrical transforming system.

For detection of the accumulated phase, there are two demodulation schemes - one is the in-phase demodulation scheme and the other is the in-phase/quadrature-phase (IQ) demodulation scheme.

3.1.1 Calculation of the longitudinal distance - the in-phase coherent demodulation scheme

In the in-phase coherent demodulation scheme, where only the in-phase reference signal is used to demodulate the detected SECG-UILF signal, the intermediate frequency (IF) signal has the form as (3.3).

$$I_{f_k}(t) = \sum_{n=0}^{N-1} A_n(t) \cos \left[2\pi \left(f_0 + \frac{\Delta_f}{N} k \right) \frac{z_n}{c} \right],$$

$$z_n = z_0 + n\Delta_z, \quad \frac{z_0}{c} \leq t < \frac{z_{N-1}}{c} + T \text{ and } k = 0, 1, \dots, N-1. \quad (3.3)$$

After multiplying $I_{f_k}(t)$ with $e^{j2\pi(f_0 + \frac{\Delta_f}{N}k)\frac{z_0}{c}}$ and applying the restrictions $\frac{\Delta_z \Delta_f}{c} = 1$ and $z_0 = \frac{3N+1}{2} \Delta_z$, $I_{f_k}(t)$ is transformed into $I'_{f_k}(t)$.

$$I'_{f_k}(t) = \sum_{n=0}^{N-1} \left[A_n(t) e^{-j2\pi f_0 \frac{n\Delta_z}{c}} e^{-j\frac{2\pi}{N}nk} + A_{N-1-n}(t) e^{j2\pi f_0 \frac{2z_0 + (N-1-n)\Delta_z}{c}} e^{-j\frac{2\pi}{N}nk} \right],$$

$$\frac{z_0}{c} \leq t < \frac{z_{N-1}}{c} + T \text{ and } k = 0, 1, \dots, N-1. \quad (3.4)$$

From (3.4), we can get that, mathematically, $I'_{f_k}(t)$ is the FFT of the summation of $A_n(t) e^{-j2\pi f_0 \frac{n\Delta_z}{c}}$ and $A_{N-1-n}(t) e^{j2\pi f_0 \frac{2z_0 + (N-1-n)\Delta_z}{c}}$. $A_n(t) e^{-j2\pi f_0 \frac{n\Delta_z}{c}}$ is an existence function of the electrical conductivity variation at $z = z_0 + n \cdot \Delta_z$, while $A_{N-1-n}(t) e^{j2\pi f_0 \frac{2z_0 + (N-1-n)\Delta_z}{c}}$ is an artificial existence function of the electrical conductivity variation at $z = z_0 + (N-1-n) \cdot \Delta_z$. Therefore, when doing IFFT on $I'_{f_k}(t)$, a real target and an artificial target are recovered for one electrical conductivity variation. The restriction of $z_0 = \frac{3N+1}{2} \Delta_z$ in the transformation from (3.3) to (3.4) guarantees the mirror for the real and artificial targets locates at $z = z_0 + \frac{N}{2} \Delta_z$. To avoid confusing the artificial targets with the real targets, the detection range is limited within $(z_0, z_0 + (\frac{N}{2} - 1) \Delta_z)$. Indeed, the recovered targets locating in the range $(z_0, z_0 + (\frac{N}{2} - 1) \Delta_z)$ are judged as the real targets, while those locating in the

range $(z_0 + \frac{N}{2}\Delta_z, z_0 + (N - 1)\Delta_z)$ are judged as the artificial targets.

3.1.2 Calculation of the longitudinal distance - the in-phase/quadrature-phase (IQ) coherent demodulation scheme

In the IQ coherent demodulation scheme, besides the in-phase IF component, the quadrature-phase IF signal is also obtained as (3.5).

$$\begin{aligned} I_{If_k}(t) &= \sum_{n=0}^{N-1} A_n(t) \cos \left[2\pi \left(f_0 + \frac{\Delta_f}{N} k \right) \frac{z_n}{c} \right], \\ I_{Qf_k}(t) &= \sum_{n=0}^{N-1} -A_n(t) \sin \left[2\pi \left(f_0 + \frac{\Delta_f}{N} k \right) \frac{z_n}{c} \right], \\ z_n &= z_0 + n \cdot \Delta_z, \frac{z_0}{c} \leq t < \frac{z_{N-1}}{c} + T \text{ and } k = 0, 1, \dots, N - 1. \end{aligned} \quad (3.5)$$

Therefore, the complex form of IF signal is obtained as (3.6) using the in-phase and quadrature-phase IF components.

$$\begin{aligned} I_{f_k}(t) &= I_{If_k}(t) + jI_{Qf_k}(t) = \sum_{n=0}^{N-1} A_n(t) e^{-j2\pi \left(f_0 + \frac{\Delta_f}{N} k \right) \frac{z_0 + n\Delta_z}{c}}, \\ \frac{z_0}{c} &\leq t < \frac{z_{N-1}}{c} + T \text{ and } k = 0, 1, \dots, N - 1. \end{aligned} \quad (3.6)$$

Reducing the constant phase by multiplying the term $e^{j2\pi \left(f_0 + \frac{\Delta_f}{N} k \right) \frac{z_0}{c}}$, $I_{f_k}(t)$ is changed to (3.7).

$$\begin{aligned} I'_{f_k}(t) &= \sum_{n=0}^{N-1} A_n(t) e^{-j2\pi f_0 \frac{n\Delta_z}{c}} e^{-j\frac{2\pi}{N} nk}, \\ \frac{z_0}{c} &\leq t < \frac{z_{N-1}}{c} + T \text{ and } k = 0, 1, \dots, N - 1. \end{aligned} \quad (3.7)$$

From (3.7), it can be gotten that $I'_{f_k}(t)$ is the FFT of $A_n(t) e^{-j2\pi f_0 \frac{n\Delta_z}{c}}$. Therefore, by IFFT of $I'_{f_k}(t)$, $A_n(t)$ - containing the location information of the electrical conductivity variations - can be reconstructed.

3.2 Theoretical analysis and experiments

Theoretical analysis of the SECG-SF-UILF using step-frequency technique are done in terms of the in-phase and IQ demodulation schemes. Generation of the SECG-SF-UILF current signal takes into consideration of the amplitude-frequency response of the transducer and the integral in the acousto-electrical transformation. System parameters used are the same as those in Figure 3.1. Two electrical conductivity variations - being respectively 78 mm and 103 mm far away from the transducer - exist. 64 discrete frequencies with equal step are used and z_0 is set to 68.93 mm so that z_0 equaled $\frac{3N+1}{2}\Delta_z$.

Experiments also are done to demonstrate the feasibility of this imaging method. The experimental setups are shown in Figure 3.2. The in-phase and quadrature-phase channels of monotonic frequency pulse are generated with pulse width 100 μ s and starting phase differing by 90 degree - i.e., the in-phase channel is $\sin(\omega t)$ and the quadrature channel is $\cos(\omega t)$. The monotonic frequency starts at 1.4 MHz and increases by a step of 31.25 kHz. And the number of frequencies used is 64, so the frequency bandwidth used is 2 MHz. The in-phase channel monotonic frequency signal is split into two channels, of which one was amplified (HSA4101) to 37.5 Vpp to stimulate the ultrasound transducer, and the other is used as the local reference signal to the mixer (Mini-Circuits ZAD-8+). The transducer used is the Olympus C306, which is a flat transducer with the element size of diameter of 1.27 cm and the -6 dB band starting at 1.4 MHz and ending at 3.38 MHz. Two permanent magnets (NdFeB N45, diameter - 15 cm and height - 3 cm) placed along the same axis and in the same direction are used to generate the static magnetic field with magnetic induction density about 260 mT.

The SECG-SF-UILF current signal detected by electrodes is first amplified (Olympus 5662) by 34 dB, high-pass and low-pass filtered, then converted to baseband by mixing (Mini-Circuits, ZAD-8+) it with the local reference signal. In the direct demodulation scheme, the detected current signal is only mixed with the in-phase local reference signal, while in the IQ demodulation scheme, the detected

current signal is first split into two channels, of which one channel is mixed with the in-phase local reference signal and the other channel is mixed with the quadrature local reference signal. The output signals of the mixers are sampled using the Tektronix oscilloscope (DPO2014B). Two frequency components - the DC and the double-frequency component - exist in the output signals of the mixers. Only the DC component is useful and the double-frequency component is filtered using a 5th order Butterworth digital low-pass filter. The DC component contains the accumulated phase information which relates to the distances between the medium of variations of $\sigma(x)$ and the transducer. The different phases are reconstructed by doing IFFT on the DC signals. And the range information of the electrical conductivity variations are finally obtained by linear operation on the reconstructed phases.

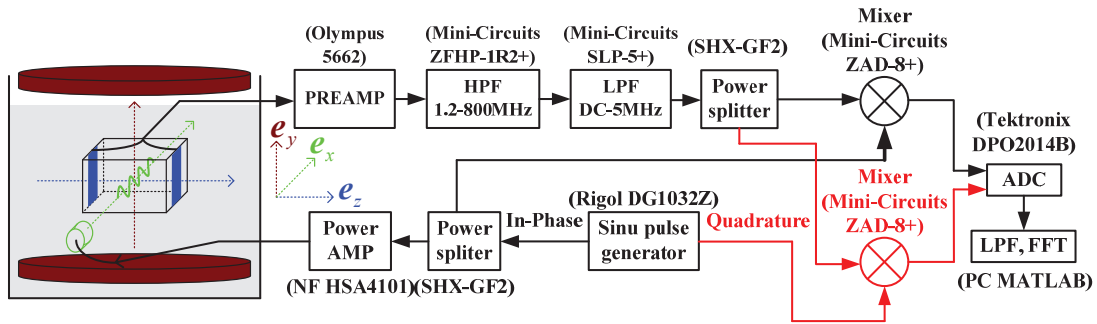


Figure 3. Schematic layout of SECG-SF-UILF experimental setup (Sun *et al.* 2018a). The parts in red were specific to the IQ demodulation scheme.

The samples used in the experiment are two narrow strips of copper foils (0.1 mm thick) - 5 mm wide and 75 mm long, as shown in Figure 3.3. Two ends of each foil stick on the acrylic sheet frame. The copper foils were placed in parallel along e_z with the plane surface perpendicular to e_x . Along e_y , the transducer is placed in the middle between the two copper foils. And along e_z , the transducer locates in the middle between the two ends of the each copper foil. And in direction x the distances between the transducer and two copper foils are 78 mm and 93 mm respectively. The transducer transmitted ultrasound right in direction x .

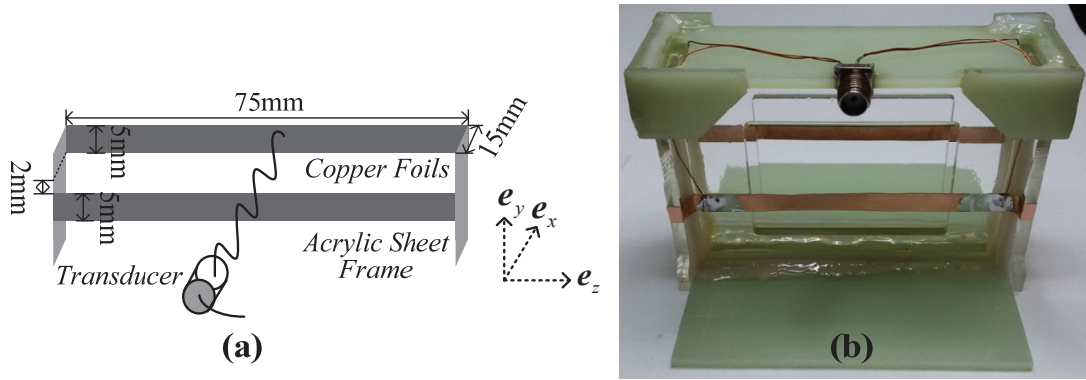


Figure. 3.3. Schematic (a) (Sun *et al.* 2018a) and photo (b) of the sample - two-layer copper foils.

Using the method described above, experiments of detection of electrical conductivity variation - the existence of copper foils here - are carried out. 64 monotonic pulses sequentially are used to stimulate the transducer. The DC signals containing the accumulated phase are used to reconstruct the range information of the electrical conductivity variation. The experiments are done only using the IQ demodulation scheme, but verification of the in-phase demodulation scheme is accomplished using only the in-phase channel signals.

3.3 Results and discussion

In Figure 3.4.a and b, the lines in black with circles represent the reconstructed electrical conductivity variations by theoretical calculation using the in-phase and the IQ demodulation schemes respectively, while the lines in red with asterisks represent the reconstructed electrical conductivity variation by experiments using the direct and IQ demodulation methods respectively.

Both theoretical calculation and experiments show that in the in-phase demodulation method (Figure 3.4.a), besides two target electrical conductivity variations - 78.21 mm and 93.21 mm far away from the transducer - being recognized, two artificial variations - respectively 104.6 mm and 89.64 mm far away from the transducer - also appear, whereas in the IQ demodulation method (Figure 3.4.b), only two electrical conductivity variations - 78.21 mm and 93.21 mm far away from the transducer - are recognized. And, the reconstructed variations - locating at

respectively 78.21 mm and 93.21 mm far away from the transducer - coincide with the real distances (78 mm and 93 mm), with a minor amount of error.

Better low-noise amplifying circuit can be explored to detect weak SECG-SF-UILF current signal in experiments using weakly conductive phantom samples. Although the method of increasing the number of the step frequencies can also improve the signal to noise ratio and increase the detecting range, this method is not preferred as the operating time of the step frequency technique increases linearly with the number of step frequencies.

3.4 Chapter summary

In this chapter, we carried out an in-depth study of scanning electric conductivity gradients with step-frequency ultrasound induced Lorentz force (SECG-SF-UILF). Theory of adaptation of step-frequency technique to SECG-UILF in terms of calculation of the longitudinal distance using either the in-phase coherent demodulation scheme and the IQ coherent demodulation scheme was formulated. Although the uneven frequency response of the transducer and the integral in the acousto-electrical transformation undermined the integrity of the accumulated phase, it was still viable to recognize the range information of electrical conductivity variations using the step-frequency technique. Using the same ultrasound stimulation, the in-phase coherent demodulation method can only detect half the range of the electrical conductivity variation as the IQ coherent demodulation method due to the mirroring artifacts, but compared with the IQ coherent demodulation method, the in-phase demodulation method has the advantage of hardware simplicity. Experimental verification of both schemes using copper foil samples was done. The results showed that the ranges of copper foil could be reconstructed precisely. Therefore, using sinusoidal pulse signal and step-frequency technique suggests an alternative direction for the development of SECG-UILF.

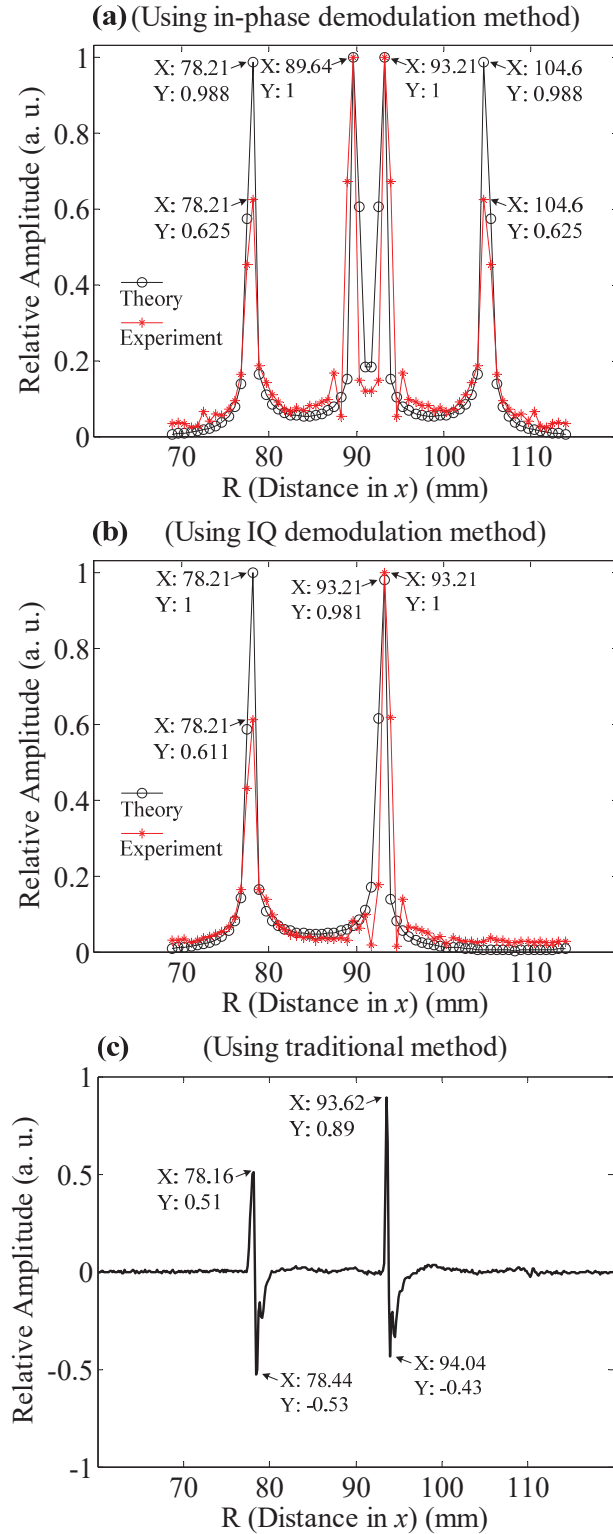


Figure 3.4. Reconstructed electrical conductivity gradient distribution from SECG-SF-UILF (a: In-phase demodulation method only using the in-phase channel signal; b: IQ demodulation method using both the in-phase and the quadrature-phase channel signal. Black circle: Results by theoretical analysis; Red asterisk: Results by experiments.) (Sun *et al.* 2018a) and from the traditional SECG-UILF using the high acoustic pressure wide-band ultrasound pulse stimulation.

Part 2 Shear wave generation by the Lorentz force and its application in elastography

Currently, clinical shear wave elastography techniques use an external vibrator (Muthupillai *et al.* 1995, Sandrin *et al.* 2003) or the acoustic radiation force (Sarvazyan *et al.* 1998, Nightingale *et al.* 2002, Bercoff *et al.* 2004b) to generate the shear wave source. However, in situations where the target region of an organ locates behind a strongly reflective medium like the heart behind the sternum and ribs or the brain behind the skull, the shear waves generated by the active methods are severely attenuated. Deriving from the noise-like signal correlation technique which had previously been applied successfully in geophysics (Campillo and Paul, 2003), crustal tomography (Shapiro *et al.* 2005), helioseismology (Duvall Jr *et al.* 1993, Giles *et al.* 1997), oceanography (Buckingham *et al.* 1992, Roux *et al.* 2004), and ultrasonics (Lobkis and Weaver 2001), the cross-correlation approach based elastography (Sabra *et al.* 2007, Gallot *et al.* 2011, Catheline *et al.* 2013, Zorgani *et al.* 2015, Nguyen *et al.* 2016, Kitazaki *et al.* 2016, Grasland-Mongrain *et al.* 2018) can use the shear wave sources passively generated by internal physiological motions accompanying respirations or cardiac pulsation without synchronizing the scanner to these shear wave sources (Sabra *et al.* 2007, Gallot *et al.* 2011, Catheline *et al.* 2013, Zorgani *et al.* 2015). The general concept consists in retrieving the Green's function from the correlation of a complex noise-like wave field. The cross-correlation approach based elastography therefore possesses the possibility of evaluating the target regions inaccessible to the methods relying on actively generating the shear wave motions.

The cross-correlation based shear wave velocity reconstruction method requires that the shear wave displacement fields have a broad frequency bandwidth. The shear wave displacement fields used in passive elastography, which are generated from the physiological activity of the human body, however, have narrow frequency bandwidth. In the passive elastography experiments, at least 500 frames of the passive shear wave displacement fields are needed to reconstruct the shear wave velocity map using the cross-correlation approach, and therefore large amount of calculation is needed.

CATHELIN Stefan's team in LabTAU investigates the active methods of generating shear wave displacement fields of broader frequency bandwidth, with the aim of improving the shear wave velocity map reconstructed using the cross-correlation approach. Compared with the passive methods of generating shear wave displacement fields, the active methods are easier in expanding the frequency bandwidth of the generated shear wave displacements. When GRASLAND-MONGRAIN Pol worked in LabTAU and LBUM between 2013 and 2016, he proposed to directly generate the Lorentz force in the biological tissue target, which then generates shear wave displacements in the target (Grasland-Mongrain *et al.* 2014, Grasland-Mongrain *et al.* 2016). The author of the thesis continues GRASLAND-MONGRAIN Pol's work, studying and developing further the generation of shear wave displacements in the soft media through the Lorentz force for the cross-correlation approach based elastography.

In 2015, GRASLAND-MONGRAIN Pol explored the Lorentz force to remotely generate shear wave displacements in soft medium: induction of the Lorentz force by combining the eddy current from transient magnetic stimulation and the static magnetic field from permanent magnets succeeded in contactlessly generating shear waves in soft biological tissues (Grasland-Mongrain *et al.* 2016). However, one serious shortcoming of his method is that the shear wave produced is too weak for clinical application - the amplitude is on the order of $0.5 \mu\text{m}$, even though the transient magnetic field \mathbf{B}_1 produced by the stimulator reaches a changing rate of 30 kTs^{-1} . Moreover, besides the stimulating coil (to generate \mathbf{B}_1 to induce electrical eddy current in the tissue), this method requires permanent magnets to create the static magnetic field \mathbf{B}_0 . In fact, the transient magnetic field produced by the electrical current in the stimulating coil reaches 0.74 T at 2 cm apart from the coil surface - almost quadruple the intensity of the static magnetic field produced by the permanent magnets (ranging from 100 mT to 200 mT) - and in the area right in front of the coil, the transient and static magnetic fields are in the same direction. Therefore, even if the static magnetic field was eliminated, the generated Lorentz force only decreases approximately 20 percent. This is quite similar to the situations in electromagnetic

forming (EMF) (Harvey and Brower 1961, Psyk *et al.* 2011) and electromagnetic acoustic transducer (EMAT) (Jian *et al.* 2006, Rueter and Morgenstern 2014), where the Lorentz force is remotely generated on the conductive target by coupling the eddy current induced from a transient magnetic field with the orthogonal component of the transient magnetic field.

In the second part of the thesis, we transfer the method in the EMF and the EMAT of remotely generating the Lorentz force to the field of elastography and presents realization of shear wave generation by remotely exciting aluminum patches actuators through a transient magnetic field and its preliminary application in the cross-correlation approach based ultrasound elastography.

In chapter four, we will study stimulating the aluminum ring or patch actuator using a transient magnetic field so as to generate the Lorentz force on the ring or patch, which vibrate and generate displacements on the surface of the soft media that propagate towards the inside of the soft medium target.

In chapter five, we will verify the performance of the cross-correlation approach based shear wave velocity reconstruction using the shear wave displacement fields generated by the method in chapter four.

Chapter 4 Shear wave generation by remotely exciting aluminum patches with a transient magnetic field

This chapter studies generating shear wave displacement fields in soft medium by stimulating an aluminum ring or patch using a transient magnetic field. The transient magnetic field from a coil induces and interacts with eddy currents in the ring or patch, producing Lorentz force on the ring or patch and generating shear wave displacement at the sample surface. Under the same transient magnetic field, multiple patches generate multiple shear wave sources at the sample surface. This chapter is organized as follows: the physics of generation of the Lorentz force on the aluminum ring actuator is first described; then the origin and the characteristics of the Lorentz force acting on and the resulting displacement of the actuator are verified; and then the shear wave field created in the soft medium is studied by experiments and by theory; and finally, the shear wave displacement fields generated by the patch actuators is demonstrated with a multi-shaped agar phantom.

4.1 Characteristics of the Lorentz force induced

To simplify the explanation of generation of Lorentz force on the actuator while keeping generality, an aluminum ring is chosen as the actuator (Figure 4.1.a). For the case of using an aluminum patch as the actuator, the patch can be treated as multiple rings of different diameters superimposed together. The ring sticks onto the surface of the sample. And a solenoid coil in front of the ring generates a transient magnetic field \mathbf{B} when an electrical current pulse I_c passes the coil, as (4.1), where \mathbf{J}_c is the current density in the coil, μ_0 is the magnetic permeability of free space, and A is the magnetic potential.

An electrical current I is induced in the ring as a result of the Faraday's law of induction as (4.2), where \mathbf{E} is the induced electrical field, \mathbf{J} is the eddy electrical current density in the ring, and σ is the electrical conductivity of the ring. The electrostatic potential created by the accumulated free charges is neglected in (4.2).

The induced eddy current I in the ring couples with the y and z components of

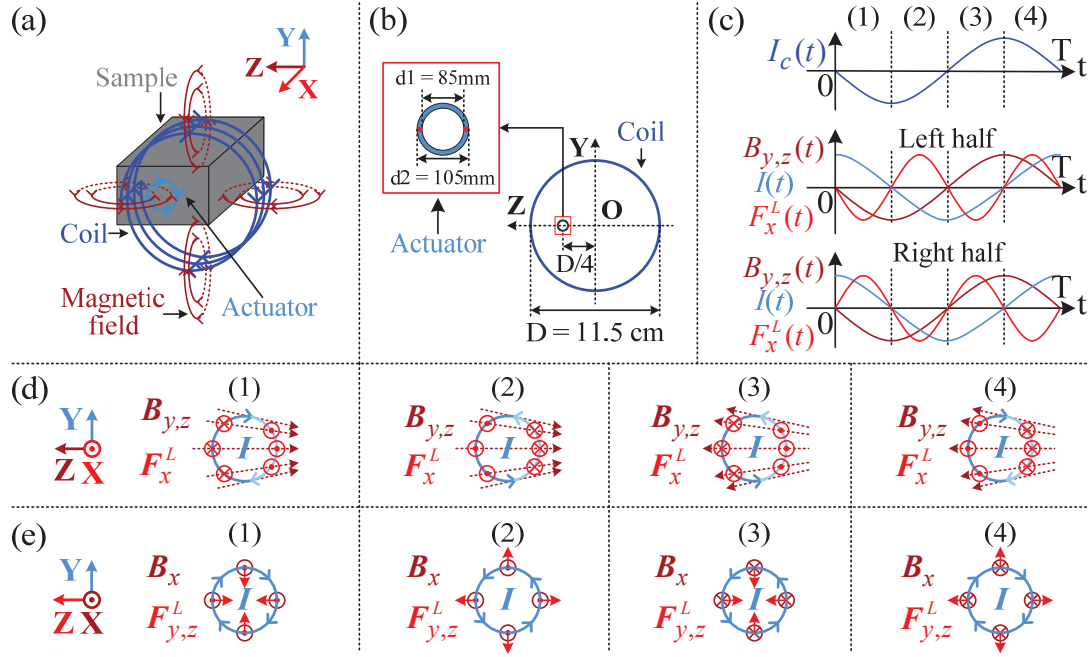


Figure 4.1. (a) Generation of Lorentz force on a non-ferromagnetic conductive ring as the actuator using a transient magnetic field from a solenoid coil. (b) The ring locates on the left half of the coil's horizontal diameter. (c) The waveforms of $I_c(t)$ (the top signal), $B_{y,z}(t)$ (the magenta signals), $I(t)$ (the cyan signals) and $F_x^L(t)$ (the red signals) on the left half (the middle set of signals) and right half (the bottom set of signals) of the ring. These waveforms are divided into four equal intervals (1), (2), (3) and (4). (d) The directions of $B_x(t)$ (the magenta arrows), $I(t)$ (the cyan arrows) and $F_x^L(t)$ (the red arrows) in each interval. (e) The directions of $B_{y,z}(t)$ (the magenta arrows), $I(t)$ (the cyan arrows) and $F_{y,z}^L(t)$ (the red arrows) in each interval. (Sun *et al.* to be submitted)

the magnetic field $B_{y,z}$ and generates the x component Lorentz force F_x^L , as (4.3), where V is the volume containing I . F_x^L (Figure 4.1.d) on the left half (and a small part of the right half) of the actuator is in the same direction, while that on the remaining right half of the actuator is in the opposite direction. F_x^L , therefore, constitutes a torque and rotates the actuator around y -axis. However, as F_x^L on the left half of the actuator is not totally symmetric with that on the right half of the actuator, F_x^L also translates the actuator in x direction.

The eddy current in the ring I also couples with the x component of the magnetic field B_x and generates the Lorentz force in the yo z plane $F_{y,z}^L$ (Figure 4.1.e).

However, $F_{y,z}^L$ is centro-symmetric and therefore cancels out and has little effect on the displacement of the actuator.

$$\nabla \times \mathbf{B} = \mu_0 \mathbf{J}_c, \mathbf{B} = \nabla \times \mathbf{A} \quad (4.1)$$

$$\mathbf{E} = -\frac{\partial \mathbf{A}}{\partial t}, \mathbf{J} = \sigma \mathbf{E} = -\sigma \frac{\partial \mathbf{A}}{\partial t} \quad (4.2)$$

$$\mathbf{F}^L = \iiint \mathbf{J} \times \mathbf{B} dV = \iiint -\sigma \frac{\partial \mathbf{A}}{\partial t} \times \mathbf{B} dV \quad (4.3)$$

If the electrical current to the coil - $I_c(t)$ - takes a sinusoidal pulse of carrier frequency f_1 (4.4), the y and z components of the magnetic field - $B_{y,z}(t)$, the eddy current in the ring - $I(t)$, and the x component Lorentz force acting on the ring - $F_x^L(t)$ - have the waveforms as (4.5), (4.6) and (4.7) (Figure 4.1.c), where A_0 is a constant, k_1 , k_2 and k_3 are variables with \mathbf{r} . f_2 differs from f_1 as a band signal shifts its carrier frequency after taking time derivative. From (4.7), $F_x^L(t)$ has two characteristics: (1) its spectrum has two carrier frequencies, which are respectively the sum and the difference of the carrier frequencies of the transient magnetic field and its time derivative; (2) its amplitude increases as power of two with the amplitude of $I_c(t)$.

$$I_c(t) = A_0 \sin(2\pi f_1 t), 0 \leq t \leq T \quad (4.4)$$

$$B_{y,z}(\mathbf{r}, t) = k_1(\mathbf{r}) A_0 \sin(2\pi f_1 t), 0 \leq t \leq T \quad (4.5)$$

$$I(\mathbf{r}, t) = k_2(\mathbf{r}) A_0 \cos(2\pi f_2 t), 0 \leq t \leq T \quad (4.6)$$

$$F_x^L(\mathbf{r}, t) = k_3(\mathbf{r}) A_0^2 \{ \sin[2\pi(f_1 + f_2)t] + \sin[2\pi(f_1 - f_2)t] \}, 0 \leq t \leq T \quad (4.7)$$

4.2 Displacement of the aluminum patch under the stimulation of a transient magnetic field

The displacement of the actuator, under the stimulation by the transient magnetic field, is studied using an interferometric laser probe (Interferometric probe SH-140, THALES LASER S.A., Orsay France) (Monchalin 1986) (Figure 4.2.a). The SH-140 optical heterodyne probe is designed to measure transient mechanical displacements of very low amplitude. It is specially devoted to measuring displacements generated

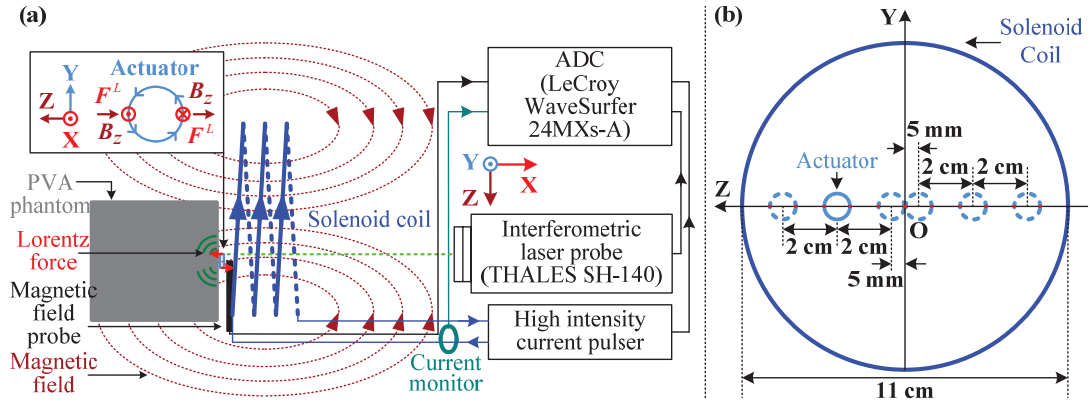


Figure 4.2. (a) Schematic layout of measurement of the actuator's displacement using an interferometric laser probe (top side view). A zoom-in of the actuator in the yoz plane is included in the top-left corner. (b) The center of the actuator (an aluminum ring) positions at $z = \pm 2.5$ cm, ± 1.5 cm and ± 0.5 cm respectively along the horizontal diameter of the coil. (Sun *et al.* to be submitted)

by the propagation of an acoustic or ultrasonic wave.

The time varying magnetic field is generated by outputting a sinusoidal electrical current pulse to a solenoid coil. An aluminum circular ring with an outer diameter of 10.5 mm, an inner diameter of 8.5 mm, and a thickness of 0.5 mm serves as the actuator. The actuator sticks on the surface of a polyvinyl alcohol (PVA) phantom, which is made from a mixture of PVA (7 wt%), graphite power (0.4 wt%) and water (Fromageau et al 2007) and of size 8 cm×8 cm×4 cm. Two freezing/thawing (12 hours/12 hours) cycles are applied to stiffen the PVA phantom. In Figure 4.2.a, the coil axis coincides with the x-axis. The optical laser beam focuses on the middle of either the left or the right half of the actuator, as indicated by the tiny red points in Figure 4.2.b. The current to the coil and the 3-D magnetic field flux density are simultaneously measured by a current monitor (Current Monitor Model 110A, Pearson Electronics, CA, USA) and a magnetic field probe (MagProbe 3D, MagVenture, Farum, Denmark).

4.2.1 The transient pulsed magnetic field

The transient pulsed magnetic field is generated by stimulating a solenoid coil

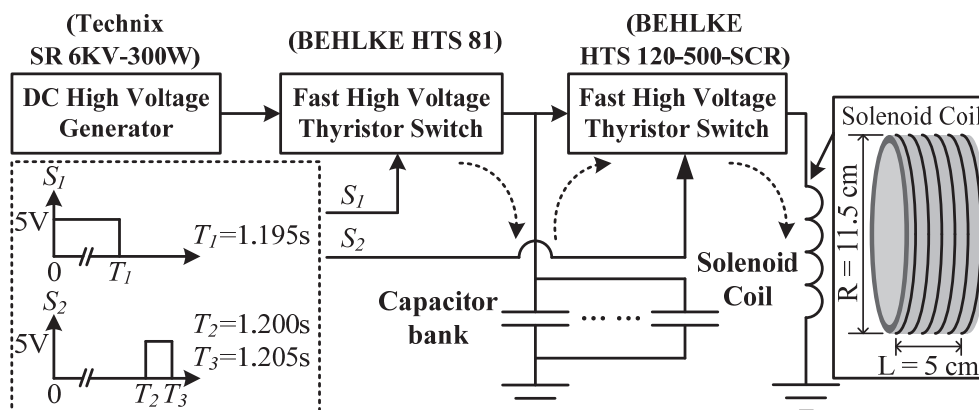


Figure 4.3. The schematic of the transient magnetic field generation. The time diagrams of the control signals S_1 and S_2 for the two fast high voltage thyristor switches are shown inside the dotted rectangle.

(Sun *et al.* to be submitted)

with a high-intensity current pulse. The working principle of the high intensity current pulser is shown in Figure 4.3 (Polson et al 1982, Barker et al 1985). In operation, by switching on the first fast high voltage thyristor switch (BEHLKE HTS 81), the charge is built on a bank of capacitors of total capacitance of $6 \mu\text{F}$. After fully charging the capacitors, the HTS 81 is switched off and the second high voltage thyristor switch (BEHLKE HTS 120-500-SCR) is switched on. The high-intensity electrical current pulse is generated when the charge releases through the coil. The intensity of the electrical current into the coil is controlled by varying the charging voltage to the capacitors. And the carrier frequency of the electrical current pulse is controlled by varying the inductance of the coil. Four solenoid coils with inductance of 2.33 mH, 615.0 μH , 265.4 μH and 151.5 μH are employed independently to alter the circuit impedance of the current pulser, which finally produce high-intensity current pulse of carrier frequencies of 1.240 kHz, 2.480 kHz, 3.815 kHz, and 4.959 kHz.

The homemade solenoid coils, all having a diameter of 11.7 cm, are made from different lengths and different numbers of turns of copper wire of a cross-section area of 0.75 mm^2 . The multiple turns of wire are wound into layers, and the wire jumps from the inner layer to the outer layer in a manner like 'Z'.

4.2.2 Three groups of experiments measuring the displacements of the aluminum ring

The first group of measurements is to confirm the source of the Lorentz force: (1) the z component magnetic field flux density; and (2) the changing rate of the x component magnetic field flux density. The displacement of the middle point of the left half of the ring, under the Lorentz force, is measured, when the ring locates at different positions on the horizontal diameter of the coil. The center of the ring positions at $z = \pm 2.5$ cm, ± 1.5 cm and ± 0.5 cm along the horizontal diameter of the coil (Figure 4.2.b).

The second group of measurements is to verify the frequency characteristics of the displacement of the actuator stimulated by the transient magnetic field. The actuator is kept fixed while the transient magnetic field is generated using each of the four coils independently. The center of the actuator positions at $z = +2.5$ cm on the horizontal diameter of the coil.

The third group of measurements is to prove the amplitude characteristics of the ring actuator's displacement upon the current of variable amplitude to the coil. The actuator is kept fixed with its center positioning at $z = +2.5$ cm spatially relative to the horizontal diameter of the coil. Electrical current pulses of step-increasing amplitude passing the coil of inductance of $265.4 \mu\text{H}$ is used to generate the transient magnetic field. The measurements are done first on the middle point of the left half and then on the middle point of the right half of the ring actuator. The amplitudes of the current and the displacement in either set of measurements are calculated by the following procedures: (1) halves of the peak-to-peak values of the current and displacement waveforms in the first measurement of the set are taken as the reference amplitudes of the current and the displacement; (2) the amplitudes of the current and the displacement in the remaining measurements of the set are converted from the spectrum peak amplitudes by assuming the same proportionality in waveform amplitudes as that in spectrum peak amplitudes between two different measurements.

4.3 The Shear wave displacement fields in the soft medium generated by the aluminum patch under the transient Lorentz force

Under the Lorentz force, the patch actuator - sticking on the surface of the PVA phantom - rotates and translates, exerting a force on the surface of the phantom. Under the force, the shear wave displacement is generated on the surface and propagates into the phantom. The longitudinal displacement generated and propagating in the PVA phantom is detected by an ultrasonic probe (PHILIPS, ATL L7-4) and a scanner (Verasonics Vantage 256TM, Washington, USA) (Figure 4.3.a). The coil of inductance of $173 \mu\text{H}$ is used to generate the transient magnetic field, and an aluminum rectangular patch of sizes of $0.5 \text{ mm} \times 15 \text{ mm} \times 10 \text{ mm}$ ($X' \times Y \times Z'$) serves as the actuator (Figure 4.3.b and d). The patch actuator sticks on the front surface of the PVA phantom, which is turned anticlockwise around the y -axis by 30 degrees to increase the Lorentz force induced. As in the experiments using the interferometric optical laser, the current to the coil is measured using the current monitor, and the x' and z' components of the magnetic field flux densities are measured using the magnetic field probe. The x' component displacement of the medium is calculated by performing cross correlation - the speckle tracking technique (Sandrin *et al.* 2002) - on the sonograms, which are acquired by the Verasonics ultrasound scanner.

4.3.1 Ultrafast ultrasound imaging and calculation of the shear wave displacement of the medium

To track the shear wave propagation inside the sample, the sample is first imaged using ultrasound ultrafast imaging with a 38 mm linear array ultrasound transducer (PHILIPS, ATL L7-4) and a scanner (Verasonics Vantage 256TM, Washington, USA), which works with the depth set to 10 cm.

The x' component displacement of the medium is calculated by performing cross correlation - the speckle tracking technique - on the ultrasound images acquired by the Verasonics ultrasound scanner (Sandrin *et al.* 2002) (Figure 4.3.a).

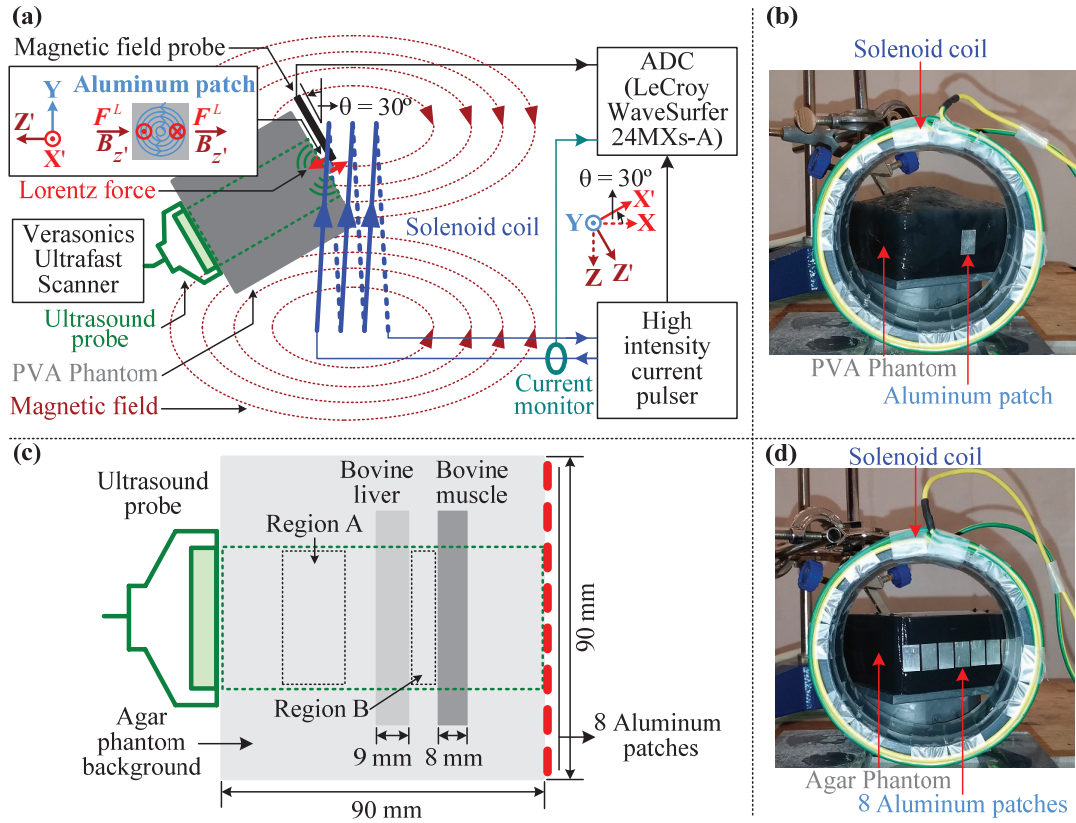


Figure 4.3. (a) Schematic layout of magnetic stimulation and ultrasound ultrafast imaging of the phantom target (top side view). The phantom is turned anticlockwise around the y-axis by 30 degrees. A zoom-in of the patch actuator in the yoz' plane is included in the top-left corner. (b) An aluminum patch of sizes of $0.5 \text{ mm} \times 15 \text{ mm} \times 10 \text{ mm}$ ($X' \times Y \times Z'$) attaches on the front surface center of the PVA phantom. (c) Ultrasound ultrafast imaging of the the multi-shaped agar phantom sample with one layer of bovine liver, one layer of bovine muscle, and a homogeneous background part of agar phantom. (d) Eight aluminum patches - each of dimensions of $0.5 \text{ mm} \times 15 \text{ mm} \times 10 \text{ mm}$ ($X' \times Y \times Z'$) - attach on the front surface of the agar phantom. (Sun *et al.* to be submitted)

4.3.2 Two experiments measuring the medium displacements

The first experiment using the ultrasound ultrafast imaging is to study the propagation of the shear wave displacement source - which is generated using one aluminum patch as the actuator - in the target of a homogeneous PVA phantom (Figure 4.3.b). The PVA phantom is made in the same way as the one used in the experiments using the interferometric optical laser. The Verasonics ultrasound scanner works at a sampling rate of 2000 frames/s.

The second experiment using the ultrasound ultrafast imaging is to study the propagation of the shear wave displacement fields in the target of a multi-shaped tissues-mimicking agar phantom (Figure 4.3.c). Eight aluminum patches sticking on the agar phantom surface (Figure 4.3.d) serve as the actuators to generate multiple shear wave displacement sources to improve the signal-to-noise-ratio for shear wave velocity reconstruction (Zemzemi *et al.* 2018). The multi-shaped agar phantom sample contains one layer of bovine liver - about 9 mm thick in x' direction, one layer of bovine muscle - about 8 mm thick in x' direction, and a background part of homogeneous agar phantom. The background part of the agar phantom is made from a mixture of agar powder (0.6 wt%), graphite powder (0.4 wt%) and pure water. The agar phantom is made by heating the pure water to the boil, adding the agar powder, heating the mixture to the boil again, cooling the hot mixture down, and adding the graphite powder. The mixture is stirred by a bar magnet and a magnetic force agitator to make the mixture to be more homogeneous until it cools down to 38 degrees Celsius. In experiments, the Verasonics ultrasound scanner works at a sampling rate of 1000 frames/s.

4.3.3 Theoretical longitudinal displacement field in the PVA phantom calculated using the Green function

In the first ultrafast ultrasound imaging experiment, the actuator sticks on the surface of the sample. When the actuator rotates and translates under the Lorentz force, the actuator exerts a force on the surface of the sample. Numerical calculation of the force is too complicated because of the boundary conditions and is beyond the scope of this work. A simple model of dipole force - one in positive x -direction and the other in negative x -direction - is adopted for the force. Theoretical calculation of the x' component displacement in the medium using the analytical Green function (Aki and Richards 2002, Grasland-Mongrain *et al.* 2014) is done.

The displacement field $\mathbf{u}(\mathbf{r}, t)$ in a homogeneous, isotropic and purely elastic solid medium when subjected to an external force $\mathbf{f}(\mathbf{r}, t)$ satisfies the classical Navier's

equation (4.8).

$$\rho \frac{\partial^2 \mathbf{u}}{\partial t^2} = (\lambda + 2\mu)\nabla(\nabla \cdot \mathbf{u}) - \mu\nabla \times (\nabla \times \mathbf{u}) + \mathbf{f}(\mathbf{r}, t) \quad (4.8)$$

where ρ is the medium density, λ is Lamé's first parameter, and μ is the medium shear modulus.

The displacement field in i (i refers to x or y or z) - $u_i(\mathbf{r}, t)$ - when the medium is subjected to a space-time Dirac function in direction j - $\mathbf{f}_0(\mathbf{r}, t)$ (4.9) - constitutes the Green function - $g_{ij}(\mathbf{r}, t)$ (4.10).

$$\mathbf{f}_0(\mathbf{r}, t) = \mathbf{e}_j \delta(\mathbf{r}) \delta(t) \quad (4.9)$$

where \mathbf{e}_j is the unit vector in direction j .

$$g_{ij}(\mathbf{r}, t) = g_{ij}^P(\mathbf{r}, t) + g_{ij}^S(\mathbf{r}, t) + g_{ij}^{PS}(\mathbf{r}, t) \quad (4.10)$$

where $g_{ij}^P(\mathbf{r}, t)$ is the far-field P-wave Green function (4.11), i.e. the far-field compression wave of $u_i(\mathbf{r}, t)$ when the medium is subjected to $\mathbf{f}_0(\mathbf{r}, t)$; $g_{ij}^S(\mathbf{r}, t)$ is the far-field S-wave Green function (4.12), i.e. the far-field shear wave of $u_i(\mathbf{r}, t)$ when the medium is subjected to $\mathbf{f}_0(\mathbf{r}, t)$; and $g_{ij}^{PS}(\mathbf{r}, t)$ is the near-field Green function (4.13), i.e. the near-field displacement (including both the compression and the shear waves) of $u_i(\mathbf{r}, t)$ when the medium is subjected to $\mathbf{f}_0(\mathbf{r}, t)$.

$$g_{ij}^P(\mathbf{r}, t) = \frac{1}{4\pi\rho c_p^2} \gamma_i \gamma_j \frac{1}{r} \delta\left(t - \frac{r}{c_p}\right) \quad (4.11)$$

$$g_{ij}^S(\mathbf{r}, t) = \frac{1}{4\pi\rho c_s^2} (\delta_{ij} - \gamma_i \gamma_j) \frac{1}{r} \delta\left(t - \frac{r}{c_s}\right) \quad (4.12)$$

$$g_{ij}^{PS}(\mathbf{r}, t) = \frac{1}{4\pi\rho} (3\gamma_i \gamma_j - \delta_{ij}) \frac{1}{r^3} \int_{r/c_p}^{r/c_s} \tau \delta(t - \tau) d\tau \quad (4.13)$$

where $c_p = \sqrt{(\lambda + 2\mu)/\rho}$ is the compression wave speed, $c_s = \sqrt{\mu/\rho}$ is the shear wave speed, and γ_i and γ_j are the direction cosines. i and j refer to x or y or z .

The displacement field in i (i refers to x or y or z) - $u_i(\mathbf{r}, t)$ - generated in the medium by any force $\mathbf{f}(\mathbf{r}, t)$ can be modeled by the spatial and temporal convolution of $\mathbf{f}(\mathbf{r}, t)$ with $g_{ij}(\mathbf{r}, t)$ as (4.14).

$$u_i(\mathbf{r}, t) = \int d\tau \sum_{j=x,y,z} \iiint d\xi^3 f_j(\xi, \tau) g_{ij}(\mathbf{r} - \xi, t - \tau) \quad (4.14)$$

where i and j refer to x or y or z .

4.4 Results and discussion

4.4.1 Confirmation of the Lorentz force origins

Figure 4.4.a.1-6 show the z component magnetic flux density - $B_z(t)$, the time derivative of the x component magnetic flux density - $\partial B_x(t)/\partial t$, the theoretical Lorentz force density - $f_x^L(t)$ ($I(t) \cdot B_z(t)$) - acting on and the displacement - $D(t)$ - of the middle points of the left half and the right half of the ring actuator in the first group of experiments using the interferometric laser probe. The spectra of each set of signals are shown in the corresponding right figures (Figure 4.4.b.1-6). The waveforms and spectra of the four set of signals of $B_z(t)$, $\partial B_x(t)/\partial t$, $f_x^L(t)$, and $D(t)$ show: (1) $B_z(t)$, $\partial B_x(t)/\partial t$, and $f_x^L(t)$ individually have quite similar spectra across the six different positions, which confirms the validity of separation of the temporal-spatial factors in (4.5) - (4.7); (2) $B_z(t)$ and $D(t)$ are largest at positions $z = \pm 2.5$ cm, smallest at positions $z = \pm 0.5$ cm, and that in-between at positions $z = \pm 1.5$ cm. Besides, $B_z(t)$ and $D(t)$ at positions $z = +2.5$ cm, $+1.5$ cm, and $+0.5$ cm have opposite polarity correspondingly to those at positions $z = -2.5$ cm, -1.5 cm, and -0.5 cm; and (3) except at position $z = -0.5$ cm, $D(t)$ has the same polarity as $f_x^L(t)$ and its amplitude varies proportionally to the amplitude of $f_x^L(t)$. These characteristics confirm the theory in section 2.1: the Lorentz force acting on the ring is contributed both by the z component magnetic field and by the time-varying x component magnetic field which induces eddy electrical current in the ring actuator.

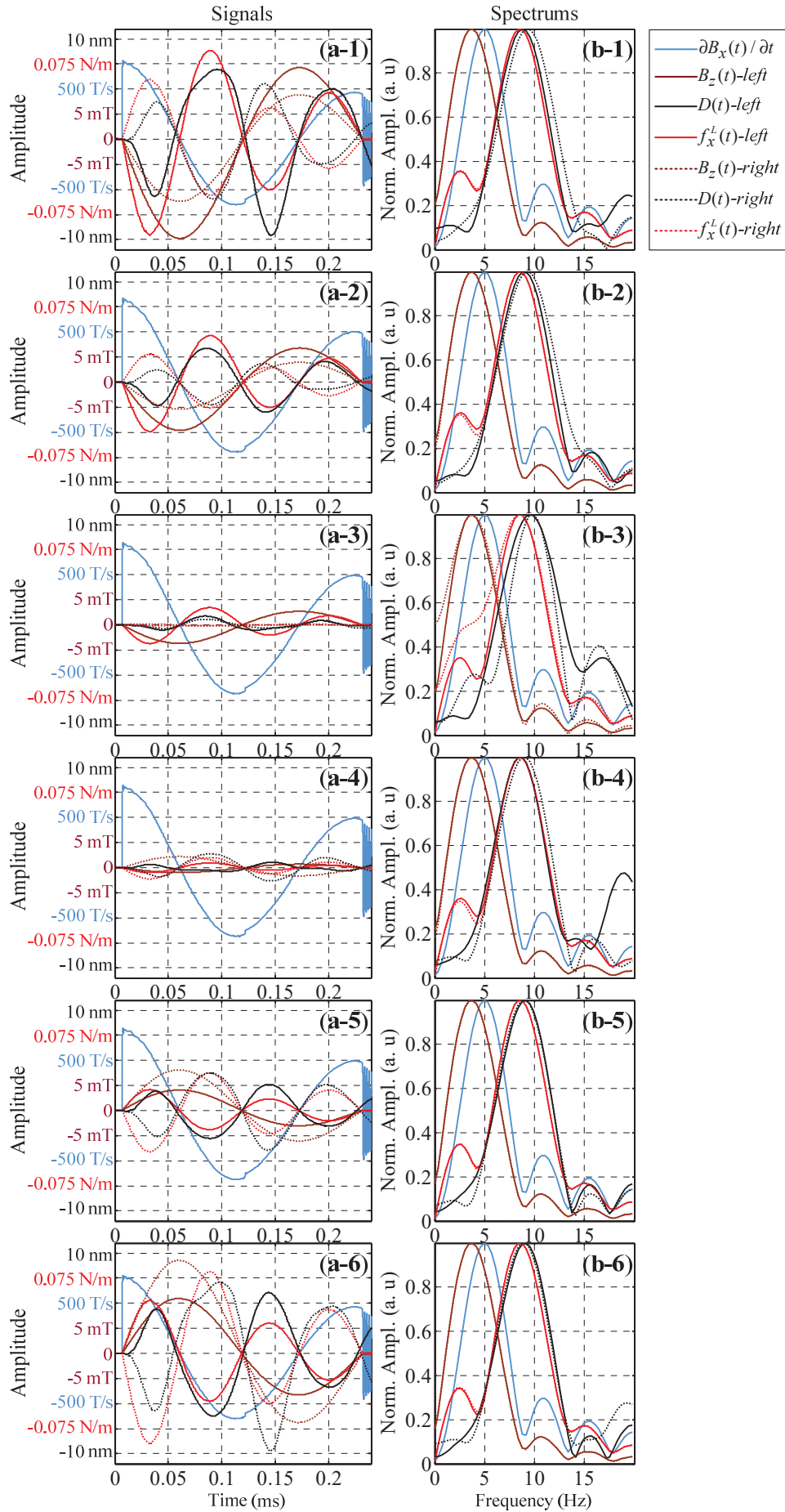


Figure 4.4. The z component magnetic flux density ($B_z(t)$) (magenta signals) at the middle of the left half (solid lines) and the right half (dashed lines) of the ring actuator, the changing rate of the x component magnetic flux density ($\partial B_x(t)/\partial t$) (cyan signals) at the center of the ring actuator, the theoretical Lorentz force density ($f_x^L(t)$) (red signals) acting on and the displacement ($D(t)$) (black signals) at the middle of the left half (solid lines) and the right half (dashed lines) of the ring actuator when the ring actuator locates independently at positions $z = +2.5$ cm (a-1), $+1.5$ cm (a-2), $+0.5$ cm (a-3), -0.5 cm (a-4), -1.5 cm (a-5), and -2.5 cm (a-6) in the first group of experiments using the interferometric laser probe. The spectra of each set of signals are also calculated using FFT and shown respectively in sub-figures (b-1), (b-2), (b-3), (b-4), (b-5), and (b-6). (Sun *et al.* to be submitted)

4.4.2 The frequency characteristics of the Lorentz force

Figure 4.5.a.1-4 show the signals of the z component magnetic flux density - $B_z(t)$, the changing rate of the x component magnetic flux density - $\partial B_x(t)/\partial t$, the theoretical Lorentz force density - $f_x^L(t)$ ($I(t) \cdot B_z(t)$) - acting on and the displacements - $D(t)$ - of the middle point of the left half and the right half of the ring actuator in the second group of experiments using the interferometric laser probe. The spectra of each set of signals are shown in the corresponding right figures (Figure 4.5.b.1-4). The carrier frequencies of the signals are summarized in Table 4.1. For each of the four coils, the carrier frequency of $f_x^L(t)$ equals the sum of the carrier frequencies of $B_z(t)$ and $\partial B_x(t)/\partial t$; and the carrier frequency of $D(t)$ is equal to or a little larger than that of $f_x^L(t)$, which confirms the $f_1 + f_2$ frequency component in Equation (4.7). The $f_1 - f_2$ frequency component can hardly be recognized in the spectra of $f_x^L(t)$ or $D(t)$ mainly because that the signal lengths are much shorter than one complete period.

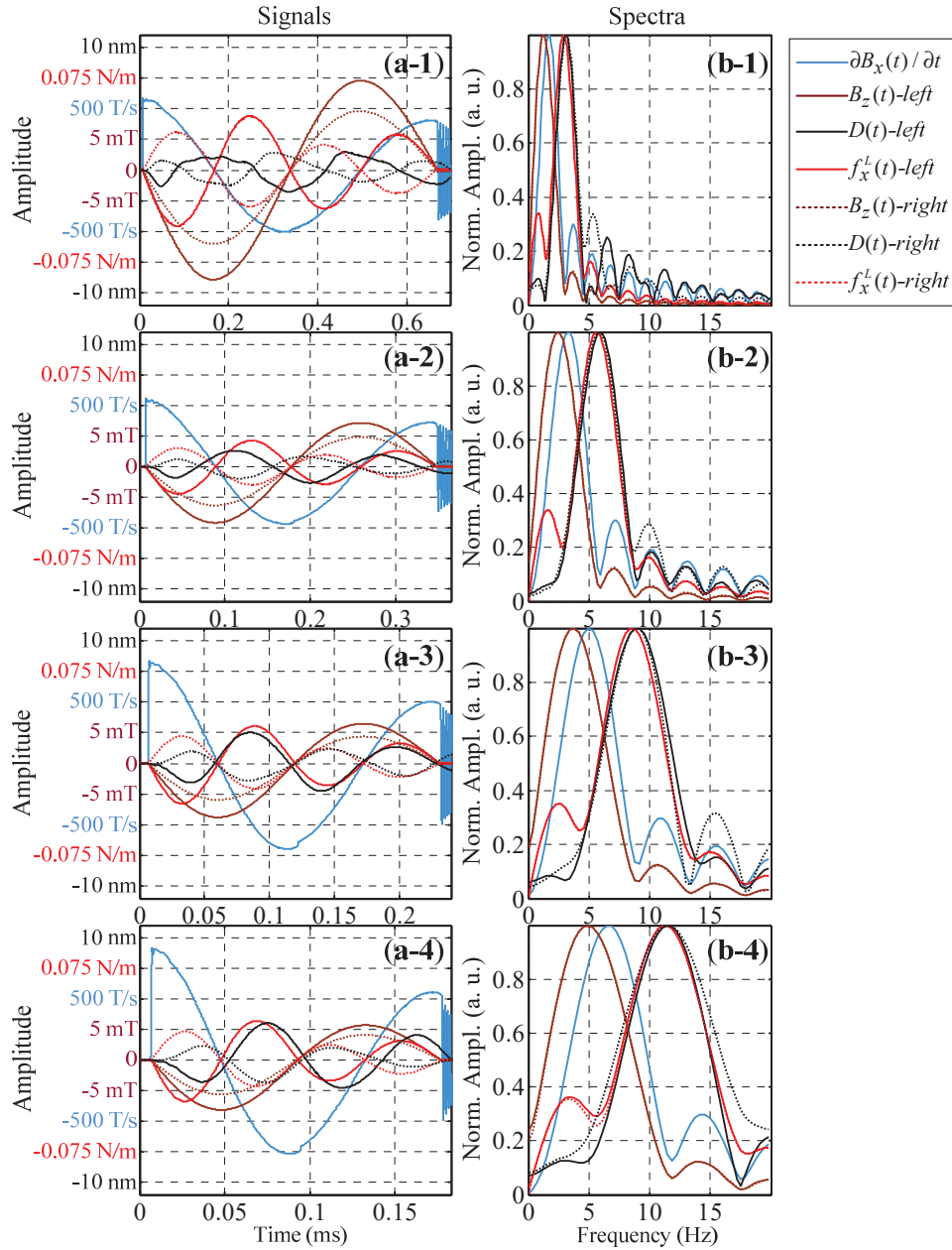


Figure 4.5. The z component magnetic flux density ($B_z(t)$) (magenta signals) at the middle of the left half (solid lines) and the right half (dashed lines) of the ring actuator, the changing rate of the x component magnetic flux density ($\partial B_x(t)/\partial t$) (cyan signals) at the center of the ring actuator, the theoretical Lorentz force density ($f_x^L(t)$) (red signals) acting on and the displacement ($D(t)$) (black signals) at the middle of the left half (solid lines) and the right half (dashed lines) of the ring actuator when solenoid coils with inductance of 2.33 mH (a-1), 615.0 μ H (a-2), 265.4 μ H (a-3), and 151.5 μ H (a.4) are employed independently to generate the transient magnetic field and the ring actuator locates at position $z = +2.5$ cm in the first group of experiments using the interferometric laser probe. The spectra of each set of signals are also calculated using FFT and shown respectively in sub-figures (b-1), (b-2), (b-3), and (b-4). (Sun *et al.* to be submitted)

Table 4.1. Carrier frequencies of the pulse signals (kHz) (Sun *et al.* to be submitted)

	1 st coil	2 nd coil	3 rd coil	4 th coil
$B_z(t)$	1.240	2.480	3.815	4.959
$\partial B_x(t)/\partial t$	1.717	3.242	4.959	6.485
$f_x^L(t)$	2.956	5.531	8.774	11.44
$D(t)$	3.052	5.722	9.155	11.44

4.4.3 The amplitude characteristic of the Lorentz force

Figure 4.6 shows the amplitudes of the displacements of the middle point of the left and the right halves of the ring actuator in the third group of experiments using the interferometric laser probe. For either set of measurements, a coefficient (α) defined as the division of the displacement amplitude by the square of the current amplitude is calculated. The average value of α from measurements on the left half of the actuator is $4.10 \cdot 10^{-4} \text{ nmA}^{-2}$ while that from measurements on the right half of the actuator is $2.57 \cdot 10^{-4} \text{ nmA}^{-2}$. The curve of $D = \alpha \cdot I_c^2$ for either set of measurements is also included in Figure 4.6 for comparison, which shows that, when the displacement amplitude is smaller than 5 nm - such as the displacements in the first eight measurements on the left half and in the first ten measurements on the right half, the displacement amplitude observed by the laser probe agrees well with the formula of $D = \alpha \cdot I_c^2$, or equivalently, the displacement amplitude follows a quadratic growth upon the amplitude of the current to the coil. This phenomenon coincides with the theory in Equation (4.7). The decrease of the displacement amplitude in the last four measurements on the left half and the last two measurements on the right half of the actuator comes from the rotating movement of the ring actuator - the rotation of the actuator decreases the laser beam reflected back to the lens and ultimately decreases the displacement signals' amplitude.

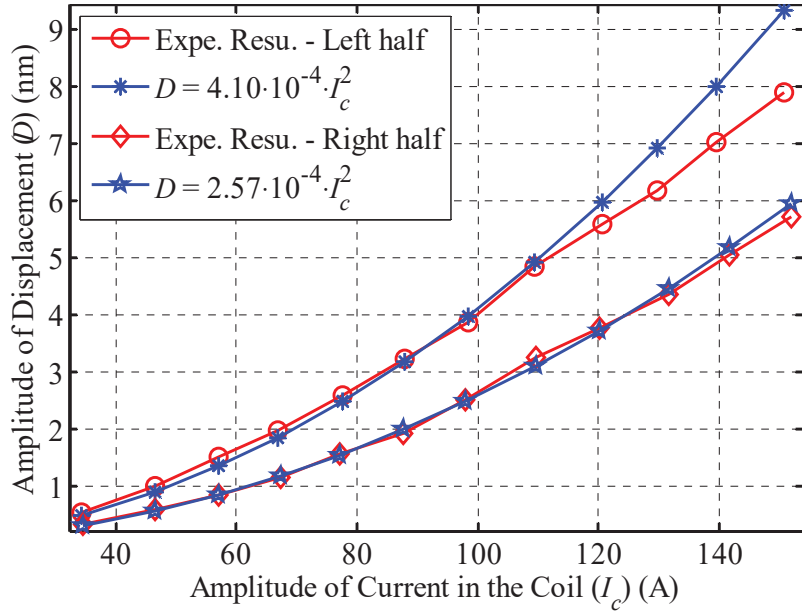


Figure 4.6. The change of the displacement amplitude upon the current of variable amplitude to the coil (the red signals). The curve of $D = \alpha \cdot I_c^2$, for either set of measurements on the left and the right halves of the ring actuator, is included (the blue signals). (Sun *et al.* to be submitted)

4.4.4 The propagation of shear wave displacement in the PVA phantom

In the first experiment using the ultrasound ultrafast imaging, the electrical current pulse to the coil - $I_c(t)$ - reaches a peak amplitude of 947.7 A; the z' component magnetic flux density - $B_{z'}(t)$ - reaches a peak amplitude of 239.6 mT; the x' component magnetic field reaches a peak changing rate - $\partial B_{x'}(t)/\partial t$ - of 10.44 kTs⁻¹; the x' component of the Lorentz force density acting on the actuator - $f_{x'}^L(t)$ - reaches a peak amplitude of 29.9 Nm⁻¹; and the x' component displacement field in the medium has a peak amplitude of 100 μm at the source and keeps a peak amplitude larger than 1 μm after propagating 2 cm away from the source. The x' component displacements of the medium at 1-15 ms after the trigger of the Lorentz force are displayed in Figure 4.7 (top row). The shear wave field generated has a propagation speed (c_s) of 1.67 ms⁻¹ and a period (T) of 10 ms. Using the shear wave speed $c_s = 1.67 \text{ ms}^{-1}$, the compression wave speed $c_p = 1500 \text{ ms}^{-1}$, the medium density $\rho = 10^3 \text{ kgm}^{-3}$, and a dipole pulse force of period $T = 10 \text{ ms}$, theoretical calculation of the x'

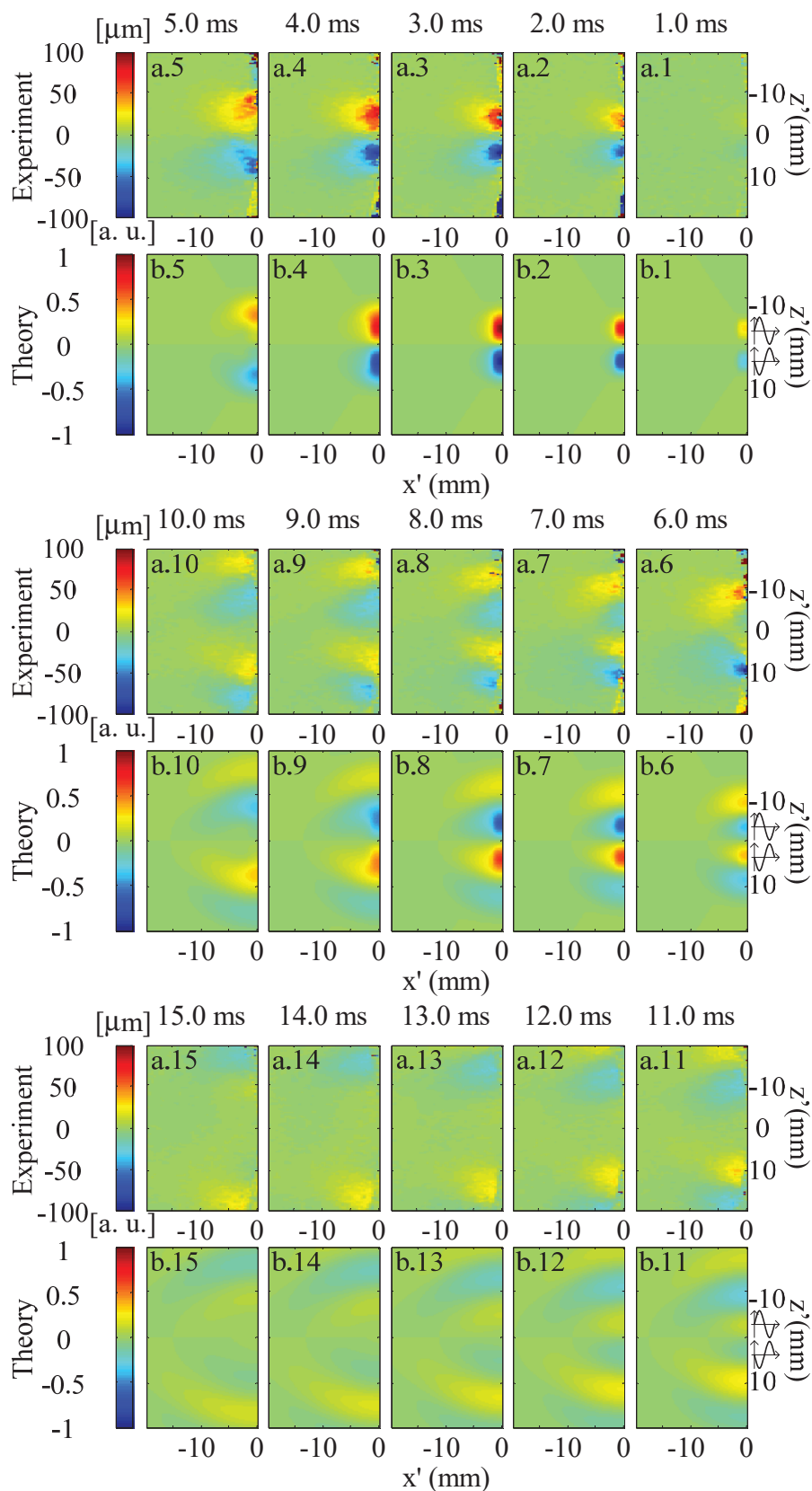


Figure 4.7. The x' component displacement field in the PVA phantom created by experiment (a.1-15) and by theoretical calculation using the Green function method (b.1-15) at 1-15 ms after the trigger of the transient magnetic field. (Sun *et al.* to be submitted)

component displacement in the medium using the analytical Green function (4.14) (Aki and Richards 2002, Grasland-Mongrain *et al* 2014) at 1-15 ms after the trigger of the force is done and shown in Figure 4.7 (bottom row). Comparison of each pair of displacement fields - by experiment and by theory - shows the experiment results agree qualitatively well with the theory.

4.4.5 Propagation of multiple shear wave sources in multi-shaped agar phantom

The multiple shear wave displacement sources created at the bottom of the multi-shaped agar phantom propagates to other parts of the agar phantom. Figure 4.8.a-r show the longitudinal shear wave displacement in the imaged area of the multi-shaped agar phantom from 2 ms, with a step of 6 ms, to 104 ms after triggering of the Lorentz force. The shear wave displacement field keeps amplitude of several micrometers after successfully penetrating through the layer of bovine muscle and the layer of bovine liver. Reverberations of the shear wave displacements from the phantom boundaries also exist in some of the shear wave displacement fields. These shear wave displacement fields are used to reconstruct the shear wave velocity map in the agar phantom, which is the subject of chapter 5.

4.5 Chapter summary

This chapter studied the Lorentz force that was generated from the transient magnetic field and the shear wave displacement source generated on the surface of the soft media. Under the transient magnetic field, the electrical eddy current was generated in the aluminum ring or patch actuator because of the Faraday's law of electromagnetic induction. At the same time, the eddy current coupled with the orthogonal magnetic field and generates the Lorentz force. The Lorentz forces on the left half and the right half of the aluminum ring or patch constituted a torque, which vibrated the ring or patch. The origin and the frequency and amplitude characteristics of the Lorentz force acting on the aluminum ring were confirmed by measuring the

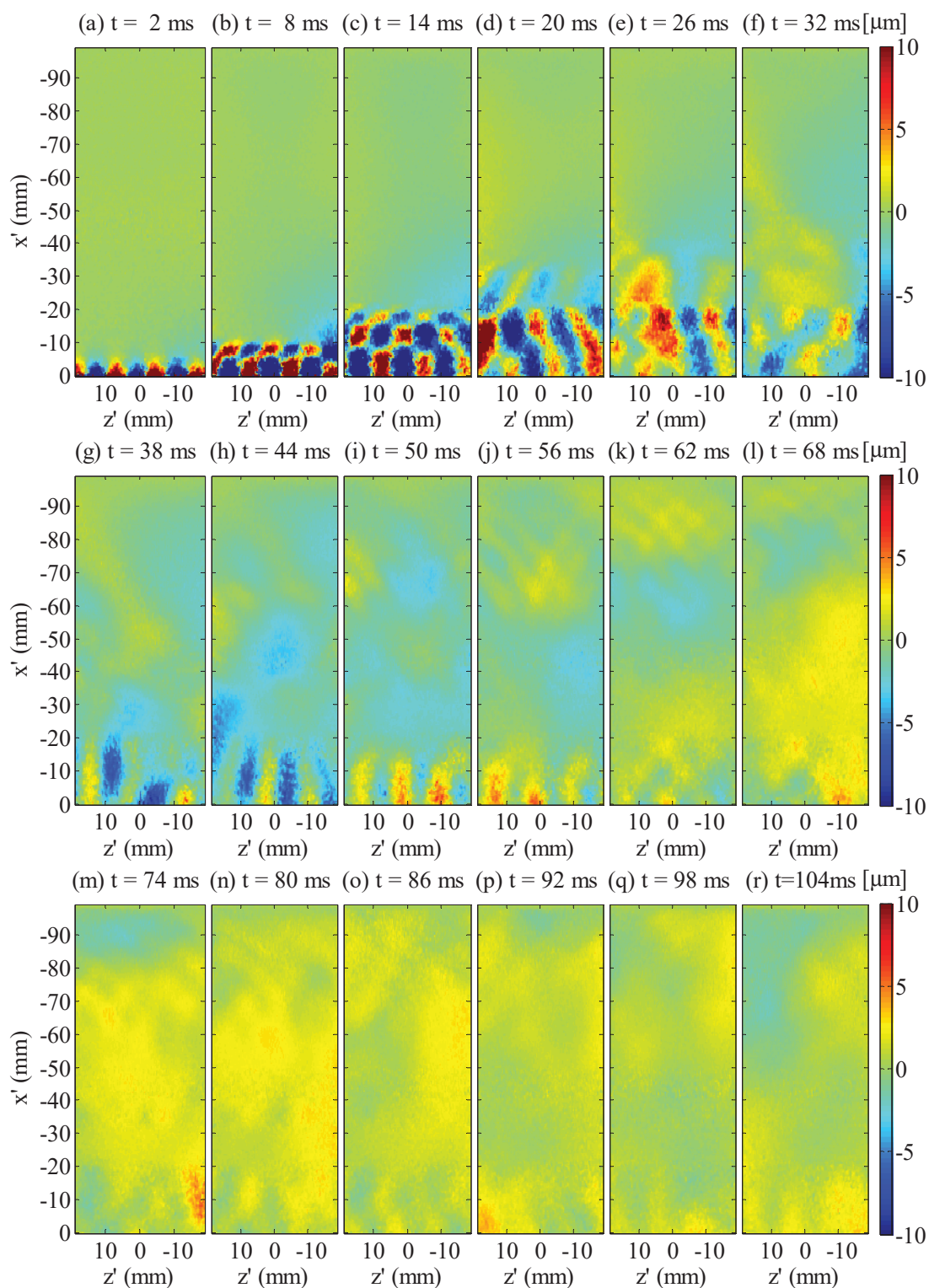


Figure 4.8. The longitudinal shear wave displacement in the imaged area of the multi-shaped agar phantom from 2 ms, with a step of 6 ms, to 104 ms after triggering of the Lorentz force.

displacement of the aluminum ring using an interferometric laser probe. Shear wave displacement source of peak amplitude of $100 \mu\text{m}$ at the target surface was

successfully generated with a transient magnetic field of changing rate of 10.4 kTs^{-1} . And the longitudinal displacement in the PVA phantom by experiment agreed qualitatively well with the theoretical longitudinal displacement calculated by the analytical Green function. Using eight aluminum patches sticking on the phantom surface and the transient magnetic field, multiple shear wave sources were successfully generated at the target surface and propagated towards the interior of the target.

Chapter 5 Ultrasound elastography with the shear wave source generated by vibrating aluminum patches with a transient magnetic field

This chapter presents ultrasound elastography experiments on multi-shaped agar phantoms samples, to investigate the potential of the shear wave displacement fields generated using the method in chapter 4 for ultrasound elastography. First, multiple shear wave displacement sources are generated on the surface of the multi-shaped agar phantoms by stimulating an array of aluminum patches with a transient magnetic field. Then, the target area is repeatedly imaged through the method of ultrafast ultrasound imaging, and the longitudinal displacements of the phantom medium, mainly the propagating shear wave displacement fields, are calculated using the speckle tracking algorithm. Finally, the shear wave velocities in the target area are calculated using the cross-correlation-based approach. Through the elastography experiments, we aim to answer the following questions: (1) from the shear wave velocity map reconstructed, is it possible to differentiate layers in layered targets having different stiffness in each layer? (2) from the shear wave velocity map reconstructed, is it possible to differentiate inclusions having different stiffness from the background part of the phantom sample? and what's the limit in terms of the inclusion's size that can be differentiated from the background? and (3) is it possible to get a quantitative shear wave velocity map, or just relative shear wave velocity difference between areas of different stiffness?

5.1 Elastography experiments on multi-shaped agar phantoms

Elastography experiments with the shear wave displacement fields generated by stimulating an array of aluminum patches with a transient magnetic field is shown in Figure 5.1: (1) generation of shear wave displacement fields and ultrafast ultrasound imaging of the medium inside the target are shown in Figure 5.1.c; and (2) calculation of the displacement fields from the ultrasound images and calculation of the velocity

map from the displacement fields are shown in Figure 5.1.d. The coordinates system is such chosen that the x -axis coincides with the coil axis, the z -axis is horizontal and the yz plane contains the left opening of the coil, as shown in Figure 5.1.c. During experiments, the aluminum patches stick on the front surface of the sample and the

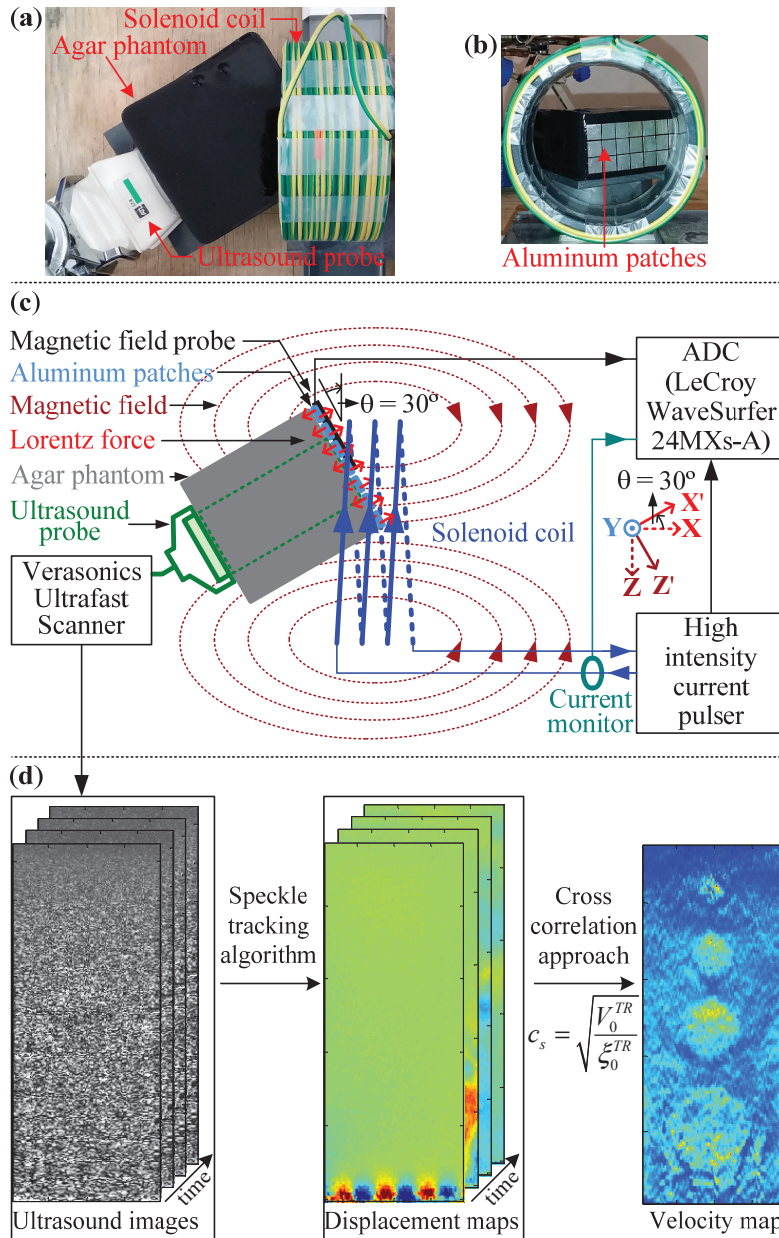


Figure 5.1. Photo (a) and schematic (c) (top side view) of ultrasound ultrafast imaging of the multi-shaped agar phantom, where the shear wave displacement fields are generated by an arrangement of aluminum patches (b) (lateral side view) under the stimulation of the transient magnetic field. (d) Computation of the shear wave displacement fields from the ultrasound images and computation of the shear wave velocity map from the displacement fields. (Sun *et al.* to be submitted)

ultrasound probe was placed on the opposite surface to image the medium inside (Figure 5.1.b). The plane containing the patches' surfaces - the $yo'z'$ plane - has an angle of 30 degrees with respect to the $yo'z$ plane to increase the intensity of the Lorentz force generated on the aluminum patches.

5.1.1 The transient pulsed magnetic field and the aluminum patches actuators

As in section 4.2, the time-varying magnetic field is generated by outputting a sinusoidal electrical current pulse to a solenoid coil (Polson et al 1982, Barker *et al.* 1985). The homemade solenoid coil used in experiments has a diameter of 11.7 cm, a length of 5 cm and was made from 39 turns of copper wire of cross-section area of 0.75 mm^2 . These 39 turns are wound into two layers - the inner layer has 20 turns and the outer layer has 19 turns. And the wire jumps from the inner layer to the outer layer in a manner like 'Z'. The solenoid coil has an inductance of $173 \mu\text{H}$ and can generate a quasi-sinusoidal electrical current pulse of carrier frequency of 5.341 kHz. The current to the coil is measured by a current monitor (Current Monitor Model 110A, Pearson Electronics, CA, USA). The transient magnetic field generated by the solenoid coil is measured using a 3D magnetic field probe (MagProbe 3D, MagVenture, Farum, Denmark). During experiments, the peak amplitude of the electrical current to the coil reaches 947.7 A; the peak changing rate of the x' component of the transient magnetic field ($\partial B_{x'}(t)/\partial t$) reaches 10.3 kTs^{-1} ; and the z' component of the transient magnetic field ($B_{z'}(t)$) reaches a peak of 238.6 mT (Figure 5.2). Aluminum patches of thickness of 0.5 mm and of different sizes - $10 \text{ mm} \times 10 \text{ mm}$, $15 \text{ mm} \times 10 \text{ mm}$, or $15 \text{ mm} \times 7.5 \text{ mm}$ - stick onto the surface of the target and serve as the actuators. Six different arrangements of aluminum patches are independently tried (Figure 5.3).

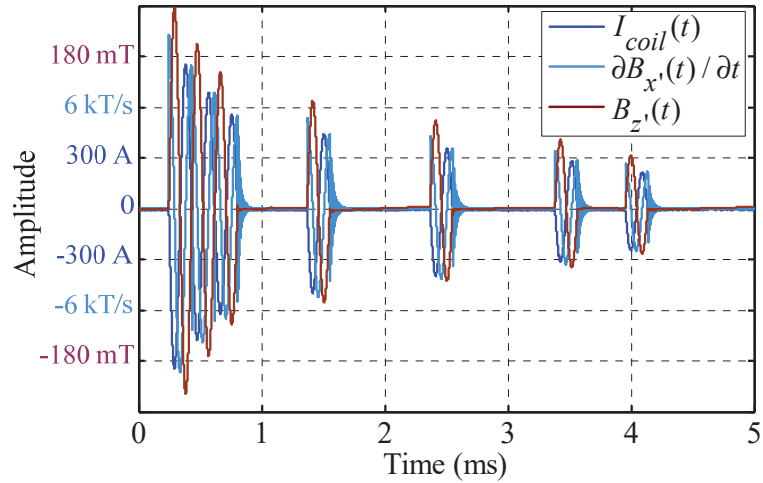


Figure 5.2. The waveforms of the coil current ($I_{coil}(t)$), the changing rate of the x' component of the transient magnetic field ($\partial B_{x'}(t)/\partial t$) and the z' component of the transient magnetic field ($B_{z'}(t)$) at $(0, 0, -2 \text{ cm})$ (x', y, z'). (Sun *et al.* to be submitted)

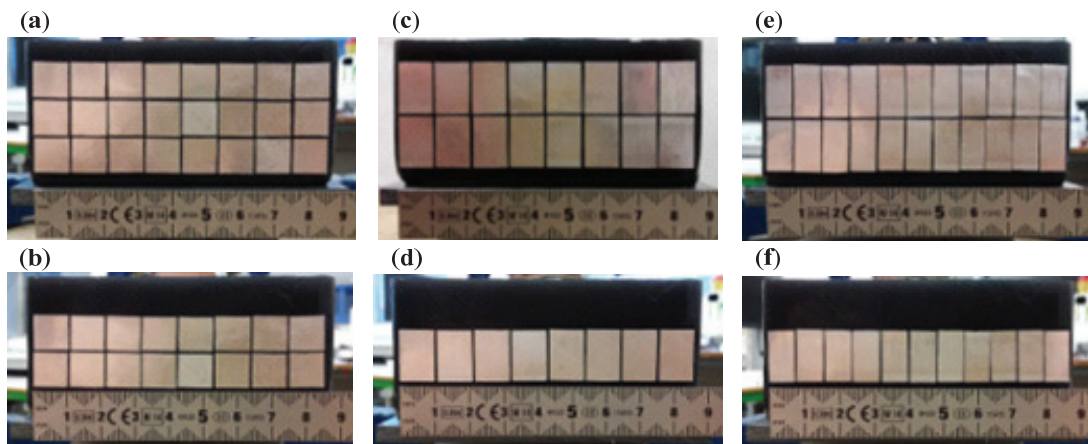


Figure 5.3. Different arrangements of aluminum patches independently stick onto the front surface of the agar phantom: (a) 24 patches of $10 \text{ mm} \times 10 \text{ mm}$ ($y \times z'$) in horizontally three rows; (b) 16 patches of $10 \text{ mm} \times 10 \text{ mm}$ ($y \times z'$) in horizontally two rows; (c) 16 patches of $15 \text{ mm} \times 10 \text{ mm}$ ($y \times z'$) in horizontally two rows; (d) 8 patches of $15 \text{ mm} \times 10 \text{ mm}$ ($y \times z'$) in horizontally one row; (e) 22 patches of $15 \text{ mm} \times 7.5 \text{ mm}$ ($y \times z'$) in horizontally two rows; and (f) 11 patches of $15 \text{ mm} \times 7.5 \text{ mm}$ ($y \times z'$) in horizontally one row. (Sun *et al.* to be submitted)

5.1.2 Ultrafast ultrasound imaging and calculation of the shear wave displacement fields

To track the shear wave propagation inside the sample, the sample is first imaged

using ultrafast ultrasound imaging with a 38 mm linear array ultrasound transducer (PHILIPS, ATL L7-4) and a scanner (Verasonics Vantage 256TM, Washington, USA), which works with the depth set to 10 cm and at a frame rate of 1000 frames per second.

The x' component displacement of the medium is calculated by performing cross correlation - the speckle tracking technique - on the ultrasound images acquired by the Verasonics ultrasound scanner (Sandrin *et al.* 2002) (Figure 5.1.c).

5.1.3 Shear wave velocity reconstruction using the cross-correlation-based approach

The generalized time reversal (TR) field of any field $\phi(\mathbf{r}, t)$ is (Catheline *et al.* 2013):

$$\Psi^{TR}(\mathbf{r}_0, \mathbf{r}, t) = \phi(\mathbf{r}_0, -t) \underset{t}{\otimes} \phi(\mathbf{r}, t) \quad (5.1)$$

The TRs of the strain, i.e. the gradient of the displacement field $\varepsilon_z = \partial\phi/\partial z$, and of the velocity, i.e. the time derivative of the displacement $v = \partial\phi/\partial t$ are:

$$\begin{cases} \xi^{TR}(\mathbf{r}_0, \mathbf{r}, t) = \varepsilon_z(\mathbf{r}_0, -t) \underset{t}{\otimes} \varepsilon_z(\mathbf{r}, t) \\ V^{TR}(\mathbf{r}_0, \mathbf{r}, t) = v(\mathbf{r}_0, -t) \underset{t}{\otimes} v(\mathbf{r}, t) \end{cases} \quad (5.2)$$

where ξ^{TR} is the time reversal strain field and V^{TR} is the time reversal velocity field.

For the plane wave at a given center frequency - $\phi(\mathbf{r}, t) = e^{i(kz - \omega t)}$, where k is the wave number and ω is the angular frequency - in an ideal isotropic diffuse field, approximations of the strain $\varepsilon_z \approx ik\phi$ and the velocity $v \approx -i\omega\phi$ are got. Therefore, (5.2) arrives at (5.3).

$$\begin{cases} \xi^{TR} \approx -k^2 \Psi^{TR} \\ V^{TR} \approx -\omega^2 \Psi^{TR} \end{cases} \quad (5.3)$$

The shear wave speed c_S can be estimated according to the classical relationship $c = \omega/k$, with the TRs in (5.3) on one single spatio-temporal point, i.e. the source at the focus time $t = 0$ s.

$$c_S = \frac{\omega}{k} = \sqrt{\frac{V_0^{TR}}{\xi_0^{TR}}} \quad (5.4)$$

where ξ_0^{TR} represents $\xi^{TR}(\mathbf{r}_0, \mathbf{r}_0, t = 0)$ and V_0^{TR} represents $V^{TR}(\mathbf{r}_0, \mathbf{r}_0, t = 0)$.

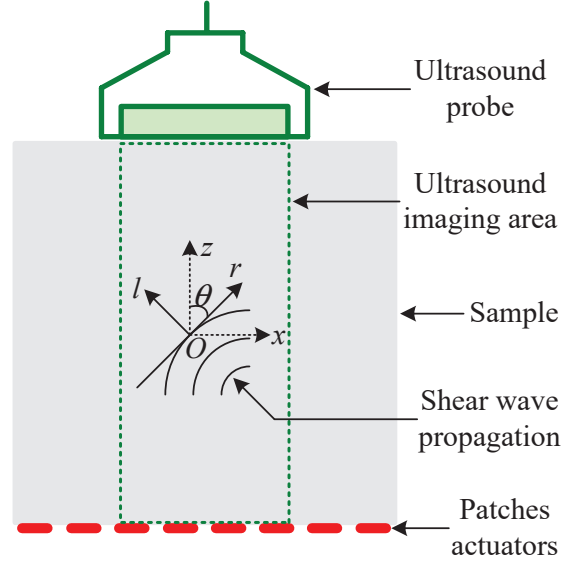


Figure 5.4. Schematic of shear wave displacement propagation in the sample: the shear wave displacement ϕ at point O moves in direction r and propagates along l . (Sun *et al.* to be submitted)

Figure 5.4 shows the schematic of shear wave displacement propagation in the sample. To calculate the shear wave velocity, we need to calculate the strain $\varepsilon_l = \partial\phi/\partial l$, and the velocity $v = \partial\phi/\partial t$.

$$\begin{cases} \varepsilon_l = \frac{\partial\phi}{\partial l} \\ v = \frac{\partial\phi}{\partial t} \end{cases} \quad (5.5)$$

We multiply $\cos(\theta)$ to the right side of (5.5) (θ is the angle between z and r in Figure 5.4) so that we can use the displacement computed from the sonograms:

$$\begin{cases} \varepsilon'_l = \varepsilon_l \cos(\theta) = \frac{\partial\phi}{\partial l} \cos(\theta) = \frac{\partial\phi_z}{\partial l} = \frac{\partial\phi_z}{\partial z} \sin(\theta) - \frac{\partial\phi_z}{\partial x} \cos(\theta) \\ v' = v \cos(\theta) = \frac{\partial\phi}{\partial t} \cos(\theta) = \frac{\partial\phi_z}{\partial t} \end{cases} \quad (5.6)$$

where ϕ_z is the z component of the displacement ϕ and can be computed from the sonograms using the speckle tracking technique.

Therefore, we can get:

$$\begin{cases} \xi'^{TR}(\mathbf{r}_0, \mathbf{r}, t) = \varepsilon'_z(\mathbf{r}_0, -t) \otimes \varepsilon'_z(\mathbf{r}, t) = \cos^2(\theta) \xi^{TR}(\mathbf{r}_0, \mathbf{r}, t) \\ V'^{TR}(\mathbf{r}_0, \mathbf{r}, t) = v'^{(\mathbf{r}_0, -t)} \otimes v'^{(\mathbf{r}, t)} = \cos^2(\theta) V^{TR}(\mathbf{r}_0, \mathbf{r}, t) \end{cases} \quad (5.7)$$

And, we can get c_s as:

$$c_s = \sqrt{\frac{V_0^{TR}}{\xi_0^{TR}}} = \sqrt{\frac{V_0'^{TR}}{\xi_0'^{TR}}} \quad (5.8)$$

The problem with Equation (5.8) is that, in the real experiment, the angle θ in (5.6) for the calculation of ε' and ν' is unknown and is not constant for the same point. Instead, in experiments, we use the following approximation to get ε' and ν' :

$$\begin{cases} \varepsilon'_l \approx \frac{\partial \phi_z}{\partial z} \\ \nu' \approx \frac{\partial \phi_z}{\partial t} \end{cases} \quad (5.9)$$

The problem for this choice is that the shear wave velocity finally calculated is not accurate. But the experiment results show that we still can get a relative shear wave velocity map using the approximation.

Another approach using the exact Green's function brings some minor corrective terms to equation 5.8 since it uses a scalar wave approximation. The exact expression of speed reconstruction should be reported in a forthcoming paper (Zorgani *et al.* Under review).

5.1.4 Five samples of multi-shaped agar phantoms

The samples used in our experiments are multi-shaped phantoms made from agar powder, graphite powder and water. For the agar phantoms, the quantity of the graphite powder used is 0.5 wt%, while that of agar powder varies according to the stiffness of the agar phantoms. The agar phantom is made by heating the pure water to the boil, adding the agar powder, stirring and heating the mixture to the boil again, cooling the hot mixture down, and adding the graphite powder. When the hot liquid agar phantom cools down to around 40 degrees Celsius, it is degassed for about 5 minutes inside a jar of ultra-low atmospheric pressure. From the beginning of heating the pure water until the end of degassing, the mixture is stirred by a bar magnet and a magnetic force agitator to make the liquid mixture to be homogeneous. After degassing, the liquid agar phantom is poured into a square plastic cabin, which is then kept in a refrigerator of 5 degrees Celsius for more than 2 hours. Five different agar phantoms made in this way are used. Each agar phantom has dimensions of 90 mm×45 mm×90 mm (X'×Y×Z').

The first multi-shaped agar phantom consists of three layers, and each layer is cut from one independent agar phantom of dimensions of 90 mm×45 mm×90 mm

($X \times Y \times Z$). The quantities of the agar powder used in the three layers are respectively 0.6 wt%, 0.8 wt% and 1.0 wt%. Figure 5.5.b and e show the dimensions of the agar phantom. The three-layer agar phantom is built by joining the three layers together. When attaching one layer to another layer of the agar phantom, the base layer is kept fixed while the layer to be added is attached by slipping from one end to the other end of the sloping interface. The three layers are joined in this way to prevent bubbles coming between the contacting sloping interfaces. Figure 5.5.a and d are the photos of agar phantom made in this way. Because the quantities of graphite powder used for the three layer are the same (0.5 wt%), there is no difference in the ultrasound images (Figure 5.5.c and f) between the three layers, although the three layers are different in stiffness.

The second agar phantom contains a homogeneous soft background part and four cylinder stiff inclusions of diameters of 5 mm, 10 mm, 15 mm and 20 mm respectively. The quantity of agar powder used for the background part is 0.6 wt% while that for the four inclusions is 1.0 wt%. Figure 5.6.b and e show the dimensions of the agar phantom. The homogeneous background part with four cylinder holes of diameters of 5 mm, 10 mm, 15 mm and 20 mm is first made by inserting four tubes of diameters of 5 mm, 10 mm, 15 mm and 20 mm made from aluminum foil paper into the liquid agar phantom and removing the cylinder phantom inside the tubes when the agar phantom becomes solid. Four cylinder inclusions are then added by pouring the degassed liquid agar phantom of 1.0 wt% of agar powder into the cylinder holes of the background part of the agar phantom. Figure 5.6.a and d are the photos of agar phantom made in this way. Because the quantities of graphite powder used for the background part and the four inclusions are the same (0.5 wt%), there is no difference in the ultrasound images (Figure 5.6.c and f) between the background part and the inclusions, although the inclusions are stiffer than the background part.

The third agar phantom has the same dimensions as the second one. But the third agar phantom has a stiff homogeneous background part of 1.0 wt% of agar powder and four soft cylinder inclusions of 0.6 wt% of agar powder. Figure 5.7.b and e show the dimensions of the agar phantom. The background part is made and the four

inclusions are added in the same way as those for the second agar phantom. Figure 5.7.a and d are the photos of agar phantom made in this way. Because the quantities of graphite powder used for the background part and the four inclusions are the same (0.5 wt%), there is no difference in the ultrasound images (Figure 5.7.c and f) between the background part and the inclusions, although the inclusions are softer than the background part.

The fourth agar phantom consists of a soft homogeneous background part having 0.6 wt% of agar powder and nine cylinder inclusions of same diameter of 10 mm. The nine inclusions are divided into three columns. The three inclusions in each column are made with the same quantity of agar powder while inclusions from different columns have different quantity of agar powder - the inclusions in the left, the middle and the right columns have respectively 0.9 wt%, 1.2 wt% and 1.5 wt% of agar powder. Figure 5.8.b and e show the dimensions of the agar phantom. The homogeneous background part and the nine inclusions are made in the similar way as for the second and the third agar phantoms. Figure 5.8.a and d are the photos of agar phantom made in this way. Because the quantities of graphite powder used for the background part and the nine inclusions are the same (0.5 wt%), there is no difference in the ultrasound images (Figure 5.8.c and f) between the background part and the three columns of inclusions, although the inclusions are stiffer than the background part.

The fifth agar phantom contains a homogeneous agar phantom background part having 0.6 wt% of agar powder and 0.5 wt% of graphite powder, one piece of bovine muscle and one piece of bovine liver. Figure 5.9.c and g show the dimensions of the agar phantom. The bovine muscle and liver are degassed and hung vertically inside a plastic square box (Figure 5.9.a and e). And then the degassed liquid agar phantom for the background part is poured into the plastic box. The phantom is ready when it cools down to the room temperature and becomes solid. Figure 5.9.b and f are the photos of agar phantom made in this way. It's the same agar phantom as the one used in the second experiment of section 4.3.2. From the ultrasound images (Figure 5.8.d and h), the two layers of bovine liver and muscle are clearly differentiated from the agar

phantom background.

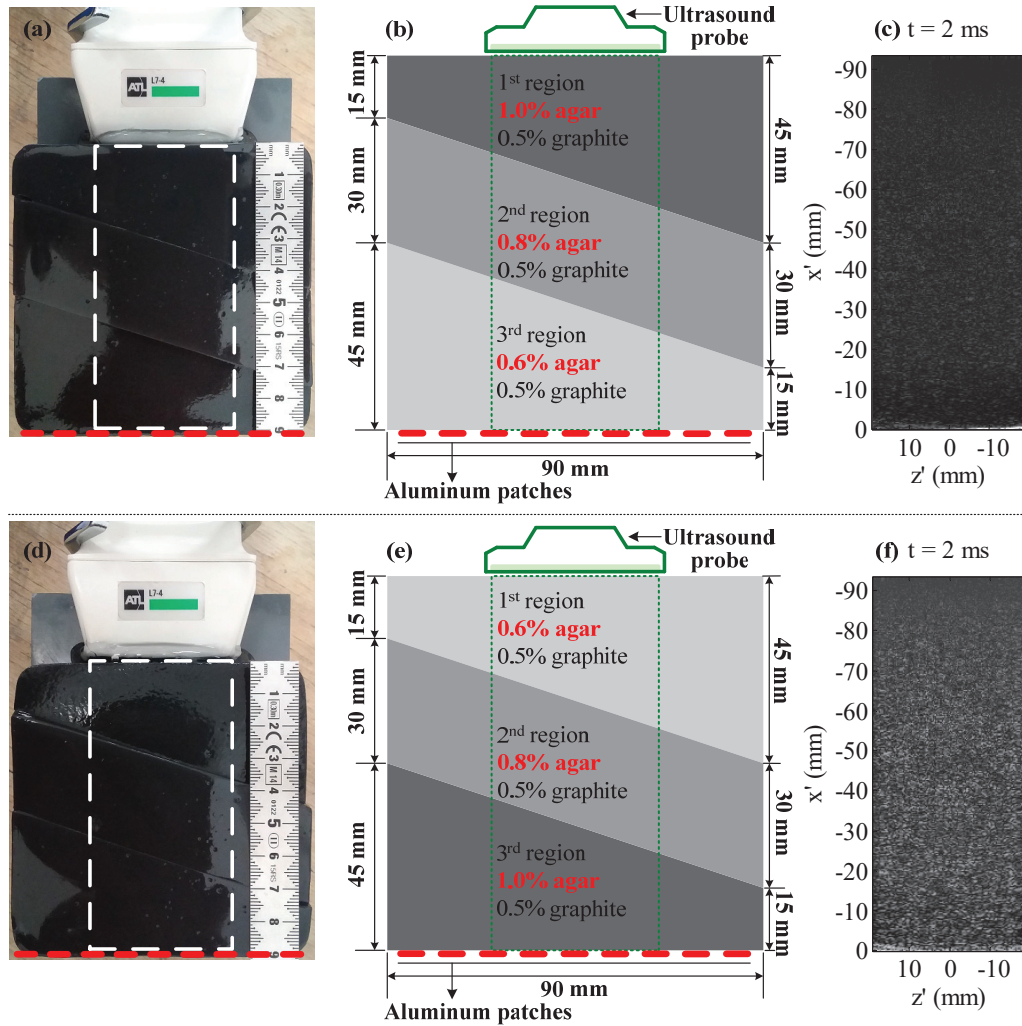


Figure 5.5. The 3-layer agar phantom (Sun *et al.* to be submitted). (a) The ultrasound array transducer is placed on the surface of the stiffest layer while the aluminum patches stick on the surface of the softest layer. The white dotted rectangle marks the imaging area by the linear array transducer. (b) The dimensions of the whole agar phantom and those of each layer. The first, the second, and the third layers have respectively 1.0 wt%, 0.8 wt%, and 0.6 wt% of agar powder. The green dotted rectangle marks the imaging area by the linear array transducer. The ultrasound imaging area is divided into three regions from the three layers. (c) The ultrasound image of the agar phantom at 2 ms after the trigger of the Lorentz force is shown, in which the interfaces between the neighboring layers are completely hidden. (d), (e), and (f) are the corresponding figures of (a), (b), and (c) when the agar phantom is inverted back to front.

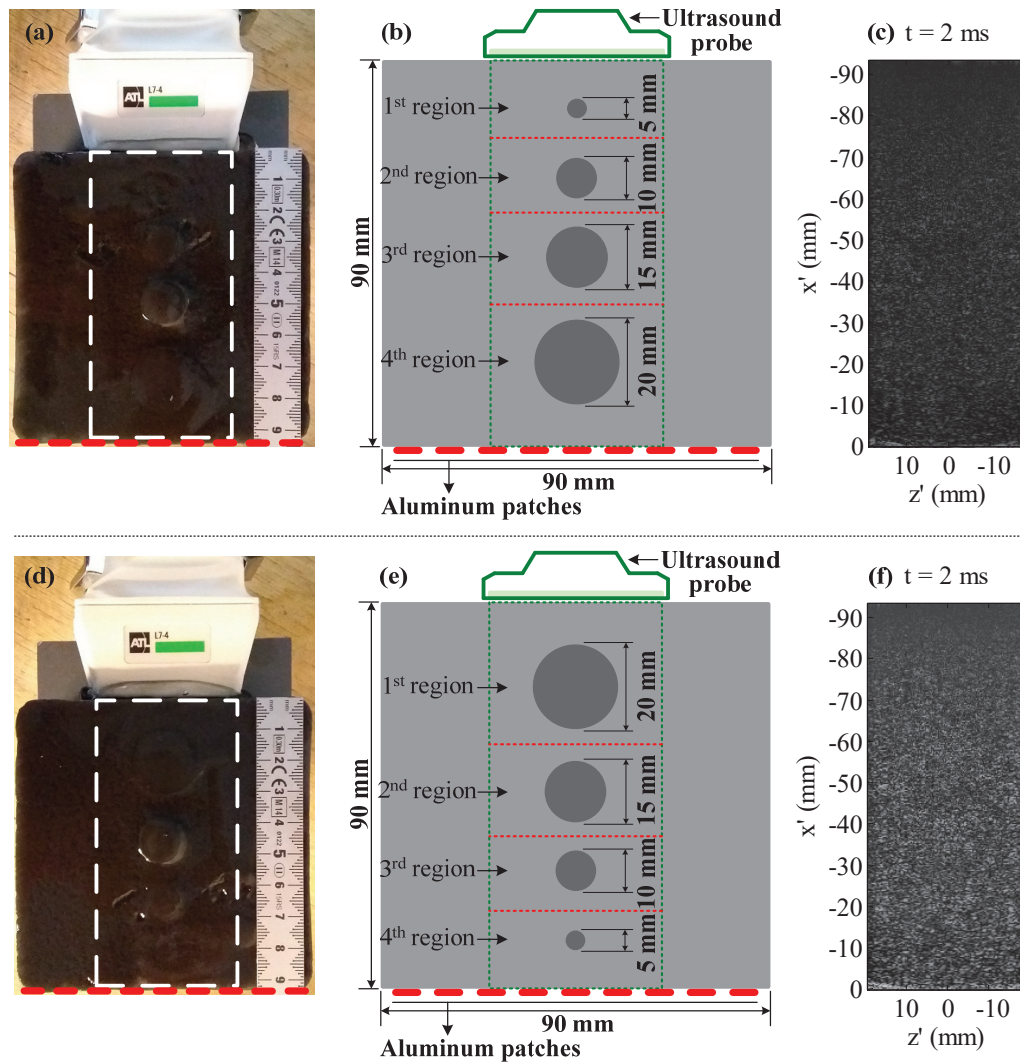


Figure 5.6 The agar phantom sample has a soft background part and four stiff cylinder inclusions (Sun *et al.* to be submitted). (a) The ultrasound array transducer is placed on the surface close to the smallest inclusion while the aluminum patches stick on the opposite surface of the phantom sample. The white dotted rectangle marks the imaging area by the linear array transducer. (b) The dimensions of the whole agar phantom and those of the four inclusions. The green dotted rectangle marks the imaging area by the linear array transducer. The background part and four inclusions have respectively 0.6 wt% and 1.0 wt% of agar powder. The ultrasound imaging area is divided into four regions (separated by the red lines) and each region contains one inclusion. (c) The ultrasound image of the phantom sample at 2 ms after the trigger of the Lorentz force is shown, in which the inclusions' boundaries are completely hidden. (d), (e), and (f) are the corresponding figures of (a), (b), and (c) when the agar phantom is inverted back to front.

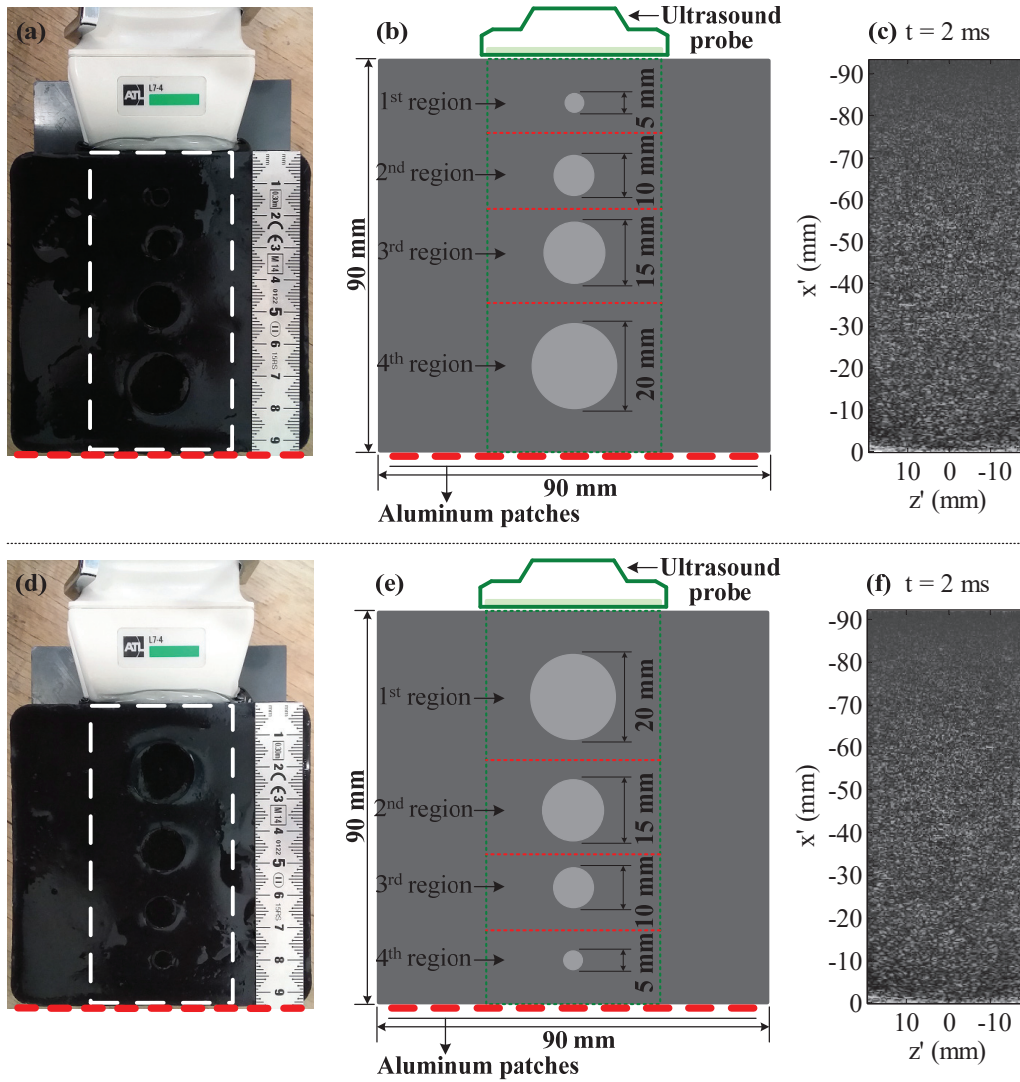


Figure 5.7. The agar phantom sample has a stiff background part and four soft cylinder inclusions (Sun *et al.* to be submitted). (a) The ultrasound array transducer is placed on the surface close to the smallest inclusion while the aluminum patches stick on the opposite surface of the phantom sample. The white dotted rectangle marks the imaging area by the linear array transducer. (b) The dimensions of the whole agar phantom and those of the four inclusions. The green dotted rectangle marks the imaging area by the linear array transducer. The background part and four inclusions have respectively 1.0 wt% and 0.6 wt% of agar powder. The ultrasound imaging area is divided into four regions (separated by the red lines) and each region contains one inclusion. (c) The ultrasound image of the agar phantom at 2 ms after the trigger of the Lorentz force is shown, in which the inclusions' boundaries are completely hidden. (d), (e), and (f) are the corresponding figures of (a), (b), and (c) when the agar phantom is inverted back to front.

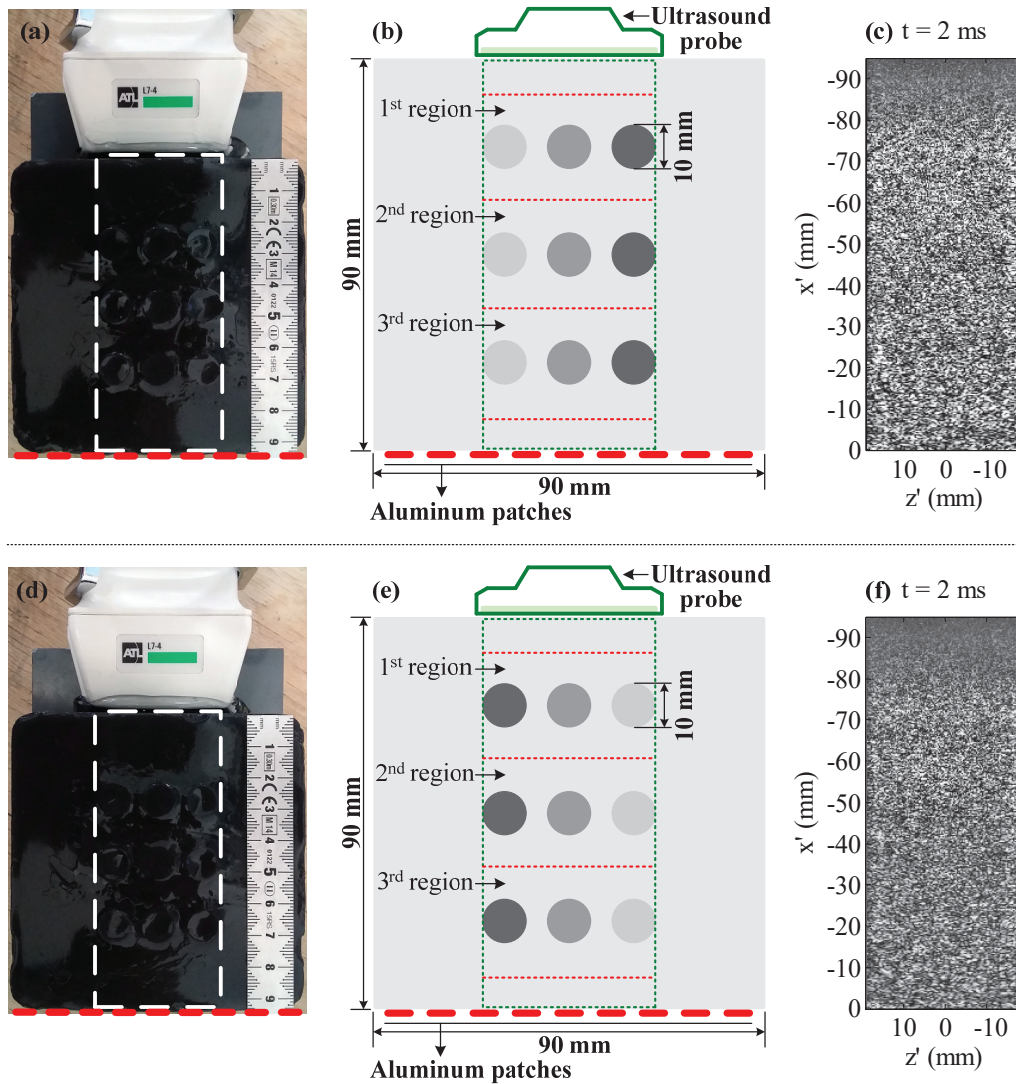


Figure 5.8. The agar phantom sample has a soft background part and nine stiff cylinder inclusions (Sun *et al.* to be submitted). (a) The agar phantom is such placed that the stiffest inclusions belong to the left column. The background part and three columns of inclusions - from left to right - have respectively 0.6 wt%, 0.9 wt%, 1.2 wt%, and 1.5 wt% of agar powder. The ultrasound array transducer is placed on the back surface while the aluminum patches stick on front surface of the phantom sample. The white dotted rectangle marks the imaging area by the linear array transducer. (b) The dimensions of the whole agar phantom and those of the nine inclusions. The green dotted rectangle marks the imaging area by the linear array transducer. The ultrasound imaging area is divided into three regions (separated by the red lines) and each region contains three inclusions - one inclusion from each column. (c) The ultrasound image of the agar phantom at 2 ms after the trigger of the Lorentz force is shown, in which the inclusions' boundaries are completely hidden. (d), (e), and (f) are the corresponding figures of (a), (b), and (c) when the agar phantom is inverted back to front.

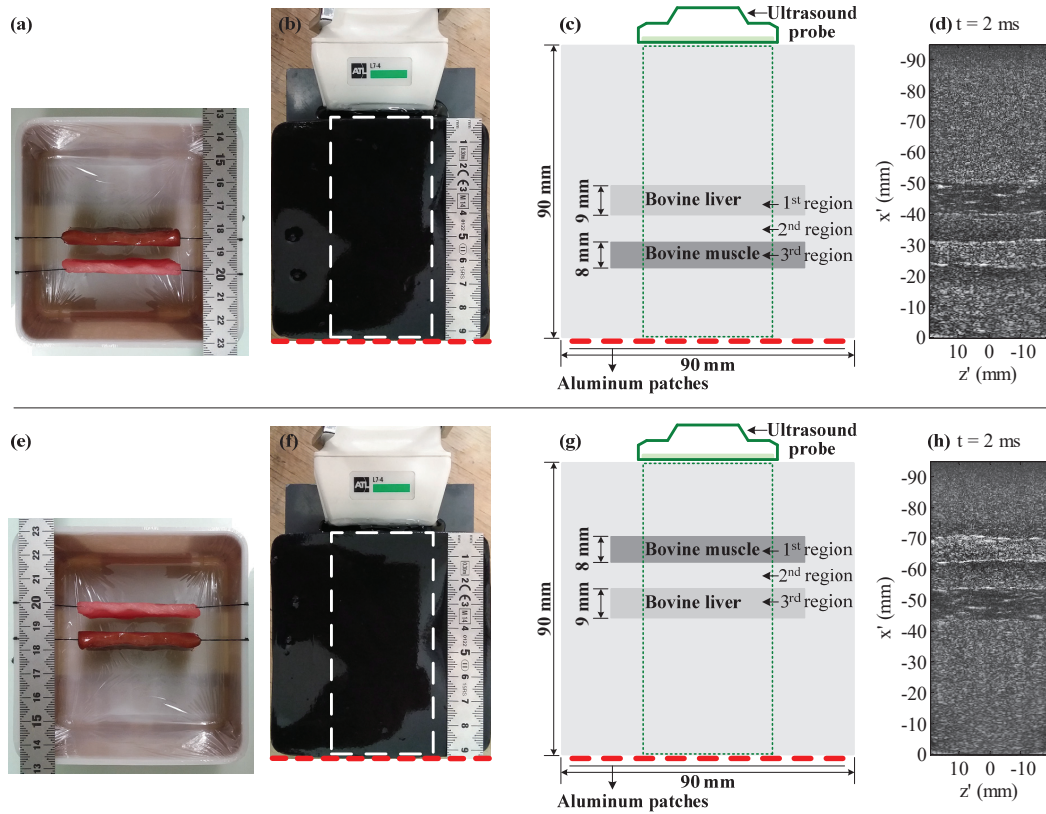


Figure 5.9. The agar phantom sample has a soft background part and one layer of bovine liver and one layer of bovine muscle (Sun *et al.* to be submitted). (a) Two layers of degassed bovine liver and muscle hung vertical in a square plastic box. (b) The ultrasound array transducer is placed on the surface far from the bovine liver and muscle while the aluminum patches stick on the opposite surface of the phantom sample. The white dotted rectangle marks the imaging area by the linear array transducer. (c) The dimensions of the whole agar phantom and those of the layers of bovine liver and muscle. The background part has 0.6 wt% of agar powder and 0.5 wt% of graphite powder. The green dotted rectangle marks the imaging area by the linear array transducer. Three regions are marked: the first region contains the bovine liver; the second region contains the layer of agar phantom between the bovine liver and the bovine muscle; and the third region contains the bovine muscle. (d) The ultrasound image of the agar phantom at 2 ms after the trigger of the Lorentz force is shown, from which those two layers of bovine liver and muscle can be recognized clearly. (e), (f), (g), and (h) are the corresponding figures of (a), (b), (c), and (d) when the agar phantom is inverted back to front.

5.1.5 Three groups of ultrasound elastography experiments

Three groups of ultrasound elastography experiments are done on the five

multi-shaped agar phantoms samples, to investigate the potential of the shear wave displacement fields generated by stimulating the aluminum patches with a transient magnetic field for shear wave velocity reconstruction. For experiments done with each multi-shaped agar phantom, the experiments are done first with the ultrasound array transducer placed on one side surface of the agar phantom sample and the aluminum patches sticking on the opposite surface, as in Figures 5.5-8.a and Figure 5.9.b. The experiments are done with the shear wave sources generated independently by stimulating each of the six arrangements of aluminum patches (Figure 5.3) with the transient magnetic field. Once the aluminum patches actuators create the displacement in the agar phantom sample, the Verasonics ultrafast ultrasound scanner repeatedly images the longitudinal displacement field in the agar phantom for 100 ms with a sampling rate of 1000 frames/s. And then the phantom is inverted back to front, and the same experiments are performed again, as shown in Figures 5.5-8.d and Figure 5.9.f. The shear wave velocity maps are computed from the 100 frames of shear wave displacement fields, which are computed from the 100 frames of ultrasound images.

(1) The purpose of the first group of experiments is to confirm the feasibility of differentiating neighboring layers of different stiffness from the velocity map, which is computed from the shear wave displacement fields generated by the method in chapter 4. The group of experiments uses the first agar phantom as the sample (Figure 5.5.a and d).

(2) The purposes of the second group of experiments are: (1) to verify the feasibility of differentiating cylinder inclusions from the velocity map computed from the shear wave displacement fields generated through the method in chapter 4; (2) to probe the minimum dimension of the inclusion that can be differentiated from the velocity map. The group of experiments uses the second (Figure 5.6.a and d) and the third (Figure 5.7.a and d) multi-shaped agar phantoms independently as the samples.

(3) The purpose of the third group of experiments is to confirm the feasibility of obtaining a qualitative shear wave velocity map from the shear wave displacements fields generated through the method developed in chapter 4. The group of experiments uses the fourth (Figure 5.8.a and d) and the fifth (Figure 5.9.b and f)

multi-shaped agar phantoms independently as the samples.

5.1.6 The control experiment - generation of shear waves using a mechanical actuator

Control elastography experiments using a mechanical actuator (LDS V201, Brüel & Kjær, Nærum, Denmark) (Figure 5.10.a,b) are done on each of the five multi-shaped agar phantoms samples in section 5.1.4. A sinusoidal pulse of 500 Hz and 500 mVpp (milli-volts peak to peak) from a generator (AFG3102, Tektronix, OR, USA) is first amplified 20 dB by a power amplifier (Type 2718, Brüel & Kjær, Nærum, Denmark) and then fed the mechanical actuator. Six plastic cubes (Figure 5.10.c) connecting to the head of the mechanical actuator actuate the front surface of the agar phantom sample and generate the shear wave displacement sources.

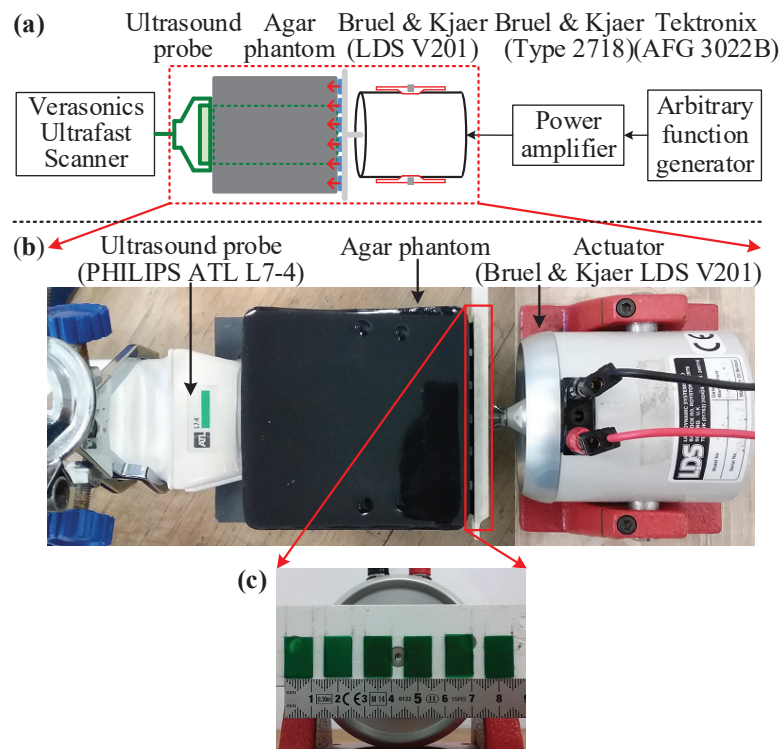


Figure 5.10. Schematic (a) and photo (b) of generation of shear wave displacement fields in a sample using a mechanical actuator. (c) Six plastic cubes connecting to the mechanical actuator generate shear wave displacements at the surface of the sample. (Sun *et al.* to be submitted)

5.2 Results and discussion

5.2.1 Elastography of the 3-layer multi-shaped agar phantom sample

In the first experiment, the ultrasound array transducer is placed on the surface of the stiffest layer and the aluminum patches stick on the opposite surface of the whole agar phantom sample (Figure 5.5.a). Figures 5.11.a.1-7 show the seven velocity maps, which are computed using the shear wave displacement fields generated by the corresponding arrangement of aluminum patches or the mechanical actuator shown in the bottom row of Figure 5.11. The interfaces between the neighboring layers can be clearly recognized from each of the velocity maps, although they are completely hidden in the ultrasound image (Figure 5.5.c). Figures 5.11.b.1-7 show the shear wave velocity along the line $z' = 0$ mm, in each of which we can see the velocity change around $x' = -30$ mm and -60 mm. The average and variation of the shear wave velocity in the region belonging to each layer of the agar phantom are calculated for each velocity map, as shown in Figures 5.11.c.1-7, which shows that: (1) the average velocity in the first (also the stiffest) layer is largest, while that in the third (also the softest) layer is smallest and that in the second layer is in between; (2) the variation of the velocity in the first layer is much larger than those in the second and the third layers.

In the second experiment, the ultrasound array transducer is placed on the surface of the softest layer and the aluminum patches stick on the opposite surface of the whole agar phantom sample (Figure 5.5.d). Figures 5.12.a.1-7 show the seven velocity maps, which are computed using the shear wave displacement fields generated by the corresponding arrangement of aluminum patches or the mechanical actuator shown in the bottom row of Figure 5.12. The interfaces between the neighboring layers can be recognized from each of the velocity maps, although they are completely hidden in the ultrasound image (Figure 5.5.f). Figures 5.12.b.1-7 show the shear wave velocity along the line $z' = 0$ mm, in each of which we can see the velocity change around $x' = -30$ mm and -60 mm. The average and variation of the shear wave velocity in the region belonging to each layer of the agar phantom are

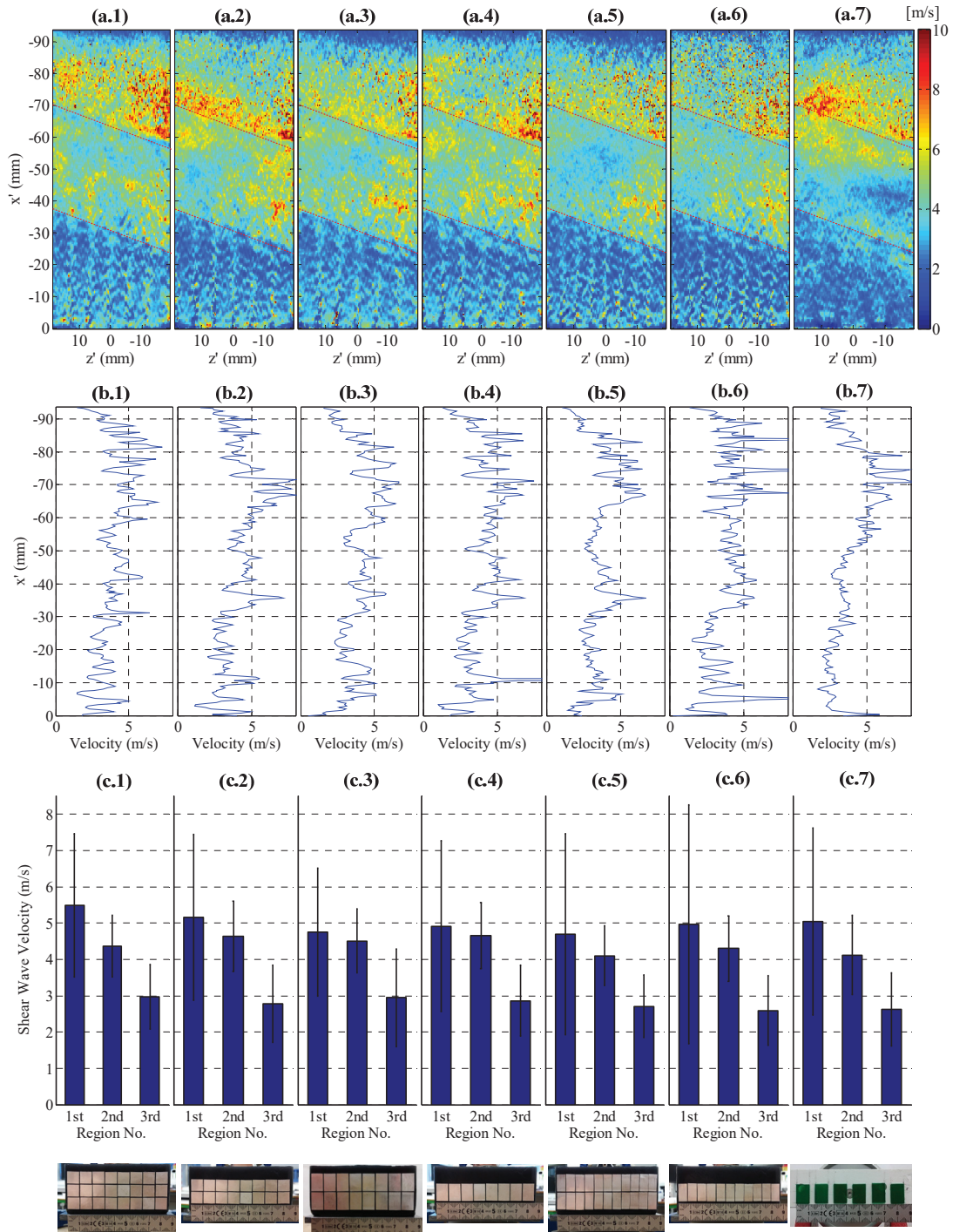


Figure 5.11. (a.1-7) The velocity maps computed from the shear wave displacement fields generated by the corresponding arrangement of aluminum patches or the mechanical actuator (see the bottom line of the figure). (b.1-7) The velocities along the line $z' = 0$ mm in each figure of (a.1-7). (c.1-7) The averages and variations of the shear wave velocity for the regions belonging to each layer of the agar phantom sample in figures (a.1-7). (Sun *et al.* to be submitted)

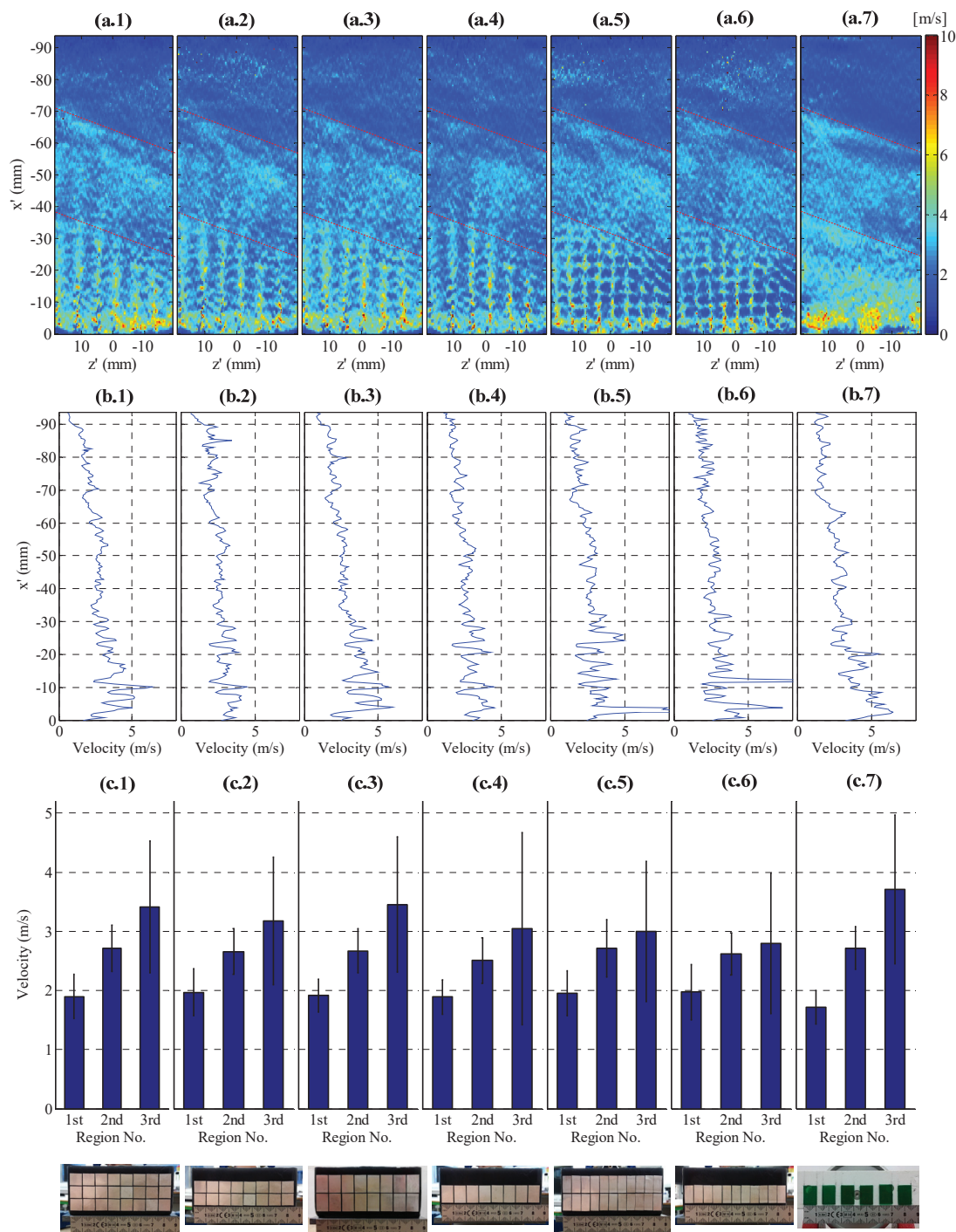


Figure 5.12. (a.1-7) The velocity maps computed from the shear wave displacement fields generated by the corresponding arrangement of aluminum patches or the mechanical actuator (see the bottom line of the figure). (b.1-7) The shear wave velocities along the line $z' = 0$ mm in each figure of (a.1-7). (c.1-7) The averages and variations of the shear wave velocity for the regions belonging to each layer of the agar phantom sample in figures (a.1-7). (Sun *et al.* to be submitted)

calculated for each velocity map, as shown in Figures 5.12.c.1-7, which shows that: (1) the average velocity in the first (also the softest) layer is smallest, while that in the third (also the stiffest) layer is largest and that in the second layer is in between; (2) the variation of the velocity in the third layer is much smaller than those in the first and the second layers.

5.2.2 Elastography of the multi-shaped agar phantoms samples with four cylinder inclusions

The first and the second experiments use the second agar phantom sample with a soft background part and four stiff cylinder inclusions.

In the first experiment, the ultrasound array transducer is placed on the surface close to the smallest inclusion and the aluminum patches stick on the opposite surface of the agar phantom sample (Figure 5.6.a). Figures 5.13.a.1-7 show the seven velocity maps, which are computed using the shear wave displacement fields generated by the corresponding arrangement of aluminum patches or the mechanical actuator shown in the bottom row of Figure 5.13. The inclusion boundaries can be clearly recognized from each of the velocity maps, although they are completely hidden in the ultrasound image (Figure 5.6.c). Figures 5.13.b.1-7 show the shear wave velocity along the line $z' = 0$ mm, in each of which the widths of the velocity peaks coincide with the diameters of the inclusions. The averages and variations of the shear wave velocity of the inclusion and of the background in each region of the agar phantom are calculated for each velocity map, as shown in Figures 5.13.c.1-7, which shows that, for each of the four regions in the agar phantom: (1) the average velocity in the background part is smaller than that in the corresponding inclusion; (2) the variation of the velocity in the background part is also smaller than that in the corresponding inclusion.

In the second experiment, the ultrasound array transducer is placed on the surface close to the largest inclusion and the aluminum patches stick on the opposite surface of the agar phantom (Figure 5.6.d). Figures 5.14.a.1-7 show the seven velocity maps, which are computed using the shear wave displacement fields generated by the

corresponding arrangement of aluminum patches or the mechanical actuator shown in the bottom row of Figure 5.14. The inclusion boundaries can be clearly recognized from each of the velocity maps, although they are completely hidden in the ultrasound image (Figure 5.6.f). Figures 5.14.b.1-7 show the shear wave velocity along the line $z' = 0$ mm, in each of which the widths of the velocity peaks coincide with the diameters of the inclusions. The averages and variations of the shear wave velocity of the inclusion and of the background in each region of the agar phantom are calculated for each velocity map, as shown in Figures 5.14.c.1-7, which shows that, for each of the four regions in the agar phantom: (1) the average velocity in the background part is smaller than that in the corresponding inclusion; (2) the variation of the velocity in the background part is also smaller than that in the corresponding inclusion.

The third and the fourth experiments use the third agar phantom sample with a stiff background part and four soft cylinder inclusions.

In the third experiment, the ultrasound array transducer is placed on the side surface close to the smallest inclusion and the aluminum patches stick on the opposite side surface of the agar phantom (Figure 5.7.a). Figures 5.15.a.1-7 show the seven velocity maps, which are computed using the shear wave displacement fields generated by the corresponding arrangement of aluminum patches or the mechanical actuator shown at the bottom row of Figure 5.15. The inclusion boundaries can be partly recognized from each of the velocity maps, although they are completely hidden in the ultrasound image (Figure 5.7.a). But at the same time, there are lots of artifacts where the velocity computed is much larger than that of the place having the same stiffness. Figures 5.15.b.1-7 show the shear wave velocity along the line $z' = 0$ mm, in each of which the widths of the velocity troughs coincide with the diameters of the inclusions. The averages and variations of the shear wave velocity of the inclusion and of the background in each region of the agar phantom are calculated for each velocity map, as shown in Figures 5.15.c.1-7, which shows that, for each of the four regions in the agar phantom: (1) the average velocity in the background part is larger than that in the corresponding inclusion; (2) the variation of the velocity in the background part is also larger than that in the corresponding inclusion.

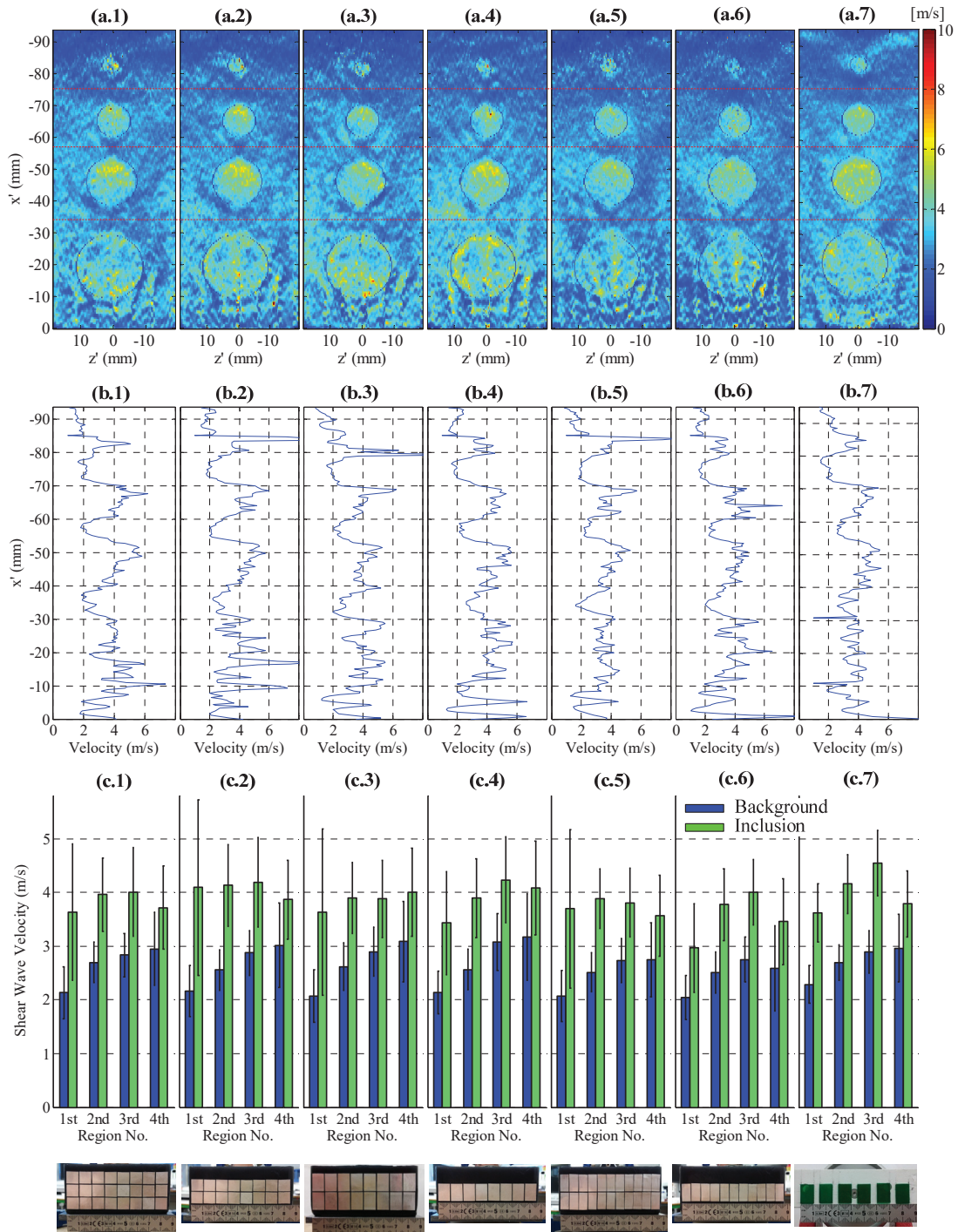


Figure 5.13. (a.1-7) The velocity maps computed from the shear wave displacement fields generated by the corresponding arrangement of aluminum patches or the mechanical actuator (see the bottom line of the figure). (b.1-7) The velocities along the line $z' = 0$ mm in each figure of (a.1-7). (c.1-7) The averages and variations of the velocity of the inclusion (the green bars) and of the background (the blue bars) in each region of the agar phantom sample in figures (a.1-7). (Sun *et al.* to be submitted)

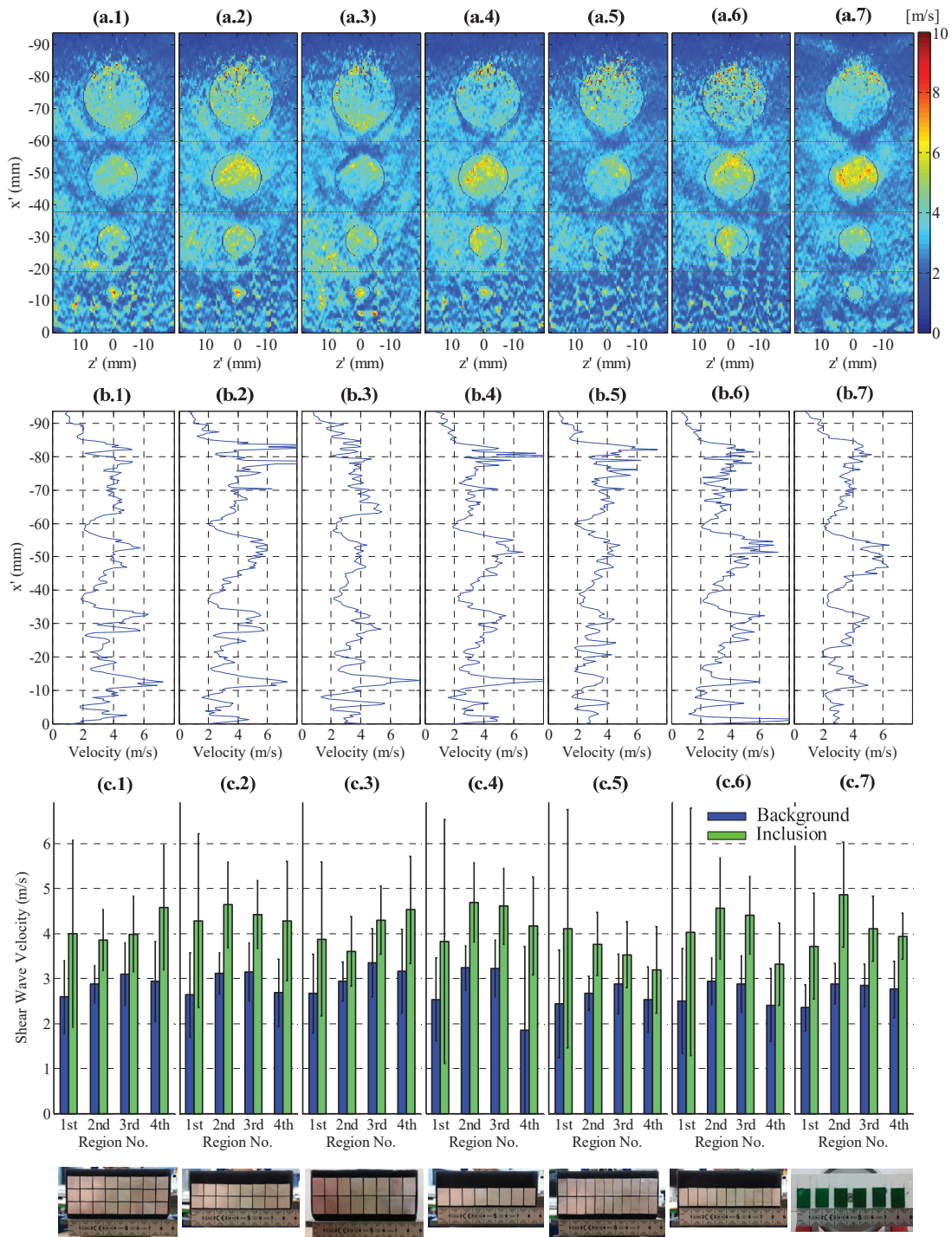


Figure 5.14. (a.1-7) The velocity maps computed from the shear wave displacement fields generated by the corresponding arrangement of aluminum patches or the mechanical actuator (see the bottom line of the figure). (b.1-7) The velocities along the line $z' = 0$ mm in each figure of (a.1-7). (c.1-7) The averages and variations of the velocity of the inclusion (the green bars) and of the background (the blue bars) in each region of the agar phantom sample in figures (a.1-7). (Sun *et al.* to be submitted)

In the fourth experiment, the ultrasound array transducer is placed on the side surface close to the largest inclusion and the aluminum patches stick on the opposite surface of the agar phantom (Figure 5.7.d). Figures 5.16.a.1-7 show the seven velocity maps of the agar phantom, which are computed using the shear wave displacement fields generated by the corresponding arrangement of aluminum patches or the mechanical actuator. The inclusion boundaries can be recognized from each of the velocity maps, although they are completely hidden in the ultrasound image (Figure 5.7.f). But at the same time, there are lots of artifacts where the velocity computed is much larger than that of the places having the same stiffness. Figures 5.16.b.1-7 show the shear wave velocity along the line $z' = 0$ mm, in each of which the widths of the velocity troughs coincide with the diameters of the inclusions. The averages and variations of the shear wave velocity of the inclusion and of the background in each region of the agar phantom are calculated for each velocity map, as shown in Figures 5.16.c.1-7, which shows that, for each of the four regions in the agar phantom: (1) the average velocity in the background part is larger than that in the corresponding inclusion; (2) the variation of the velocity in the background part is also larger than that in the corresponding inclusion.

5.2.3 Qualitative rather than quantitative reconstruction of shear wave velocity

The first and the second experiments use the fourth agar phantom sample with a soft background part and nine stiff inclusions.

In the first experiment, the softest inclusions locate in the left column (Figure 5.8.b). The ultrasound array transducer is placed on the back surface and the aluminum patches stick on the front surface of the agar phantom sample (Figure 5.8.a). Figures 5.17.a.1-7 show the seven velocity maps, which are computed using the shear wave displacement fields generated by the corresponding arrangement of aluminum patches and the mechanical actuator in the bottom row of Figure 5.17. The inclusion boundaries can be clearly recognized from each of the velocity maps, although they are completely hidden in the ultrasound image (Figure 5.8.c). Figures 5.17.b.1-7 show

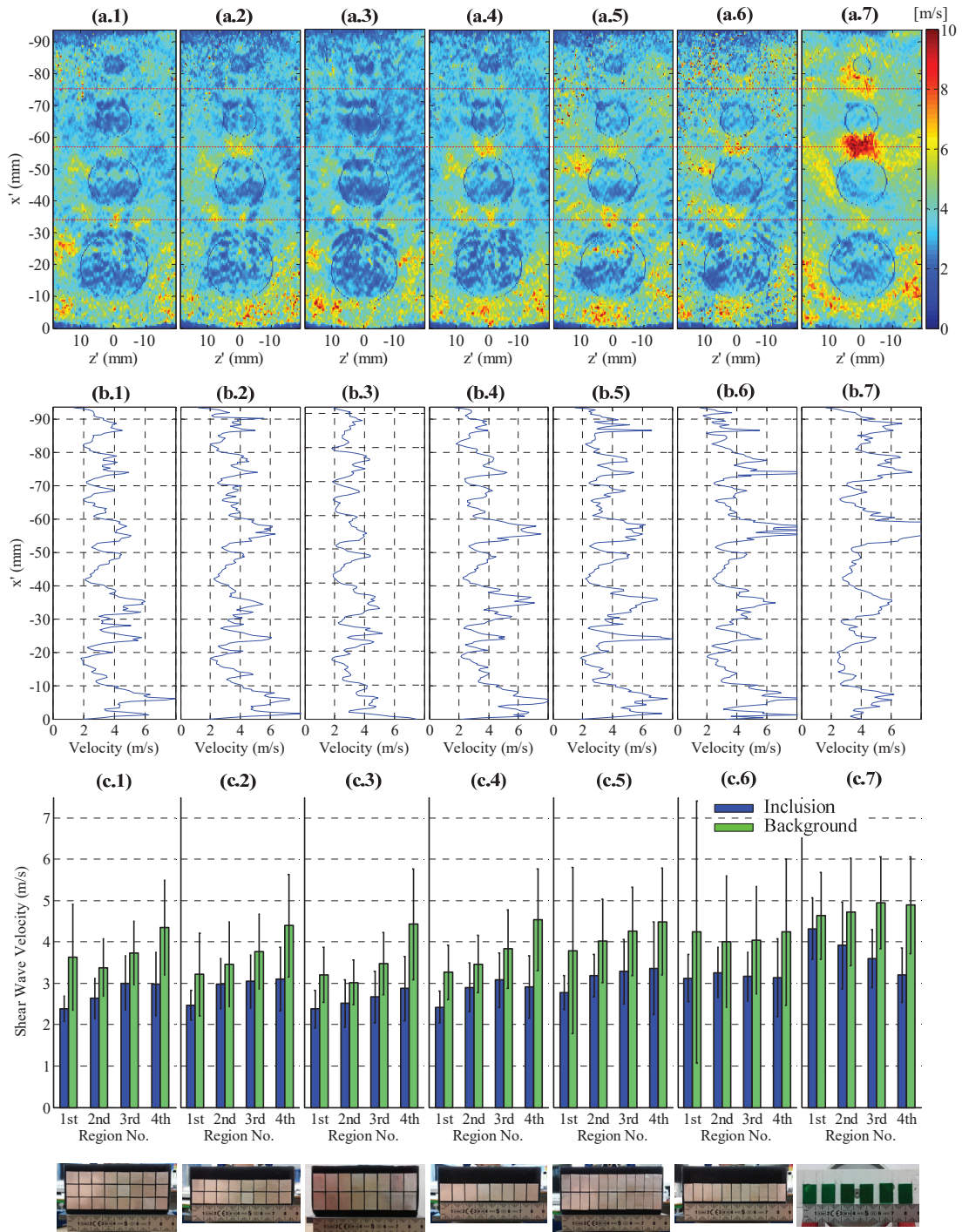


Figure 5.15. (a.1-7) The velocity maps computed from the shear wave displacement fields generated by the corresponding arrangement of aluminum patches or the mechanical actuator (see the bottom line of the figure). (b.1-7) The velocities along the line $z' = 0$ mm in each figure of (a.1-7). (c.1-7) The averages and variations of the velocity of the inclusion (the blue bars) and of the background (the green bars) in each region of the agar phantom sample in figures (a.1-7). (Sun *et al.* to be submitted)

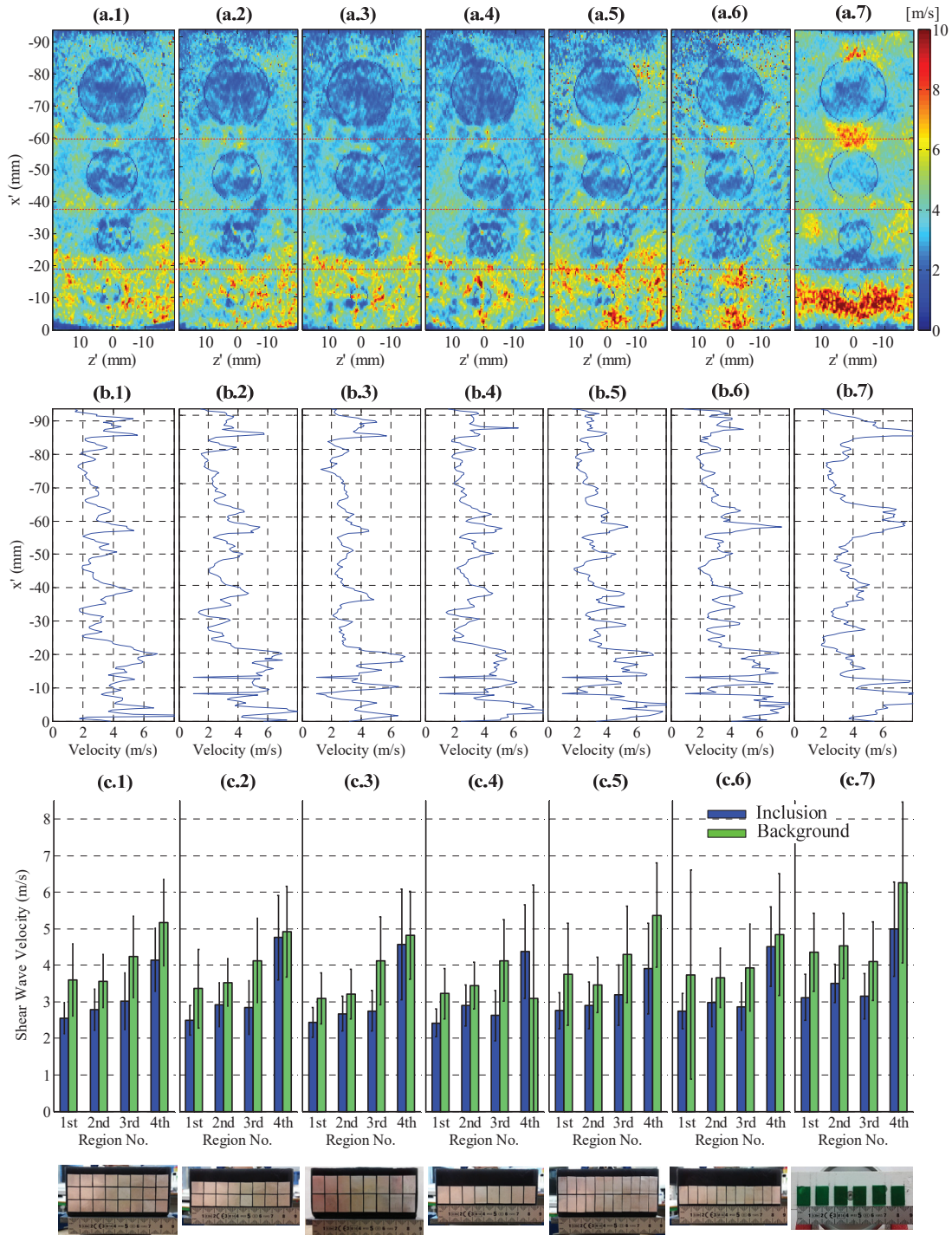


Figure 5.16. (a.1-7) The velocity maps computed from the shear wave displacement fields generated by the corresponding arrangement of aluminum patches or the mechanical actuator (see the bottom line of the figure). (b.1-7) The velocities along the line $z' = 0$ mm in each figure of (a.1-7). (c.1-7) The averages and variations of the velocity of the inclusion (the blue bars) and of the background (the green bars) in each region of the agar phantom sample in figures (a.1-7). (Sun *et al.* to be submitted)

the shear wave velocity along the lines crossing the centers of each row of inclusions - $x' = -24.36$ mm, -45.88 mm, and -67.39 mm, in each of which the widths of the velocity peaks coincide with the diameter of the inclusions. The averages and variations of the shear wave velocity of the background and of the three inclusions in each region of the agar phantom are calculated for each velocity map, as shown in Figures 5.17.c.1-7. Each sub-figure (except the ones in the bottom row of Figure 5.17.c.2, the middle row of Figure 5.17.c.5 and the middle row of Figure 5.17.c.7) shows that: (1) for each of the three regions in the agar phantom, the average velocity of the background part is smallest, that of the left column is next smallest, that of the middle column is the third smallest, and that of the right column is largest; (2) for the three inclusions in the same column, the averages and deviations of the velocities differ, especially the right column of inclusions.

In the second experiment, the stiffest inclusions locate in the left column (Figure 5.8.e). The ultrasound array transducer is placed on the back surface and the aluminum patches stick on the front surface of the agar phantom (Figure 5.8.d). Figure 5.18.a.1-7 show the seven velocity maps, which are computed using the shear wave displacement fields generated by the corresponding arrangement of aluminum patches and the mechanical actuator in the bottom row of Figure 5.18. The inclusion boundaries can be clearly recognized from each of the velocity maps, although they are completely hidden in the ultrasound image (Figure 5.8.f). Figures 5.18.b.1-7 show the shear wave velocity along the lines crossing the centers of each row of inclusions - $x' = -24.36$ mm, -45.88 mm, and -67.39 mm, in each of which the widths of the velocity peaks coincide with the diameters of the inclusions. The averages and variations of the shear wave velocity of the background and of the three inclusions in each region of the agar phantom are calculated for each velocity map, as shown in Figure 5.18.c.1-7. Each sub-figure (except the ones in the middle and bottom rows of Figure 5.18.c.2, the middle and bottom rows of Figure 5.18.c.3, the bottom row of Figure 5.18.c.4, the middle and bottom rows of Figure 5.18.c.5, the bottom row of Figure 5.18.c.6 and the middle and bottom rows of Figure 5.18.c.7) shows that: (1) for each of the three regions in the agar phantom, the average velocity of the left column

is largest, that of the middle column is next largest, that of the right column is the third largest, and that of the background part is smallest; (2) for the three inclusions in the same column, the averages and deviations of the velocities differ, especially the left column of inclusions.

Comparison of the velocities of the same inclusion in Figure 5.17.a.1-7 and Figures 5.18.a.1-7 show that, for the same inclusion, there are differences in averages and variations of the velocity. For instance, for the inclusion in the first row and the right column in Figure 5.17.a.1, it has an average velocity of 7.49 m/s with a standard deviation of 7.77 m/s in Figure 5.17.a.1 but an average velocity of 5.33 m/s with a standard deviation of 2.62 m/s in Figure 5.18.a.1.

The third and the fourth experiment use the fifth agar phantom sample with one piece of bovine liver and one piece of bovine muscle.

Figure 5.9.c shows the arrangement of ultrasound array transducer, the phantom sample, and the aluminum patches in the third experiment. Figure 5.19.a.1-7 show the seven velocity maps, which are computed using the shear wave displacement fields generated by the corresponding arrangement of aluminum patches and the mechanical actuator in the bottom row of Figure 5.19. The bovine muscle boundary can be clearly recognized from each velocity map while the bovine liver boundary can not be recognized, although both of them are clearly recognized in the ultrasound image (Figure 5.9.d). Figures 5.19.b.1-7 show the shear wave velocity along the line $z' = 0$ mm, in which the widths of the velocity peaks coincide with the thickness of the bovine muscle. The average and deviation of the shear wave velocity in the three regions (Figure 5.9.c) are calculated for each velocity map, as shown in Figures 5.19.c.1-7, which shows that: (1) the average velocity in the bovine muscle is much larger than those in the bovine liver and the agar phantom. In Figures 5.19.c.1-3 and 5, the average velocity in the bovine liver is close to that in the agar phantom. In Figure 5.19.c.4, 6 and 7, average velocity in the bovine liver is much larger than that in the agar phantom; (2) the deviations of the shear wave velocities in the bovine muscle are much larger than those in the bovine liver and the agar phantom, but it's not possible to judge whether the large deviations come from the bovine muscle itself or from the

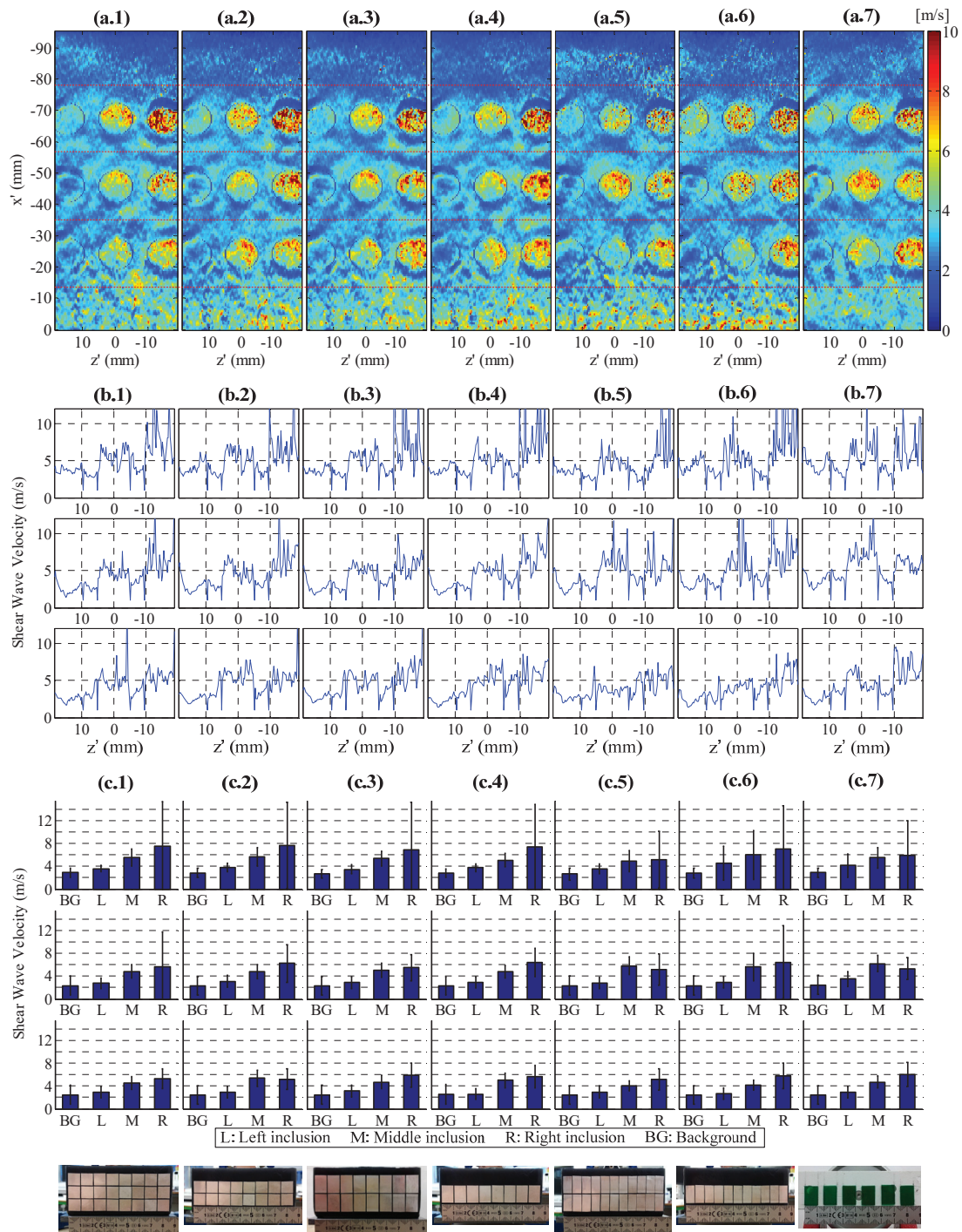


Figure 5.17. The velocity maps computed from the shear wave displacement fields generated by the corresponding arrangement of aluminum patches or the mechanical actuator (see the bottom row of the figure). (b.1-7) The velocities along the lines crossing the centers of each row of inclusions - $x' = -24.36$ mm, -45.88 mm, and -67.39 mm - in each figure of (a.1-7). (c.1-7) The averages and variations of the shear wave velocity of the inclusions and of the background in each region of the agar phantom sample in figures (a.1-7). (Sun *et al.* to be submitted)

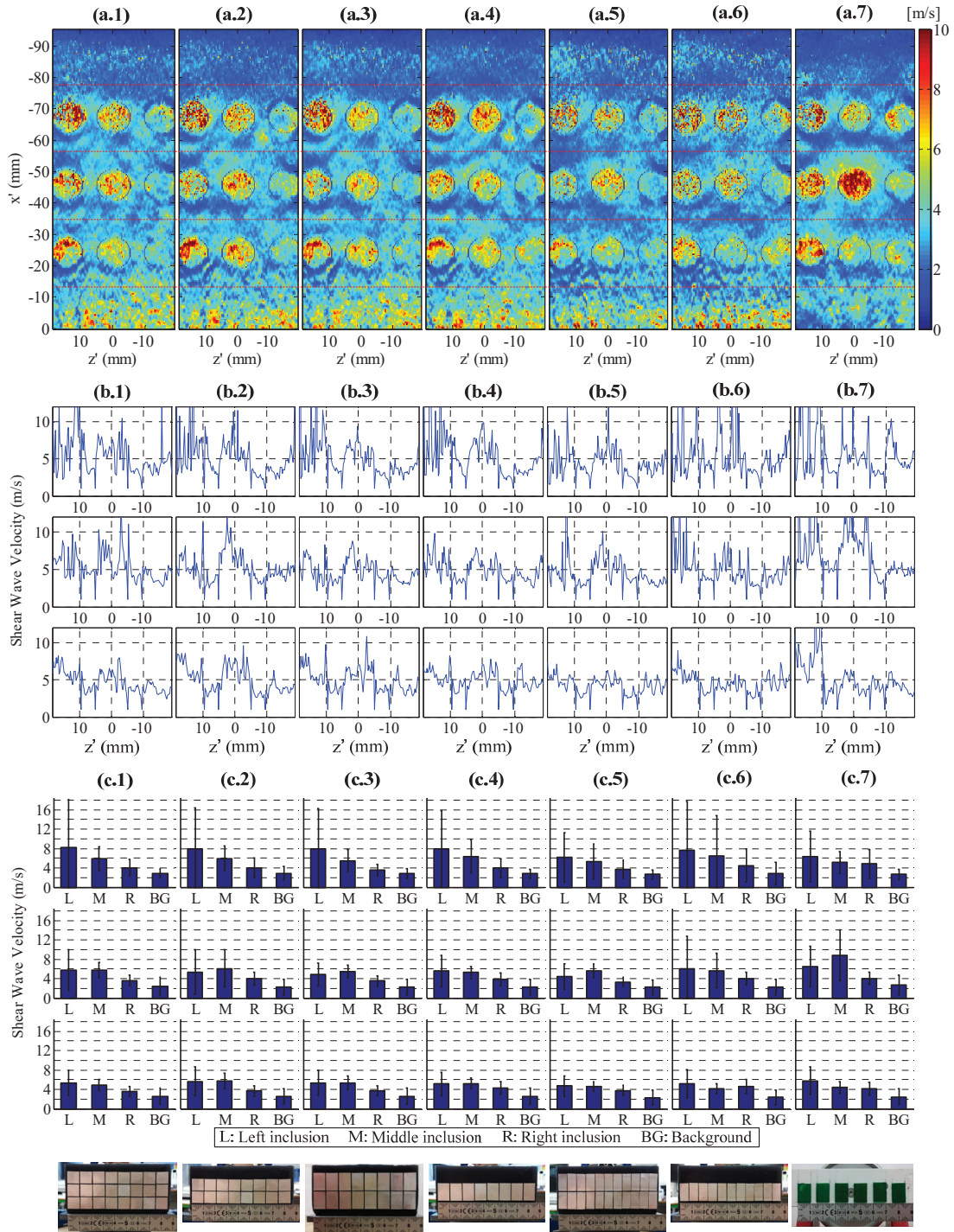


Figure 5.18. The velocity maps computed from the shear wave displacement fields generated by the corresponding arrangement of aluminum patches or the mechanical actuator (see the bottom row of the figure). (b.1-7) The velocities along the lines crossing the centers of each row of inclusions - $x' = -24.36$ mm, -45.88 mm, and -67.39 mm - in each figure of (a.1-7). (c.1-7) The averages and variations of the shear wave velocity of the inclusions and of the background in each region of the agar phantom sample in figures (a.1-7). (Sun *et al.* to be submitted)

reconstruction algorithm.

Figure 5.9.g shows the arrangement of ultrasound array transducer, the phantom sample, and the aluminum patches in the fourth experiment. Figures 5.20.a.1-7 show the seven velocity maps, which are computed using the shear wave displacement fields generated by the corresponding arrangement of aluminum patches and the mechanical actuator in the bottom row of Figure 5.20. The bovine muscle boundary can be clearly recognized from each velocity map while the bovine liver boundary can not be recognized, although both of them are clearly recognized in the ultrasound image (Figure 5.9.h). Figures 5.20.b.1-7 show the shear wave velocity along the line $z' = 0$ mm, in which the widths of the velocity peaks coincide with the thickness of the bovine muscle. The average and deviation of the shear wave velocity in the three regions (Figure 5.9.g) are calculated for each velocity map, as shown in Figure 5.20.c.1-7, which shows that: (1) the average velocity in the bovine muscle is much larger than those in the bovine liver and the agar phantom. The average velocity in the bovine liver is close to that in the agar phantom; (2) the deviations of the shear wave velocities in the bovine muscle are much larger than those in the bovine liver and the agar phantom, but as in the third experiment it's not possible to judge whether the large deviations come from the bovine muscle itself or from the reconstruction algorithm.

Comparison of the sub-figures in Figure 5.19.a.1-7 and Figure 5.20.a.1-7 shows that: the difference in the average velocity in the regions of bovine liver, the agar phantom and the bovine muscle are respectively 9.8%, 15.63% and 26.3%. The larger average velocity differences in the regions of the agar phantom and the bovine muscle between two experiments come from the change of positions relative to the aluminum patches, which changes the set of frames having shear wave displacements in these two regions and finally results in large differences in the average velocity computed through (5.8).

To sum up, we can only get qualitative rather than quantitative velocity maps of the sample using the shear wave displacement fields generated through the method in Chapter 4 and the cross-correlation-based velocity reconstruction approach.

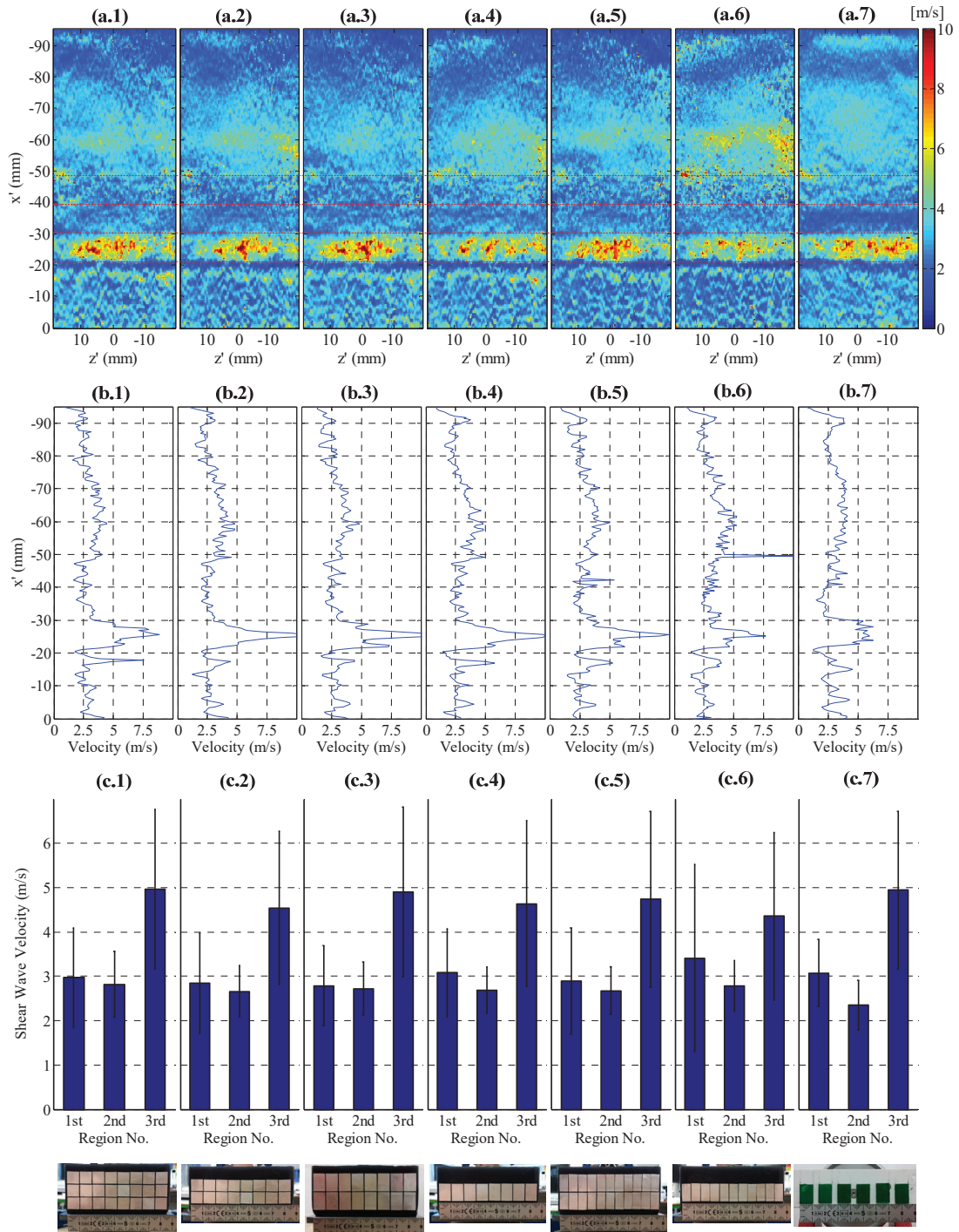


Figure 5.19. (a.1-7) The shear wave velocity maps computed from the shear wave displacement fields generated by the corresponding arrangement of aluminum patches or the mechanical actuator (see the bottom row of the figure). (b.1-7) The shear wave velocities along the line $z' = 0$ mm in each figure of (a.1-7). (c.1-7) The averages and variations of the shear wave velocity of the three regions of the agar phantom sample in figures (a.1-7). (Sun *et al.* to be submitted)

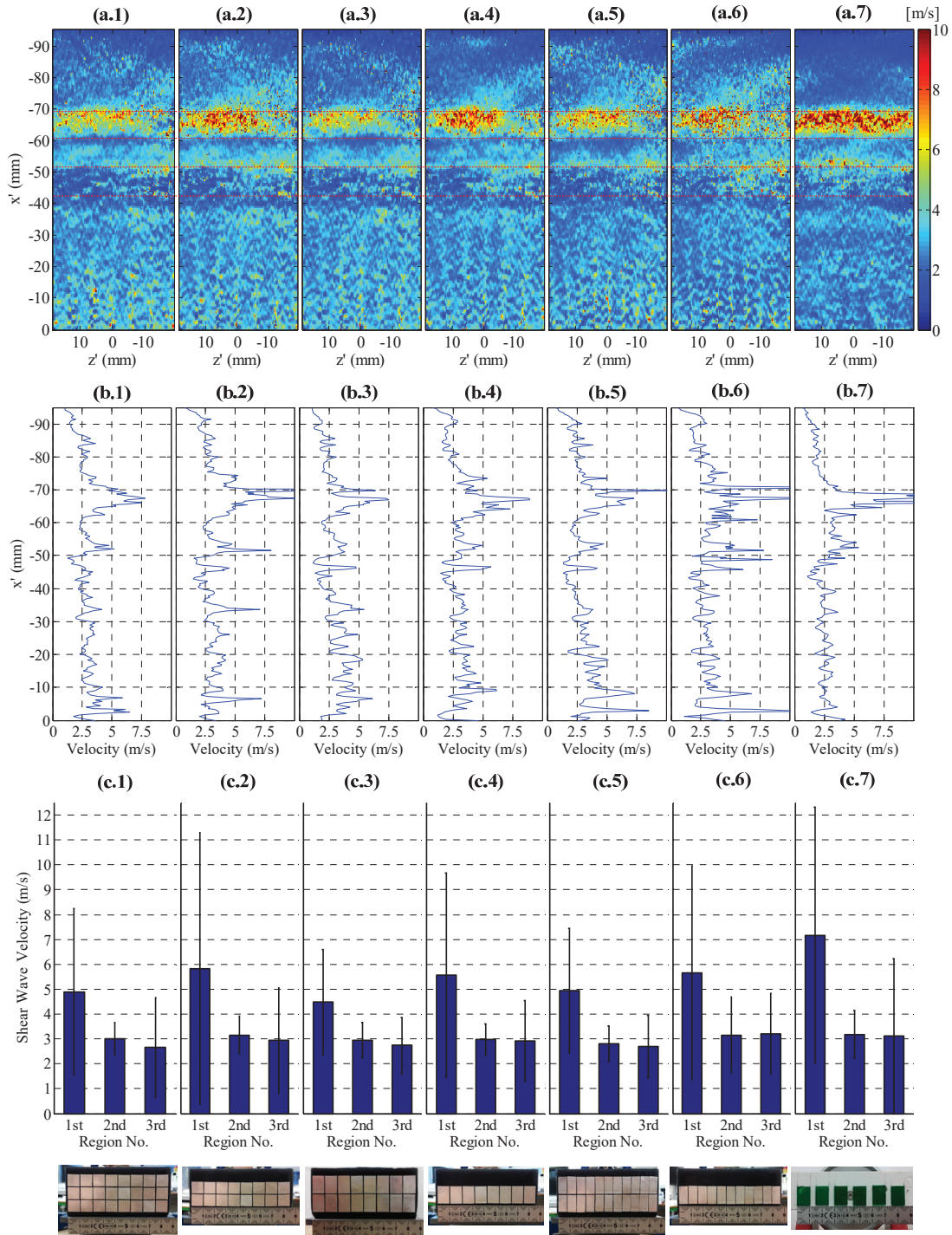


Figure 5.20. The shear wave velocity maps computed from the shear wave displacement fields generated by the corresponding arrangement of aluminum patches or the mechanical actuator in the bottom row of the figure. (b.1-7) The shear wave velocities along the line $z' = 0$ mm in each figure of (a.1-7). (c.1-7) The averages and variations of the shear wave velocity of the three regions of the agar phantom sample in figures (a.1-7). (Sun *et al.* to be submitted)

5.3 Chapter summary

In this chapter, we presented ultrasound elastography experiments using the five multi-shaped agar phantoms samples, through which we studied the performance of the cross-correlation-based ultrasound elastography using the shear wave displacements generated by the method in chapter 4. In each experiment, the shear wave velocity map was reconstructed from 100 frames of shear wave displacement fields, which were calculated from 100 frames of ultrasound images sampled at a rate of 1000 frames per second. From the reconstructed shear wave velocity maps, (1) interfaces or boundaries of layered or cylindered regions of different stiffness were clearly recognized, which were completely concealed in the ultrasound images; (2) cylinder inclusions of diameter as small as 5 mm can be differentiated from the background, but at the same time, there are artifacts which undermine the quality of velocity map; and (3) only qualitative rather than quantitative shear wave velocity maps were reconstructed using the cross-correlation-based approach.

Chapter 6 Conclusions and future work

6.1 Overall conclusions

In the first part of the thesis, we studied the applications of the wide linearly frequency-modulated (LFM) ultrasound pulse stimulation and the wide sinusoidal step-frequency ultrasound pulse stimulation in SECG-UILF with the goal of reducing the peak instantaneous ultrasound stimulation power to the sample while keeping the signal-to-noise ratio (SNR) and the longitudinal resolution. In the second part of the thesis, we studied generation of shear wave displacement fields for elastography through stimulating aluminum patches with a transient magnetic field.

In the scanning electric conductivity gradients with linearly frequency modulated ultrasound induced Lorentz force (SECG-LFM-UILF), first, two independent signal processing techniques - the coherent demodulation technique and the pulse compression technique - were applied independently for the calculation of the longitudinal distance of the electrical conductivity variations; and then, experiments using four multi-shaped saline agar phantoms samples confirmed the feasibility and the performance of the method, by comparisons with the traditional SECG-UILF using the high acoustic pressure wide-band ultrasound pulse. The experiment results showed that, for the SECG-LFM-UILF using electrical pulse of peak instantaneous power to the ultrasound transducer of 39.54 dBm and the traditional SECG-UILF using negative spike pulse of peak instantaneous power of 65.05 dBm: (1) the SECG-LFM-UILF using either the coherent demodulation method or the pulse compression method can detect the electrical conductivity variations precisely, with a reduction of peak instantaneous power of 25.5 dB to the ultrasound transducer and a comparable SNR; (2) the reconstructed B-scan images of the electrical conductivity discontinuity by the SECG-LFM-UILF using either the coherent demodulation method or the pulse compression method are comparable to that obtained through traditional SECG-UILF; and (3) using modulation frequency bandwidth of 2MHz and modulation duration of 500 μ s, the SECG-LFM-UILF using either the coherent demodulation method or the pulse compression method achieved a longitudinal

resolution of 1 mm.

In the scanning electric conductivity gradients with step-frequency ultrasound Induced Lorentz force (SECG-SF-UILF), the theory of application of the step-frequency technique was formulated in terms of the in-phase demodulation method and the in-phase/quadrature-phase (IQ) demodulation method. Compared with the IQ demodulation method, the in-phase demodulation method was simple in realization but could only detect half of the range. Experiments on a sample of two-layer copper foil as proof of concept demonstrated that, using 2 MHz frequency bandwidth and 64 discrete frequencies, the range of the sample could be detected precisely.

In the method of generation of multiple shear wave sources on the soft medium surface through stimulating aluminum patches actuators with a transient magnetic field, the origins and the characteristics of the Lorentz force acting on the actuator were confirmed by the displacement measurement using an interferometric laser probe: (1) the eddy current induced in the ring or patch actuator due to the transient magnetic field and orthogonal magnetic field constitutes the two basic elements of the Lorentz force; (2) its carrier frequency equals the sum of the carrier frequencies of the stimulating transient magnetic field and its time derivative; and (3) its amplitude increases quadratically with the stimulating current to the coil. Under a transient magnetic field of changing rate of 10.44 kTs^{-1} , the actuator generates a shear wave field source of amplitude of $100 \mu\text{m}$ on the surface of the polyvinyl alcohol (PVA) phantom sample. The shear wave fields created in the PVA phantom by experiments agrees qualitatively well with that by theory.

Finally, the cross-correlation-approach-based elastography experiments were done on five multi-shaped agar phantoms samples, to evaluate the potential of the generated shear wave displacement fields for shear wave velocity computation. The shear wave velocity maps reconstructed using 100 ultrasound images sampled at a rate of 1000 frames/s showed that: (1) the interfaces or boundaries between regions of different stiffness can be clearly recognized, which were completely concealed in the ultrasound images; (2) inclusions of diameter as small as 5 mm can be differentiated from the background, but at the same time, there were artifacts which undermined the

quality of the velocity maps; and (3) qualitative rather than quantitative computation of the shear wave velocity is achieved.

6.2 Challenges and possible solutions

The first and foremost challenge with the SECG-LFM-UILF is the weak electrical current generated. Using the high acoustic pressure wide-band ultrasound pulse based SECG-UILF (Section 2.5.6, Figure 2.7), I successfully detected the current signal generated by the target when using the pork muscle as the sample. But, using the SECG-LFM-UILF (Figure 2.5 or Figure 2.6), I didn't detect the intermediate frequency (IF) signal generated by the pork muscle. The decreases of SNR might come from the uneven amplitude of the ultrasound pulse and/or the demodulation in SECG-LFM-UILF. The uneven amplitude-frequency response of the ultrasound transducer undermining the SNR can be compensated by increasing the amplitude of the stimulating electrical signal to the transducer at frequencies where the transducer amplitude frequency response is low. The mixer used in the coherent demodulation method also added conversion loss (around 4.9 dB) to the IF signal, but it is difficult to reduce the conversion loss as the mixer used (ZAD-8+, Mini-Circuits, USA) is almost the best in performance among the similar mixers. For all modalities of SECG-UILF, the current signal (2.5) is directly proportional to the magnetic field, therefore the SNR can be increased by using a stronger magnetic field. Using the main magnetic field of MRI scanner, the intensity and homogeneity of the magnetic field can be increased with the expense of loss in lightness and cost. The magnetic field strength can be increased without known biological risk until at least 2 T (Schenck, 2000).

Another challenge with the SECG-LFM-UILF is retrieving the polarity information of the electrical conductivity variations. The SECG-LFM-UILF using the IQ demodulation method is not well-developed while that using the in-phase demodulation method is entirely incapable of retrieving the polarity information. The phase of the frequency spectrum of the IF signals calculated by FFT needs to be studied. And methods capable of finding out the phase variations produced by the FFT

can also get rid of the phase variations. For the SECG-LFM-UILF using the pulse compression technique, although the compressed pulse keeps the polarity information, it has one negative main-lobe and one positive main-lobe for both the positive and the negative conductivity gradient, which makes it difficult to differentiate between the positive and the negative conductivity gradients. A better matched compression filter based on the waveform of the raw SECG-LFM-UILF current signal can compress the generated interaction current signal into a single main-lobe, which improves the SNR and renders it easier to get the polarity information.

The leading challenge with the generation of shear wave displacement is the weak displacement generated when applying the technique in vitro, on the chicken breast, or in vivo, on the gastrocnemius muscle or the triceps brachii of the human body, as we got with the experiment setup in section 5.1 (Figures 5.1.a-c). One possible solution of increasing the intensity of the Lorentz force induced on the patches actuators is to use a transient magnetic field that is stronger and changes faster, like the transcranial magnetic stimulation (TMS) system (MagPro X100, MagVenture, Farum, Denmark) connected with a butterfly coil (C-B60, MagVenture, Farum, Denmark). The MagPro X100 together with the C-B60 can generate a transient magnetic field of peak amplitude of 2 T and of peak changing rate of 35 kT/s. Therefore, the amplitude of the Lorentz force will be increased by over 10 times. And the amplitude of the shear wave displacement generated in the sample will consequently be increased multiple times. Another way to increase the intensity of the Lorentz force is to use a strong static magnetic field, like in the TMS interleaved with functional magnetic resonance imaging system (fMRI) (Siebner, 2009), the eddy current induced by the transient magnetic field couples with the main magnetic field of the MRI scanner and generates the strong Lorentz force.

Failing to quantitatively calculate the shear wave velocity represents one important challenge in using the shear wave displacement fields for the cross-correlation-approach-based elastography. Adaptation of the cross-correlation approach to the shear wave displacement fields generated through stimulating the aluminum patches with the transient magnetic field is needed.

Appendix 1 Derivation of (2.8)

Here we list the detailed derivation of (2.8) in section 2.3. First, (2.6.1) and (2.7) are rewritten as (A1.1) and (A1.2):

$$T_x = A_0 \cos \left\{ 2\pi \left[f_0 + \frac{\Delta f}{2T} (t - kT_1) \right] (t - kT_1) + \phi_0 \right\},$$

$$kT_1 \leq t < kT_1 + T, k = 0, \pm 1, \pm 2, \dots \quad (\text{A1.1})$$

$$R_x = A \cos \left\{ 2\pi \left[f_0 + \frac{\Delta f}{2T} \left(t - kT_1 - \frac{R}{c} \right) \right] \left(t - kT_1 - \frac{R}{c} \right) + \phi \right\},$$

$$kT_1 + R/c \leq t < kT_1 + R/c + T, k = 0, \pm 1, \pm 2, \dots \quad (\text{A1.2})$$

Using the trigonometric identity $\cos(\alpha) \cdot \cos(\beta) = 0.5 \cdot [\cos(\alpha + \beta) + \cos(\alpha - \beta)]$, $T_x \cdot R_x$ is transformed into the sum of ① and ②, where ① is the first part of (A1.3) and ② is the second part of (A1.3).

$$T_x \cdot R_x = \frac{1}{2} A_0 A \cos \left\{ \begin{array}{l} 2\pi \left[f_0 + \frac{\Delta f}{2T} (t - kT_1) \right] (t - kT_1) + \phi_0 \\ + 2\pi \left[f_0 + \frac{\Delta f}{2T} \left(t - kT_1 - \frac{R}{c} \right) \right] \left(t - kT_1 - \frac{R}{c} \right) + \phi \end{array} \right\} +$$

$$\frac{1}{2} A_0 A \cos \left\{ \begin{array}{l} 2\pi \left[f_0 + \frac{\Delta f}{2T} (t - kT_1) \right] (t - kT_1) + \phi_0 \\ - 2\pi \left[f_0 + \frac{\Delta f}{2T} \left(t - kT_1 - \frac{R}{c} \right) \right] \left(t - kT_1 - \frac{R}{c} \right) - \phi \end{array} \right\}$$

$$= \text{①} + \text{②} \quad kT_1 + R/c \leq t < kT_1 + R/c + T, k = 0, \pm 1, \pm 2, \dots \quad (\text{A1.3})$$

And ① is further transformed as:

$$\text{①} = \frac{1}{2} A_0 A \cos \left\{ \begin{array}{l} 2\pi \left[f_0 + \frac{\Delta f}{2T} (t - kT_1) \right] (t - kT_1) + \phi_0 + \\ 2\pi \left[f_0 + \frac{\Delta f}{2T} \left(t - kT_1 - \frac{R}{c} \right) \right] \left(t - kT_1 - \frac{R}{c} \right) + \phi \end{array} \right\}$$

$$= \frac{1}{2} A_0 A \cos \left\{ \begin{array}{l} 2\pi \left[f_0 + \frac{\Delta f}{2T} (t - kT_1) \right] (t - kT_1) + \phi_0 + \\ 2\pi \left[f_0 + \frac{\Delta f}{2T} \left(t - kT_1 - \frac{R}{c} \right) \right] (t - kT_1) - \\ 2\pi \left[f_0 + \frac{\Delta f}{2T} \left(t - kT_1 - \frac{R}{c} \right) \right] \frac{R}{c} + \phi \end{array} \right\}$$

$$= \frac{1}{2} A_0 A \cos \left\{ \begin{array}{l} 2\pi \left[f_0 + \frac{\Delta f}{2T} (t - kT_1) \right] (t - kT_1) + \phi_0 + \\ 2\pi \left[f_0 + \frac{\Delta f}{2T} (t - kT_1) \right] (t - kT_1) - \\ 2\pi \left[f_0 + \frac{\Delta f}{2T} \left(2t - 2kT_1 - \frac{R}{c} \right) \right] \frac{R}{c} + \phi \end{array} \right\}$$

$$\begin{aligned}
 &= \frac{1}{2}A_0A\cos \left\{ \begin{array}{l} 4\pi \left[f_0 + \frac{\Delta f}{2T}(t - kT_1) \right] (t - kT_1) - \\ 2\pi \left[f_0 + \frac{\Delta f}{2T} \left(2t - 2kT_1 - \frac{R}{c} \right) \right] \frac{R}{c} + \phi_0 + \phi \end{array} \right\} \\
 &= \frac{1}{2}A_0A\cos \left\{ \begin{array}{l} 4\pi \left[f_0 + \frac{\Delta f}{2T}(t - kT_1) \right] (t - kT_1) - \\ 4\pi \frac{\Delta f}{2T} \left(t - kT_1 - \frac{R}{2c} \right) \frac{R}{c} - 2\pi f_0 \frac{R}{c} + \phi_0 + \phi \end{array} \right\} \\
 &= \frac{1}{2}A_0A\cos \left\{ \begin{array}{l} 4\pi \left[f_0 + \frac{\Delta f}{2T}(t - kT_1) \right] (t - kT_1) - 4\pi \frac{\Delta f}{2T} (t - kT_1) \frac{R}{c} + \\ 4\pi \frac{\Delta f}{2T} \frac{R}{2c} \frac{R}{c} - 2\pi f_0 \frac{R}{c} + \phi_0 + \phi \end{array} \right\} \\
 &= \frac{1}{2}A_0A\cos \left\{ \begin{array}{l} 4\pi \left[f_0 + \frac{\Delta f}{2T} \left(t - kT_1 - \frac{R}{c} \right) \right] (t - kT_1) - \\ 2\pi \left(f_0 - \frac{\Delta f}{2T} \frac{R}{c} \right) \frac{R}{c} + \phi_0 + \phi \end{array} \right\} \\
 &\hspace{10em} kT_1 + R/c \leq t < kT_1 + R/c + T, k = 0, \pm 1, \pm 2, \dots \quad (\text{A1.4})
 \end{aligned}$$

And ② is further transformed as:

$$\begin{aligned}
 \textcircled{2} &= \frac{1}{2}A_0A\cos \left\{ \begin{array}{l} 2\pi \left[f_0 + \frac{\Delta f}{2T}(t - kT_1) \right] (t - kT_1) + \phi_0 - \\ 2\pi \left[f_0 + \frac{\Delta f}{2T} \left(t - kT_1 - \frac{R}{c} \right) \right] \left(t - kT_1 - \frac{R}{c} \right) - \phi \end{array} \right\} \\
 &= \frac{1}{2}A_0A\cos \left\{ \begin{array}{l} 2\pi \left[f_0 + \frac{\Delta f}{2T}(t - kT_1) \right] (t - kT_1) + \phi_0 - \\ 2\pi \left[f_0 + \frac{\Delta f}{2T} \left(t - kT_1 - \frac{R}{c} \right) \right] (t - kT_1) + \\ 2\pi \left[f_0 + \frac{\Delta f}{2T} \left(t - kT_1 - \frac{R}{c} \right) \right] \frac{R}{c} - \phi \end{array} \right\} \\
 &= \frac{1}{2}A_0A\cos \left\{ \begin{array}{l} 2\pi \left[f_0 + \frac{\Delta f}{2T}(t - kT_1) \right] (t - kT_1) + \phi_0 - \\ 2\pi \left[f_0 + \frac{\Delta f}{2T}(t - kT_1) \right] (t - kT_1) + 2\pi \frac{\Delta f}{2T} \frac{R}{c} (t - kT_1) + \\ 2\pi \left[f_0 + \frac{\Delta f}{2T} \left(t - kT_1 - \frac{R}{c} \right) \right] \frac{R}{c} - \phi \end{array} \right\} \\
 &= \frac{1}{2}A_0A\cos \left\{ \phi_0 + 2\pi \frac{\Delta f}{2T} \frac{R}{c} (t - kT_1) + 2\pi \left[f_0 + \frac{\Delta f}{2T} \left(t - kT_1 - \frac{R}{c} \right) \right] \frac{R}{c} - \phi \right\}
 \end{aligned}$$

$$\begin{aligned}
 &= \frac{1}{2} A_0 A \cos \left\{ 2\pi \frac{\Delta f R}{T c} (t - kT_1) + 2\pi \left[f_0 - \frac{\Delta f R}{2T c} \right] \frac{R}{c} + \phi_0 - \phi \right\} \\
 & \quad kT_1 + R/c \leq t < kT_1 + R/c + T, k = 0, \pm 1, \pm 2, \dots \quad (\text{A1.5})
 \end{aligned}$$

Uniting (A1.4) and (A1.5), $T_x \cdot R_x$ therefore is transformed into (A1.6), which is (2.8).

$$\begin{aligned}
 T_x \cdot R_x &= \frac{A_0 A}{2} \cos \left\{ \begin{aligned} &4\pi \left[f_0 + \frac{\Delta f}{2T} \left(t - kT_1 - \frac{R}{c} \right) \right] (t - kT_1) - \\ &2\pi \left(f_0 - \frac{\Delta f}{2T} \cdot \frac{R}{c} \right) \frac{R}{c} + \phi_0 + \phi \end{aligned} \right\} + \\
 & \quad \frac{A_0 A}{2} \cos \left[2\pi (t - kT_1) \frac{\Delta f}{T} \cdot \frac{R}{c} + 2\pi \left(f_0 - \frac{\Delta f}{2T} \cdot \frac{R}{c} \right) \frac{R}{c} + \phi_0 - \phi \right] \\
 & \quad kT_1 + R/c \leq t < kT_1 + R/c + T, k = 0, \pm 1, \pm 2, \dots \quad (\text{A1.6})
 \end{aligned}$$

Appendix 2: Derivation of (3.4)

Here we list the detailed derivation of (3.4) in section 3.1.1. First, (3.2) is rewritten as (A2.1), and the coherent local oscillator signal is denoted as $L_{If_k}(t)$ (A2.2):

$$R_{f_k}(t) = \sum_{n=0}^{N-1} A_n(t) \sin \left[2\pi \left(f_0 + \frac{\Delta f}{N} k \right) \left(t - \frac{z_n}{c} \right) + \phi_0 \right],$$

$$z_n = z_0 + n\Delta_z, \frac{z_n}{c} \leq t < \frac{z_n}{c} + T \text{ and } k = 0, 1, \dots, N-1. \quad (\text{A2.1})$$

$$L_{If_k}(t) = 2 \sin \left[2\pi \left(f_0 + \frac{\Delta f}{N} k \right) t + \phi_0 \right],$$

$$0 \leq t < T, k = 0, 1, \dots, N-1. \quad (\text{A2.2})$$

Therefore, the output signal of the mixer is:

$$R_{f_k}(t) \cdot L_{If_k}(t) = \sum_{n=0}^{N-1} \left\{ \begin{array}{l} A_n(t) \sin \left[2\pi \left(f_0 + \frac{\Delta f}{N} k \right) \left(t - \frac{z_n}{c} \right) + \phi_0 \right] \cdot \\ 2 \sin \left[2\pi \left(f_0 + \frac{\Delta f}{N} k \right) t + \phi_0 \right] \end{array} \right\}$$

$$= \sum_{n=0}^{N-1} A_n(t) \left\{ \begin{array}{l} \cos \left[2\pi \left(f_0 + \frac{\Delta f}{N} k \right) \frac{z_n}{c} \right] - \\ \cos \left[4\pi \left(f_0 + \frac{\Delta f}{N} k \right) t - 2\pi \left(f_0 + \frac{\Delta f}{N} k \right) \frac{z_n}{c} + 2\phi_0 \right] \end{array} \right\}$$

$$z_n = z_0 + n\Delta_z, \frac{z_n}{c} \leq t < T \text{ and } k = 0, 1, \dots, N-1. \quad (\text{A2.3})$$

Filtering the double carrier frequency signal, the intermediate frequency signal, which is denoted as $I_{f_k}(t)$, is obtained:

$$I_{f_k}(t) = \sum_{n=0}^{N-1} A_n(t) \cos \left[2\pi \left(f_0 + \frac{\Delta f}{N} k \right) \frac{z_n}{c} \right],$$

$$= \sum_{n=0}^{N-1} A_n(t) \left[e^{-j2\pi \left(f_0 + \frac{\Delta f}{N} k \right) \frac{z_0 + n\Delta_z}{c}} + e^{j2\pi \left(f_0 + \frac{\Delta f}{N} k \right) \frac{z_0 + n\Delta_z}{c}} \right],$$

$$z_n = z_0 + n\Delta_z, \frac{z_n}{c} \leq t < T \text{ and } k = 0, 1, \dots, N-1. \quad (\text{A2.4})$$

Multiplying $e^{j2\pi \left(f_0 + \frac{\Delta f}{N} k \right) \frac{z_0}{c}}$ to both sides of (A2.4) so as to get rid of the constant phase item $e^{-j2\pi \left(f_0 + \frac{\Delta f}{N} k \right) \frac{z_0}{c}}$ of the first part in the bracket in (A2.4), we can get:

$$\begin{aligned}
 I_{f_k}(t)e^{j2\pi\left(f_0+\frac{\Delta_f}{N}k\right)\frac{z_0}{c}} &= \sum_{n=0}^{N-1} A_n(t) \left[e^{-j2\pi\left(f_0+\frac{\Delta_f}{N}k\right)\frac{n\Delta_z}{c}} + e^{j2\pi\left(f_0+\frac{\Delta_f}{N}k\right)\frac{2z_0+n\Delta_z}{c}} \right] \\
 &= \sum_{n=0}^{N-1} A_n(t) \left[e^{-j2\pi f_0\frac{n\Delta_z}{c}} e^{-j2\pi\frac{nk\Delta_z\Delta_f}{c}} + \right. \\
 &\quad \left. e^{j2\pi f_0\frac{2z_0+n\Delta_z}{c}} e^{j2\pi k\frac{2z_0\Delta_f+n\Delta_z\Delta_f}{cN}} \right] \\
 z_n &= z_0 + n\Delta_z, \quad \frac{z_n}{c} \leq t < T \text{ and } k = 0, 1, \dots, N-1. \quad (\text{A2.5})
 \end{aligned}$$

Applying constraints $\frac{\Delta_z\Delta_f}{c} = 1$ and $\frac{2z_0}{\Delta_z} = 3N + 1$ to (A2.5) and multiplying $e^{-j8\pi k}$ to the second part in the bracket, (A2.5) is transformed into (A2.8), where

$$I'_{f_k}(t) = I_{f_k}(t)e^{j2\pi\left(f_0+\frac{\Delta_f}{N}k\right)\frac{z_0}{c}}.$$

$$\frac{\Delta_z\Delta_f}{c} = 1, \quad \text{即: } \Delta_z = \frac{c}{\Delta_f} \quad (\text{A2.6})$$

$$\frac{2z_0}{\Delta_z} = 3N + 1, \quad \text{即: } z_0 = \frac{3N+1}{2}\Delta_z \quad (\text{A2.7})$$

$$\begin{aligned}
 I'_{f_k}(t) &= \sum_{n=0}^{N-1} A_n(t)e^{-j2\pi f_0\frac{n\Delta_z}{c}} e^{-j2\pi\frac{nk}{N}} + \\
 &\quad \sum_{n=0}^{N-1} A_n(t)e^{j2\pi f_0\frac{2z_0+n\Delta_z}{c}} e^{-j2\pi k\left(\frac{N-1-n}{N}\right)} \\
 z_n &= z_0 + n\Delta_z, \quad \frac{z_n}{c} \leq t < T \text{ and } k = 0, 1, \dots, N-1. \quad (\text{A2.8})
 \end{aligned}$$

Replacing $N - 1 - n$ in the second part of the right side of (A2.8) with n' , (A2.8) is transformed into (A2.9).

$$\begin{aligned}
 I'_{f_k}(t) &= \sum_{n=0}^{N-1} A_n(t) \left[e^{-j2\pi f_0\frac{n\Delta_z}{c}} e^{-j2\pi\frac{nk}{N}} \right] + \\
 &\quad \sum_{n'=0}^{N-1} A_{N-1-n'}(t) \left[e^{j2\pi f_0\frac{2z_0+(N-1-n')\Delta_z}{c}} e^{-j2\pi k\left(\frac{n'}{N}\right)} \right] \\
 z_n &= z_0 + n\Delta_z, \quad \frac{z_n}{c} \leq t < T \text{ and } k = 0, 1, \dots, N-1. \quad (\text{A2.9})
 \end{aligned}$$

And replacing n' in the second part in (A2.9) with n , (A2.9) is transformed into (A2.10), which also is (3.4).

$$\begin{aligned}
 I'_{f_k}(t) &= \sum_{n=0}^{N-1} \left[A_n(t)e^{-j2\pi f_0\frac{n\Delta_z}{c}} e^{-j2\pi\frac{nk}{N}} + \right. \\
 &\quad \left. A_{N-1-n}(t)e^{j2\pi f_0\frac{2z_0+(N-1-n)\Delta_z}{c}} e^{-j2\pi\frac{nk}{N}} \right], \\
 z_n &= z_0 + n\Delta_z, \quad \frac{z_n}{c} \leq t < T \text{ and } k = 0, 1, \dots, N-1. \quad (\text{A2.10})
 \end{aligned}$$

Appendix 3: Derivation of (3.7)

Here we list the detailed derivation of (3.7) in section 3.1.2. First, (3.2) is rewritten as (A3.1), and the coherent local oscillator signals of the in-phase channel and the quadrature-phase channel are denoted respectively as $L_{If_k}(t)$ (A3.2) and $L_{Qf_k}(t)$ (A3.3):

$$R_{f_k}(t) = \sum_{n=0}^{N-1} A_n(t) \sin \left[2\pi \left(f_0 + \frac{\Delta f}{N} k \right) \left(t - \frac{z_n}{c} \right) + \phi_0 \right],$$

$$z_n = z_0 + n\Delta_z, \quad \frac{z_n}{c} \leq t < \frac{z_n}{c} + T \text{ and } k = 0, 1, \dots, N-1. \quad (\text{A3.1})$$

$$L_{If_k}(t) = 2 \sin \left[2\pi \left(f_0 + \frac{\Delta f}{N} k \right) t + \phi_0 \right], \quad 0 \leq t < T, k = 0, 1, \dots, N-1. \quad (\text{A3.2})$$

$$L_{Qf_k}(t) = 2 \cos \left[2\pi \left(f_0 + \frac{\Delta f}{N} k \right) t + \phi_0 \right], \quad 0 \leq t < T, k = 0, 1, \dots, N-1. \quad (\text{A3.3})$$

Therefore, the output of the mixer of the in-phase channel is:

$$R_{f_k}(t) \cdot L_{If_k}(t) = \sum_{n=0}^{N-1} \left\{ \begin{array}{l} A_n(t) \sin \left[2\pi \left(f_0 + \frac{\Delta f}{N} k \right) \left(t - \frac{z_n}{c} \right) + \phi_0 \right] \cdot \\ 2 \sin \left[2\pi \left(f_0 + \frac{\Delta f}{N} k \right) t + \phi_0 \right] \end{array} \right\}$$

$$= \sum_{n=0}^{N-1} A_n(t) \left\{ \begin{array}{l} \cos \left[2\pi \left(f_0 + \frac{\Delta f}{N} k \right) \frac{z_n}{c} \right] - \\ \cos \left[4\pi \left(f_0 + \frac{\Delta f}{N} k \right) t - 2\pi \left(f_0 + \frac{\Delta f}{N} k \right) \frac{z_n}{c} + 2\phi_0 \right] \end{array} \right\}$$

$$z_n = z_0 + n\Delta_z, \quad \frac{z_n}{c} \leq t < T \text{ and } k = 0, 1, \dots, N-1. \quad (\text{A3.4})$$

And the output of the mixer of the quadrature-phase channel is:

$$R_{f_k}(t) \cdot L_{Qf_k}(t) = \sum_{n=0}^{N-1} \left\{ \begin{array}{l} A_n(t) \sin \left[2\pi \left(f_0 + \frac{\Delta f}{N} k \right) \left(t - \frac{z_n}{c} \right) + \phi_0 \right] \cdot \\ 2 \cos \left[2\pi \left(f_0 + \frac{\Delta f}{N} k \right) t + \phi_0 \right] \end{array} \right\}$$

$$= \sum_{n=0}^{N-1} A_n(t) \left\{ \begin{array}{l} -\sin \left[2\pi \left(f_0 + \frac{\Delta f}{N} k \right) \frac{z_n}{c} \right] + \\ \sin \left[4\pi \left(f_0 + \frac{\Delta f}{N} k \right) t - 2\pi \left(f_0 + \frac{\Delta f}{N} k \right) \frac{z_n}{c} + 2\phi_0 \right] \end{array} \right\}$$

$$z_n = z_0 + n\Delta_z, \quad \frac{z_n}{c} \leq t < T \text{ and } k = 0, 1, \dots, N-1. \quad (\text{A3.5})$$

Filtering the double carrier frequency signals, the intermediate frequency signals of the in-phase channel and the quadrature channel, which are denoted as $I_{If_k}(t)$ and

$I_{Qf_k}(t)$, are obtained:

$$I_{If_k}(t) = \sum_{n=0}^{N-1} A_n(t) \cos \left[2\pi \left(f_0 + \frac{\Delta f}{N} k \right) \frac{z_n}{c} \right],$$

$$z_n = z_0 + n\Delta_z, \quad \frac{z_n}{c} \leq t < T \text{ and } k = 0, 1, \dots, N-1. \quad (\text{A3.6})$$

$$I_{Qf_k}(t) = \sum_{n=0}^{N-1} -A_n(t) \sin \left[2\pi \left(f_0 + \frac{\Delta f}{N} k \right) \frac{z_n}{c} \right],$$

$$z_n = z_0 + n\Delta_z, \quad \frac{z_n}{c} \leq t < T \text{ and } k = 0, 1, \dots, N-1. \quad (\text{A3.7})$$

From $I_{If_k}(t)$ and $I_{Qf_k}(t)$, the complex form of the intermediate frequency signal $I_{f_k}(t)$ is obtained as (A3.8):

$$I_{f_k}(t) = I_{If_k}(t) + jI_{Qf_k}(t) = \sum_{n=0}^{N-1} A_n(t) e^{-j2\pi \left(f_0 + \frac{\Delta f}{N} k \right) \frac{z_n}{c}}$$

$$z_n = z_0 + n\Delta_z, \quad \frac{z_n}{c} \leq t < T \text{ and } k = 0, 1, \dots, N-1. \quad (\text{A3.8})$$

Multiplying $e^{j2\pi \left(f_0 + \frac{\Delta f}{N} k \right) \frac{z_0}{c}}$ to both sides of (A3.8), the constant phase $e^{-j2\pi \left(f_0 + \frac{\Delta f}{N} k \right) \frac{z_0}{c}}$ is removed:

$$I_{f_k}(t) e^{j2\pi \left(f_0 + \frac{\Delta f}{N} k \right) \frac{z_0}{c}} = \sum_{n=0}^{N-1} A_n(t) e^{-j2\pi \left(f_0 + \frac{\Delta f}{N} k \right) \frac{n\Delta_z}{c}}$$

$$= \sum_{n=0}^{N-1} A_n(t) e^{-j2\pi f_0 \frac{n\Delta_z}{c}} e^{-j2\pi \frac{nk\Delta_z \Delta f}{c}}$$

$$z_n = z_0 + n\Delta_z, \quad \frac{z_n}{c} \leq t < T \text{ and } k = 0, 1, \dots, N-1. \quad (\text{A3.9})$$

Denoting $I'_{f_k}(t) = I_{f_k}(t) e^{j2\pi \left(f_0 + \frac{\Delta f}{N} k \right) \frac{z_0}{c}}$ and applying $\frac{\Delta_z \Delta f}{c} = 1$ to (A3.9), (A3.9) is transformed into (A3.11), which also is (3.7).

$$\frac{\Delta_z \Delta f}{c} = 1, \quad \text{即: } \Delta_z = \frac{c}{\Delta f} \quad (\text{A3.10})$$

$$I'_{f_k}(t) = \sum_{n=0}^{N-1} A_n(t) e^{-j2\pi f_0 \frac{n\Delta_z}{c}} e^{-j2\pi \frac{nk}{N}}$$

$$z_n = z_0 + n\Delta_z, \quad \frac{z_n}{c} \leq t < T \text{ and } k = 0, 1, \dots, N-1. \quad (\text{A3.11})$$

Bibliography

- Aki K, Richards P G. Quantitative seismology. Second Edition (Sausalito, California: University Science Books) 2002.
- Aliroteh M S, Scott G, Arbabian A. Frequency-modulated magneto-acoustic detection and imaging. *Electronics letters*, 2014, 50(11): 790-792.
- Aliroteh M S, Scott G C, Arbabian A. Frequency-modulated magneto-acoustic detection and imaging: Challenges, experimental procedures, and B-scan images[Online]. (Feb. 2016). Available: [ht.tps://arxiv.org/abs/1602.06931](https://arxiv.org/abs/1602.06931)
- Baehe R J, Harley A, Greenfield J C. Evaluation of thoracic impedance plethysmography as an indicator of stroke volume in man. *The American journal of the medical sciences*, 1969, 258(2): 100-113.
- Baker L E, Geddes L A. The measurement of respiratory volumes in animals and man with use of electrical impedance. *Annals of the New York Academy of Sciences*, 1970, 170(2): 667-688.
- Barber D C, Brown B H. Applied potential tomography. *Journal of Physics E: Scientific Instruments*, 1984, 17(9): 723.
- Barker A T, Jalinous R, Freeston I L. Non-invasive magnetic stimulation of human motor cortex. *The Lancet*, 1985, 325(8437): 1106-1107.
- Barnett S B, Ter Haar G R, Ziskin M C, et al. International recommendations and guidelines for the safe use of diagnostic ultrasound in medicine. *Ultrasound in medicine & biology*, 2000, 26(3): 355-366.
- Basford A T, Basford J R, Kugel J, et al. Lorentz-force-induced motion in conductive media[J]. *Magnetic resonance imaging*, 2005, 23(5): 647-651.
- Battaglini L, Burrascano P, De Angelis A, et al. A low-cost ultrasonic rangefinder based on frequency modulated continuous wave//Proc. 20th IMEKO TC4 Int. Symp. 2014: 1124-1126.
- Bercoff J. L'imagerie échographique ultrarapide et son application à l'étude de la viscoélasticité du corps humain. ESPCI ParisTECH, 2004.
- Bercoff J, Chaffai S, Tanter M, et al. In vivo breast tumor detection using transient elastography. *Ultrasound in medicine & biology*, 2003, 29(10): 1387-1396.
- Bercoff J, Tanter M, Muller M, et al. The role of viscosity in the impulse diffraction field of elastic waves induced by the acoustic radiation force. *IEEE transactions on ultrasonics, ferroelectrics, and frequency control*, 2004, 51(11): 1523-1536.
- Bercoff J, Tanter M, and Fink M. Supersonic shear imaging: a new technique for soft tissue elasticity mapping. *IEEE transactions on ultrasonics, ferroelectrics, and frequency control*, 2004, 51(4): 396-409.
- Bolomey J C, Izadnegahdar A, Jofre Roca L, et al. Microwave diffraction tomography for

- biomedical applications. *IEEE Transactions on Microwave Theory and Techniques*, 1982, 30(11): 1998-2000.
- Braun J, Braun K, Sack I. Electromagnetic actuator for generating variably oriented shear waves in MR elastography. *Magnetic Resonance in Medicine: An Official Journal of the International Society for Magnetic Resonance in Medicine*, 2003, 50(1): 220-222.
- Buckingham M-J, Berkhouse B-V, and Glegg S-A-L. Passive imaging of targets with ambient noise. *Nature London*, 1992, 365: 327-329.
- Campillo M and Paul A. Long-range correlations in the diffuse seismic coda. *Science*, 2003, 299(5606): 547-549.
- Catheline S. *Interférométrie-Speckle ultrasonore: Application à la mesure d'élasticité*. Université Paris-Diderot-Paris VII, 1998.
- Catheline S, Wu F, Fink M. A solution to diffraction biases in sonoelasticity: The acoustic impulse technique. *The Journal of the Acoustical Society of America*, 1999, 105(5): 2941-2950.
- Catheline S, Souchon R, Rupin M, et al. Tomography from diffuse waves: Passive shear wave imaging using low frame rate scanners. *Applied Physics Letters*, 2013, 103(1): 014101.
- Chiao R Y, Hao X. Coded excitation for diagnostic ultrasound: A system developer's perspective. *IEEE transactions on ultrasonics, ferroelectrics, and frequency control*, 2005, 52(2): 160-170.
- Cobbold R S C. *Foundations of biomedical ultrasound*. Oxford university press, 2006.
- Cook C E. Pulse compression-key to more efficient radar transmission. *Proceedings of the IRE*, 1960, 48(3): 310-316.
- Court I N. Microwave Acoustic Devices for Pulse Compression Filters. *IEEE Transactions on Microwave Theory and Techniques*, 1969, 17(11): 968-986.
- Dickinson R J, Hill C R. Measurement of soft tissue motion using correlation between A-scans. *Ultrasound in medicine & biology*, 1982, 8(3): 263-271.
- Duck F A. Medical and non-medical protection standards for ultrasound and infrasound. *Progress in biophysics and molecular biology*, 2007, 93(1-3): 176-191.
- Duvall Jr T-L, Jefferies S-M, Harvey J-W, et al. Time-distance helioseismology. *Nature*, 1993, 362(6419): 430.
- Eisenscher A, Schweg-Toffler E, Pelletier G, et al. Rhythmic echographic palpation. Echosisomography. A new technic of differentiating benign and malignant tumors by ultrasonic study of tissue elasticity. *Journal de radiologie*, 1983, 64(4): 255-261.
- Fatemi M, Greenleaf J F. Vibro-acoustography: An imaging modality based on ultrasound-stimulated acoustic emission. *Proceedings of the National Academy of Sciences*, 1999, 96(12): 6603-6608.
- Flower, M A. (ed). *Webb's physics of medical imaging*. CRC Press, London, 2012.
- Fromageau J, Gennisson J L, Schmitt C, et al. Estimation of polyvinyl alcohol cryogel mechanical

- properties with four ultrasound elastography methods and comparison with gold standard testings. *IEEE transactions on ultrasonics, ferroelectrics, and frequency control*, 2007, 54(3): 498-509.
- Gabriel S, Lau R W, Gabriel C. The dielectric properties of biological tissues: II. Measurements in the frequency range 10 Hz to 20 GHz. *Physics in medicine & biology*, 1996, 41(11): 2251.
- Gallot T, Catheline S, Roux P, et al. Passive elastography: shear-wave tomography from physiological-noise correlation in soft tissues. *IEEE transactions on ultrasonics, ferroelectrics, and frequency control*, 2011, 58(6): 1122-1126.
- Giles P-M, Duvall Jr T-L, Scherrer P-H, et al. A subsurface flow of material from the sun's equator to its poles. *Nature*, 1997, 390(6655): 52.
- Glover G H. Overview of functional magnetic resonance imaging. *Neurosurgery Clinics*, 2011, 22(2): 133-139.
- Grasland-Mongrain P, Destrempe F, Mari J M, et al. Acousto-electrical speckle pattern in Lorentz force electrical impedance tomography. *Physics in Medicine & Biology*, 2015, 60(9): 3747.
- Grasland-Mongrain P, Lu Y, Lesage F, et al. Generation of shear waves by laser in soft media in the ablative and thermoelastic regimes. *Applied physics letters*, 2016, 109(22): 221901.
- Grasland-Mongrain P, Mari J M, Chapelon J Y, et al. Lorentz force electrical impedance tomography. *Irbm*, 2013, 34(4-5): 357-360.
- Grasland-Mongrain P, Miller-Jolicoeur E, Tang A, et al. Contactless remote induction of shear waves in soft tissues using a transcranial magnetic stimulation device. *Physics in Medicine & Biology*, 2016, 61(6): 2582.
- Grasland-Mongrain P, Souchon R, Cartellier F, et al. Imaging of shear waves induced by Lorentz force in soft tissues. *Physical review letters*, 2014, 113(3): 038101.
- Grasland-Mongrain P, Zorgani A, Nakagawa S, et al. Ultrafast imaging of cell elasticity with optical microelastography. *Proceedings of the National Academy of Sciences*, 2018, 115(5): 861-866.
- Griffiths H, Stewart W R, Gough W. Magnetic induction tomography: a measuring system for biological tissues. *Annals Of The New York Academy Of Sciences*, 1999, 873(1): 335-345.
- Guo L, Liu G, Xia H. Magneto-acousto-electrical tomography with magnetic induction for conductivity reconstruction. *IEEE Transactions on Biomedical Engineering*, 2015, 62(9): 2114-2124.
- Haemmerich D, Staelin S T, Tsai J Z, et al. In vivo electrical conductivity of hepatic tumours. *Physiological measurement*, 2003, 24(2): 251.
- Haider, Syed, Magneto-acousto-electrical tomography: a potential imaging method for current density and electrical impedance. Master Theses, Ryerson University, 2008.
- Haider S, Hrbek A, Xu Y. Magneto-acousto-electrical tomography: a potential method for imaging current density and electrical impedance. *Physiological measurement*, 2008, 29(6): S41.

- Harvey G W, Brower D F. Metal forming device and method: U.S. Patent 2,976,907. 1961-3-28.
- He B. Modeling and imaging of bioelectrical activity - principles and applications. (Kluwer Academic Publishers), 2004.
- Hu G, Cressman E, He B. Magnetoacoustic imaging of human liver tumor with magnetic induction[J]. Applied physics letters, 2011, 98(2): 023703.
- Hu G, He B. Magnetoacoustic imaging of electrical conductivity of biological tissues at a spatial resolution better than 2 mm. PloS one, 2011, 6(8): e23421.
- Hu G, Li X, He B. Imaging biological tissues with electrical conductivity contrast below 1 S m^{-1} by means of magnetoacoustic tomography with magnetic induction. Applied physics letters, 2010, 97(10): 103705.
- Iizuka K, Freundorfer A P. Detection of nonmetallic buried objects by a step frequency radar. Proceedings of the IEEE, 1983, 71(2): 276-279.
- Iizuka K, Freundorfer A P, Wu K H, et al. Step - frequency radar. Journal of Applied physics, 1984, 56(9): 2572-2583.
- Iizuka K, Ogura H, Yen J L, et al. A hologram matrix radar. Proceedings of the IEEE, 1976, 64(10): 1493-1504.
- Islam M R, Towe B C. Bioelectric current image reconstruction from magneto-acoustic measurements. IEEE transactions on medical imaging, 1988, 7(4): 386-391.
- Jian X, Dixon S, Edwards R S, et al. Coupling mechanism of electromagnetic acoustical transducers for ultrasonic generation. The Journal of the acoustical society of America, 2006, 119(5): 2693-2701.
- Jossinet J. The impedivity of freshly excised human breast tissue. Physiological measurement, 1998, 19(1): 61.
- Joy M, Scott G, Henkelman M. In vivo detection of applied electric currents by magnetic resonance imaging. Magnetic resonance imaging, 1989, 7(1): 89-94.
- Kanai H. Propagation of spontaneously actuated pulsive vibration in human heart wall and in vivo viscoelasticity estimation. IEEE transactions on ultrasonics, ferroelectrics, and frequency control, 2005, 52(11): 1931-1942.
- Kanai H, Sato M, Koiwa Y, et al. Transcutaneous measurement and spectrum analysis of heart wall vibrations. IEEE Transactions on Ultrasonics, Ferroelectrics, and Frequency Control, 1996, 43(5): 791-810.
- Khang H S, Lee B I, Oh S H, et al. J-substitution algorithm in magnetic resonance electrical impedance tomography (MREIT): phantom experiments for static resistivity images. IEEE transactions on medical imaging, 2002, 21(6): 695-702.
- Kim S G, Richter W, Uğurbil K. Limitations of temporal resolution in functional MRI. Magnetic resonance in medicine, 1997, 37(4): 631-636.

- Kitazaki T, Kondo K, Yamakawa M, et al. Shear wavelength estimation based on inverse filtering and multiple-point shear wave generation. *Japanese Journal of Applied Physics*, 2016, 55(7S1): 07KF10.
- Kock W E. Radar, sonar, and holography: an introduction. Academic press, New York 1973.
- Konofagou E E, D'hooge J, Ophir J. Myocardial elastography—A feasibility study in vivo. *Ultrasound in medicine & biology*, 2002, 28(4): 475-482.
- Krestel E. Imaging Systems for Medical Diagnosis: Fundamentals and Technical Solutions-X-Ray Diagnostics-Computed Tomography-Nuclear Medical Diagnostics-Magnetic Resonance Imaging-Ultrasound Technology. *Imaging Systems for Medical Diagnosis: Fundamentals and Technical Solutions-X-Ray Diagnostics-Computed Tomography-Nuclear Medical Diagnostics-Magnetic Resonance Imaging-Ultrasound Technology*, by Erich Krestel (Editor), pp. 627. ISBN 3-8009-1564-2. Wiley-VCH, October 1990., 1990: 627.
- Krouskop T A, Dougherty D R, Vinson F S. A pulsed Doppler ultrasonic system for making noninvasive measurements of the mechanical properties of soft tissue. *Journal of rehabilitation research and development*, 1987, 24(2): 1.
- Kunita M. Range measurement in ultrasound FMCW system. *Electronics and Communications in Japan (Part III: Fundamental Electronic Science)*, 2007, 90(1): 9-19.
- Kunita M, Sudo M, Mochizuki T. Range measurement using ultrasound FMCW signals//2008 IEEE Ultrasonics Symposium. IEEE, 2008: 1366-1369.
- Lerner R M, Parker K J, Holen J, et al. Sono-elasticity: Medical elasticity images derived from ultrasound signals in mechanically vibrated targets//Acoustical imaging. Springer, Boston, MA, 1988: 317-327.
- Li C, Guan G, Huang Z, et al. Noncontact all-optical measurement of corneal elasticity. *Optics letters*, 2012, 37(10): 1625-1627.
- Li X, He B. Multi-excitation magnetoacoustic tomography with magnetic induction for bioimpedance imaging. *IEEE transactions on medical imaging*, 2010, 29(10): 1759-1767.
- Li X, Xu Y, He B. Magnetoacoustic tomography with magnetic induction for imaging electrical impedance of biological tissue. *Journal of Applied Physics*, 2006, 99(6).
- Li X, Yu K, He B. Magnetoacoustic tomography with magnetic induction (MAT-MI) for imaging electrical conductivity of biological tissue: a tutorial review. *Physics in Medicine & Biology*, 2016, 61(18): R249.
- Lobkis O-I and Weaver R-L. On the emergence of the Green's function in the correlations of a diffuse field. *The Journal of the Acoustical Society of America*, 2001, 110(6): 3011-3017.
- Meaney P M, Fanning M W, Li D, et al. A clinical prototype for active microwave imaging of the breast. *IEEE Transactions on Microwave Theory and Techniques*, 2000, 48(11): 1841-1853.
- Malmivuo P, Malmivuo J, Plonsey R. *Bioelectromagnetism: principles and applications of bioelectric and biomagnetic fields*. Oxford University Press, USA, 1995.

- Mariappan L, He B. Magnetoacoustic Tomography with Magnetic Induction: Bioimpedance reconstruction through vector source imaging. *IEEE transactions on medical imaging*, 2013, 32(3): 619-627.
- Mariappan L, Hu G, He B. Magnetoacoustic tomography with magnetic induction for high - resolution bioimpedance imaging through vector source reconstruction under the static field of MRI magnet. *Medical physics*, 2014, 41(2).
- Mariappan L, Shao Q, Jiang C, et al. Magneto acoustic tomography with short pulsed magnetic field for in-vivo imaging of magnetic iron oxide nanoparticles. *Nanomedicine: Nanotechnology, Biology and Medicine*, 2016, 12(3): 689-699.
- Meaney P M, Fanning M W, Li D, et al. A clinical prototype for active microwave imaging of the breast. *IEEE Transactions on Microwave Theory and Techniques*, 2000, 48(11): 1841-1853.
- Meltzer R S. Food and Drug Administration ultrasound device regulation: the output display standard, the “mechanical index,” and ultrasound safety. *Journal of the American Society of Echocardiography*, 1996, 9(2): 216-220.
- Miller D L. A review of the ultrasonic bioeffects of microsonation, gas-body activation, and related cavitation-like phenomena. *Ultrasound in medicine & biology*, 1987, 13(8): 443-470.
- Miller D L. Update on safety of diagnostic ultrasonography. *Journal of clinical ultrasound*, 1991, 19(9): 531-540.
- Misaridis T X, Gammelmark K, Jørgensen C H, et al. Potential of coded excitation in medical ultrasound imaging. *Ultrasonics*, 2000, 38(1-8): 183-189.
- Misaridis T X, Jensen J A. An effective coded excitation scheme based on a predistorted FM signal and an optimized digital filter//1999 IEEE Ultrasonics Symposium. Proceedings. International Symposium (Cat. No. 99CH37027). IEEE, 1999, 2: 1589-1593.
- Modeling & Imaging of Bioelectrical Activity: Principles and Applications. Springer Science & Business Media, 2005.
- Monchalin J P. Optical detection of ultrasound. *IEEE Transactions on Ultrasonics Ferroelectrics and Frequency Control*, 1986, 33: 485-499.
- Montalibet A, Jossinet J, Matias A. Scanning electric conductivity gradients with ultrasonically-induced Lorentz force. *Ultrasonic imaging*, 2001, 23(2): 117-132.
- Montalibet A, Jossinet J, Matias A, et al. Electric current generated by ultrasonically induced Lorentz force in biological media. *Medical and Biological Engineering and Computing*, 2001, 39(1): 15-20.
- Montalibet A. Etude du couplage acousto-magnétique: détection des gradients de conductivité électrique en vue de la caractérisation tissulaire. INSA Lyon, 2002.
- Morucci J P, Rigaud B. Bioelectrical impedance techniques in medicine part III: impedance imaging third section: medical applications. *Critical Reviews™ in Biomedical Engineering*, 1996, 24(4-6).

- Muthupillai R, Ehman R L. Magnetic resonance elastography. *Nature medicine*, 1996, 2(5): 601.
- Muthupillai R, Lomas D J, Rossman P J, et al. Magnetic resonance elastography by direct visualization of propagating acoustic strain waves. *science*, 1995, 269(5232): 1854-1857.
- Muthupillai R, Rossman P J, Lomas D J, et al. Magnetic resonance imaging of transverse acoustic strain waves. *Magnetic Resonance in Medicine*, 1996, 36(2): 266-274.
- Nan H, Arbabian A. Stepped-frequency continuous-wave microwave-induced thermoacoustic imaging. *Applied Physics Letters*, 2014, 104(22): 224104.
- Natarajan S, Singh R S, Lee M, et al. Accurate step-FMCW ultrasound ranging and comparison with pulse-echo signaling methods//*Medical Imaging 2010: Ultrasonic Imaging, Tomography, and Therapy*. International Society for Optics and Photonics, 2010, 7629: 76290D.
- Nightingale K, Soo M S, Nightingale R, et al. Acoustic radiation force impulse imaging: in vivo demonstration of clinical feasibility. *Ultrasound in medicine & biology*, 2002, 28(2): 227-235.
- O'Donnell M. Coded excitation system for improving the penetration of real-time phased-array imaging systems. *IEEE transactions on ultrasonics, ferroelectrics, and frequency control*, 1992, 39(3): 341-351.
- Ogawa S, Lee T M, Kay A R, et al. Brain magnetic resonance imaging with contrast dependent on blood oxygenation. *Proceedings of the National Academy of Sciences*, 1990, 87(24): 9868-9872.
- Ogawa S, Lee T M, Nayak A S, et al. Oxygenation - sensitive contrast in magnetic resonance image of rodent brain at high magnetic fields. *Magnetic resonance in medicine*, 1990, 14(1): 68-78.
- Ogawa S, Lee T M. Magnetic resonance imaging of blood vessels at high fields: in vivo and in vitro measurements and image simulation. *Magnetic resonance in medicine*, 1990, 16(1): 9-18.
- Oldenburg A L, Wu G, Spivak D, et al. Imaging and elastometry of blood clots using magnetomotive optical coherence tomography and labeled platelets. *IEEE Journal of Selected Topics in Quantum Electronics*, 2012, 18(3): 1100-1109.
- Ophir J, Cespedes I, Ponnekanti H, et al. Elastography: a quantitative method for imaging the elasticity of biological tissues. *Ultrasonic imaging*, 1991, 13(2): 111-134.
- Oyan M J, Hamran S E, Hanssen L, et al. Ultrawideband gated step frequency ground-penetrating radar. *IEEE Transactions on Geoscience and Remote Sensing*, 2012, 50(1): 212-220.
- Parks S I, Linzer M. Application of pulse compression techniques to medical ultrasound//*Application of Optical Instrumentation in Medicine V*. International Society for Optics and Photonics, 1976, 96: 349-354.
- Podilchuk C, Bajor M, Stoddart W, et al. Speckle reduction using stepped-frequency continuous wave ultrasound//*2012 IEEE Signal Processing in Medicine and Biology Symposium (SPMB)*. IEEE, 2012: 1-4.
- Polson M J R, Barker A T, Freeston I L. Stimulation of nerve trunks with time-varying magnetic

- fields. *Medical and Biological Engineering and Computing*, 1982, 20(2): 243-244.
- Psyk V, Risch D, Kinsey B L, et al. Electromagnetic forming - a review. *Journal of Materials Processing Technology*, 2011, 211(5): 787-829.
- Renzhiglova E, Ivantsiv V, Xu Y. Difference frequency magneto-acousto-electrical tomography (DF-MAET): Application of ultrasound-induced radiation force to imaging electrical current density. *IEEE transactions on ultrasonics, ferroelectrics, and frequency control*, 2010, 57(11): 2391-2402.
- Rossmann P J, Muthupillai R, Ehman R L. Driver device for MR elastography: U.S. Patent 5,952,828. 1999-9-14.
- Roth B J, Basser P J. Mechanical model of neural tissue displacement during Lorentz effect imaging. *Magnetic Resonance in Medicine: An Official Journal of the International Society for Magnetic Resonance in Medicine*, 2009, 61(1): 59-64.
- Roth B J, Basser P J, Wikswo J P. A theoretical model for magneto-acoustic imaging of bioelectric currents. *IEEE transactions on biomedical engineering*, 1994, 41(8): 723-728.
- Roth B J, Hobbie R K. A collection of homework problems about the application of electricity and magnetism to medicine and biology. *American Journal of Physics*, 2014, 82(5): 422-427.
- Roth B J, Luterek A, Puwal S. The movement of a nerve in a magnetic field: application to MRI Lorentz effect imaging. *Medical & biological engineering & computing*, 2014, 52(5): 491-498.
- Roth B J, Wikswo J P, Wen H, et al. Comments on "Hall Effect Imaging"[with reply]. *IEEE Transactions on Biomedical Engineering*, 1998, 45(10): 1294-1296.
- Roux P, Kuperman W-A, Colosi J-A, et al. Extracting coherent wave fronts from acoustic ambient noise in the ocean. *The Journal of the Acoustical Society of America*, 2004, 116(4): 1995-2003.
- Rueter D, Morgenstern T. Ultrasound generation with high power and coil only EMAT concepts. *Ultrasonics*, 2014, 54(8): 2141-2150.
- Sabra K G, Conti S, Roux P, et al. Passive in vivo elastography from skeletal muscle noise. *Applied physics letters*, 2007, 90(19): 194101.
- Sandrin L, Tanter M, Catheline S, et al. Shear modulus imaging with 2-D transient elastography. *IEEE transactions on ultrasonics, ferroelectrics, and frequency control*, 2002, 49(4): 426-435.
- Sandrin L, Fourquet B, Hasquenoph J-M, et al. Transient elastography: a new noninvasive method for assessment of hepatic fibrosis. *Ultrasound in medicine & biology*, 2003, 29(12): 1705-1713.
- Sarvazyan A P, Rudenko O V, Swanson S D, et al. Shear wave elasticity imaging: a new ultrasonic technology of medical diagnostics. *Ultrasound in medicine & biology*, 1998, 24(9): 1419-1435.
- Schenck J F. Safety of strong, static magnetic fields. *Journal of magnetic resonance imaging*, 2000, 12(1): 2-19.
- Schmitt J M. OCT elastography: imaging microscopic deformation and strain of tissue. *Optics express*, 1998, 3(6): 199-211.

- Shapiro N M, Campillo M, Stehly L, et al. High-resolution surface-wave tomography from ambient seismic noise. *Science*, 2005, 307(5715): 1615-1618.
- Siebner H R, Bergmann T O, Bestmann S, et al. Consensus paper: combining transcranial stimulation with neuroimaging. *Brain stimulation*, 2009, 2(2): 58-80.
- Sinkus R, Dargatz M W P, Kuhl C. Mechanical oscillator for MR elastography: U.S. Patent 6,833,703. 2004-12-21.
- Sinkus R, Lorenzen J, Schrader D, et al. High-resolution tensor MR elastography for breast tumour detection. *Physics in Medicine & Biology*, 2000, 45(6): 1649.
- Sinkus R, Tanter M, Catheline S, et al. Imaging anisotropic and viscous properties of breast tissue by magnetic resonance - elastography. *Magnetic Resonance in Medicine: An Official Journal of the International Society for Magnetic Resonance in Medicine*, 2005, 53(2): 372-387.
- Song A W, Takahashi A M. Displacement encoded imaging of small electric current//*Proc. Int. Soc. Mag. Reson. Med.* 2000, 8.
- Song A W, Takahashi A M. Lorentz effect imaging. *Magnetic resonance imaging*, 2001, 19(6): 763-767.
- Squire W D, Alsup J M. Linear signal processing and ultrasonic transversal filters. *NAVAL UNDERSEA RESEARCH AND DEVELOPMENT CENTER PASADENA CA*, 1969.
- Stove A G. Linear FMCW radar techniques//*IEEE Proceedings F (Radar and Signal Processing)*. IET Digital Library, 1992, 139(5): 343-350.
- Sun Z, Giammarinaro B, Birer A, Liu G, and Catheline S. Shear Wave Generation by Remotely Exciting Aluminum Patches with a Transient Magnetic Field and its Application in Ultrasound Elastography. *IEEE Transactions on Biomedical Engineering*, Under review.
- Sun Z, Giammarinaro B, Birer A, Liu G, and Catheline S. Ultrasound elastography with the shear wave Source generated by non-ferromagnetic conductive patches. To be submitted.
- Sun Z, Liu G, Xia H. Lorentz force electrical impedance tomography using pulse compression technique. *Chinese Physics B*, 2017, 26(12).
- Sun Z S, Liu G Q, Xia H. Lorentz Force Electrical Impedance Detection Using Step Frequency Technique. *Chinese Physics Letters*, 2018, 35(1): 014301.
- Sun Z, Liu G, Xia H, et al. Lorentz Force Electrical-Impedance Tomography Using Linearly Frequency-Modulated Ultrasound Pulse. *IEEE transactions on ultrasonics, ferroelectrics, and frequency control*, 2018, 65(2): 168-177.
- Surowiec A J, Stuchly S S, Barr J R, et al. Dielectric properties of breast carcinoma and the surrounding tissues. *IEEE Transactions on Biomedical Engineering*, 1988, 35(4): 257-263.
- Takeuchi Y. An investigation of a spread energy method for medical ultrasound systems: Part one: Theory and investigation. *Ultrasonics*, 1979, 17(4): 175-182.
- Takeuchi Y. Chirped excitation for <-100 dB time sidelobe echo sounding//1995 *IEEE Ultrasonics*

- Symposium. Proceedings. An International Symposium. IEEE, 1995, 2: 1309-1314.
- Tidswell A T, Gibson A, Bayford R H, et al. Validation of a 3D reconstruction algorithm for EIT of human brain function in a realistic head-shaped tank. *Physiological measurement*, 2001, 22(1): 177.
- Towe B C, Islam M R. A magneto-acoustic method for the noninvasive measurement of bioelectric currents. *IEEE Transactions on Biomedical Engineering*, 1988, 35(10): 892-894.
- Truong T K, Avram A, Song A W. Lorentz effect imaging of ionic currents in solution. *Journal of Magnetic Resonance*, 2008, 191(1): 93-99.
- Truong T K, Song A W. Finding neuroelectric activity under magnetic-field oscillations (NAMO) with magnetic resonance imaging in vivo. *Proceedings of the National Academy of Sciences*, 2006, 103(33): 12598-12601.
- Truong T K, Wilbur J L, Song A W. Synchronized detection of minute electrical currents with MRI using Lorentz effect imaging. *Journal of Magnetic Resonance*, 2006, 179(1): 85-91.
- Urban M W, Kinnick R R, Mehrmohammadi M, et al. Shear waves generated with magnetomotive force on an embedded sphere//2014 IEEE International Ultrasonics Symposium. IEEE, 2014: 723-726.
- Varghese T, Zagzebski J A, Lee Jr F T. Elastographic imaging of thermal lesions in the liver in vivo following radiofrequency ablation: preliminary results. *Ultrasound in medicine & biology*, 2002, 28(11-12): 1467-1473.
- Wen H, Bennett E, Shah J, et al. An imaging method using the interaction between ultrasound and magnetic field//1997 IEEE Ultrasonics Symposium Proceedings. An International Symposium (Cat. No. 97CH36118). IEEE, 1997, 2: 1407-1410.
- Wen H, Bennett E, Wiesler D G. Shielding of piezoelectric ultrasonic probes in Hall effect imaging. *Ultrasonic imaging*, 1998, 20(3): 206-220.
- Wen H, Shah J, Balaban R S. Hall effect imaging. *IEEE transactions on biomedical engineering*, 1998, 45(1): 119-124.
- Wen H. Feasibility of biomedical applications of Hall effect imaging. *Ultrasonic imaging*, 2000, 22(2): 123-136.
- Wen H. Volumetric Hall effect tomography - a feasibility study. *Ultrasonic imaging*, 1999, 21(3): 186-200.
- Woo E J, Lee S Y, Mun C W. Impedance tomography using internal current density distribution measured by nuclear magnetic resonance//Mathematical Methods in Medical Imaging III. International Society for Optics and Photonics, 1994, 2299: 377-386.
- Xia R, Li X, He B. Magnetoacoustic tomographic imaging of electrical impedance with magnetic induction. *Applied physics letters*, 2007, 91(8): 083903.
- Xu Y, Haider S, Hrbek A. Magneto-acousto-electrical tomography: A new imaging modality for electrical impedance//13th International Conference on Electrical Bioimpedance and the 8th

- Conference on Electrical Impedance Tomography. Springer, Berlin, Heidelberg, 2007: 292-295.
- Xu Y, He B. Magnetoacoustic tomography with magnetic induction (MAT-MI). *Physics in Medicine & Biology*, 2005, 50(21): 5175.
- Yeh W C, Li P C, Jeng Y M, et al. Elastic modulus measurements of human liver and correlation with pathology. *Ultrasound in medicine & biology*, 2002, 28(4): 467-474.
- Yu K, Shao Q, Ashkenazi S, et al. In Vivo Electrical Conductivity Contrast Imaging in a Mouse Model of Cancer Using High-Frequency Magnetoacoustic Tomography With Magnetic Induction (hfMAT-MI). *IEEE transactions on medical imaging*, 2016, 35(10): 2301-2311.
- Zemzemi C, Aichele J, Catheline S. Multiple sources array controls shear-wave field in soft tissue using time reversal. *Physics in Medicine & Biology*, 2018, 63(18): 18NT02.
- Zorgani A, Souchon R, Dinh A H, et al. Brain palpation from physiological vibrations using MRI. *Proceedings of the National Academy of Sciences*, 2015, 112(42): 12917-12921.
- Zorgani A, Zemzemi C, Daunizeau L, et al. Resolution limit of shear wave elastography. *Europhysics Letters*, under review.

Biography

SUN Zhishen

Date of Birth: May 1st, 1985

Place of Birth: Jiaxiang Country, Jining City, Shandong Province, P. R. China

Education:

Université Claude Bernard Lyon 1, Ecole Doctorale Interdisciplinaire Sciences Santé, Lyon, France

Ph.D. in Biological and medical engineering, expected in January 2020

University of Chinese Academy of Sciences, Institute of Electrical Engineering, Chinese Academy of Sciences (CAS), Beijing, P. R. China

Ph.D. in Theory and New Technology of Electrical Engineering, expected in January 2020

Graduate University of Chinese Academy of Sciences, Institute of Electronics, CAS, Beijing, P. R. China

M.S. in Signal and Information Processing, July 2011

Southwest University, College of Electronic and Information Engineering, Chongqing, P. R. China

B.S. in Communication Engineering, June 2008

Research and working experience:

2016.11- Present Laboratory of Therapeutic Applications of Ultrasound - LabTAU (INSERM Unit 1032), Lyon, France

Graduate research assistant on the ultrasound elastography with the shear wave source generated by the Lorentz force

2014.9 - 2019.6 Institute of Electrical Engineering, CAS, Beijing P. R. China

Graduate research assistant on the scanning electric conductivity gradients with ultrasonically-induced Lorentz force

2013.10 - 2014.9 Beijing Trans-Microwave Technology Co. Ltd, Beijing, P. R. China

System engineer on the CW/FMCW/FSK radar for detecting moving and stationary targets

2013.5 - 2014.9 Peking University, School of Electronics Engineering and Computer Science, Beijing, P. R. China

Research assistant on the Interferometric Synthetic Aperture Radar

2011.7 - 2012.7 Raisecom Technology Co. Ltd, Beijing, P. R. China

Software engineer on VOIP embedded system.

2008.9 - 2011.7 Key Laboratory of Electromagnetic Radiation and Sensing Technology, Institute of Electronics, CAS, Beijing P. R. China

Graduate research assistant on the FPGA-based ionosonde central control system

Honors and Awards:

Joint Ph.D. Student Scholarship granted by China Scholarship Council (2016)

Excellent Student Cadre University of Chinese Academy of Sciences (2016)

Excellent Tri-A student (twice) University of Chinese Academy of Sciences (2015, 2016)

Journal Publications:

1. Sun Zhishen, Giammarinaro B., Birer A., Liu G.*, and Catheline S.*. Shear Wave Generation by Remotely Exciting Aluminum Patches with a Transient Magnetic Field and its Application in Ultrasound Elastography. *IEEE Transactions on Biomedical Engineering*, Under review.
2. Sun Zhishen, Liu G.*, Xia H., and Catheline S.. Lorentz force electrical impedance tomography using linearly frequency-modulated pulse. *IEEE Transactions on Ultrasonics, Ferroelectrics, and Frequency Control*, 65.2 (2018): 168-177.
3. Sun Zhishen, Liu G.*, and Xia H.. Lorentz force electrical impedance tomography using pulse compression technique. *Chinese Physics B*, 26.12 (2017): 124302.
4. Sun Zhishen, Liu G. *, and Xia H.. Lorentz force electrical impedance detection using step-frequency technique. *Chinese Physics Letters* 35.1 (2018): 014301.
5. Sun Zhishen, Liu G.*, Guo L., Xia H., and Wang X.. Effect of the secondary process on mass point vibration velocity propagation in MAT and MAET. *Technology and Health Care* 24.s2 (2016): S683-S689.
6. Li Y., Liu G.*, Sun Zhishen, Xia H., and Xia Z.. Magneto-Acousto-Electrical Tomography for High Resolution Electrical Conductivity Contrast Imaging. *Journal of Medical Imaging and Health Informatics* 8.7 (2018): 1402-1407.

Patents:

1. Sun Zhishen, Catheline Stefan. Method and device for generating mechanical shear waves inside a soft material, shear wave imaging method and apparatus for the same. Exam. EP, JP, and US. filed on July 16th, 2018.

Conference Proceedings:

1. Sun Zhishen, Giammarinaro B., Birer A., Liu G., and Catheline S.*. Ultrasound Elastography with the shear wave source by magnetic induction: a phantom study. *Le 23eme Journee Scientifique de l'ediss*, October 11th 2018, Villeurbanne Frane. Oral Presentation
2. Sun Zhishen, Giammarinaro B., Birer A., Liu G., and Catheline S.*. Generation of shear waves in soft media by an electromagnetic actuator. *The 16th international tissue elasticity conference*, Sept. 9th 2018, Avignon France. Oral Presentation
3. Sun Zhishen, Liu G.*, Xia H., and Catheline S.. Lorentz force electrical impedance tomography using linearly frequency-modulated pulse. *Le 22eme Journee Scientifique de l'ediss*, October 12th 2017, Villeurbanne Frane. Oral Presentation
4. Sun Zhishen, Liu G. *, Guo L., Xia H., and Wang X.. Analysis of the Effect of the Secondary Process in Magneto-Acoustic Tomography and Magneto-Acousto-Electrical Tomography. *The 4th ICBE*, August 18th 2015, Shanghai China. Oral Presentation